Quantum state generation in mesoscopic systems of photons and atoms

by

Valerio Crescimanna

A thesis submitted to the University of Ottawa
in partial fulfillment of the requirements
for the degree of
Doctor of Philosophy in Physics

Department of Physics
Faculty of Science
University of Ottawa

Abstract

Besides the genuine interest in investigation of natural phenomena, the possibility of exploiting properties of quantum theory for technical improvements, by achieving a more efficient manipulation, readout and transmission of the information, resulted one of the main drivers that attracted the interest of public opinion and led to incessant research in this field both from public and private organizations.

In principle, quantum superposition and entanglement, once handled the intrinsic limits of quantum theory, such as no-cloning theorem and uncertainty principle, would guarantee a scaling advantage of quantum computation over its classical counterpart. While the quantum advantage becomes more important with the dimensionality of the algorithm that is used, the computation itself becomes proportionally more sensitive to the undesired interactions with the environment and thus prone to errors. The research conducted to prove the working principles of quantum schemes, being sources, algorithm or measurements is thus conveniently realized on mesoscopic scale system where the dimension cardinality of the setup is big enough to show a significative advantage over classical schemes but constrained as well to be described either analytically or through numerical simulations, or experimentally realized in a research laboratory. Specific criteria for efficient quantum computation have been introduced in 1996 by David DiVincenzo, they include conditions on the physical system to encode the information, the ability to prepare the system in a given quantum states, long coherence times, a universal set of quantum gates, and the ability of measuring the qubits the state preparation. This thesis deals with the second of the DiVincenzo's criteria, by investigating the state preparation of quantum states using linear optics and Rydberg atoms. Disposing of universal and efficient sources of quantum states is indeed crucial to perform versatile fault tolerant quantum compu-

tation. In fact, producing quantum states with high fidelity allows to perform more accurate computation. Similarly, the source must be reliable to guarantee that the least amount of decoherence, occurs while waiting for the next quantum state. Universal quantum computation in photonic implementation can be realized only with non-gaussian resources. In this thesis, we propose to alternative schemes to produce non-Gaussian quantum states to produce any general non-Gaussian quantum state with higher levels of fidelity and success probability compared to those achievable by the current conditional sources. It is given also an exact description of the Gottesman-Kitaev-Preskill states produced by the breeding protocol, comparing the results with numerical simulations and the Gaussian Random Noise description that is used to parametrize the non-ideal GKP states produced by this protocol. Finally, a universal protocol to prepare a quantum states or circuit with arbitrary fidelity using Rydberg atoms is introduced.

Acknowledgments

This thesis would not have been possible without the supervision, encouragement, help, and support of the many people I had the luck to encounter during the program.

First, I am thankful to my supervisor Khabat Heshami, for his constant guidance, support, and encouragement.

Invaluable companions in this process have been all the past and present members and collaborators who have mentored me, introduced me to new concepts, helped, and motivated me over these years: Aaron, Fred, Utkarsh, Jacob, Xiaochin, Mikka, Jasper, Guillaume, Anaelle, Milica, Arezoo, Noah, Zahra, Tamal, Alex, Tom, Dharmik, Juba, and Nira.

I would also like to thank Raj Patel for hosting me and overseeing my work during my stay at Imperial College in London. In this regard, I would like to thank all the colleagues who welcomed me and helped me settle in there: Zheangao, Matthieu, Gerard, Ewan, Aonan, Steven, Shang, Riccardo, Mikhael and Yazeed.

Similarly, I am grateful to Stephan De Bievre for kindly hosting me at the University of Lille. I would like to take this opportunity to thank all those who made my stay in France enjoyable and productive: Giuseppe, Christopher, Mathhieu and Mateo.

I acknowledge the financial support of the Natural Sciences and Engineering Research Council of Canada (NSERC).

I acknowledge the use of the generative AI tools ChatGPT by OpenAI, and Gemini by Google, which assisted in grammar correction and limited rephrasing throughout the writing process.

Statement of Originality and Contributions

To the best of his knowledge, the author states that the work described in this PhD thesis constitutes original research in the field of physics. Below, we provide the collaborative contributions of each participant for every publication in this thesis.

Chapter 2 contains the article entitled "Seeding Gaussian boson samplers with single photons for enhanced state generation", published in *Physical Review A* in 2024. V. Crescimanna, A. Goldberg, and K. Heshami conceived the idea for this work. V. Crescimanna developed the model for the paper and the `Python` simulations, collected and processed the data, drafted the original manuscript and created the figures for the paper. A. Goldberg, and K. Heshami supervised the project. V. Crescimanna handled the paper submission process and correspondence with the editor. All authors reviewed and contributed to the submitted manuscript.

Chapter 3 contains the article entitled "Adaptive Non-Gaussian Quantum State Engineering", published in *Physical Review A* in 2025. V. Crescimanna, S. Yu, and R. B. Patel conceived the idea for this work. V. Crescimanna developed the model for the paper and the `Python` simulations, collected and processed the data, drafted the original manuscript and created the figures for the paper. K. Heshami, and R. B. Patel supervised the project. V. Crescimanna handled the paper submission process and correspondence with the editor. All authors reviewed and contributed to the submitted manuscript.

Chapter 4 contains the article entitled "Exact simulation of realistic Gottesman-Kitaev-Preskill cluster states", published in *Physical Review A* in 2025. The idea of the manuscript arose from discussion between all the authors. V. Crescimanna developed the `Python` simulations of the quantum states in Fock basis representation and performed the analytical simulations of Gaussian Random Noise states. M. Banić

performed the theoretical calculations to find the exact description of the model and wrote the `Python` code to calculate the exact solutions. M. Banić, and V. Crescimanna collected and processed the data for the paper. M. Banić drafted the original manuscript. M. Banić, and V. Crescimanna created the figures for the paper. J. E. Bourassa, R. N. Alexander, and K. Heshami supervised the project. M. Banić handled the paper submission process and correspondence with the editor. All authors reviewed and contributed to the submitted manuscript.

Chapter 5 contains the article entitled "Quantum Control of Rydberg Atoms for Mesoscopic Quantum State and Circuit Preparation", published in *Physical Review Applied* in 2023. J. Taylor, A. Goldberg, and K. Heshami conceived the idea for this work. J. Taylor developed the `Python` simulations. J. Taylor, and V. Crescimanna collected and processed the data for the paper. J. Taylor, and V. Crescimanna drafted the original manuscript and created the figures for the paper. A. Goldberg, and K. Heshami supervised the project. V. Crescimanna and A. Goldberg handled the paper submission process and correspondence with the editor. All authors reviewed and contributed to the submitted manuscript.

Contents

List of Figures

Acronyms

CNOT controlled-NOT

CV continuous variable

DV discrete variable

FTQC fault-tolerant quantum computing

GBS Gaussian boson sampling

GKP Gottesmann-Kitaev-Preskill

GRN Gaussian random noise

MBQC measurement-based quantum computating

PNR photon-number-resolving

POVM probability-operator-valued measure

QA quantum annealing

QAOA quantum approximate optimization algorithm

Chapter 1

Introduction

1.1 Overview

In this chapter, we present some introductory concepts that are used in the works discussed throughout the remainder of the thesis. First, in Section 1.2, we introduce quantum states and the Dirac notation. In the subsequent Section 1.3, we describe the time evolution of quantum states, which is implicitly used throughout all chapters and applied more extensively in Chapter 5, which focuses on the control of Rydberg atoms. Then, in Section 1.4, we give a presentation of measurement theory in order to provide the minimal theoretical background to the measures used in the sources of chapters 2, 3, and 4. Similarly, in Section 1.5 discrete variables and continuous variables encodings are briefly introduced; these encodings are employed in chapter 5 and chapters 2, 3, and 4 respectively. Two more extended sections on Quantum optics (Sec. 1.6) and linear optics (Sec. 1.7) are used to describe properties and limitations of the implementation used in chapters 2, 3, and 4. In Section 1.8, we introduce the description of quantum states in phase space through quasi-probability distributions, while in Section 1.9, we outline how the Gaussian operations introduced in Section 1.7

act on the phase space representations of quantum states. The section 1.10 that follows outlines how quasi-probability distributions are affected by the measurements, which is relevant to explain how the sources of chapters rely on the measurement of some modes of a multi-mode states. Then non-Gaussian states are defined in section 1.11, we give two classical examples of non-Gaussian states that are then targeted to benchmark the sources proposed in Chapters 2, 3, and 4. Section 1.12 presents the source, which is later modified according to the alternatives proposed in Chapters 2 and 3, as well as the state generation scheme explored in the work of Chapter 4. Finally, section 1.13 is dedicated to the introduction of the Rydberg Physics used to develop the theory proposed in Chapter 5.

1.2 Quantum States

Every quantum state is fully described by a complex function $\psi(x,t)$ [1].$\psi(x,t)$ is known as the wavefunction associated to the state of the system and its intensity $|\psi(x,t)|^2$ provides the probability of finding the system at position x at time t. It is custom to think of the quantum states as vectors in the Hilbert space $\mathcal{H}$ of functions. The Hilbert space is equipped with a complete inner product $\langle\ ,\ \rangle$ between its elements ϕ and ψ [2]

$$\langle\phi,\psi\rangle = \int_{\mathbb{R}} \phi^*(x)\psi(x)\mathrm{d}x. \tag{1.1}$$

Two states ϕ, and ψ are orthogonal between each other if their inner product $\langle\phi,\psi\rangle = 0$.

By introducing an orthonormal basis of the Hilbert space $\mathcal{H}$, $\{\phi_1\ \ldots,\phi_N\}$, such

that $\langle \phi_i, \phi_j \rangle = \delta_{i,j}$, then any state in $\mathcal{H}$ can be defined as

$$\psi(x) = \sum_{i=1}^{N} c_i \phi_i(x), \quad \forall x \in \mathbb{R}, \tag{1.2}$$

such that $\langle \phi_k, \psi \rangle = c_k$, and $\sum_{i=1}^{N} |c_i|^2 = 1$.

The state $\psi(x,t)$ can be conveniently defined using the Bra-ket notation introduced by Dirac $\psi \equiv |\psi\rangle$ [3]. With Dirac notation the inner product between the states $|\psi\rangle$, and $|\phi\rangle$ is written as $\langle \phi | \psi \rangle$ while Eq. (1.2) can be rewritten as $|\psi\rangle = \sum_{i=0}^{n} c_i |\phi_i\rangle$. However, in general, not all system can be described with the state vector shown above, as some quantum systems may be in a statistical mixture of two or more quantum states. Given p_i the probability of the system of being in the state $|\psi_i\rangle$, $i = 1, \ldots, N$, the density operator of the state ρ is defined as

$$\rho = \sum_{i=1}^{N} p_i |\psi_i\rangle\langle\psi_i| . \tag{1.3}$$

Thus, ρ is defined as the linear combination of the outer products of the possible states weighted by the the probability of the system being in that state. Given that the density operator in Eq. (1.3) is Hermitian, the spectral theorem allows one to write the state via its spectral decomposition

$$\rho = \sum_{i=1}^{N} \lambda_i |\phi_i\rangle\langle\phi_i| , \tag{1.4}$$

where $|\phi_i\rangle$ is the orthonormal basis of eigenstates of ρ. The description in terms of the density operator is general, and can be used with either a partial or complete knowledge of the system [4]. In the case the state of the system is known with $p = 1$ to be $|\psi\rangle$, then the density operator reduced to $\rho = |\psi\rangle\langle\psi|$. In general, expanding $|\psi\rangle$

in a basis like done in Eq. (1.2), the expansion of ρ becomes

$$\rho(|\psi\rangle) = \sum_{ij} c_i c_j^* \, |\phi_i\rangle\langle\phi_j| \, . \tag{1.5}$$

Just by comparing Eq. (1.3) and Eq. (1.5), it is not trivial to distinguish the density matrix corresponding to a state $|\psi\rangle$ which is assigned with certainty, and the density matrix defined by a statistical ensemble of states. In quantum mechanics, the purity of a state is a quantity introduced precisely to determine this distinction and quatify the degree of ignorance on the state of the system. The purity $\mathcal{P}$ of a density operator ρ is defined as $\mathcal{P}(\rho) = \mathrm{Tr}\{\rho^2\} \leq 1$. When $\mathcal{P}(\rho) = 1$, then the state is known with certainty and the state is called pure. Otherwise, when $\mathcal{P}(\rho) < 1$ system is said to have a mixed state. The minimum value of $\mathcal{P}$ is $1/d$ where d is the dimension of the Hilbert space upon which the state is defined. A state ρ with $\mathcal{P}(\rho) = 1/d$ is maximally mixed.

The scalar product in Eq. (1.1) can be used also as a measure of similarity between two quantum states, which is known as fidelity. The fidelity $\mathcal{F}$ between two pure states $|\psi\rangle$ and $|\phi\rangle$ is given by $\mathcal{F} = |\langle\psi|\phi\rangle|^2$. In general, for any mixed states ρ, σ we have that $\mathcal{F} = \left(\mathrm{Tr}\left[\sqrt{\sqrt{\sigma}\rho\sqrt{\sigma}}\right]\right)^2$

The description given so far and introduced with Eq. (1.2) has been given using discrete variables c_n and a discrete, either finite or infinite set of vectors $\{\phi_1, \ldots, \phi_n\}$ forming the basis of $\mathcal{H}$. We can extend the description made so far to continuous variable description. For example, we can introduce a continuous variable $a \in \mathbb{R}$ and define a new orthogonal basis of $\mathcal{H}$, $\{|a\rangle \mid a \in \mathbb{C}\}$ such that $\langle b|a\rangle = \delta(a - b)$. Any state in $\mathcal{H}$ can be defined in this basis as

$$|\psi\rangle = \int_{\mathbb{R}} \psi(a) \, |a\rangle \, . \tag{1.6}$$

The position x in the quadrature space is one example for the continuous variable a one can choose. We should observe that Discrete Variable (DV) and Continuous Variable (CV) description are not mutually exclusive, since in general any state $|\psi\rangle$ can be described in either way. However, the convenience of either of the two approaches depend on the particular states considered and the manipulations foreseen on these states.

Quantum states are used in all the chapters of this thesis. Chapters 2 and 3 introduce sources of quantum states. Chapter 4 gives an exact description of physical states generated via a specific generation protocol known as Schrödinger cat breeding. Similarly, quantum states are the target of the control of Rydberg atoms described in Chapter 5.

1.3 Quantum Evolution

1.3.1 Schrödinger equation

Describing the evolution of a state serves to determine the state of a system at a time t given knowledge of the state at a previous time t_0 with $t_0 < t$ [5]. To do this, one must determine the time-evolution operator $\widehat{U}(t, t_0)$ which transforms the state $|\psi(t_0)\rangle$ into the state $|\psi(t)\rangle$ such that

$$|\psi(t)\rangle = \widehat{U}(t, t_0)\,|\psi(t_0)\rangle\,. \tag{1.7}$$

For probability conservation we expect that for any $|\psi(t_0)\rangle$

$$\langle\psi(t)|\psi(t)\rangle = \langle\psi(t_0)|\widehat{U}^{\dagger}(t, t_0)\widehat{U}(t, t_0)|\psi(t_0)\rangle = \langle\psi(t_0)|\psi(t_0)\rangle\,, \tag{1.8}$$

and the last equation is fulfilled only if $\widehat{U}^{\dagger}(t,t_0)\widehat{U}(t,t_0) = \mathbb{I}$, which means that the time-evolution operator must be unitary. Moreover, another condition expected from a properly defined time-evolution operator is that it satisfies the composition property. This means that given the times $t_0 < t_1 < t_2$ one has that

$$\widehat{U}(t_2,t_1)\widehat{U}(t_1,t_0) = \widehat{U}(t_2,t_0). \tag{1.9}$$

The infinitesimal transformation after a time $\mathrm{d}t$ will be given by

$$\widehat{U}(t_0+\mathrm{d}t,t_0) = \mathbb{I} - i\widehat{\Omega}(t_0)\mathrm{d}t, \tag{1.10}$$

where $\widehat{\Omega}(t_0)$ is Hermitian to guarantee that $\widehat{U}$ is unitary. By analogy with classical mechanics, we can postulate that the generator of the time evolution $\widehat{\Omega}(t_0)$ is given by the Hamiltonian of the system such that $\widehat{\Omega}(t_0) = \widehat{H}(t_0)/\hbar$ [6], such that, if $\widehat{H}(t_0) \equiv \widehat{H}$ is time independent, Eq. (1.7) is equivalent to

$$|\psi(t)\rangle = e^{-i\widehat{H}(t-t_0)/\hbar}\,|\psi(t_0)\rangle \tag{1.11}$$

which is the solution of the Schrödinger equation that describes the evolution of the state

$$i\hbar\frac{\partial\,|\psi\rangle}{\partial t} = \widehat{H}\,|\psi\rangle\,. \tag{1.12}$$

1.3.2 Heisenberg Picture

So far, we have considered the quantum state of the system as changing under the action of the time evolution operator. This interpretation of the system's dynamics is known as the Schrödinger picture. From the perspective of the observer, the

measurable properties of the system may change over time. If, for example, $\widehat{Q}$ is the observable under investigation, then one can describe the system's dynamics by keeping the quantum state $|\psi\rangle$ fixed and treating the observable $\widehat{Q}$ as a time-dependent operator, whose evolution is governed by the Hamiltonian $\widehat{H}$. Anticipating the theory of measurement discussed in Sec. 1.4, we now consider what it means to measure an observable $\widehat{Q}$ on a quantum state evolving under the influence of a Hamiltonian.

1.3.2.1 Observables and operators

Following a probabilistic interpretation of the wave function ψ, one has that the expectation value of any observable physical quantity Q whose value depends on the coordinate x can be determined by [7]

$$\langle Q\rangle = \int_{\mathbb{R}} Q(x)|\psi(x)|^2 \mathrm{d}x = \int_{\mathbb{R}} \psi^*(x)Q(x)\psi(x)\mathrm{d}x = \left\langle \psi \middle| \widehat{Q}\psi \right\rangle \tag{1.13}$$

where the last equality comes from the definition of Eq. (1.1), and the operator $\widehat{Q}$ is introduced to satisfy the equation. Because of the linearity in quantum mechanics [8], every operator $\widehat{Q}$ can be expressed as a matrix in the Hilbert space of the quantum states such that $\left|\widehat{Q}\psi\right\rangle \equiv \widehat{Q}\,|\psi\rangle$. Since the value of a physical observable is real, we have that [1] $\left\langle \psi \middle| \widehat{Q}\psi \right\rangle = \left\langle \widehat{Q}\psi \middle| \psi \right\rangle = \langle\psi|\widehat{Q}^\dagger|\psi\rangle$ thus proving that the operator $\widehat{Q}$ associated to any physical observable is Hermitian $\widehat{Q}^\dagger = \widehat{Q}$. So in general, the operational definition of the expecation value of the operator $\widehat{Q}$ on the state $|\psi\rangle$ is given by

$$\left\langle \widehat{Q} \right\rangle_\psi = \langle\psi|\widehat{Q}|\psi\rangle\,. \tag{1.14}$$

Using the Schrödinger picture, the expectation value evolves accordingly to the evolution of the state such that

$$\left\langle \widehat{Q} \right\rangle_{t_0} = \langle \psi(t_0)|\widehat{Q}|\psi(t_0)\rangle \rightarrow \left\langle \widehat{Q} \right\rangle_{t} = \langle \psi(t)|\widehat{Q}|\psi(t)\rangle = \langle \psi(t_0)|\widehat{U}^{\dagger}(t,t_0)\widehat{Q}\widehat{U}(t,t_0)|\psi(t_0)\rangle \,. \tag{1.15}$$

Instead, if in Eq. (1.15), we take the state time independent such that $|\psi(t_0)\rangle = |\psi_0\rangle$, we observe that the time evolution affects the observable itself that trasforms as

$$\widehat{Q}(t) = \widehat{U}^{\dagger}(t,t_0)\widehat{Q}(t_0)\widehat{U}(t,t_0). \tag{1.16}$$

which is the solution to the Heisenberg equation of motion

$$\frac{\partial \widehat{Q}}{\partial t} = \frac{1}{i\hbar}\left[\widehat{Q}, \widehat{H}\right]. \tag{1.17}$$

The interpreation of the dynamics, in which the states are time constant and the operators are time dependent is known as Heisenberg picture.

1.3.3 Interaction Picture

Up to this point, we supposed to deal with a time constant Hamiltonian. In the more general case of a time dependent Hamiltonian, it can be useful to use not the Shrödinger nor the Heisenberg picture but introduce the so called Interaction picture. First of all, it is convenient to separate the Hamiltonian $\widehat{H}(t)$ into a constant term $\widehat{H}_0$ and a time-dependent term $\widehat{V}(t)$ such that

$$\widehat{H}(t) = \widehat{H}_0 + \widehat{V}(t). \tag{1.18}$$

In the interaction picture both the states and the observables are time-dependent. In particular, supposing $t_0 = 0$ the states are defined as

$$|\psi(t)\rangle_I = e^{-i\widehat{V}(t)/\hbar} |\psi_0\rangle_I = e^{i\widehat{H}_0 t/\hbar} |\psi(t)\rangle_S \,. \tag{1.19}$$

where the subscripts S and I are the labels for the states defined in the Schrödinger, and interaction picture respectively. The operators instead evolve as

$$\widehat{Q}_I(t) = e^{i\hat{H}_0 t/\hbar} \widehat{Q}_S e^{-i\hat{H}_0 t/\hbar}. \tag{1.20}$$

Thus, it follows that the time-evolution of the state is described by the solution of the following equation

$$i\hbar \frac{\partial}{\partial t} |\psi\rangle_I = \widehat{V}_I(t) |\psi\rangle_I \,, \tag{1.21}$$

while the observable $\widehat{Q}_I(t)$ solves

$$\frac{\partial \widehat{Q}_I}{\partial t} = \frac{1}{i\hbar} \left[\widehat{Q}_I, \widehat{H}_0\right] \tag{1.22}$$

1.3.4 Quantum gates

Quantum information processing represents one of the most promising applications of quantum theory. Superposition and entanglement can, in fact, be used effectively to achieve a speed-up over classical simulation, as proven with Shor's algorithm [9]. In continuity with classical computation based on semiconductors, where binary information bits are processed, quantum computation has similarly been historically proposed in terms of the generation, control, and measurement of quantum bits, known as qubits [10]. In this framework, information is encoded in the states of a two-level quantum system, which, by analogy with the classical case, we can label

as $|0\rangle$ and $|1\rangle$. In general, the state of the system will be in a superposition of the two states $|\psi\rangle = \alpha\,|0\rangle + \beta\,|1\rangle$ such that $|\alpha|^2 + |\beta|^2 = 1$. Usually the state $|\psi\rangle$ is given in terms of its vector representation $(\alpha, \beta)^\intercal$. As for state manipulation, this is performed via unitary operations, among the most famous of which are the Pauli gates $\widehat{\boldsymbol{\sigma}} = \left(\widehat{X}, \widehat{Y}, \widehat{Z}\right)^\intercal$, whose matrix representation is given by

$$\widehat{X} = \begin{pmatrix} 0 & 1 \\ 1 & 0 \end{pmatrix}, \quad \widehat{Y} = \begin{pmatrix} 0 & -i \\ i & 0 \end{pmatrix}, \quad \widehat{Z} = \begin{pmatrix} 1 & 0 \\ 0 & -1 \end{pmatrix}. \tag{1.23}$$

It is possible to prove that a general operation on a single qubit state is given by

$$\widehat{U}(\alpha, \theta) = \exp(i\alpha)\widehat{R}_{\boldsymbol{n}}(\theta) \tag{1.24}$$

where $\boldsymbol{n}$ is a three-dimensional unit vector of coordinates (n_x, n_y, n_z), and $\widehat{R}_{\boldsymbol{n}}(\theta)$ is given by

$$\widehat{R}_{\boldsymbol{n}}(\theta) = \cos(\theta/2)\widehat{\mathbb{I}} - i\sin(\theta/2)\boldsymbol{n}\cdot\widehat{\boldsymbol{\sigma}}. \tag{1.25}$$

Other relevant single qubit gates are the Hadamard gate $\widehat{H}$, the phase gate $\widehat{S}$ and the $\pi/8$ gate $\widehat{T}$ with matrix representation

$$\widehat{H} = \frac{1}{\sqrt{2}}\begin{pmatrix} 1 & 1 \\ 1 & -1 \end{pmatrix}, \quad \widehat{S} = \begin{pmatrix} 1 & 0 \\ 0 & i \end{pmatrix}, \quad \widehat{T} = \exp\left(i\pi/8\right)\begin{pmatrix} e^{-i\pi/8} & 0 \\ 0 & e^{i\pi/8} \end{pmatrix}. \tag{1.26}$$

For multi-qubit operations, the unitary matrices can be expressed as tensor products of multiple single-qubit operations. However, some multi-qubit operations cannot be written in this form, and the concept of controlled or entangling gates must instead

be introduced. A well-known example of a two-qubit gate is the controlled-NOT gate

$$\mathrm{CNOT} = \begin{pmatrix} 1 & 0 & 0 & 0 \\ 0 & 1 & 0 & 0 \\ 0 & 0 & 0 & 1 \\ 0 & 0 & 1 & 0 \end{pmatrix}. \tag{1.27}$$

The Hadamard, Phase, and CNOT gates defined in Eqs. (1.26) and (1.27) form a generating set for the Clifford group $\mathbf{C}$. By definition, Clifford gates map tensor products of Pauli matrices to tensor products of Pauli matrices $\mathbf{P}_n$ via conjugation, which means that for any n-qubit gate V in the Clifford group $\mathbf{C}_n$, we have $VP_iV^\dagger = P_j$ for some $P_i, P_j \in \mathrm{P}_n$. According to the Gottesman-Knill theorem [11], however, quantum computation with Clifford gates alone cannot guarantee any quantum advantage. Specifically, a computation realized using only initial states in the computational basis, Clifford gates and measurements of observables in the Pauli group, can be simulated efficiently in a classical computer. The stabilizer formalism is taken into account to prove the theorem. In the stabilizer formalism, a group of operators, the stabilizers, is associated to the quantum state. In fact, considering this biunivocal correspondence between states and stabilizers, the evolution of the state can be studied looking into the evolution of the stabilizers that can be efficiently simulated. Clifford and T gates form, instead, a universal set of operations, meaning that any unitary operation can be approximated to arbitrary precisions using only these gates. In particular, according to the Solovay-Kitaev theorem any single qubit gate can be approximated to an accuracy ϵ using $O(\log^c(1/\epsilon))$ with $c \sim 2$ [12].

1.3.4.1 Quantum Approximate Optimization Algorithm

Although Pauli gates, T gates, phase gates, and one-controlled gates can be used to realize any unitary operation on multimode states, the composition of operations required to obtain a specific unitary matrix or to generate a particular quantum state is not always trivial to determine. A possible solution to generate a given target quantum states relies on the evolution of an accessible quantum state under a time dependent Hamiltonian.

A classic example of algorithm that realizes this task is Quantum Annealing (QA) [13]. The goal of QA is to find the ground state of a cost Hamiltonian $\widehat{H}_Z$ which is diagonal in the computational basis, such that, for any state $|\boldsymbol{y}\rangle$ in the computational basis, $\widehat{H}_z |\boldsymbol{y}\rangle = f(\boldsymbol{y}) |\boldsymbol{y}\rangle$. In QA, the initial quantum state $|\psi_{\text{in}}\rangle$ is prepared in a superposition of all the possible solutions of the ground state problem for the Hamiltonian $\widehat{H}_Z$. The initial state $|\psi_{\text{in}}\rangle$ is the ground state of the mixing Hamiltonian $\widehat{H}_X$ [14, 15]. The initial state $|\psi_{\text{in}}\rangle$ is then evolved under the time-dependent Hamiltonian

$$\widehat{H}(t) = \left(1 - \frac{t}{\tau}\right) \widehat{H}_X + \frac{t}{\tau} \widehat{H}_Z, \tag{1.28}$$

such that for a sufficiently long time τ, the resulting state is indeed an eigenstate of $\widehat{H}_Z$. Now, to evolve the system under the two non-commuting Hamiltonians independently, the Suzuki-Trotter decomposition must be used, which corresponds to an infinite number of alternating steps of applications of each of the two Hamiltonians $\exp\left(\widehat{A} + \widehat{B}\right) = \lim_{p\to\infty}(e^{\widehat{A}/p} e^{\widehat{B}/p})^p$. However, the solution is exact only as $p \to \infty$. The Quantum Approximate Optimization Algorithm (QAOA) [16, 17], on the other

hand, aims to reach the state with a finite number of steps p,

$$|\psi_f\rangle = \exp\Big(-i\alpha_p \widehat{H}_X\Big) \exp\Big(-i\beta_p \widehat{H}_Z\Big) \ldots \exp\Big(-i\beta_1 \widehat{H}_Z\Big) |\psi_i\rangle \tag{1.29}$$

where the coefficients α_i, β_i are classically optimized to maximize the fidelity between the generated state $|\psi_f\rangle$ and the target state. In fact, if the mixing and cost Hamiltonians are defined as follows

$$\begin{aligned} \widehat{H}_X &= \sum_i \widehat{X}_i, \\ \widehat{H}_Z &= \sum_i \beta^{(0)} \widehat{Z}_{2i} + \beta^{(1)} \widehat{Z}_{2i+1} + \gamma^{(0)} \widehat{Z}_{2i} \widehat{Z}_{2i+1} + \gamma^{(1)} \widehat{Z}_{2i+1} \widehat{Z}_{2i} \\ &\equiv \beta^{(0)} \widehat{H}_Z^{(0)} + \beta^{(1)} \widehat{H}_Z^{(1)} + \gamma^{(0)} \widehat{H}_{ZZ}^{(0)} + \gamma^{(1)} \widehat{H}_{ZZ}^{(1)}, \end{aligned} \tag{1.30}$$

it can be shown that the algorithm is universal, meaning it can be used to reach any state, even when the target is not the eigenstate of any Hamiltonian. In Eq. (1.30), $\widehat{X}_i$ and $\widehat{Z}_i$ represent the application of the $\widehat{X}$ and $\widehat{Z}$ gates as they are introduced in Eq. (1.23) to the i-th qubit of the multiqubit state $|\psi_i\rangle$. Coefficient β is used for the single-qubit operations, while coefficient γ is used for the two-qubit operations. The superscripts (0), and (1) are used to distinguish the real coefficients β, and γ depending on wether the corresponding gates are applied to qubits or pairs of qubits labeled by even or odd indices. For pairs of qubit, the superscript (0) is used if the first gate is applied to an even qubit, while the index (1) is used when the first gate of the pair is applied to an odd qubit.

Quantum evolution is implicitly used in all the chapter of the thesis. The evolution of quantum states in the Schrödinger picture is used in Chapter 5 to describe the control of Rydberg atoms via QAOA, aimed at generating multi-qubit states with high fidelity.

1.4 Measurements

1.4.1 Classical measurements

Given a classical physical system, certain variables correspond to measurable features that characterize the system. These features distinguish it from other systems for which the same variables can also be defined and measured. The set of variables that describe the system is referred to as its configuration. To each physical system, one can then associate a state, defined as the collection of probability distributions assigned to the system's measurable variables. For example, the state of the system associated with the variable X in the configuration space $\mathbb{S}$ is given by the probability distribution $P(x)$, which is the probability that the system has $X = x$. If X is a continuous variable, then $P(x)$ would be a probability density. The state of the system thus defines the degree of knowledge of the system by the observer and is not independent of the observer, to the point that different states may be attributed to the same physical system by different observers. The maximum level of knowledge is acquired when the observer can assign a single value to each variable in the configuration space of the state. Such knowledge about the system is obtained through measurements of it. For a classical system, it is reasonable to assume that each of the variables in the configuration space can be measured independently. The process of measuring a variable of the state can be modeled as follows: A copy of the system under investigation is subjected to a measurement apparatus. This measurement apparatus will be able to provide a result that is a function G of the unknown variable X and of a noise-related variable Ξ, so that the observer is provided with the variable $Y = G(X, \Xi)$ by the measurement apparatus. As an example, if x is the value of the variable X and $\Xi = \xi$, then the value observed by the measurement apparatus is

$y = G(x, \xi)$. Here we assume that neither the measurement nor the noise affects the system under investigation. Nevertheless, we expect that the measurement changes the state of the system. Bayesian inference can in fact be used to understand how the measurement affects the state of the system. Given two events A and B, the probability of A given B, $P(A \mid B)$, is related to the probability of the intersection between A and B, $P(A \cap B)$, via the following equation [18]

$$P(A|B) = \frac{P(A \cap B)}{P(B)} \tag{1.31}$$

From Eq. (1.31), it is straightforward to show that the conditional probability $p(x|y)$ is given by

$$p(x|y) = \frac{p(y|x)p(x)}{p(y)}. \tag{1.32}$$

Where $p(y)$ is the normalization factor

$$p(y) = \sum_x p(y|x)p(x) \tag{1.33}$$

If x and y of Eq. (1.32) are the possible outcomes of variables X and Y of the system configuration space and of the measurement apparatus, then the conditional probability $p(x|y)$ corresponds to the state of the system as it has been modified by the measure of y. Observing that y depends on x and ξ through the function G such that $y = G(x, \xi)$, we can write

$$p(y|x) = \sum_\xi p(y|x, \xi)p(\xi) = \sum_\xi \delta_{y,G(x,\xi)}p(\xi). \tag{1.34}$$

If it is possible to define the inverse function G^{-1} such that $G^{-1}(x,y)=\xi$, then

$$p(y|x)=\sum_{\xi}\delta_{\xi,G^{-1}(x,y)}p(\xi)=p(\xi=G^{-1}(x,y)), \tag{1.35}$$

and the updated state of Eq. (1.32) becomes

$$p(x|y)=\frac{p(\xi=G^{-1}(x,y))p(x)}{p(y)}. \tag{1.36}$$

In the description given so far, the probability distribution has evolved exclusively because of the knowledge acquired on the system via the measurements procedure. We consider now the more general case in which the probability distributions is affected also by the modification of the system due to its interaction with the measurement apparatus. Given a variable X that lives in a discrete variable n-dimensional configuration space, we can suppose that the measurement with results y leads to a change of variable described by the $n\times n$ matrix with elements $\mathcal{B}_y(x|x')$. This means that, with probability $\mathcal{B}_y(x|x')$ the measurement transform the variable x' into variable x. The posterior system state will then be given by

$$p(x|y)=\frac{\sum_{x'}\mathcal{B}_y(x|x')p(y|x')p(x')}{p(y)}. \tag{1.37}$$

We can now introduce a new matrix $\mathcal{O}_y(x|x')$ that combines that transformation of the state due to the Bayesian theorem and the back action of the measurement:

$$\mathcal{O}_y(x|x')=\mathcal{B}_y(x|x')p(y|x'). \tag{1.38}$$

In terms of the operator $\mathcal{O}_y$ the state updated by the measurement y can be written

as

$$p(x|y) = \frac{\sum_{x'} \mathcal{O}_y(x|x')p(x')}{p(y)}. \tag{1.39}$$

We can further simplify Eq. (1.37) by introducing the n-dimensional vector E_y with elements $E_y(x)$ where

$$E_y(x) = \frac{\sum_{x'} \mathcal{O}_y(x|x')}{p}(x')p(x). \tag{1.40}$$

So we can conclude that, in general, the state is transformed by the measurement y of the variable x as

$$p(x|y) = \frac{E_y(x)p(x)}{p(y)}. \tag{1.41}$$

1.4.2 Quantum measurement

Analogously to the classical case, the quantum state of a system also expresses the observer's knowledge about the probability distributions associated with the system's measurable variables. However, in the classical context, it is, in principle, possible to gain complete knowledge of a system by performing repeated measurements on identically prepared copies. This allows each measurable feature to be assigned a definite value, rather than being described by a probability distribution. In the quantum case, by contrast, the uncertainty principle and the no-cloning theorem prevent such complete knowledge for all measurable variables of a quantum state.

Here, we describe projective measurement, a canonical form of measurement in quantum mechanics, and then present a more general measurement framework by introducing a system state that, in analogy with the classical case, plays the role of the measurement apparatus.

1.4.2.1 Projective measurement

Given a quantum variable Λ, the spectral theorem guarantees that it is always possible to diagonalize the associated observable operator $\widehat{\Lambda}$ as

$$\widehat{\Lambda} = \sum_{\lambda} \lambda \widehat{\Pi}_{\lambda} \tag{1.42}$$

where $\widehat{\Pi}_{\lambda}$ is the projector operator that projects states onto the subspace of the eigenstates of $\widehat{\Lambda}$ corresponding to the eigenvalue λ. If the spectrum of $\widehat{\Lambda}$ is non-degenerate, then we can define $|\pi_{\lambda}\rangle$ as the unique eigenstate with eigenvalue λ, and Eq. (1.42) simplifies to

$$\widehat{\Lambda} = \sum_{\lambda} \lambda \, |\pi_{\lambda}\rangle\langle\pi_{\lambda}| \tag{1.43}$$

which is known as the von Neumann measurement of the observable $\widehat{\Lambda}$. From Eq. (1.14), the expectation value of $\widehat{\Lambda}$ on the state $\widehat{\rho} = \sum_i p_i \, |\psi_i\rangle\langle\psi_i|$ is given by

$$\begin{aligned} \left\langle \widehat{\Lambda} \right\rangle_{\rho} &= \sum_i p_i \, \langle\psi_i|\widehat{\Lambda}|\psi_i\rangle = \sum_i p_i \, \langle\psi_i|\widehat{\Lambda}\widehat{\mathbb{I}}|\psi_i\rangle = \sum_{ij} p_i \, \langle\psi_i|\widehat{\Lambda} \, |\phi_j\rangle\langle\phi_j||\psi_i\rangle \\ &= \sum_{ij} p_i \, \langle\phi_j||\psi_i\rangle\langle\psi_i| \, \widehat{\Lambda}|\phi_j\rangle = \sum_j \, \langle\phi_j|\widehat{\rho}\widehat{\Lambda}|\phi_j\rangle = \mathrm{Tr}\left[\widehat{\rho}\widehat{\Lambda}\right]. \end{aligned} \tag{1.44}$$

where we used the decomposition of the identity $\widehat{\mathbb{I}} = \sum_j |\phi_j\rangle\langle\phi_j|$. From Eq. (1.44), and defining the probability distribution $p(\lambda)$ such that $\langle\Lambda\rangle = \sum_{\lambda} \lambda p(\lambda)$, we find that the probability of measuring the result outcomes λ is

$$p(\lambda) = \mathrm{Tr}\left[\widehat{\rho}(t)\widehat{\Pi}_{\lambda}\right] = \mathrm{Tr}\left[\widehat{\rho}(t) \, |\pi_{\lambda}\rangle\langle\pi_{\lambda}|\right] = \, \langle\pi_{\lambda}|\widehat{\rho}(t)|\pi_{\lambda}\rangle \, . \tag{1.45}$$

If T is the duration of the measurement process, the post-measurement state resulting from a von Neumann measurement on $\widehat{\rho}(t)$ is

$$\widehat{\rho}_\lambda(t+T) = \frac{\widehat{\Pi}_\lambda \widehat{\rho}(t) \widehat{\Pi}_\lambda}{\mathrm{Tr}\left[\widehat{\rho}(t)\widehat{\Pi}_\lambda\right]}. \tag{1.46}$$

Thus the state is said to be reduced or collapsed to the eigenstate $|\pi_\lambda\rangle$ depending on the measurement outcome λ [18].

1.4.2.2 Measurement operator

To define quantum measurements more generally, one needs to introduce an auxiliary state $|\theta\rangle$, referred to as the apparatus state by analogy with the measurement device in the classical case, which is coupled to the system state $|\psi\rangle$. The total state at time t is then given by the tensor product of these two states

$$|\Psi(t)\rangle = |\theta(t)\rangle\,|\psi(t)\rangle\,. \tag{1.47}$$

The measurement consists of two steps: first, a unitary evolution $\widehat{U}(T)$ is applied to the composite state; second, a projective measurement is performed on the first subsystem, projecting onto the eigenstates $|r\rangle$ of an observable R. The evolved state is then given by

$$|\Psi_r(t+T)\rangle = \frac{|r\rangle\langle r|\,\widehat{U}(T)\,|\theta(t)\rangle\,|\psi(t)\rangle}{\sqrt{p(r)}} = |r\rangle\,\frac{\widehat{M}_r\,|\psi(t)\rangle}{\sqrt{p(r)}} \tag{1.48}$$

where $\widehat{M}_r = \left\langle r|\widehat{U}(T)\middle|\theta(t)\right\rangle$ is the measurement operator associated with the outcome r, and $p(r) = \langle\psi|\widehat{M}^\dagger\widehat{M}|\psi\rangle$. The operator $\widehat{M}^\dagger\widehat{M}$ is the so-called effect operator $\widehat{E}_r$

associated to the measurement $\widehat{M}_r$. For mixed states, the post-measurement state is

$$\widehat{\rho}_r(t+T) = \frac{\mathcal{J}[\widehat{M}_r]\widehat{\rho}(t)}{p(r)} \tag{1.49}$$

where the superoperator $\mathcal{J}$ acts on any operators $\widehat{A}$ and $\widehat{B}$ as $\mathcal{J}[\widehat{A}]\widehat{B} = \widehat{A}\widehat{B}\widehat{A}^\dagger$. The set of all effects $\{\widehat{E}_r : r\}$ is known as the probability-operator-valued measure (POVM) on the space of results r. In this way, Eq.(1.49) mirrors the classical evolution of the state described in Eq.(1.41).

The concepts introduced in this section are primarily applied in Chapters 2, 3, and 4 where measurements are employed to implement conditional quantum state generation.

1.5 Encoding of quantum states

1.5.1 Discrete Variables

Historically, the development of quantum theory has been framed in terms of discrete variables, as many properties of physical systems at quantum scales appear to be discrete. The quantized energy levels in Bohr's model of the atom [19] represent one of the earliest examples of this discretization of nature. Other prominent instances include energy levels in trapped ions, electron occupancy or vacancies in quantum dots, current rotation directions in superconducting loops, and the polarization states of light. All of these systems are naturally suited to be described using a DV framework.

The states of such systems can be represented by wavefunctions (1.2) that are superpositions of orthogonal basis states. Furthermore, in the context of quantum computation, the DV formalism arises as a natural extension of classical information theory based on bits. Classical bits can be encoded in the quantum domain using two-

level systems, but the DV framework can also be generalized to higher-dimensional computational bases, depending on the number of available orthogonal states.

1.5.2 Continuous Variables

An alternative to the discrete-variable formalism is the continuous-variable framework. The CV approach is employed when the variables used to encode quantum information are continuous rather than discrete, as in the cases discussed in the previous paragraph. As a result, quantum states are parameterized over continuous values. This description becomes relevant when the set of accessible quantum states is not finite, allowing for the definition of an infinite, potentially orthogonal, set of states. These states can be expressed as superpositions in Hilbert space, analogous to Eq.(1.2), in the limit $N \to \infty$. Any other quantum state can thus be described starting from these continuous basis states, following the formalism introduced in Eq.(1.6). This framework is applicable to trapped ions [20], and is widely used in quantum optics [21]. In fact, entanglement between individual photons is challenging to achieve deterministically, as it often relies on postselected measurement outcomes. Consequently, performing computations using discrete-variable encodings of photons, such as polarization or path degrees of freedom, is generally less practical, particularly when targeting large-scale quantum computation. In contrast, nonlinear crystals enable the efficient generation of squeezed states, which are naturally described by the CV formalism and can be entangled deterministically. The discrete-variable encoding is used in Chapter 5, whereas the continuous-variable encoding is employed in Chapters 2,3, and4.

1.6 Quantum optics

1.6.1 Classical fields

The interdependence between the electric field $\boldsymbol{E}$ and magnetic field $\boldsymbol{B}$ in vacuum is determined by Maxwell's equations [22]:

$$\boldsymbol{\nabla} \times \boldsymbol{E} = \frac{\partial \boldsymbol{B}}{\partial t}, \tag{1.50}$$

$$\boldsymbol{\nabla} \times \boldsymbol{B} = \mu_0 \varepsilon_0 \frac{\partial \boldsymbol{E}}{\partial t}, \tag{1.51}$$

$$\boldsymbol{\nabla} \cdot \boldsymbol{B} = 0, \tag{1.52}$$

$$\boldsymbol{\nabla} \cdot \boldsymbol{E} = 0, \tag{1.53}$$

where ε_0 and μ_0 are the vacuum permittivity and permeability, respectively. If the fields are constrained in a one-dimensional cavity along the z-axis, such that they vanish at $z = 0$ and $z = L$, and assuming that the electric field is aligned along the x-axis, i.e., $\boldsymbol{E}(\boldsymbol{r}, t) = \boldsymbol{e}_x E_x(z, t)$, then a solution to Maxwell's equations is

$$E_x(z, t) = \sqrt{\frac{2\omega^2}{L\varepsilon_0}}\, q(t) \sin(kz). \tag{1.54}$$

which is the single-mode solution for the mode of frequency ω. Here, $k = \omega/c$ is the wavenumber, c is the speed of light, and $q(t)$ is the only time-dependent parameter of Eq. (1.54). The boundary condition $E_x(0, t) = E_x(L, t) = 0$ fixes the allowed frequency to $\omega = c(m\pi/L)$ with $m \in \mathbb{N}$. From Maxwell's equations and Eq. (1.54), it follows that the magnetic field is aligned along the y-axis, i.e., $\boldsymbol{B}(\boldsymbol{r}, t) = \boldsymbol{e}_y B_y(z, t)$, with magnitude

$$B_y(z, t) = \frac{\mu_0 \varepsilon_0}{k} \sqrt{\frac{2\omega^2}{L\varepsilon_0}}\, \dot{q}(t) \sin(kz). \tag{1.55}$$

Using Eqs. (1.54) and (1.55), the Hamiltonian of the electromagnetic field can be written as

$$\mathcal{H} = \frac{1}{2}\int_0^L \mathrm{d}z \left(\varepsilon_0 E_x^2(z,t) + \frac{1}{\mu_0} B_y^2(z,t)\right). \tag{1.56}$$

By introducing $p(t) \equiv \dot{q}(t)$, which, analogous to a mechanical harmonic oscillator, corresponds to the canonical momentum of a particle of unit mass at position $q(t)$, we can write Eq. (1.56) as

$$\mathcal{H} = \frac{1}{2}\left(p^2(t) + \omega^2 q^2(t)\right), \tag{1.57}$$

which is the Hamiltonian of a harmonic oscillator of unit mass.

1.6.2 Quantization

Highlighting the analogy with the harmonic oscillator Hamiltonian allows to identify the canonical variables q and p and proceed with the Bohr's correspondence rule to substitute them with the corresponding quantum operators $\widehat{q}$ and $\widehat{p}$ that have to fulfill the canonical commutation relations

$$[\widehat{q}, \widehat{p}] = i\hbar \tag{1.58}$$

$$[\widehat{q}, \widehat{q}] = 0 \tag{1.59}$$

$$[\widehat{p}, \widehat{p}] = 0. \tag{1.60}$$

The electric and magnetic amplitudes of Eq. (1.54) and Eq. (1.55) then corresponds to the quantum operators

$$\widehat{E}_x(z,t) = \sqrt{\frac{2\omega^2}{L\epsilon_0}}\widehat{q}(t)\sin(kz). \tag{1.61}$$

and

$$\widehat{B}_y(z,t) = \frac{\mu_0\epsilon_0}{k}\sqrt{\frac{2\omega^2}{L\epsilon_0}}\widehat{p}(t)\sin(kz), \tag{1.62}$$

while the energy operator derived from the Hamiltonian in Eq. (1.56) is

$$\widehat{\mathcal{H}} = \frac{1}{2}\left(\widehat{p}^2(t) + \omega^2\widehat{q}^2(t)\right). \tag{1.63}$$

Along with the Hermitian operators $\widehat{q}$ and $\widehat{p}$, corresponding to the physical observables position and momentum, two other non-hermitian operators are introduced to express the Hamiltonian of Eq. (1.63), which are the annihilation and creation operators $\widehat{a}$ and $\widehat{a}^\dagger$ respectively. The annihilation and creation operator are defined in terms of $\widehat{q}$ and $\widehat{p}$ as

$$\widehat{a} = \frac{\omega\widehat{q} + i\widehat{p}}{\sqrt{2\hbar\omega}} \quad \text{and} \quad \widehat{a}^\dagger = \frac{\omega\widehat{q} - i\widehat{p}}{\sqrt{2\hbar\omega}}. \tag{1.64}$$

From the commutation relations of $\widehat{q}$ and $\widehat{p}$ in Eqs. (1.58), (1.59), and (1.60), it follows that the creation and annihilation operators fulfill the commutation relation

$$\left[\widehat{a}, \widehat{a}^\dagger\right] = 1. \tag{1.65}$$

The Hamiltonian of Eq. (1.63) can be expressed in terms of annihilation and creation operator as

$$\widehat{\mathcal{H}} = \hbar\omega\left(\widehat{a}^\dagger\widehat{a} + \frac{1}{2}\right). \tag{1.66}$$

The time-evolution of $\widehat{a}$ and $\widehat{a}^\dagger$ in the Heisenberg picture is given by

$$\frac{\mathrm{d}\widehat{a}}{\mathrm{d}t} = \left[\widehat{\mathcal{H}}, \widehat{a}\right] = -i\omega\widehat{a}, \tag{1.67}$$

which is solved by setting

$$\widehat{a}(t) = \widehat{a}(0)e^{-i\omega t}. \tag{1.68}$$

For $\widehat{a}^\dagger$ one would get

$$\widehat{a}^\dagger(t) = \widehat{a}^\dagger(0)e^{i\omega t}. \tag{1.69}$$

The energy operator can be further simplified by introducing another operator that depends on the creation and annihilation operator $\widehat{n} = \widehat{a}^\dagger\widehat{a}$ such that Eq. (1.66) becomes

$$\widehat{\mathcal{H}} = \hbar\omega\left(\widehat{n} + \frac{1}{2}\right). \tag{1.70}$$

Whose eigenstates are the states $|n\rangle$ such that

$$\hbar\omega\left(\widehat{n} + \frac{1}{2}\right)|n\rangle = E_n|n\rangle \tag{1.71}$$

1.6.2.1 Fock states

The state $\widehat{a}^\dagger|n\rangle$ is also an eigenstate of $\widehat{\mathcal{H}}$ with eigenvalue $E_n + \hbar\omega$, since

$$\hbar\omega\left(\widehat{n} + \frac{1}{2}\right)\widehat{a}^\dagger|n\rangle = \widehat{a}^\dagger\hbar\omega\left(\widehat{n} + \frac{3}{2}\right)|n\rangle = (E_n + \hbar\omega)\widehat{a}^\dagger|n\rangle. \tag{1.72}$$

Thus, the state $\widehat{a}^\dagger|n\rangle$ can be interpreted as having a quantum of energy $\hbar\omega$ more than the state $|n\rangle$. Conversely, the state $\widehat{a}|n\rangle$ has eigenvalue $E_n - \hbar\omega$, which is a quantum of energy less than E_n. Creation and annihilation operator are named after the fact they create eigenstates with one more or one less quantum of energy, or photon, in the state. At the lowest rung of the ladder, there corresponds a state with the minimal energy, such that no state exists with smaller energy. This is the so-called vacuum

state $|0\rangle$, which fulfills

$$\widehat{a}\,|0\rangle = 0 \tag{1.73}$$

We observe that the energy of the vacuum state is not zero, as might be anticipated, but

$$\widehat{\mathcal{H}}\,|0\rangle = \hbar\omega\left(\widehat{a}^{\dagger}\widehat{a} + \frac{1}{2}\right)|0\rangle = \frac{\hbar\omega}{2}\,|0\rangle\,. \tag{1.74}$$

Hence, $\frac{\hbar\omega}{2}$ is the zero-point energy of the mode. More generally, the energy of a state with n photons, known as Fock number state $|n\rangle$, is $\hbar\omega\left(n+\frac{1}{2}\right)$. The operator $\widehat{n}$ is the so-called number operator as it counts the number of photons in the mode.

The expectation value of the electric field in Eq. (1.61) respect to the energy eigenstates $|n\rangle$ is

$$\langle n|\widehat{E}_x(z,t)|n\rangle = \langle n|\mathcal{E}_0(\widehat{a}+\widehat{a}^{\dagger})\sin(kz)|n\rangle = 0 \tag{1.75}$$

where $\mathcal{E}_0 = \sqrt{\hbar\omega/\varepsilon_0 L}$. Therefore, the mean electric field of the state $|n\rangle$ is zero, suggesting the Fock states are not suitable to describe classical field, even for large n. In fact, the number operator does not commute with the electric field operator

$$\left[\widehat{n}, \widehat{E}_x\right] = \mathcal{E}_0 \sin(kz)(\widehat{a}^{\dagger} - \widehat{a}). \tag{1.76}$$

The fluctuations of the field are estimated by the variance

$$\langle n|(\Delta\widehat{E}_x(z,t))^2|n\rangle = \langle n|(\widehat{E}_x(z,t))^2|n\rangle - (\,\langle n|(\widehat{E}_x(z,t))|n\rangle)^2 = \mathcal{E}_0 \sin^2(kz)\,(2n+1) \tag{1.77}$$

We observe that the fluctuations are more intense for large number of photons, however there is a non-null fluctuation of the electric field observed for the vacuum state as

well. This conclusion is consistent with the Heisenberg uncertainty principle implied by the commutation relation of Eq. (1.76) such that

$$\Delta n \Delta E_x \geq \frac{1}{2}\mathcal{E}_0 \left| \sin(kz) \left\langle (\widehat{a}^\dagger - \widehat{a}) \right\rangle \right|, \tag{1.78}$$

which correlates a high accuracy on the electric field with the uncertainty on the number of photons.

1.6.2.2 Coherent states

The coherent states $|\alpha\rangle$ are the eigenstates with eigenvalue α of the annihilation operator, i.e., $\widehat{a}\,|\alpha\rangle = \alpha\,|\alpha\rangle$. Coherent states indeed provide a quantum description of classical fields [22, 23]. The mean field of the electric field for coherent states $|\alpha\rangle$ with $\alpha = |\alpha| e^{i\theta}$, is

$$\langle \alpha | E_x(z,t) | \alpha \rangle = -\sqrt{2}|\alpha| \mathcal{E}_0 \sin(kz - \omega t + \theta) \tag{1.79}$$

while the variance is

$$\langle \alpha | (\Delta \widehat{E}_x(z,t))^2 | \alpha \rangle = \sqrt{2}\mathcal{E}_0. \tag{1.80}$$

which corresponds to the uncertainty of the vacuum state. We observe that the space-time dependence of the mean electric field in Eq. (1.79) is consistent with that expected by the classical counterpart, while the fluctuations correspond to the quantum noise that disappear in the classical limit $\hbar \to 0$, confirming coherent states as the most classical-like quantum states. The basis of coherent states is commonly used in quantum optics, exactly because they naturally describe the classical electromagnetic field and and exhibits minimal, unbiased uncertainty in the phase space [24].

The relation between coherent basis and Fock basis is given by

$$|\alpha\rangle = \exp\{-|\alpha|^2/2\} \sum_{n=0}^{\infty} \frac{\alpha^n}{n!} |n\rangle \tag{1.81}$$

However, unlike the CV basis introduced in Eq. (1.6), coherent states do not fulfill the orthogonality relation $\langle\beta|\alpha\rangle = \delta(\alpha - \beta)$. Instead, for any amplitudes $\alpha, \beta \in \mathbb{C}$, $\langle\beta|\alpha\rangle = e^{-\frac{1}{2}(|\alpha|^2+|\beta|^2-2\beta^*\alpha)}$. A basis with this property is called overcomplete, meaning it contains more vectors than are minimally required to span the space, and any state in the basis can be written as a linear combination of the others [25].

Chapters 2, 3, and 4 focus on the generation and characterization of non-classical states of light and rely upon the basic quantum optics concepts discussed above.

1.7 Linear optics

In optical implementations, a preliminary distinction is often made between linear and nonlinear optics, based on the type of manipulation performed on the quantum state of the system. Linear optics encompasses those manipulations of quantum states that correspond to classical superpositions of electromagnetic fields [26]. Linear regime is generally easier to describe from a mathematical point of view and is relatively simple to implement compared to nonlinear optics. In fact, its physical implementation relies on widely available tools that offer good efficiency. Linear optical operations correspond to unitary transformations of the ladder operators, such that [27]

$$\widehat{a}_i \to \sum_j U_{ij} \widehat{a}_j. \tag{1.82}$$

These transformations are realized through the unitary evolution generated by Hamiltonians that are bilinear in the creation and annihilation operators

$$\widehat{H} = \sum_{jk} A_{jk} \widehat{a}_j^\dagger \widehat{a}_k \tag{1.83}$$

where A is a Hermitian matrix [28, 29]. We observe that the Hamiltonian commutes with the total photon number operator $\widehat{n}$, implying that the field intensity is conserved under linear optical transformations. More generally, in addition to operations obtained through the evolution of a quadratic Hamiltonian, linear Bogoliubov transformations of the annihilation operator [28–30]

$$\widehat{a}_j \to \sum_k A_{jk} \widehat{a}_k + B_{jk} \widehat{a}_k^\dagger + \beta_j \tag{1.84}$$

are also included among linear operations. However, unlike passive linear transformations, Bogoliubov transformations do not conserve the number of photons of the field [31]. The matrices A and B can be expressed in terms of diagonal matrices A_D and B_D via the decompositions

$$A = U A_D V^\dagger, \quad B = U B_D V^T, \tag{1.85}$$

where U and V are unitary matrices. The standard linear operations introduced in the next section are indeed generated by the Bogoliubov transformation introduced in Eq. (1.84).

In 1994 Reck *et al.* [32] proved that the most general linear optical unitary operation U that transforms the annihilation operator as in Eq. (1.82) can be realized using beam splitter and phase shifter operations only. Specifically, any N-dimensional

unitary transformation can be realized with $N(N-1)/2$ beam splitters and $N(N+1)/2$ phase shifters.

1.7.1 Linear optical operations

The best known quantum gate realizable in photonic implementation through a linear Hamiltonian are the rotation, displacement, and beam splitter gate [30, 33].

1.7.1.1 Rotation gate

The rotation or phase shift operator is defined as

$$R(\phi) = \exp(i\phi\widehat{n}). \tag{1.86}$$

This operator introduces a phase ϕ to the annihilation operator

$$R^{\dagger}(\phi)\widehat{a}R(\phi) = e^{i\phi}\widehat{a}. \tag{1.87}$$

1.7.1.2 Displacement gate

The displacement operator

$$\widehat{D}(\alpha) = \exp\left(\alpha\widehat{a} - \alpha^{*}\widehat{a}^{\dagger}\right) \tag{1.88}$$

displaces a state into another position of the phase space such that

$$\widehat{D}^{\dagger}(\alpha)\widehat{a}\widehat{D}(\alpha) = \widehat{a} + \alpha, \tag{1.89}$$

This means that a coherent state $|\beta\rangle$ goes into the coherent state $\widehat{D}(\alpha)\,|\beta\rangle = e^{i\varphi}\,|\alpha+\beta\rangle$ with $\varphi = \mathrm{Im}\{\alpha\beta^{*}\}$, and a coherent state is nothing else but a displaced vacuum state

$|\alpha\rangle = \widehat{D}(\alpha)\,|0\rangle$.

1.7.1.3 Beamsplitting gate

Then the two-mode beam splitting gate $B(\theta)$ is defined as [34]

$$B(\theta) = \exp\left[\theta(\widehat{a}^\dagger \widehat{b} - \widehat{a}\widehat{b}^\dagger)\right] \tag{1.90}$$

such that

$$B(\theta)^\dagger \widehat{a} B(\theta) = \widehat{a}\cos(\theta) + \widehat{b}\sin(\theta), \tag{1.91}$$

where $\widehat{b}$ is the annihilation operator of the second mode.

However, performing rotations and beam splitter operations on displaced vacuum states only, does not lead to any significative advantage compared to classical optics. In fact, coherent states can be treated as classical coherent light modes [23]. Moreover they are the only pure states that do not get entangled by beam splitter operation and N input coherent states are just converted into other N output coherent states by beam splitters and phase shifters [35].

1.7.1.4 Squeezing gate

Besides proper linear transformations, some nonlinear transformations, which do not fulfill the superposition principle but are obtained via Bogoliubov transformations, are sometimes included among the linear optical operations and referred to as active linear operations [36]. This is the case for the squeezing operator, governed by the Hamiltonian $\widehat{H} = ir(\widehat{a}^{\dagger 2} - \widehat{a}^2)$, which is quadratic in the ladder operators. The corresponding squeezing operator $\widehat{S}(r)$ is given by

$$\widehat{S}(r) = \exp\left[r(\widehat{a}^{\dagger 2} - \widehat{a}^2)\right], \tag{1.92}$$

and transforms the annihilation operator $\widehat{a}$ as

$$\widehat{S}^{\dagger}(r),\widehat{a},\widehat{S}(r) = \widehat{a}\cosh(r) - \widehat{a}^{\dagger}\sinh(r). \tag{1.93}$$

Squeezing results in a reduction of uncertainty in one quadrature at the expense of increased uncertainty in the conjugate quadrature. The Heisenberg uncertainty principle is not violated in this transformation:

$$\widehat{q} \to \widehat{q}e^{-r}, \quad \widehat{p} \to \widehat{p}e^{r}. \tag{1.94}$$

In comparison with the displacement, which is the other active operation defined in this section, squeezing generates non-classical states that can get entangled by the action of passive interferometers and can guarantee some advantages with respect to classical light [37, 38].

1.7.1.5 Physical realizations

Displacement gate Any general quantum optical state $|\psi\rangle$ can be displaced by letting it interfere with a coherent state $|\beta\rangle$ in a almost transparent beamsplitter of transmittance angle $\theta \sim 0$ [39]. If a is the label for the mode in which it is encoded the state $|\psi\rangle$, and b labels the mode with the coherent state $|\beta\rangle$, then the operator describing the evolution of the state $|\psi\rangle$, can be obtained by tracing out the action of the beam splitter at the other mode such that it reads

$$\mathrm{Tr}_b\left(\widehat{\mathbb{I}} \otimes |\beta\rangle\langle\beta|\, \widehat{B}(\theta)\right) = \langle\beta|\widehat{B}(\theta)|\beta\rangle \tag{1.95}$$

where the trace is made over the mode b and $\widehat{B}(\theta)$ is the unitary operator describing the action of the beam splitter as defined in Eq. (1.90). Given that $|\beta\rangle$ is an eigenstate

of the annihilation operator $\widehat{b}$, the operator describing the evolution of the state in mode a in Eq. (1.95) becomes

$$\langle\beta|\widehat{B}(\theta)|\beta\rangle = \langle\beta|\exp\left[\theta(\widehat{a}^{\dagger}\widehat{b} - \widehat{a}\widehat{b}^{\dagger})\right]|\beta\rangle \tag{1.96}$$

$$= \langle\beta|\sum_{n=0}^{\infty}\frac{\theta^n}{n!}\left(\widehat{a}^{\dagger}\widehat{b} - \widehat{a}\widehat{b}^{\dagger}\right)^n|\beta\rangle \tag{1.97}$$

$$= \sum_{n=0}^{\infty}\frac{\theta^n}{n!}\langle\beta|\left(\widehat{a}^{\dagger}\widehat{b} - \widehat{a}\widehat{b}^{\dagger}\right)^n|\beta\rangle \tag{1.98}$$

We introduce now the displaced operators $\widehat{c} \equiv \widehat{b} - \beta$, $\widehat{c}^{\dagger} \equiv \widehat{b}^{\dagger} - \beta^*$ such that $\widehat{c}\,|\beta\rangle = 0$. The operators $\widehat{c}$, and $\widehat{c}^{\dagger}$ satisfy the commutation relation $\left[\widehat{c}, \widehat{c}^{\dagger}\right] = 1$. Moreover, the operators $\widehat{A} \equiv |\beta|\left(e^{i\varphi}\widehat{a}^{\dagger} - e^{-i\varphi}\widehat{a}\right)$, and $\widehat{B} \equiv \widehat{a}^{\dagger}\widehat{c} - \widehat{a}\widehat{c}^{\dagger}$ commute with each other $\left[\widehat{A}, \widehat{B}\right] = 0$ and allow one to write Eq. (1.96) as

$$\langle\beta|\widehat{B}(\theta)|\beta\rangle = \sum_{n=0}^{\infty}\frac{\theta^n}{n!}\langle\beta|\left(\widehat{A} + \widehat{B}\right)^n|\beta\rangle = \sum_{n=0}^{\infty}\frac{\theta^n}{n!}\sum_{m=0}^{n}\binom{n}{m}\widehat{A}^{n-m}\langle\beta|\widehat{B}^m|\beta\rangle \tag{1.99}$$

$$= \sum_{n=0}^{\infty}\frac{\theta^n}{n!}|\beta|^n\sum_{m=0}^{n}|\beta|^{-m}\binom{n}{m}\left(e^{i\varphi}\widehat{a}^{\dagger} - e^{-i\varphi}\widehat{a}\right)^{n-m}\langle\beta|\widehat{B}^m|\beta\rangle \tag{1.100}$$

$$= \sum_{n=0}^{\infty}\frac{(\theta|\beta|)^n}{n!}\left[\left(e^{i\varphi}\widehat{a}^{\dagger} - e^{-i\varphi}\widehat{a}\right)^n + \frac{n(n-1)}{|\beta|^2}\left(e^{i\varphi}\widehat{a}^{\dagger} - e^{-i\varphi}\widehat{a}\right)^{n-2} + o\left(1/|\beta|^3\right)f(\widehat{a}, \widehat{a}^{\dagger})\right] \tag{1.101}$$

So, in the limit $|\beta| \to \infty$, Eq. (1.96) becomes

$$\langle\beta|\widehat{B}(\theta)|\beta\rangle = \exp\left[\theta(\beta\widehat{a}^{\dagger} - \beta^*\widehat{a})\right] \tag{1.102}$$

which is equivalent to the operational definition of the displacement gate given in Eq. (1.88) when $\theta\beta = -\alpha^*$.

Squeezing gate The squeezing operation can be physically realized via degenerate parametric-down conversion [22, 24]. In this process, some photons of a pump field of frequency ω_p hits are transformed by a nonlinear medium to pairs of photons of frequency $\omega = \omega_p/2$. The Hamiltonian for this process is given by

$$\widehat{H} = \hbar\omega\widehat{a}^\dagger\widehat{a} + \hbar\omega_p\widehat{b}^\dagger\widehat{b} + i\hbar\chi^{(2)}\left(\widehat{a}^2\widehat{b}^\dagger - \widehat{a}^{\dagger 2}\widehat{b}\right), \tag{1.103}$$

where a is the annihilation operator of the signal field with frequency ω, while b is the annihilation operator of the pump field of frequency ω_p. The Hamiltonian in Eq. (1.103) is made of three terms. The first term gives the contribution to the energy coming from the signal field, the second term gives the energy contribution of the pump field, while the last term describes the non-linear interaction introduced by the medium that leads to the generation of the signal photon pairs out of single pump photons. Now, if we suppose to have a strong pump field in which the fraction of photon lost is negligible, and that this field is coherent $|\beta e^{-i\omega_p t}\rangle$, we can use the so-called parametric approximation and substitute $\widehat{b}$ with $\beta e^{-i\omega_p t}$ and $\widehat{b}^\dagger$ with $\beta^* e^{i\omega_p t}$ such that the Hamiltonian in Eq. (1.103) becomes

$$\widehat{H} = \hbar\omega\widehat{a}^\dagger\widehat{a} + i\hbar\chi^{(2)}\left(\widehat{a}^2\beta^* e^{i\omega_p t} - \widehat{a}^{\dagger 2}\beta e^{-i\omega_p t}\right). \tag{1.104}$$

that in the interaction picture becomes

$$\widehat{H} = i\hbar r\left(\widehat{a}^2 e^{i\omega_p t} - \widehat{a}^{\dagger 2} e^{-i\omega_p t}\right). \tag{1.105}$$

where we set $r = \chi^{(2)}\beta$. The Hamiltonian in Eq. (1.105) is in fact the Hamiltonian that generate the squeezing operation introduced in Eq. (1.92).

Inline squeezing The squeezing of quantum states with non-zero average photon number is conceptually identical to the squeezing of vacuum states. However, from a practical point of view, it is significantly more challenging to implement. While the application of the squeezing operator deterministically produces a squeezed state when acting on the vacuum in a given mode of the field, applying the same operator to a non-vacuum state requires mode matching between the excited modes in which the quantum state is defined and the modes affected by the squeezing operation. Nonetheless, recent progress has been made toward increasingly efficient implementations of deterministic squeezing on arbitrary quantum states [40, 41].

1.7.2 Measurements

1.7.2.1 Homodyne detection

Homodyne detection allows one to measure the quadrature components of a quantum state, denoted by q and p. In the limit of large coherent amplitude, it is equivalent to a projective measurement onto the position (momentum) eigenstates $|q\rangle$ ($|p\rangle$) [34, 42]. The canonical method for performing homodyne detection on a general state $|\psi\rangle$ involves the use of an auxiliary coherent state $|\beta\rangle$, with $\beta = |\beta|e^{i\phi}$, and a balanced beam splitter [24]. The input-output relations between the annihilation operators of the input modes $\widehat{a}, \widehat{b}$ and those of the output modes $\widehat{c}, \widehat{d}$ are

$$\widehat{c} = \frac{\widehat{a} + i\widehat{b}}{\sqrt{2}}, \quad \text{and} \quad \widehat{d} = \frac{i\widehat{a} + \widehat{b}}{\sqrt{2}}. \tag{1.106}$$

The difference in photon number between the two output ports is given by

$$\widehat{n}_c - \widehat{n}_d = \widehat{c}^\dagger\widehat{c} - \widehat{d}^\dagger\widehat{d} = -i\left(\widehat{a}^\dagger\widehat{b} - \widehat{b}^\dagger\widehat{a}\right). \tag{1.107}$$

The actual measured quantity is the difference in photocurrents from the two detectors:

$$\begin{aligned} i_{cd} = i_c - i_d &\propto \langle\psi| \langle\beta| \left(\widehat{n}_c - \widehat{n}_d\right) |\psi\rangle |\beta\rangle \\ &= -i \langle\psi| \langle\beta| \left(\widehat{a}^\dagger \widehat{b} - \widehat{b}^\dagger \widehat{a}\right) |\psi\rangle |\beta\rangle = -i \langle\psi| \left(\widehat{a}^\dagger \beta - \widehat{a}\beta^*\right) |\psi\rangle \\ &= -i|\beta| \langle\psi| \left(\widehat{a}^\dagger e^{i\phi} - \widehat{a}e^{-i\phi}\right) |\psi\rangle = -2|\beta| \left\langle \widehat{X}(\phi + \pi/2) \right\rangle, \end{aligned} \tag{1.108}$$

where we introduced the quadrature operator $\widehat{X}(\phi) = \widehat{a}e^{-i\phi} + \widehat{a}^\dagger e^{i\phi}$,, which corresponds to the canonical quadrature operators $\widehat{q}$ and $\widehat{p}$ for $\phi = 0$ and $\phi = \pi/2$, respectively. The variance of the quadrature is then given by

$$\left[\Delta X(\phi + \pi/2)\right]^2 = \left(\Delta i_{cd}\right) / |\beta|^2, \tag{1.109}$$

and can thus be reduced by increasing the intensity of the local oscillator, $|\beta|$.

1.7.2.2 Photon Number Resolving Detections

A second class of measurements in quantum optics used in the thesis is photon-number-resolving detection. Its measurement operator is given by $M_r = |0\rangle\langle r|$, where $|r\rangle$ is the photon number state introduced in Eq. (1.71). PNR detectors are thus used to count the number of photons in a given quantum state. This kind of detector can be implemented by multiplexing a series of single-photon detectors in either time or space [43, 44]. Indeed, single-photon detectors, such as avalanche photodiodes, are less technically demanding to implement; however, they can only determine whether one or more photons are present, without resolving the exact number.

The notions of this sections are used for the manuscripts of chapters 2, 3, and 4 of this thesis.

1.8 Quasi Probability Distributions

It is convenient to describe CV quantum systems using a characteristic function defined over phase space, which is the space spanned by the quadrature coordinates q and p [45, 46] . Quasiprobability distributions associated with quantum states are experimentally accessible through homodyne tomography. Moreover, the effect of all the operations listed in 1.7.1 can be easily visualized in this representation. In this section, we define the characteristic function over phase space and introduce the associated quasiprobability distributions.

1.8.1 Characteristic function

The displacement operator defined in Eq. (1.88) can be used to introduce a function, the Weil characteristic function χ_ρ of the quadrature coordinates α that unambiguously describes a given quantum state ρ

$$\chi_{s,\rho}(\alpha) = \mathrm{Tr}\left[D(\alpha)\rho\right] \exp\left(s|\alpha|^2/2\right) \tag{1.110}$$

Inversely, the state ρ is determined by the characteristic function through the Fourier-Weyl relation as [47]

$$\rho = \frac{1}{\pi}\int \mathrm{d}^2\alpha \chi_{0,\rho}(\alpha)\widehat{D}(-\alpha) \tag{1.111}$$

The characteristic function allows to introduce the Wigner function of order s

$$W_{s,\rho}(\alpha) = \int \mathrm{d}^2\beta e^{(\alpha\beta^* - \alpha^*\beta)}\chi_{s,\rho}(\beta). \tag{1.112}$$

1.8.1.1 Wigner quasiprobability

The Wigner function $W_{0,\rho}$ of the state ρ serves as a quasiprobability distribution of the state in analogy with the classical state, in the sense that the expectation value of an observable $\widehat{O}$ onto the state ρ is given by

$$\left\langle \widehat{O} \right\rangle_{\rho} = \mathrm{Tr}\left[\widehat{O}(\widehat{a}, \widehat{a}^{\dagger})\widehat{\rho}\right] = \int \mathrm{d}^2\alpha W_{0,\rho}(\alpha) O(\alpha, \alpha^*) \tag{1.113}$$

This formula holds if the expectation value is evaluated on the symmetrically ordered operator $\widehat{O}(\widehat{a}, \widehat{a}^{\dagger})$. Analogous quasiprobability functions are defined for normal ordered ($s = 1$) and antinormal ordered ($s = -1$) operators [24]. Moreover, for any operators $\widehat{O}_1$ and $\widehat{O}_2$, we have [48]

$$\mathrm{Tr}\left[\widehat{O}_1 \widehat{O}_2\right] = \frac{1}{\pi} \int \mathrm{d}^2\alpha W_{s,\widehat{O}_1}(\alpha) W_{-s,\widehat{O}_2}(\alpha) \tag{1.114}$$

1.8.1.2 Glauber-Sudarshan quasiprobability

For normal ordered operators, in which all the creation operators are on the left-hand side and all the annihilation operators are all on the right-hand side, the quasiprobaility distribution that satisfies Eq. 1.113 is the Glauber-Sudarshan P-representation that gives the coherent representation of the state [49]

$$\rho = \int P(\alpha) \left|\alpha\right\rangle\!\left\langle\alpha\right| \mathrm{d}^2\alpha. \tag{1.115}$$

1.8.1.3 Husimi quasiprobability

For anti-normal ordered operators, we define instead the Husimi Q-representation [50], which satisfies

$$Q(\alpha) = \frac{1}{\pi} \langle \alpha | \rho | \alpha \rangle \, . \tag{1.116}$$

Since all the representations introduced above are equivalent, without loss of generality, we restrict our attention to the Wigner representation. Similar to a classical probability distribution, the value of the Wigner function at α, denoted $W(\alpha)$, corresponds to the probability density of measuring the system in the state α, provided the state is classical. Even for non-classical states, the Wigner function behaves like a probability distribution when marginal distributions are considered. However, we should note that the real and imaginary parts of α correspond to conjugate quadratures, which cannot be simultaneously measured due to the non-commutativity of the creation and annihilation operators [51]. Moreover, unlike true probability distributions, the Wigner function can assume negative values, a property that reflects non-classical features and cannot be interpreted within classical probability theory.

1.9 Gaussian operations

The linear operations described in Sec. 1.7 transform the quadrature operator $\widehat{\boldsymbol{r}} = (\widehat{q}_1, \widehat{p}_1, \ldots, \widehat{q}_N, \widehat{p}_N)^\intercal$ as [33]

$$\widehat{\boldsymbol{r}} \to F\widehat{\boldsymbol{r}} + \boldsymbol{d}, \tag{1.117}$$

where F is a symplectic matrix that fulfills $F\Omega F^\intercal = \Omega$ with

$$\Omega = \bigoplus_{k=1}^{2N} \begin{pmatrix} 0 & 1 \\ -1 & 0 \end{pmatrix} \tag{1.118}$$

such that the canonical commutation relation for quadrature operators $[\widehat{r}_k, \widehat{r}_l] = i\Omega_{kl}$ does not get violated in the transformation. For any quantum state, it is then possible to define the its displacement vector o $\boldsymbol{\xi} = \langle \widehat{\boldsymbol{r}} \rangle$ and its covariance matrix $\boldsymbol{\sigma}$ with elements

$$\sigma_{k,l} = \frac{1}{2} \langle \{\widehat{\boldsymbol{r}}_k, \widehat{\boldsymbol{r}}_l\} \rangle - \langle \widehat{\boldsymbol{r}}_k \rangle \langle \widehat{\boldsymbol{r}}_l \rangle , \tag{1.119}$$

where $\{\widehat{A}, \widehat{B}\} = \widehat{A}\widehat{B} + \widehat{B}\widehat{A}$ is the anticommutator. It can be proven that a state ρ with a Gaussian Wigner function depends on the displacement vector and on the covariance matrix only, such that its Wigner function can be expressed as

$$W_\rho(\boldsymbol{r}) = \frac{\exp\left[-\frac{1}{2}(\boldsymbol{r} - \boldsymbol{\xi})^\intercal \boldsymbol{\sigma}^{-1} (\boldsymbol{r} - \boldsymbol{\xi})\right]}{(2\pi)^N \sqrt{\det(\boldsymbol{\sigma})}}. \tag{1.120}$$

As a consequence, from Eq. (1.117) it follows that the symplectic operations obtainable in linear optics transform a Gaussian state into another Gaussian state and are therefore called gaussian operations. All symplectic operations, which corresponds to Hamiltonians that are at most quadratic in the creation and annihilation operator, can be realized using only beam splitters, phase shifters, displacements and squeezing. Specifically according to the Bloch Messiah decomposition [52], any symplectic operation is equivalent to the action of a sequence of one universal passive interferometer, a layer of single mode inline squeezing, and a final passive interferometer acting on the displaced states. To generalize further it can be shown that any transformation can be realized with a combination with Hamiltonians this set of at most quadratic Hamiltonians and one cubic Hamiltonian [53]. To illustrate the proof, we observe that, given two canonically commuting operators $\widehat{o}_a$ and $\widehat{o}_b$ such that $[\widehat{o}_a, \widehat{o}_b] = 1$, we have that $[\widehat{o}_a^3, \widehat{o}_a^m \widehat{o}_b^n] \sim \widehat{o}_a{}^{m+2} \widehat{o}_b^{n-1}$ where we neglect the lower order terms. As a consequence, opportune commutation of at least cubic terms can lead to operators of

any order [54]. However in photonic implementation obtaining this class of gates is extremely challenging [53].

Gaussian operations are used in Chapters 2, 3, and 4 for CV state generation.

1.10 Projective measurement on Wigner function

Since the measurement-heralded generation of specific quantum states in CV is a central theme for Chapters 2, 3, and 4, in this section we describe how the Wigner Function of multimode states, introduced in Sec. 1.8, is modified by projective measurements on some of the modes. Concepts from Sec. 1.4 are applied here to analyze the impact of these measurements on the Wigner functions. In this context, the expression measurement-heralded generation signifies that the generation is signaled by some given measurement outcomes. The object being generated with the heralding measurement is the heralded object. Two classes of measurements are considered: projections onto Gaussian and non-Gaussian states. Projections onto non-Gaussian states are employed in Chapters 2 and 3, using PNRDs. In contrast, the Schrödinger cat breeding protocol discussed in Chapter 4 is realized via homodyne measurements, which are equivalent to projections onto infinitely squeezed Gaussian states.

1.10.1 Projection on Gaussian states

The most general Gaussian projective measurement is the so-called generaldyne measurement. The resolution of the identity corresponding to a projection onto a multimode Gaussian state ρ_M, centered at the origin, is given by [47]:

$$\widehat{\mathbb{I}} = \frac{1}{(2\pi)^m} \int_{\mathbb{R}^{2m}} \mathrm{d}\boldsymbol{r}_m \, \widehat{D}(-\boldsymbol{r}_m) \, \rho_M \, \widehat{D}(\boldsymbol{r}_m), \tag{1.121}$$

where $\widehat{D}(\boldsymbol{r}_m)$ is the multimode displacement operator. Suppose we want to measure an $(n+m)$-mode Gaussian state ρ, partitioned into an n-mode subsystem A and an m-mode subsystem B, with covariance matrix and first moments given by

$$\boldsymbol{\sigma} = \begin{pmatrix} \boldsymbol{\sigma}_A & \boldsymbol{\sigma}_{AB} \\ \boldsymbol{\sigma}_{AB}^{\intercal} & \boldsymbol{\sigma}_B \end{pmatrix}, \quad \boldsymbol{\xi} = \begin{pmatrix} \boldsymbol{\xi}_A \\ \boldsymbol{\xi}_B \end{pmatrix}. \tag{1.122}$$

The measurement transforms the input Gaussian state into an n-mode Gaussian state, where the covariance matrix and displacement vector of subsystem A are updated as follows

$$\boldsymbol{\sigma}_A \to \boldsymbol{\sigma}_A - \boldsymbol{\sigma}_{AB} \frac{1}{\boldsymbol{\sigma}_B + \boldsymbol{\sigma}_M} \boldsymbol{\sigma}_{AB}^{\intercal}, \tag{1.123}$$

$$\boldsymbol{\xi}_A \to \boldsymbol{\xi}_A - \boldsymbol{\sigma}_{AB} \frac{1}{\boldsymbol{\sigma}_B + \boldsymbol{\sigma}_M} (\boldsymbol{\xi}_B - \boldsymbol{r}_m). \tag{1.124}$$

Here, $\boldsymbol{\sigma}_M$ is the covariance matrix of the measured Gaussian state ρ_M used in the projection. Notably, only the updated displacement vector in Eq. (1.124) depends on the specific measurement outcome $\boldsymbol{r}_m$. We now consider how general POVMs can be used to herald the generation of non-Gaussian states. The discussion is general, although the non-Gaussian measurements considered in the remainder of the thesis are limited to projections onto Fock number states. [55–57].

1.10.2 POVM measurement

We now consider the more general case of a measurement $\widehat{A}$ performed on some of the modes of a pure multimode Gaussian state with Wigner function $W(\boldsymbol{r})$ [53]. Here, $\boldsymbol{r}$ denotes the vector of quadrature coordinates, so for an m-mode state, we have $\boldsymbol{r} \in \mathbb{R}^{2m}$. Suppose that only the last l' modes are measured. Then, the phase

space $\mathbb{R}^{2m}$ can be conveniently decomposed as $\mathbb{R}^{2m} = \mathbb{R}^{2l} \oplus \mathbb{R}^{2l'}$, and the quadrature vector as $\boldsymbol{r} = \boldsymbol{r}_f \oplus \boldsymbol{r}_g$, where f and g play roles analogous to subsystems A and B in Eq. (1.122). As described in Sec. 1.9, the Wigner function of a Gaussian state is fully characterized by its covariance matrix $\boldsymbol{\sigma}$ and displacement vector $\boldsymbol{\xi}$, whose block decomposition is given in Eq. (1.122). This partition of the m-mode phase space allows us to define reduced Wigner functions $W_f(\boldsymbol{r}_f)$ and $W_g(\boldsymbol{r}_g)$ by tracing out the complementary subsystem from the global Wigner function $W(\boldsymbol{r}_f \oplus \boldsymbol{r}_g)$. Specifically, we have:

$$W_f(\boldsymbol{r}_f) = \int_{\mathbb{R}^{2l'}} \mathrm{d}\boldsymbol{r}_g \, W(\boldsymbol{r}_f \oplus \boldsymbol{r}_g), \tag{1.125}$$

$$W_g(\boldsymbol{r}_g) = \int_{\mathbb{R}^{2l}} \mathrm{d}\boldsymbol{r}_f \, W(\boldsymbol{r}_f \oplus \boldsymbol{r}_g). \tag{1.126}$$

The conditional state resulting from applying the measurement operator $\widehat{A}$, as defined in Eq. (1.48), is given by

$$\widehat{\rho}_{f|A} = \frac{\mathrm{Tr}_g \left[\widehat{A}\widehat{\rho}\right]}{\mathrm{Tr}\left[\widehat{A}\widehat{\rho}\right]}, \tag{1.127}$$

which, using Eq. (1.114), leads to:

$$W_{f|A}(\boldsymbol{r}_f) = \frac{\int_{\mathbb{R}^{2l'}} \mathrm{d}\boldsymbol{r}_g \, W_A(\boldsymbol{r}_g) W(\boldsymbol{r}_f \oplus \boldsymbol{r}_g)}{\int_{\mathbb{R}^{2l'}} \mathrm{d}\boldsymbol{r}_g \, W_A(\boldsymbol{r}_g) W_g(\boldsymbol{r}_g)}. \tag{1.128}$$

According to Bayesian theory, and as shown in Eq. (1.31), the conditional probability distribution $W(\boldsymbol{r}_g|\boldsymbol{r}_f)$ is given by

$$W(\boldsymbol{r}_g|\boldsymbol{r}_f) = \frac{W(\boldsymbol{r}_f \oplus \boldsymbol{r}_g)}{W_f(\boldsymbol{r}_f)}. \tag{1.129}$$

As a result, the Wigner function in Eq. (1.128) can be rewritten as

$$W_{f|A}(\boldsymbol{r}_f) = \frac{\left\langle \widehat{A} \right\rangle_{g|\boldsymbol{r}_f}}{\left\langle \widehat{A} \right\rangle} W_f(\boldsymbol{r}_f), \tag{1.130}$$

where

$$\left\langle \widehat{A} \right\rangle = \int_{\mathbb{R}^{2l'}} \mathrm{d}\boldsymbol{r}_g \, W_A(\boldsymbol{r}_g) W_g(\boldsymbol{r}_g), \tag{1.131}$$

$$\left\langle \widehat{A} \right\rangle_{g|\boldsymbol{r}_f} = \int_{\mathbb{R}^{2l'}} \mathrm{d}\boldsymbol{r}_g \, W_A(\boldsymbol{r}_g) W_g(\boldsymbol{r}_g|\boldsymbol{r}_f). \tag{1.132}$$

Although $W_g(\boldsymbol{r}_g|\boldsymbol{r}_f)$ is a well-defined probability distribution, it is not itself the Wigner function of a quantum state. Consequently, the conditional expectation value $\left\langle \widehat{A} \right\rangle_{g|\boldsymbol{r}_f}$ can, in general, take negative values, even though both $\left\langle \widehat{A} \right\rangle$ and the reduced Gaussian Wigner function $W_f(\boldsymbol{r}_f)$ are always non-negative. It follows that the heralded state described by Eq. (1.130) can exhibit negativity, which is a necessary and sufficient condition for the non-Gaussianity of pure states [58, 59].

Projective measurements are used for non-Gaussian states generations in the manuscript of chapters 2, 3, and 4.

1.11 Non-Gaussian states

Quantum states whose Wigner functions are non-Gaussian in phase space are referred to as non-Gaussian quantum states. These states play a crucial role in quantum information science, as they are necessary for many applications, ranging from fault-tolerant quantum computation to quantum communication [53, 60–62]. The most prominent examples of non-Gaussian quantum states in photonic implementations are the Fock number states, with the only exception being the vacuum state, which

is also a coherent state. The Wigner function of a Fock state $|n\rangle$ is given by [63]

$$W_n(\alpha) = \frac{2}{\pi}(-1)^n \exp\big(-2|\alpha|^2\big) L_n(4|\alpha|^2), \tag{1.133}$$

where L_n denotes the n-th Laguerre polynomial. Other common examples of single-mode quantum states include statistical mixtures. For instance, the Wigner function of the mixed state $\rho \propto |\alpha\rangle\langle\alpha| + |\beta\rangle\langle\beta|$, where $|\alpha\rangle$ and $|\beta\rangle$ are pure coherent states, is given by the sum of two Gaussian functions in phase space.

1.11.1 Schrödinger cat state

A Schrödinger cat state is defined as the coherent superposition of two coherent states [45]:

$$|\mathrm{cat}_\theta\rangle = \frac{|\alpha\rangle + e^{i\theta}\,|-\alpha\rangle}{\sqrt{2\,(1 + e^{-2|\alpha|^2}\cos\theta)}}. \tag{1.134}$$

The state $|\mathrm{cat}_\theta\rangle$ is named after the quantum state hypothesized by Erwin Schrödinger in his famous *Gedankenexperiment*, in which a quantum superposition of two macroscopically distinct states leads to the paradoxical scenario of a cat being simultaneously dead and alive [64]. Beyond its historical and philosophical significance, particularly in debates surrounding the interpretation of quantum mechanics, the cat state in Eq. (1.134) has been extensively studied both in foundational theoretical contexts [65–67] and for practical applications in quantum information science. These include quantum computation [68–70], quantum metrology [71, 72], and quantum communication [73]. The Wigner function of a Schrödinger cat state in phase space is illustrated in Fig. 1.1.

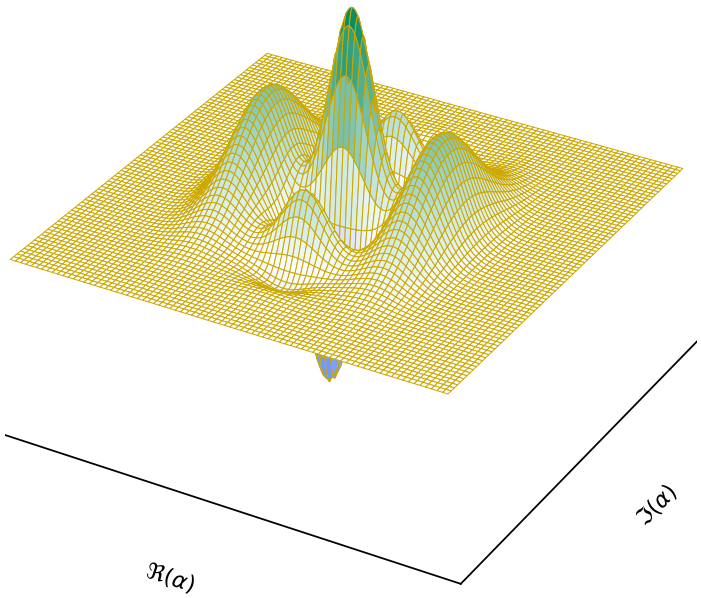

Figure 1.1: Wigner function of a Schrödinger cat state.

1.11.2 Gottesman-Kitaev-Preskill state

While the substantial advantages of encoding information in quantum states, arising from uniquely quantum features such as superposition and entanglement, have already been discussed, it is equally important to recognize that quantum states are inherently more vulnerable to decoherence than their classical counterparts. This is because interactions with the environment are harder to isolate, often resulting in undesired and unpredictable changes to the state. For example, in the Wigner representation introduced in Sec. 1.8, such interactions may cause unwanted displacements in the quadrature space along either direction. When these types of errors cannot be completely prevented, it becomes crucial to detect and correct them. One method for doing so is quantum error correction, which can be implemented by encoding logical information into states whose Wigner functions form a grid of delta peaks in phase space, as proposed in the Gottesman-Kitaev-Preskill scheme [60]. Any shift in

the quadrature coordinates smaller than the grid spacing can then be detected using ancillary qubits and corrected by applying the appropriate displacement to restore the state to its original position. In particular, a logical qu*d*it in the GKP encoding is represented by such a grid state, where any general Pauli operation $\widehat{X}^a\widehat{Z}^b$ (with $a, b = 1, 2, \ldots, d-1$) corresponds to a displacement operator. These logical operations act as follows:

$$\widehat{X}\,|j\rangle = |j+1 \pmod d\rangle\,, \quad \text{and} \quad \widehat{Z}\,|j\rangle = e^{2\pi i j/d}\,|j\rangle\,. \tag{1.135}$$

If we associate displacements along q with $\widehat{X}$ operations and displacements along p with $\widehat{Z}$ operations, then we can express them as:

$$\widehat{X} = \widehat{D}(\alpha), \quad \text{and} \quad \widehat{Z} = \widehat{D}(i\beta), \tag{1.136}$$

for some real α and β. From Eq. (1.135), it follows that $\widehat{Z}\widehat{X} = e^{2\pi i/d}\widehat{X}\widehat{Z}$, which, using Eq. (1.136), implies the commutation relation:

$$\widehat{D}(i\beta)\widehat{D}(\alpha) = e^{2\pi i/d}\widehat{D}(\alpha)\widehat{D}(i\beta). \tag{1.137}$$

We observe that the displacement parameters α and β determine the lattice spacing that defines the logical states in the GKP encoding. Since shift errors smaller than $\alpha/2$ and $\beta/2$ can be corrected, it is desirable to make these parameters as large as possible. However, they are mutually constrained by Eq. (1.137), which imposes the condition $\alpha\beta = 2\pi/d$. A standard choice is to set $\alpha = \beta = \sqrt{2\pi/d}$, yielding a square lattice in phase space [74]. As an example, the logical GKP qubit states $|\bar{0}\rangle$ and $|\bar{1}\rangle$

can be written as [75]:

$$|\bar{0}\rangle \propto \sum_{n=-\infty}^{\infty} \left|2n\sqrt{\pi}\right\rangle_q, \quad |\bar{1}\rangle \propto \sum_{n=-\infty}^{\infty} \left|(2n+1)\sqrt{\pi}\right\rangle_q, \tag{1.138}$$

where $|x\rangle_q$ denotes the eigenstate of the position operator $\widehat{q}$ with eigenvalue x. These ideal GKP states are unphysical, as their Wigner representation consists of an infinite series of delta peaks that would require infinite energy to generate. Moreover, they are defined over the entire real line and are therefore non-normalizable. In practice, physical realizations of GKP states are necessarily approximations of the ideal ones. A canonical approach to approximate the GKP states in Eq. (1.138) is to replace each delta function in the Wigner distribution with a Gaussian peak centered at the corresponding grid point and with standard deviation σ. The entire state is then modulated by a Gaussian envelope centered at the origin with standard deviation $1/\kappa$ to ensure normalizability. The ideal GKP state is recovered in the limit $\sigma, \kappa \to 0$. The Wigner function of an approximate GKP state is shown in Fig. 1.2.

The discussion above focuses on cat states and GKP states, as they are extremely relevant for several applications, but more generally, access to non-Gaussian states is crucial for universal quantum computation in CV encodings [54]. In contrast, Gaussian measurements on Gaussian states can be efficiently simulated classically. [76]. However, as mentioned in Sec.1.9, generating non-Gaussian states starting from the vacuum requires at least one cubic Hamiltonian, which is extremely challenging to implement deterministically in photonic platforms [53, 77–79].

Both the Schrödinger cat states and the GKP states are used in the chapters 2, 3, and 4.

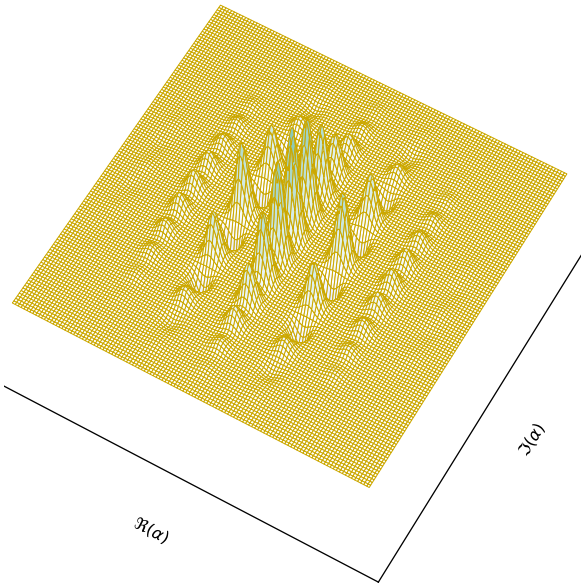

Figure 1.2: Wigner function of an approximate GKP state.

1.12 Non-Gaussian state generation

Since the deterministic generation of non-Gaussian states is, in general, very challenging in photonic implementations, conditional sources are usually preferred. Two possible strategies for generating non-Gaussianity involve photon subtraction and photon addition applied to a Gaussian state. Given a Gaussian state ρ, the photon-subtracted state is defined as

$$\rho^{-} = \frac{\widehat{a}\rho\widehat{a}^{\dagger}}{\mathrm{Tr}\left[\widehat{a}^{\dagger}\widehat{a}\rho\right]}. \tag{1.139}$$

The state ρ^{-} can be realized by using a beam splitter that interferes one mode of the Gaussian state ρ with an auxiliary mode prepared in the vacuum state. A single-photon Fock state is then post-selected on the auxiliary mode. The action of the beam splitter on the two-mode system is described by the transformation in Eq. (1.90). Neglecting normalization, the resulting state produced by this protocol, for a general

value of θ, is denoted by ρ_θ and is given by

$$\rho_\theta = \frac{\widehat{B}(\theta)\left(\rho \otimes |0\rangle\langle 0|\right)\widehat{B}(\theta)^\dagger\left(\mathbb{I} \otimes |1\rangle\langle 1|\right)}{\mathrm{Tr}\left[\widehat{B}(\theta)\left(\rho \otimes |0\rangle\langle 0|\right)\widehat{B}(\theta)^\dagger\left(\mathbb{I} \otimes |1\rangle\langle 1|\right)\right]} \tag{1.140}$$

For small values of θ, the beam splitter operator can be approximated as $\widehat{B}(\theta) \approx \widehat{\mathbb{I}} + \theta\left[\widehat{a}^\dagger\widehat{b} - \widehat{a}\widehat{b}^\dagger\right]$. In this approximation, the resulting state becomes

$$\rho^- = \lim_{\theta \longrightarrow 0} \rho_\theta = \frac{\widehat{a}\rho\widehat{a}^\dagger}{\mathrm{Tr}\left[\widehat{a}^\dagger\widehat{a}\rho\right]} \tag{1.141}$$

as desired. Analogously, photon addition can be realized using a similar protocol, where the beam splitter is replaced by a two-mode squeezed operator, $\widehat{U}(\theta) = \exp\left[\theta\left(\widehat{a}^\dagger\widehat{b}^\dagger - \widehat{a}\widehat{b}\right)\right]$. The desired state ρ^+ is obtained in the limit of small θ, such that

$$\rho^+ = \frac{\widehat{a}^\dagger\rho\widehat{a}}{\mathrm{Tr}\left[\widehat{a}^\dagger\widehat{a}\rho\right]}. \tag{1.142}$$

Photon-subtracted and photon-added states are specific cases of conditional non-Gaussian state generation. More generally, non-Gaussian states can be probabilistically obtained by projective measurement onto a non-Gaussian state [80–83], as outlined in Sec. 1.10. A general scheme for non-Gaussian state generation conditioned on the measurement outcome has, for instance, been proposed by Su *et al.* [57] using Gaussian Boson Sampling-like sources.

1.12.1 State generation with GBS-like devices

1.12.1.1 Boson Sampling

Although non-Gaussian states are essential for achieving universal quantum computation [84], it is, in principle, possible to achieve a quantum advantage by performing

non-Gaussian measurements on Gaussian states. In fact, Gaussian Boson Sampling relies on non-Gaussian measurements of photonic states to perform computations, offering advantages over classical protocols [85]. GBS is a non-universal computing scheme based on the Boson Sampling model. In Boson Sampling, m single-photon states are injected as inputs into an n-mode passive interferometer, where $n \geq m$. PNR detectors are used at the output to count the number of photons in each of the n output ports of the interferometer. A general input state is given by $|\psi_{\text{in}}\rangle = |1_1 \cdots 1_m \cdots 0_n\rangle$, which evolves under the unitary operation defined by the interferometer U_I to the state $|\psi_{\text{out}}\rangle = U_I |\psi_{\text{in}}\rangle = \sum_S \gamma_S |s_1 \dots s_n\rangle$ where the sum runs over all possible combinations S of m photons in n output ports [86]. The sampling allows us to evaluate the probabilities $p(S) = |\gamma_S|^2$, which can, in turn, be related to the permanent of U_I as follows [87]:

$$p(S) = \frac{|\text{per}\,(U_S)|^2}{s_1! \cdots s_n!} \tag{1.143}$$

where U_S is an $m \times m$ sub-matrix of U_I in which row i is repeated s_i times, and only the first m columns are used. The permanent of an $n \times n$ matrix A is defined as

$$\text{per}(A) = \sum_{\sigma \in S_n} \prod_{i=1}^{n} A_{i,\sigma(i)} \tag{1.144}$$

where S_n is the set of all permutations of n elements.

1.12.1.2 Gaussian Boson Sampling

Gaussian Boson Sampling is analogous to standard Boson Sampling, but it uses squeezed vacuum states in the input ports of the interferometer instead of vacuum and single-photon Fock states. In GBS, the probability of detecting a given photon

output pattern is related to the Hafnian of a matrix that encodes the interferometer's transformation, as expressed in the following equation [88]:

$$p(S) = \frac{\left|\mathrm{Haf}\left[(U_I \,\mathrm{diag}(\tanh r_1, \ldots, \tanh r_n)\, U_I^{\intercal})_S\right]\right|^2}{\prod_{i=1}^{n} s_i! \cosh r_i}, \tag{1.145}$$

where, similarly to Eq. (1.143), the subscript S of a matrix M denotes the matrix obtained by repeating the i-th row and column of M exactly s_i times. The Hafnian of a $2n \times 2n$ matrix A is defined as [89]:

$$\mathrm{Haf}(A) = \frac{1}{2^n n!} \sum_{\sigma \in S_{2n}} \prod_{i=1}^{n} A_{\sigma(2i-1),\sigma(2i)}. \tag{1.146}$$

Equivalently, the probability in Eq. (1.145) can be written as [85, 90]:

$$p(S) = \frac{\mathrm{Haf}(A_S)^2}{\sqrt{\det(Q)} \prod_{i=1}^{n} s_i!}, \tag{1.147}$$

where we define $Q = \sigma + \mathbb{I}/2$, with σ the covariance matrix of the state prepared by the passive interferometer. The matrix $\tilde{A} = A \oplus A^*$ is given by $\tilde{A} = X(\mathbb{I} - Q^{-1})$, $X = \left(\begin{smallmatrix} 0 & \mathbb{I} \\ \mathbb{I} & 0 \end{smallmatrix}\right)$. The most general case for GBS with pure states is reached by applying displacements to the squeezed vacuum input states. The probability of detecting a given combination of photons S at the output, when the input states are displaced squeezed vacuum states $\bigotimes_{i=1}^{n} \widehat{D}(d_i)\widehat{S}(r_i)\,|0\rangle$, is given by [90]:

$$p(S) = \frac{\exp\left(-\frac{1}{2}\boldsymbol{d}^\dagger Q^{-1} \boldsymbol{d}\right)}{\sqrt{\det(Q)} \prod_{i=1}^{n} s_i!} \left[\sum_{l=0}^{n} \sum_{\{i_1,\ldots,i_l\} \subseteq \mathcal{I}_n} b_{i_1} \ldots b_{i_l} \mathrm{Haf}(A_{S-\{i_1,\ldots,i_l\}})\right]^2, \tag{1.148}$$

where $\boldsymbol{d} = (d_1, \ldots, d_n, d_1^*, \ldots, d_n^*)^T$ is the displacement vector, $\boldsymbol{b} = \boldsymbol{d}^\dagger Q^{-1}$, and $\mathcal{I}_n = \{1, \ldots, n\}$ is the index set. Approximating the Hafnian of a given matrix is

computationally hard for classical algorithms, with current runtimes scaling exponentially [91–93]. As a consequence, Gaussian Boson Sampling has been proposed as a promising platform to demonstrate quantum advantage, motivating both the development of classical simulation techniques [85,92,94–96] and experimental implementations [97–101].

1.12.1.3 Conditional generation with PNRDs.

The Gaussian Boson Sampling devices can be appropriately modified to become conditional sources of non-Gaussian states. The interference performed by the passive interferometer on the input squeezed state generates a multimode Gaussian state, and the PNRDs at the end perform a projective measurement on it. If only a portion of the modes is measured, the state resulting in the output mode is a non-Gaussian state, as outlined in Sec. 1.10.2. The states generated will depend on the actual measurement outcome of the source, as well as on the parameters of the source. These parameters include the squeezing intensities, displacement of the input state, and the transmittance and phase angles of the beam splitters and phase shifters that comprise the interferometer. Crucially, the conditional source requires optimization to improve both the success probability and the quality of the output state. Optimization can be achieved by fixing a measurement outcome that heralds the production of the non-Gaussian state and tuning the parameters of the source, squeezing, displacement, and interferometer angles accordingly for the given target. The target state $|\psi\rangle$ can be expressed in terms of a superposition of Fock states followed by Gaussian operations at the end, as follows [75]:

$$|\psi\rangle = \widehat{S}(\boldsymbol{\xi})\widehat{D}(\boldsymbol{\alpha}) \sum_{n=0}^{n_{\max}} c_n \, |n\rangle \,, \tag{1.149}$$

which is the so-called stellar representation of the state $|\psi\rangle$ [102]. The minimal $n_{\max}$ necessary to define the state exactly is known as the stellar rank of the state and is determined by the zeros of its Husimi Q function. To give a few examples: Gaussian states have stellar rank $r^\star = 0$, Fock number states $|n\rangle$ have $r^\star = n$, and Schrödinger cat states and GKP states have $r^\star \to \infty$. Consequently, Eq. (1.149) is exact only if $n_{\max} \geq r^\star$. Otherwise, the target state $|\psi\rangle$ is approximated up to the given Fock order $n_{\max}$. In the context of state generation with GBS-like devices, the stellar representation of Eq. (1.149) is particularly useful. The value of $n_{\max}$ is constrained by N, the number of photons detected by the PNRDs of the source. It has also been conjectured that the number of independent coefficients c_n scales as $(N+2)(N-1)/2$ [57]. The Gaussian operations applied at the end to the state expressed in stellar representation can always be mapped onto Gaussian operations on the input states. These operations are not constrained by the architecture of the sources, but only by the maximum squeezing or displacement intensity achievable on the single-mode inputs, if any. As a result, if no bound is set on the Gaussian operations, the optimization can focus on the core state of the stellar representation, the linear combination of Fock number states, without needing to consider the Gaussian operations. Since both the probability of success and the fidelity must be maximized during optimization, the reward function should increase with respect to both figures of merit. A straightforward choice is to use a linear combination with equal weights for both. However, the selection of the reward function is crucial for the optimization, and this choice remains largely arbitrary. It is evaluated on a case-by-case basis based on the results of the optimization. It's also worth noting that the two figures of merit are mutually limiting: Fidelity can be improved at the expense of probability, and vice versa. This limitation also applies to the size of the source. Larger sources allow for the genera-

tion of higher fidelity states, particularly for high stellar rank states, but with lower success rates.

1.12.2 GKP qubit state engineering with cat state breeding

If one has access to non-Gaussian states that might be easier to generate, these can be manipulated with Gaussian operations and measurements to generate other non-Gaussian states. The cat-breeding protocol is one such method that uses homodyne measurements on Schrödinger cat states to herald the generation of GKP grid states [103–107]. Specifically, two copies of a squeezed cat state are interfered on a 50:50 beam splitter. One of the modes of the output state is then measured by homodyne detection of the q-quadrature. The state heralded by the measurement, resulting from post-selection on $q = 0$, is then interfered with another possibly squeezed cat state to proceed with another iteration of the protocol. The state heralded at the end of the protocol will have a GKP-stabilizer value greater than that of the input squeezed cat state used to produce it, which depends on the amplitude, squeezing of the cat states, and the number of iterations. In fact, the state can be realized deterministically, without post-selection, by applying a final displacement to the resulting state [108].

Alternative schemes to non-Gaussian states generation are proposed in chapters 2, 3, and 4.

1.13 Rydberg Physics

Rydberg physics describes systems whose Hamiltonian behaves like the Hamiltonian of a hydrogen atom [109]

$$E_n = -\frac{R_H}{n^2}, \tag{1.150}$$

where R_H is the Rydberg's constant, and n represents the principal quantum number. Rydberg physics is used, for example, to describe the physics of atoms of elements whose atoms have a highly-excited electron that experiences a force field similar to the one generated by a point-like source with an opposite charge. In fact, although Rydberg atoms are generally used to describe any system with a similar Hamiltonian, Rydberg physics also applies to other physical systems, such as molecules and electron-hole pairs in semiconductors.

The interest in Rydberg atoms arises from the peculiar characteristics of these systems, which offer the possibility of being employed in a variety of applications. First of all, the highly excited electron is weakly bound to the atom's nucleus and is therefore very sensitive to any external electromagnetic field. For this reason, Rydberg atoms are particularly suited for quantum sensing applications [110].

Secondly, the dipole matrix element that determines the strength of the coupling between two consecutive states, e.g. the n-th and the $(n+1)$-th, scales as n^2, which means that the interaction between two consecutive Rydberg states increases quadratically with the energy level n. Moreover, the lifetime at high energy levels actually increases with the n^3 [111, 112]. In fact, on the one hand, spontaneous emission to the ground state is extremely small, due to the minimal overlap between the wave function of the state at a high energy level and the ground state, and on the other hand the spontaneous decay to the lower energetic level, via coupling with the vacuum mode, is unlikely due to the scarcity of vacuum modes at small frequencies $\omega \sim (\frac{1}{n} - \frac{1}{n+1})$.

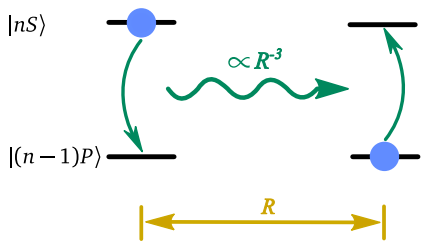

Figure 1.3: Dipole-dipole interaction.

1.13.1 Interactions

Let us now consider how the interaction mediated by virtual photons can be described for Rydberg atoms. First, we study the case of two Rydberg atoms in two consecutive energy states, interacting in a so-called dipole-dipole interaction, which is described in Fig. 1.3.

This interaction can be interpreted as the emission of a virtual photon from the excited state to the ground state of the first atom, followed by the absorption of the same photon by the atom in the ground state, which is consequently excited to the next level n. The intensity of this dipole-dipole interaction scales as R^{-3}. Additionally, the optical dipole coupling between consecutive principal quantum numbers increases with the square of the energy level. Therefore, the intensity of this interaction scales as n^4/R^6.

A second kind of interaction, known as van der Waals interaction, can be established between atoms that are at the same energy level. A depiction of the van der Walls' interaction is given in Fig. 1.4.

One can imagine that a photon spontaneously emitted from the first atom in the state $|nS\rangle$ is absorbed by the nearby atom, which is then excited from the level $|nS\rangle$ to the level $|n''P\rangle$. This process, however, presents an energy detuning, so the virtual photon is re-emitted by the second atom, which returns to its ground state, and then

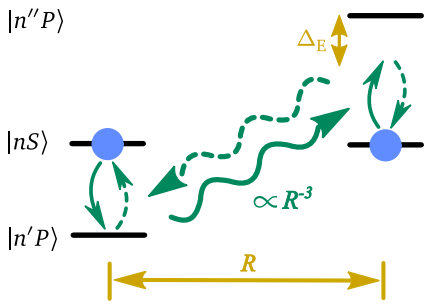

Figure 1.4: van der Walls interaction.

it is absorbed by the first atom, which is excited from the state $|n'P\rangle$ and returns to its initial state. Given the two dipole-dipole interactions, this kind of interaction scales as R^{-6} with respect to the distance, while it increases as n^{11} with respect to the energy level because there are two emissions and two absorptions, each of which has an intensity scaling as n^2, but there is also the detuning, which introduces an additional scaling factor of n^3. Both dipole-dipole interactions, therefore, become particularly intense for high n, but they can be suppressed by increasing the distance between the atoms. The van der Walls' interaction is especially interesting as the energy potential that it introduces $V(r) \propto n^{11}/r^6$, is responsible for the Rydberg blockade phenomenon, which is used in quantum information to implement controlled gates. When atoms are within a certain threshold distance, known as the blockade distance, the energy level of the Rydberg state $|r\rangle$ is detuned from the level it would be for an isolated atom. This detuning ensures that the driving laser, which is used on isolated atoms to excite states to the Rydberg level, has no effect if the addressed atom is near another atom in the Rydberg state. A pictorial illustration of the Rydberg Blockade is given in Fig. 1.5, where $|g\rangle$ and $|e\rangle$ label the two computational quantum states: ground and excited.

The notions of this section are used to develop the model described in chapter 5.

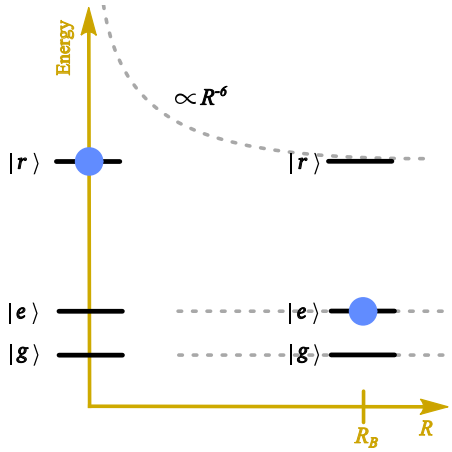

Figure 1.5: Rydberg blockade.

Chapter 2

Seeding GBS-like sources with single photons

2.1 Introduction

The advantages promised by quantum information theory have led to an extensive effort aimed at identifying the problems that are best suited to be solved by encoding the information into quantum states and by algorithms capable of doing so with the fewest possible resources. Depending on the specific task, researchers have also sought to determine which physical platforms are better suited to provide an actual advantage deriving from uniquely quantum properties. For many applications and features, quantum optics has often been proposed as an excellent candidate for observing such a quantum advantage. If compared with superconducting qubits or trapped ions, photonic implementation requires much less cooling and therefore could potentially be more resource-efficient in terms of space, cost, and energy. Moreover, photons suffer very little decoherence, and fundamental quantum gates can be realized with relative ease using linear optical elements such as beam splitters, mirrors,

and phase shifters. On the other hand, quantum optical computation also has its limits, which mainly stem from the fact that nonlinear operations between modes are much more complicated to implement, and cubic evolutions are essentially unfeasible in a deterministic way. Yet, as described in Sec. 1.12, the generation of non-Gaussian bosonic states is essential for fault-tolerant quantum computation, and more generally, non-Gaussianity is necessary to achieve universal computation that cannot be classically simulated. An example of non-universal quantum computation is that of Gaussian Boson Sampling. With GBS, M squeezed vacuum states are injected into an N-dimensional passive interferometer, and the number of photons at the output of each port is eventually measured using PNRDs (Photon-Number Resolving Detectors). Sampling over many trials of this process leads to a distribution of combinations that can be linked to the Hafnian of a matrix that depends on the circuit parameters and is classically hard to compute. A slight modification of the GBS device can then be employed to probabilistically produce non-Gaussian states. If only some of the modes are measured, the state heralded at the other ports can potentially be a non-Gaussian state. In fact, the measurement performed by PNRDs is a projective measurement on Fock states, which are non-Gaussian states. The non-Gaussian state generation obtained with a GBS-like source is probabilistic, since the projective measurement itself is probabilistic. In general, the state obtained changes depending on the measurement result on the other modes. Once a target state is defined, we say that the source has successfully produced the state only if a given measurement pattern appears. The parameters of the source are then optimized to maximize the probability of obtaining this measurement pattern, as well as the quality of the produced state—for example, using fidelity with the target state as a measure of quality.Now, one of the main limitations of this source is that optimizing

fidelity limits the achievable probability with the same source. In fact, for high-energy states, obtaining a state with satisfactory fidelity is only possible with extremely low probabilities. Since the states we aim to produce are often used to encode a single qubit—and more and more are needed for fault-tolerant quantum computation—it becomes necessary for these sources to be highly efficient. A slow source risks making the computation more susceptible to noise, and performing multiplexing requires adding resources such as PNRDs, which we would actually prefer to avoid. In this article, we therefore aim to investigate whether it is possible to improve the quality of GBS sources by introducing a source of non-Gaussianity already at the level of the input states. Indeed, one of the best-known examples of non-Gaussian states is the single-photon Fock state. These states can be efficiently generated using various protocols. Adding non-Gaussianity with single photons has in fact also proven useful in other quantum protocols. By adding one or more squeezed single-photon states and re-optimizing the sources, we observed a significant increase in the success probability compared to the case of sources seeded with squeezed vacuum states only. Preliminary results also suggest that using photons across multiple modes can give better results than having a single mode where a single Fock state is squeezed with the same input photons in one mode while leaving squeezed vacuum states in the other modes. This result would, on the other hand, be consistent with results found regarding simulability by coherent state decomposition [113].

Seeding Gaussian boson samplers with single photons for enhanced state generation

Valerio Crescimanna [1,2], Aaron Z. Goldberg [1,2] and Khabat Heshami [1,2,3]

[1]*National Research Council of Canada, 100 Sussex Drive, Ottawa, Ontario K1N 5A2, Canada*

[2]*Department of Physics, University of Ottawa, 25 Templeton Street, Ottawa, Ontario, K1N 6N5 Canada*

[3]*Institute for Quantum Science and Technology, Department of Physics and Astronomy, University of Calgary, Alberta T2N 1N4, Canada*

(Received 4 November 2023; revised 27 December 2023; accepted 16 January 2024; published 23 February 2024)

Non-Gaussian quantum states are crucial to fault-tolerant quantum computation with continuous-variable systems. Usually, generation of such states involves trade-offs between success probability and quality of the resultant state. For example, injecting squeezed light into a multimode interferometer and postselecting on certain patterns of photon-number outputs in all but one mode, a fundamentally probabilistic task, can herald the creation of cat states, Gottesman-Kitaev-Preskill (GKP) states, and more. We consider the addition of a non-Gaussian resource state, particularly single photons, to this configuration and show how it improves the qualities and generation probabilities of desired states. With only two modes, adding a single-photon source improves GKP-state fidelity from 0.68 to 0.95 and adding a second then increases the success probability eightfold; for cat states with a fixed target fidelity, the probability of success can be improved by factors of up to four by adding single-photon sources. These demonstrate the usefulness of additional commonplace non-Gaussian resources for generating desirable states of light.

DOI: 10.1103/PhysRevA.109.023717

I. INTRODUCTION

The magic of quantum states is a mixed blessing: one rarely finds useful quantum states in nature. This makes clever state generation protocols essential to proposed quantum advantages from sensing to computation. In the particular context of light-based quantum systems, most of the known methods for generating non-Gaussian states, a prerequisite for photonic fault-tolerant quantum computation, have limited or trade-offs in success probabilities and state fidelities [1–16]. We here explore how the combination of single-photon sources and Gaussian-boson-sampling (GBS) devices can improve creating these building blocks for photonic quantum information processing.

Light is a superior medium for encoding quantum information because of its speed and resistance to decoherence at room temperature, but the information is naturally encoded in the continuous variable (CV) degrees of freedom of harmonic-oscillator modes as opposed to the discrete variable (DV) systems made from qubits, where most quantum computing algorithms and error-correcting codes have been developed for the latter paradigm. At the start of the century, Gottesman, Kitaev, and Preskill introduced a method for robustly encoding a qubit in a harmonic-oscillator mode [17] (requiring only one physical mode for one logical qubit [12]) and their eponymous "GKP states" are now highly sought [18,19] for fast, decoherence-free, fault-tolerant quantum computation.

Another desirable set of CV states are "cat states" that are superpositions of two states that each on their own have highly classical properties [20]. Cat states are useful for quantum information processing in their own right [21–25], for breeding GKP states [6,18,26], for quantum sensing protocols [27–29], and for exemplifying the differences between quantum and classical theory [30–33]. We focus our attention on creating GKP and cat states, while our method can be broadly applied to generate any desired CV state.

Two checkpoints along the road to fault-tolerant quantum computation are boson sampling and its Gaussian (GBS) counterpart. Both inject nonclassical light into a linear optical network followed by photon counting, with output distributions that are challenging to recreate or sample from on a classical computer. The light injected for GBS is squeezed vacuum, a Gaussian state that is nonclassical in its ability to generate entanglement through a linear optical network [34], and this setup has been proposed for heralded generation of useful non-Gaussian states by choosing particular photon-number distributions among a subset of the output modes [15,16]. A boson sampler, in contrast, directly injects what are arguably the most basic non-Gaussian resources, single-photon states. The classical hardness of predicting outcomes of quantum experiments was recently shown to depend on the amount of squeezing and number of single photons added to a network [35]. Since the abilities to generate both squeezed vacuum and single photons are always improving, especially with promise of them both being feasible on similar physical platforms, we ask and answer the logical question: do single photons help GBS-like devices for generating interesting and useful states of light?

II. BACKGROUND

A. Non-Gaussian quantum states

For a state defined on N modes with bosonic annihilation operators $\hat{a}_i$, we define position and momentum operators as $\hat{q}_i = (\hat{a}_i + \hat{a}_i^\dagger)/\sqrt{2\hbar}$ and $\hat{p}_i = -i(\hat{a}_i - \hat{a}_i^\dagger)/\sqrt{2\hbar}$ and combine them into a single vector of operators $\hat{\boldsymbol{x}} = (\hat{q}_1, \hat{p}_1, \ldots, \hat{q}_N, \hat{p}_N)$. Gaussian states are uniquely character-

ized by the $2N$ first-order moments encoding the "displacements" of the state $\boldsymbol{\xi} = \langle \hat{\boldsymbol{x}} \rangle$ and the $2N \times 2N$ second-order moments encoded in the symmetric "covariance matrix" $\boldsymbol{V}$ with elements $V_{ij} = \langle \frac{\hat{x}_i \hat{x}_j + \hat{x}_j \hat{x}_i}{2} \rangle - \langle \hat{x}_i \rangle \langle \hat{x}_j \rangle$; whereas, non-Gaussian states need higher-order moments of $\hat{\boldsymbol{x}}$ to be uniquely specified. Indeed, a convenient description of a state is through its Wigner function, which is responsible for the name "Gaussian state" because the latter have Gaussian Wigner functions [36]:

$$W_G(\boldsymbol{x}) = \frac{\exp\left[\frac{1}{2}(\boldsymbol{x}-\boldsymbol{\xi})^\top \boldsymbol{V}^{-1}(\boldsymbol{x}-\boldsymbol{\xi})\right]}{(2\pi)^N \sqrt{\det(\boldsymbol{V})}}. \tag{1}$$

Due to the symmetrization in the covariance matrix, $\boldsymbol{V}$ does not have to be necessarily positive; instead, the standard uncertainty relations $[\hat{q}_i, \hat{p}_j] = i\hbar\delta_{ij}$ dictate that [37]

$$\boldsymbol{V} + i\boldsymbol{\Omega} \geqslant 0, \tag{2}$$

where $\Omega_{ij} = \delta_{i,j-1} - \delta_{i,j+1}$ are the elements of the N-mode symplectic form $\boldsymbol{\Omega}$. We henceforth set $\hbar = 1$.

Despite the fact that a wide range of tasks in quantum information can be accomplished using Gaussian states [38–40], non-Gaussianity has been recognized as an essential resource for quantum computation [41–45]. Non-Gaussian states can be particularly advantageous in achieving fault-tolerant universal quantum computing [46]. Additionally, non-Gaussian states exhibit greater entanglement, as measured by superadditive measures, compared with Gaussian states with the same correlation matrix [36].

The space of non-Gaussian states is indeed broad, with Schrödinger cat states and Gottesman-Kitaev-Preskill states being among the most well-known members of this group, alongside Fock states. Cat and GKP states have indeed several relevant applications [47,48] that motivate the research conducted toward their more efficient generation [13,49–51].

1. GKP states

GKP states are an encoding of qubits as two logical basis states $|\bar{0}\rangle$ and $|\bar{1}\rangle$ in a single harmonic-oscillator mode that are simultaneous eigenstates of commuting displacements $e^{2\sqrt{\pi}iq_1}$ and $e^{-2\sqrt{\pi}ip_1}$ of momentum and position, respectively, where the displacement operators are termed stabilizers [17]. These states natively support error correction of amplitude- and phase-quadrature shifts because measurements of the stabilizers can detect such shifts without changing the state, making them ideal for fault-tolerant quantum information processing.

The encoded qubits can be set to be the following superposition of infinitely squeezed states

$$|\bar{0}_I\rangle \equiv \sum_{n=-\infty}^{\infty} |2n\sqrt{\pi}\rangle_q; \quad |\bar{1}_I\rangle \equiv e^{-\sqrt{\pi}ip_1}|\bar{0}_I\rangle, \tag{3}$$

where the I subscripts denote the ideal states and the q subscript denotes a position eigenstate. After verifying that these states indeed have the correct eigenvalue properties, one can observe the following two displacement operators to be the encoded Pauli operators acting on the encoded qubit states:

$$\bar{Z} = \exp(i\sqrt{\pi}q), \quad \bar{X} = \exp(-i\sqrt{\pi}p). \tag{4}$$

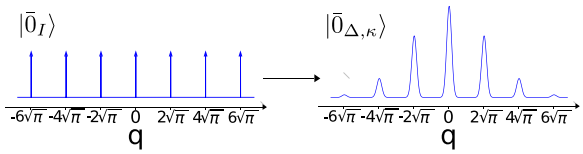

FIG. 1. Distribution of the position q for the ideal GKP state $|\bar{0}_I\rangle$ and the normalized GKP state $|\bar{0}_{\Delta,\kappa}\rangle$ with $\Delta = \kappa = 1/4$.

These satisfy the commutation relation

$$\bar{X}\bar{Z} = -\bar{Z}\bar{X}, \tag{5}$$

which allows them to detect shifts along p_1 and q_1 up to $\sqrt{\pi}/2$. That the stabilizers are the squares of the logical operators $\bar{X}$ and $\bar{Z}$ accords with the squares of Pauli matrices being identity.

The Wigner function of the state $|\bar{0}_I\rangle$ is

$$W_{\mathrm{GKP}\,\bar{0}_I}(q,p) = \sum_{s,t=-\infty}^{\infty} (-1)^{st} \delta\left(p - \frac{s\sqrt{\pi}}{2}\right)\delta(q - t\sqrt{\pi}). \tag{6}$$

Since the ideal state defined here is non-normalizable and made of infinitely squeezed states, we can work with normalizable states that approximate the ideal ones. There exist several possible approximations for GKP states, and the canonical approximation [52] is one of the most common ones. In the canonical approximation, the Dirac deltas in the Wigner functions are approximated by Gaussian functions with finite standard deviation Δ, and the overall Wigner function is enveloped in another Gaussian function with width κ^{-1},

$$|\bar{0}_I\rangle \to |\bar{0}_{\Delta,\kappa}\rangle \propto \sum_{n=-\infty}^{\infty} e^{\frac{1}{2}\kappa^2(2n\sqrt{\pi})^2 \bar{X}^2}|\Delta\rangle_q, \tag{7}$$

where

$$\langle q|\Delta\rangle = \left(\frac{1}{\pi\Delta^2}\right)^{\frac{1}{4}} e^{-\frac{q^2}{2\Delta^2}}. \tag{8}$$

The ideal GKP state is then restored when $\Delta, \kappa \to 0$. The Wigner functions, integrated over p, of the ideal basis states $|\bar{0}\rangle_{\mathrm{GKP}}$ and its approximation $|\tilde{0}\rangle_{\mathrm{GKP}} \equiv |\bar{0}_{\Delta,\kappa}\rangle$ are shown in Fig. 1. An extremely useful property of GKP states is that Gaussian noise from effects such as finite squeezing can be converted into errors on the encoded qubit, which can in turn be corrected by error-correcting codes known for DV quantum computation [53].

2. Cat states

Cat states are symmetric (even) or antisymmetric (odd) pure superpositions of two coherent states with opposite amplitudes $\pm\alpha$:

$$|\mathrm{cat}_{e/o}(\alpha)\rangle = \frac{1}{N_\pm(\alpha)}(|\alpha\rangle \pm |-\alpha\rangle), \tag{9}$$

where $N_{\pm}(\alpha) = [2(1 \pm e^{-2|\alpha|^2})]^{1/2}$. The cat state is a non-Gaussian state with Wigner function given by [54]

$$W_{\mathrm{cat}_{e/o(\beta)}}(\alpha) = \frac{2}{\pi\left(1 \pm e^{-2|\beta|^2}\right)} \times (e^{-2|\alpha-\beta|^2} + e^{-2|\alpha+\beta|^2} \pm 2e^{-2|\alpha|^2} \cos\left[4\mathrm{Im}(\alpha\beta^*)\right]). \tag{10}$$

By expanding the coherent states in terms of Fock states, we observe that the even (odd) cat states can also be expressed as a linear superposition of solely even (odd) photon-number states:

$$|\mathrm{cat_e}(\alpha)\rangle \propto \frac{\alpha^0}{\sqrt{0!}}|0\rangle + \frac{\alpha^2}{\sqrt{2!}}|2\rangle + \frac{\alpha^4}{\sqrt{4!}}|4\rangle + \cdots, \tag{11}$$

$$|\mathrm{cat_o}(\alpha)\rangle \propto \frac{\alpha^1}{\sqrt{1!}}|1\rangle + \frac{\alpha^3}{\sqrt{3!}}|3\rangle + \frac{\alpha^5}{\sqrt{5!}}|5\rangle + \cdots. \tag{12}$$

Cat states are extremely versatile, with applications in quantum communication and quantum metrology [55,56]. Encoding qubits in cat states can help fault-tolerant quantum computation [21,57,58]. They can be employed also as a resource to prepare GKP grid states [6,18], or can be used themselves to perform quantum error correction [59,60] and have been generated using nonlinear media [61].

B. Non-Gaussian optical state preparation

Any N-mode Gaussian state can be generated by applying Gaussian operators to a given initial Gaussian state, e.g., the N-mode vacuum state $|0\rangle^{\otimes N}$. Gaussian operations are those operations defined by unitary evolutions under Hamiltonians that are at most quadratic in creation and annihilation operators $\hat{a}^\dagger, \hat{a}$. Under these evolutions, the displacement vector $\boldsymbol{\xi}$ and covariance matrix $\boldsymbol{V}$ that univocally determine a Gaussian state are transformed according to the so-called symplectic transformations [62]

$$\boldsymbol{V} \to \boldsymbol{F}\boldsymbol{V}\boldsymbol{F}^\top \text{ and } \boldsymbol{\xi} \to \boldsymbol{F}\boldsymbol{\xi} + \boldsymbol{d}, \tag{13}$$

where $\boldsymbol{d}$ is the $2N$ real vector of displacements, and $\boldsymbol{F}$ satisfies

$$\boldsymbol{F}\boldsymbol{\Omega}\boldsymbol{F}^\top = \boldsymbol{\Omega}. \tag{14}$$

In this way, the transformed $\boldsymbol{\xi}$ and $\boldsymbol{V}$ respectively remain a $2N$-dimensional real vector and a $2N \times 2N$ real symmetric matrix that satisfies Eq. (2). These transformed parameters unambiguously define a new Gaussian state.

From a practical perspective, in optical implementations, all Gaussian transformations can be realized using squeezing and displacement operators, as well as an N-mode interferometer composed of beam splitters and phase shifters. These operations are commonly implemented in current experimental setups, with the squeezing amplitude being the main constraining parameter.

The actions of a squeezer S, and beam splitter B are respectively defined in terms of creation $\hat{a}_i^\dagger$ and annihilation operator $\hat{a}_i$ on the ith mode as

$$S(r) = \exp\left[\frac{r}{2}(\hat{a}^2 - \hat{a}^{\dagger 2})\right], \tag{15}$$

$$B_{ij}(\theta, \varphi) = \exp[\theta(e^{i\varphi}\hat{a}_i\hat{a}_j^\dagger - e^{-i\varphi}\hat{a}_i^\dagger\hat{a}_j)]. \tag{16}$$

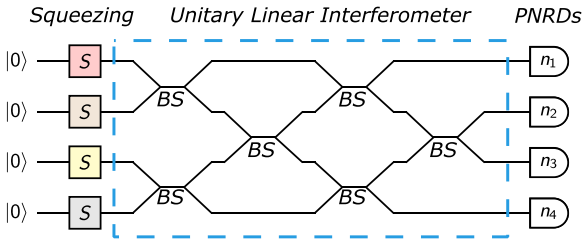

FIG. 2. GBS schematic with four modes. The $N(N-1)/2$ beam splitters and phase shifters (BS) are arranged in the so-called rectangular scheme [70]. *BS* label the beam splitters whose action in terms of the creation (annihilation) operators $a_i^\dagger$ (a_i) of the ith mode depend on the angles θ and φ as defined in Eq. (16).

Non-Gaussian unitary evolutions are generated by Hamiltonians containing terms that are at least cubic in the creation and annihilation operators [63]. However, these operators are difficult to realize on optical tables [64,65]. An alternative and often preferred approach to generating non-Gaussian states involves performing a measurement on a Gaussian state ρ [66,67] such that

$$\rho \to \frac{\sum_j X_j \rho X_j^\dagger}{\mathrm{Tr}\{\rho \sum_j X_j^\dagger X_j\}}, \tag{17}$$

where X_j represents a linear operator in the Fock space. For instance, in the case of photon-number-resolving detectors (PNRDs), we have $X_{ijk\ldots} = |ijk\cdots\rangle\langle ijk\cdots|$. Performing a measurement on m modes of an n-mode Gaussian state using PNRDs provides a practical method for conditionally generating a $(n-m)$-mode non-Gaussian state. The scheme originally developed for Gaussian boson sampling can indeed be modified for this purpose.

C. Gaussian boson sampling and state generation

Gaussian boson sampling is a quantum computational method that provides a significant advantage over classical computers for some specific problems [68]. The method consists of two steps. First a n-mode Gaussian state is generated by injecting n squeezed vacuum states into a linear interferometer. Then, each mode of the output Gaussian state is measured with a PNRD. The measurement pattern is the output of the computation. Finding the probability of any measurement pattern is in fact a problem with several relevant applications but classically hard to solve [69]. Since it is only possible to sample from such an output distribution, the applications are tempered, but even the sampling problem is computationally challenging for classical machines.

The GBS device described thus far, and displayed in Fig. 2 for four modes, can be slightly modified to serve as a conditional source of non-Gaussian states. In fact, if some modes are left unmeasured, the corresponding heralded mode is proven to be non-Gaussian, provided that at least one photon is detected in the other modes. In general, in an n-mode GBS-like device, $(n-m)$ modes are measured to produce an m-mode non-Gaussian state. However, from now on, we consider the case where only one mode is left unmeasured because our goal is to produce single-mode non-Gaussian states.

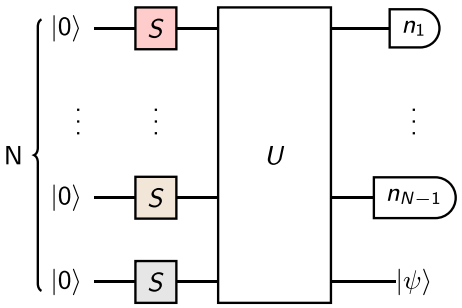

FIG. 3. GBS device with n squeezed displaced input vacuum states and $n-1$ PNRDs.

An example of GBS device used for state preparation [52,71], with n input modes, and $n-1$ PNRDs is shown in Fig. 3. Any unitary operation $U(\boldsymbol{\theta})$ on the n modes can be realized using a linear interferometer with as few as $n(n-1)/2$ beam splitters and phase shifters [70,72].

When no photons are detected by the PNRDs the Wigner function of the heralded state is Gaussian and is unambiguously determined by squeezing and displacement coefficients. In general, if n_T photons are detected in the measurement, then the output state can be expressed as a squeezed and displaced linear superposition of Fock states

$$|\psi_{\text{out}}\rangle = \hat{D}(d)\hat{S}(\zeta)\sum_{n=0}^{n_{\max}} c_n|n\rangle. \tag{18}$$

Equation (18) is known as the stellar representation of the state $|\psi\rangle$ with a stellar rank $r^* = n_{\max} \leqslant n_T$ [73]. The value of $n_{\max}$ depends on the connections established between the modes by $U(\boldsymbol{\theta})$. Gaussian states indeed have a stellar rank of $r^* = 0$, while $n_{\max}$ is equal to n_T only when the heralded mode is fully connected with all the detected modes. Furthermore, the number of independent coefficients c_n is constrained by the angles $\boldsymbol{\theta}$ that unambiguously determine the N-mode linear interferometer. In fact, the maximum number of independent parameters is given by $\mathcal{D} = (N+2)(N-1)/2$.

III. GBS-LIKE DEVICE WITH SINGLE-PHOTON SOURCES

Conditional state generation via a GBS-like device uses measurements with PNRDs as a source of non-Gaussianity, which is required to generate non-Gaussian states. The nonlinearity of the measurement is, in fact, a technique frequently employed to produce quantum optical non-Gaussian states [74–79]. It has even been used to develop a systematic technique that generates GKP qubits by exploiting the symmetries of the target states [71]. Conditional state generation provides an alternative to the use of challenging-to-realize deterministic non-Gaussian operators and offers easier implementation. However, it has a drawback due to the probabilistic nature of the outcome. The desired state is actually generated only when certain conditions are met. If the conditions are not satisfied, one has two options: either choose to encode the qubit into a Gaussian state, thereby losing protection against noise, or run the non-Gaussian source again until the conditions are fulfilled. Each iteration of the source, however, delays the encoding and actual processing of the information, exposing the system to decoherence and photon loss. For this reason, enhancing the probability of non-Gaussian state generation is crucial for scalable quantum computation. Multiplexing can be used to get around this problem but at the cost of added loss in the system. As an alternative, to increase the probability of success, we can introduce an additional source of non-Gaussianity alongside the measurements with PNRDs. Specifically, instead of using vacuum states, non-Gaussian states can be employed in some of the modes of the interferometer. The generation of single-mode non-Gaussian states has indeed been theorized [1,13,80–86] and successfully realized [2,87,88] in less general setups by incorporating non-Gaussian resources at the input and utilizing PNRDs.

Naturally, this approach is helpful as long as the elected input non-Gaussian states can be produced with a highly efficient alternative approach. Single-photon states, for example, can be generated with several efficient protocols [89,90] that are compatible [91,92] with the integrated photonics platforms on which GBS experiments have been demonstrated. In fact, squeezed single-photon states proved to be advantageous compared with squeezed vacuum states in other applications [93,94] and practical routes to squeezing single photons have been demonstrated [95–97], following the general trend of developing the ability to add light to nonvacuum light fields [4,98,99]. In this work, we evaluate the impact of using single-photon Fock states instead of vacuum states on the performance of non-Gaussian state generation. We compare the results achieved with a standard GBS-like device depicted in Fig. 3 and thoroughly described in Ref. [15] where the only non-Gaussian resource is the type of measurement being conducted. The two schemes are essentially the same when no single-photon sources are integrated into the protocol. Furthermore, an equivalence can be established between the two schemes even when single-photon Fock states are used as inputs in our approach. This equivalence arises when, in the full Gaussian scheme, one considers a portion of the interferometer as serving as a conditional single-photon source, achieved through generalized photon subtraction at the cost of one additional ancillary mode per input Fock state. We observe that the theory developed for GBS enables the analytical determination of the generated heralded state when $(n-m)$ modes are measured out of an n-mode linear interferometer receiving squeezed vacuum states as input. However, for a desired target state, finding the parameters that ensure high levels of fidelity and probability in the measurement pattern becomes impractical to solve analytically. In such cases, numerical optimizations are often preferred to address this problem effectively. The libraries provided by Xanadu are optimal tools for simulating GBS devices and optimizing their tunable parameters. Specifically, the library Mr Mustard is employed here both for GKP and cat states.

The approximate GKP state used as a target is the truncated core state of

$$|0_{A4}\rangle = S(r)\underbrace{\sum_{n=0}^{4} c_n|n\rangle}_{\text{Core state}}, \tag{19}$$

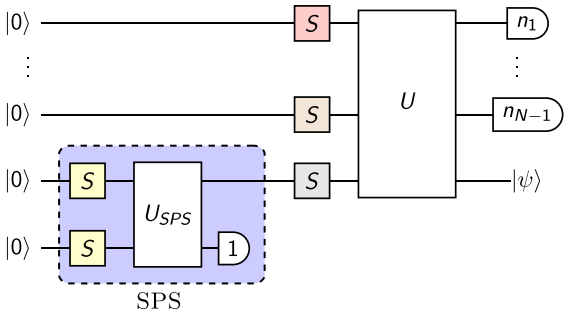

FIG. 4. GBS-like device with one single-photon source in the purple box.

where $|0_{A4}\rangle$ maximizes $\langle 0_{A4}|0_\Delta|0_{A4}\rangle$, where $|0_\Delta\rangle$ corresponds to the canonical normalization of the ideal GKP state $|0_I\rangle \to |0_{\Delta,\kappa}\rangle$ defined in Eq. (7) with $\kappa = \Delta$. In fact, the same state is used as a target by Tzitrin *et al.* in Ref. [52].

The target cat state is instead, in turn, defined as

$$|\mathrm{cat}_e(2)\rangle = \frac{1}{\sqrt{2}}(|2\rangle + |-2\rangle), \tag{20}$$

which is the even cat state defined in Eq. (9) with amplitude $\alpha = 2$.

Since both the probability p and the fidelity $\mathcal{F}$ to the target state are relevant features of a desirable source, the reward function maximized by the optimized parameters is set as a linear combination of these figures of merit. While the choice of the reward function is essentially arbitrary, it requires careful consideration because of the nature of the optimizer used in simulations, especially when dealing with larger circuits. Prioritizing probability over fidelity runs the risk of generating a state far from the target. Conversely, assigning excessive weight to fidelity can slow down optimization and lead to the generation of nearly unattainable states.

For our specific objective, we opt for a reward function $\mathcal{F} + p$ that evenly balances both probability and fidelity in all the optimizations, regardless of the number of modes and the target. This is simply a means to an end: we then report the results of all of these optimizations in terms of both $\mathcal{F}$ and p to see how single-photon sources can simultaneously improve both quantities. The actual relationship between the number of single-photon sources and a combined figure-of-merit parameter is more complicated; *quod vide* Fig. 9.

The squeezing amplitude r is a tunable parameter optimized in the simulations, but a maximum energy threshold is set for it at 12 dB. As a final remark, ancillary GBS has been introduced as a single-photon source instead of directly using the single-photon Fock state $|1\rangle$ in the input modes of the interferometer. The example of a scheme of a GBS-like device with one single-photon source into the Nth mode is shown in Fig. 4. This choice is made because non-Gaussian input states could potentially make the simulation with the libraries less reliable (see Appendix A for a discussion of how we numerically introduce single-photon sources based on physical architectures).

The photon subtraction technique is also used to prepare squeezed single-photon states [100]. Here, instead, the simulations of the inline squeezing of single photons are performed independently of the state-generation process since optimal single-photon sources are intended to replace the GBS-like devices employed in the simulation. In fact, we assume to have a deterministic single-photon source.

The measurement patterns are chosen with a small total number of subtracted photons to prioritize the probability of generating the state over the fidelity with the target state, which is already satisfactory for many applications. We indeed expect to increase the fidelity at the cost of smaller probability when more photons are detected [14]. This choice also helps reduce the runtime of the optimizations. We investigate multiple measurement patterns to evaluate the expected trend of the results with the number of detected photons. In all measurements, however, all the PNRDs detect at least one photon.

Furthermore, we observe that both the target GKP and even cat states can be expressed as linear combinations of even number states in the Fock representation. The same argument holds for the squeezed vacuum states in each input mode:

$$S(r)|0\rangle = \sum_{n=0}^{\infty} \frac{\tanh^n r}{\sqrt{\cosh r}} \frac{\sqrt{(2n)!}}{2^n n!} |2n\rangle. \tag{21}$$

Since beam splitters and phase shifters conserve the number of photons in the state, the N-mode output state can be expressed as

$$|\psi_{\mathrm{out}}\rangle = \sum_{n=0}^{\infty} \sum_{m_1+\cdots+m_M=2n} c_{m_1,\ldots,m_N} |m_1,\ldots,m_N\rangle. \tag{22}$$

As a consequence, in order to herald a state with an even number of photons, the PNRDs have to detect an even number of photons in total. If, instead, single-photon sources are used, then the necessary parity of the measured photons depends on how many squeezed single-photon states are present in the input.

IV. RESULTS AND DISCUSSION

First, we consider the case of a 2-mode GBS-like device and target state given by the approximate GKP states $|0_{A4}\rangle$ defined in Eq. (19). The probabilities p and fidelities $\mathcal{F}$ obtained with $n = 0, 1$ and two single-photon sources are plotted in Fig. 5. The best results are also reported in Table I.

The results obtained with the target state given by the even cat state of amplitude $\alpha = 2$ are displayed in Figs. 6 and 7 for two-mode and three-mode GBS-like devices, respectively. The best results are listed in Tables II and III.

As expected, the results reported in Table II for the case without any single-photon sources align with those presented in Table II of Ref. [15], where slightly improved fidelity and probability are achieved only with squeezing amplitudes exceeding the threshold considered in our work.

Each data point depicted in the two-dimensional plots corresponds to an optimization run utilizing the Python libraries "Mr Mustard" developed by Xanadu. Mr Mustard [101] is a Python library particularly suited for simulating Gaussian boson sampling devices. It efficiently handles the phase-space representation of Gaussian states and Gaussian channels, and it possesses several built-in functions simulating the action

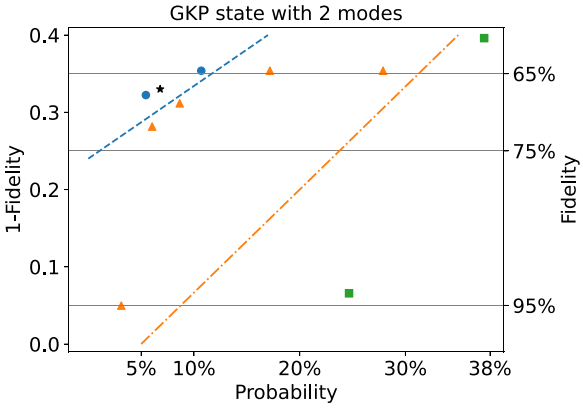

FIG. 5. Plot of the results obtained with a 2-mode GBS-like device when the target state is the approximate GKP state $|0_{A4}\rangle$. The blue dots represent the optima found without single-photon sources. The star refers to the best result reported in Ref. [52] without any single-photon sources ($n = 0$). The orange triangles depict the results obtained with one single-photon source. The green squares correspond to the results obtained with two single-photon sources. Diagonal lines limit regions in the fidelity-probability space where results of the corresponding color can be found.

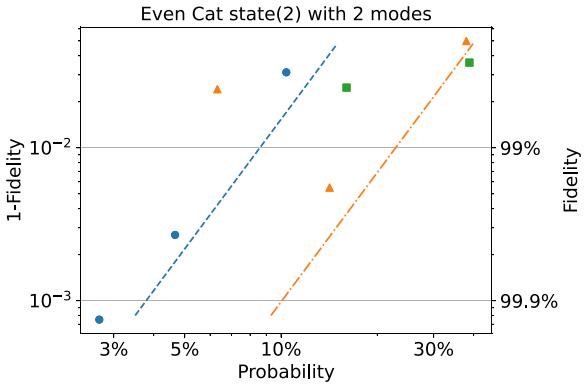

FIG. 6. Plot of the results obtained with a 2-mode GBS-like device when the target state is the cat state $|\text{cat}_e(2)\rangle$. The blue dots refer to the optima found without single-photon sources. The orange triangles correspond to the results obtained with one single-photon source. The green squares indicate the results obtained with two single-photon sources.

of various optical devices used in GBS protocols, such as beam splitters, phase shifters, squeezers, Mach-Zender interferometers, and PNRDs. The description in the number representation, especially useful at the last measurement stage of the protocol, can be realized with this library with arbitrary precision and cutoff for any Gaussian state. Finally, the library is equipped with optimization routines expressly dedicated to the specific gate. Unitary optimization is used in our optimizations for the linear interferometer, while optimization in Euclidean space is adopted for the squeezing amplitudes at the input modes. On the vertical axis, the plots report the fidelity between the state generated by simulating a photonic circuit with the given optimized parameters and the predefined target state. On the horizontal axis, it is reported the probability that the PNRDs measure the detection pattern that guarantees the generation of the desired state. Irrespective of the number of Fock states in the input modes of the interferometer, the optimization of the circuit's tunable parameters can yield varying outcomes. These outcomes depend on the initial parameters and the specific measurement pattern considered. As a consequence, the optimizations over a GBS-like device with a fixed number of modes and of input Fock states can lead to possibly very different results in terms of fidelity and probability. Nevertheless, a general trend can be identified, and it is highlighted by straight lines in the fidelity-probability space that demarcate the regions where given classes of results are present and where they are absent.

As expected [14], at a fixed number of single-photon sources, the fidelity increases at the expense of lower prob-

TABLE I. Table showing the fidelities $\mathcal{F}$ and probabilities p obtained by a 2-mode GBS-like device when the target state is the approximate GKP state $|0_{A4}\rangle$. The parameter n represents the number of input modes receiving the single-photon state $|1\rangle$, while n_T denotes the number of photons observed in the detected mode.

n	$1-\mathcal{F}$	p	n_T
0	0.35	11%	4
	0.32	5.4%	4
1	0.35	27%	3
	0.31	8.6%	3
	4.9×10^{-2}	3.1%	5
2	0.40	37%	2
	6.6×10^{-2}	24%	2

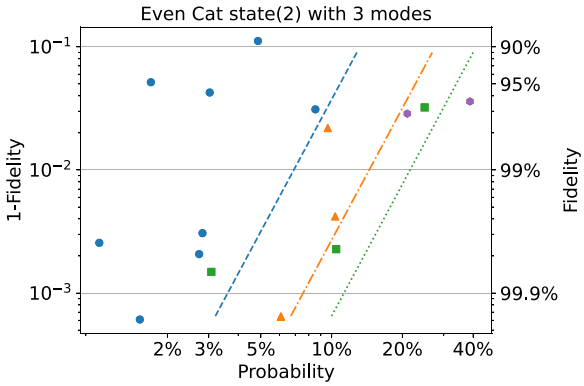

FIG. 7. Plot of the results obtained with a 3-mode GBS-like device when the target state is the cat state $|\text{cat}_e(2)\rangle$. The blue dots refer to the optima found without single-photon sources. The orange triangles correspond to the results obtained with one single-photon source. The green squares indicate the results obtained with two single-photon sources. The purple hexagons indicate the results obtained with three single-photon sources. Diagonal lines limit regions in the fidelity-probability space where results of the corresponding color can be found.

TABLE II. Same as Table I but with the target state being the even cat state of amplitude $\alpha = 2$.

n	$1-\mathcal{F}$	p	n_T
0	3.1×10^{-2}	10%	2
	2.7×10^{-3}	4.7%	4
	7.5×10^{-4}	2.7%	6
1	5.0×10^{-2}	38%	1
	5.5×10^{-3}	14%	3
2	3.6×10^{-2}	39%	2

ability when more photons are measured. Overall, we observe that the efficiency of the non-Gaussian state source, realized with a boson sampling-like device, experiences improvement when single-photon states are injected into the input modes of the interferometer. For example, when considering the three-mode GBS-like device, the probability of generating a cat state with fidelity around 97% steadily increases, potentially doubling its value, every time a squeezed single-photon state is used instead of a squeezed vacuum state. The improvement in the state generation is qualitatively displayed in Fig. 8 through a comparison of the Wigner functions of the target cat state and the states generated using a three-mode GBS-like device with and without SPSs.

From a comparison between the outcomes related to cat-state generation with 2- and 3-mode networks, no improvements emerge from using more modes. Indeed, it appears that the additional resources do not play a significant role in increasing fidelity with the target state, as one might expect. In fact, in the context of state generation with purely Gaussian states, the number $\mathcal{D}$ of independent parameters c_i in (18) grows quadratically with the number of modes, as conjectured in Ref. [15]. However, if the total number of measured photons, $n_T < \mathcal{D}$, the problem of finding the best parameters is underdetermined, and the optimal result can be found with smaller Gaussian states. A similar argument holds even when the number of measured photons $n_t \geqslant \mathcal{D}$, but the target state can be well approximated by a quantum state with a small rank, as is the case for the cat state with amplitude $\alpha = 2$. In this scenario, the state that can be generated by the smaller circuit exhibits satisfactory fidelity, and the search for a better state attainable with additional modes becomes unfeasible for the optimizer.

Finally, in Fig. 9, we plot the results presented in Table III by showing how the relationship between the quality of the

TABLE III. Same as Table II but with a 3-mode GBS-like device.

n	$1-\mathcal{F}$	p	n_T
0	3.1×10^{-2}	8.5%	2
	2.1×10^{-3}	2.7%	4
	3.1×10^{-3}	2.8%	4
	6.1×10^{-4}	1.5%	6
1	4.2×10^{-3}	10%	3
	6.4×10^{-4}	6.1%	5
2	3.2×10^{-2}	25%	2
	2.3×10^{-3}	10%	4
3	3.6×10^{-2}	39%	3

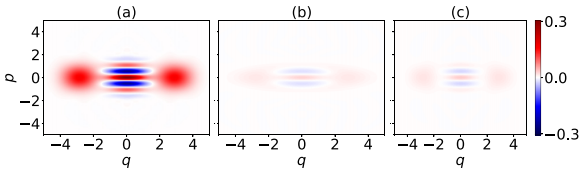

FIG. 8. Color maps of the Wigner functions of (a) the target cat state, (b) the state generated using a GBS-like device without any single-photon sources, and (c) the state generated using a GBS-like device with one single-photon source. The probability of generating the state P is higher when a single Fock state is injected into an input mode, $P = 10.5\%$. In comparison, the probability achieved solely with Gaussian inputs is $P = 8.5\%$. Moreover, an improvement in fidelity is observed, with an increase from 96.9% to 99.6%. This enhancement is visually apparent in the Wigner function plotted. The differences in color shading between the generated states and the target state correspond to reduced values of the Wigner function, where the norm of this function corresponds to the probability of generating the displayed states.

results changes with the number of single-photon sources used to generate the state. The figure of merit for quantifying the quality of these results is determined as the difference between the probability p of generating the state and the quantum angle $QA \equiv \cos^{-1}\sqrt{\mathcal{F}}$ [102], which serves as the measure of the distance between the generated and target state. Our analysis reveals that the quality of the results consistently improves as the number of single-photon sources employed increases. Indeed, these two quantities are positively correlated, with a Pearson correlation coefficient of approximately 92% the sample Pearson correlation coefficient between the variable $\boldsymbol{x}$ and $\boldsymbol{y}$, $r_{x,y} \simeq 92\%$, where the coefficient $r_{x,y}$ is defined as

$$r_{x,y} = \frac{\sum_i (x_i - \bar{x})(y_i - \bar{y})}{\sqrt{\sum_i (x_i - \bar{x})^2}\sqrt{\sum_i (y_i - \bar{y})^2}}, \tag{23}$$

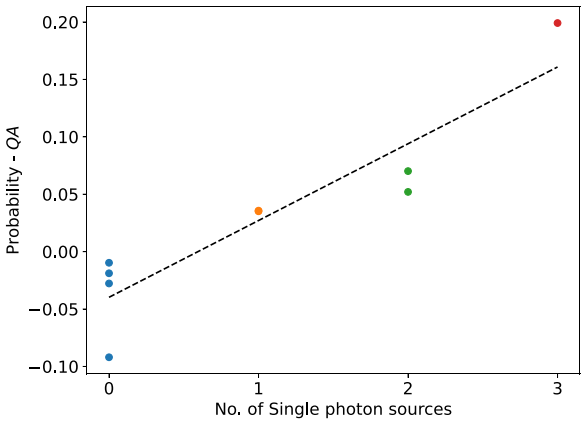

FIG. 9. Plot depicting the difference between the probability of state generation and the quantum angle with the target state as a function of the number of single-photon sources, using the data from the Table III. The dashed line represents the linear regression of the data, with a slope of approximately 6.7×10^{-2} and an intercept of approximately -4.0×10^{-2}; note that this difference can indeed be negative

$\bar{x}$ is the sample mean of $\boldsymbol{x}$, while x_i and y_i are respectively the number of single-photon sources, and the difference between probability and QA of the ith optimization.

We close with a brief discussion of single-photon sources on or compatible with integrated photonic devices. Currently, these have efficiencies above 84% that are constantly improving via advances such as better mode coupling [90]. They have high purities (99.3%) and indistinguishabilities (98%) [90]. Together, purities and indistinguishabilities may each multiply our fidelities and the efficiencies may drop our success probabilities by a factor of 0.84^m for m single-photon sources. Even so, the states generated using these noisy single-photon sources will be better than what is possible with ideal GBS devices alone, with $1-\mathcal{F}$ and p on the last lines of Tables II, III, and I being updated to $0.12 < 0.32$ and $17\% > 11\%$, 8.7×10^{-2} and $27\% > 10\%$, and 1.1×10^{-1} and $23\% > 8.5\%$, respectively. Moreover, adding realistic noise only on the single-photon sources elicits a new trade-off, with even cat states of amplitude $\alpha = 2$ having higher overall success probabilities with one single-photon source than with two. As single-photon-source qualities improve including via quantum memories and as realistic noise sources such as loss on ideal GBS devices are considered, we expect the optimal results to converge to following the trends in Fig. 9.

V. CONCLUSIONS

We have introduced and evaluated an alternative scheme to non-Gaussian state generation with GBS-like devices presented in Ref. [15]. Specifically, we have compared the performance of the source when single photons and inline squeezing are employed in place of squeezed vacuum states in the input modes, serving as additional non-Gaussian resources for the PNRDs. Fidelity with the target state and probability of success of the conditional source have been used as figures of merit of the performance. We tested the efficiency of the model on 2- and 3-mode devices by targeting the Schrödinger cat state and the GKP code state, as two prominent examples of non-Gaussian states that complement Gaussian resources to realize universal quantum computation in the continuous-variable domain. Despite a variability in the results, ascribable to the dependence of the classical optimization on the initial conditions of the quantum circuit, overall, we observe that the introduction of single photons successfully increases the probability of generating the states as well as their fidelity with the target. The 4-photon GKP core state $|0_4\rangle$, can be generated with fidelities greater than 90% only when at least one squeezed photon interferes with the other mode. Moreover, the probability of generating a state with a fidelity above this threshold appears to be eight times larger when two single-photon sources are employed instead of one. Similarly, looking at the optimal probability of generating states whose fidelity with cat states of amplitude $\alpha = 2$ is approximately equal to 95%, we see that it increases monotonically with the number of single photons introduced. Analogous evaluations with higher fidelities or more complex targets could be conducted with additional simulation resources, enabling the study of schemes with modes and measuring patterns that account for a greater number of photons. The advantage of the presented scheme over a traditional one can also be experimentally assessed using high efficiency single-photon sources and inline squeezing. Since state generation is used numerous times at the heart of quantum computation protocols, the advantages presented here should compound to make a marked difference in reducing the overhead for fault-tolerant quantum computation.

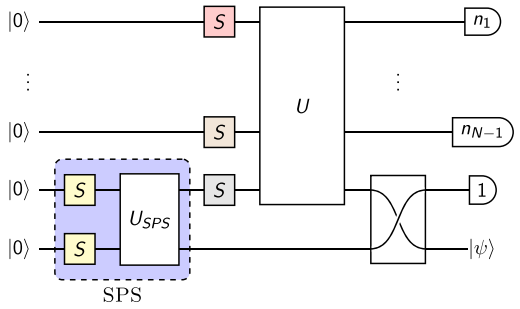

FIG. 10. GBS device with single-photon source. The SPS is necessary because single-photon Fock states are not handled by the optimizer.

ACKNOWLEDGMENTS

The authors thank Guillaume Thekkadath and Anaelle Hertz for fruitful discussions and Filippo Miatto and Xanadu for technical support on their software packages. The authors acknowledge that the NRC headquarters is located on the traditional unceded territory of the Algonquin Anishinaabe and Mohawk people. A.Z.G. acknowledges funding from the NSERC PDF program. K.H. acknowledges funding from NSERC's Discovery Grant.

APPENDIX: SINGLE-PHOTON SOURCE

The Python libraries Strawberry Fields [103,104] and Mr Mustard [101], developed by Xanadu and used in this work, are indeed effective to simulate GBS devices. Non-Gaussian input states are, however, often mishandled by the logic of those libraries due to the inevitable need to truncate Fock spaces. As such, it is convenient using always squeezed vacuum states in the input modes of the interferometer. To overcome this problem, whenever a single-photon Fock state $|1\rangle$ is chosen as input state, another 2-mode GBS is introduced as source of the Fock state $|1\rangle$. The two input states for this source are indeed Gaussian as well and the PNRD on the ancillary mode can be simulated when all the other modes of the main GBS are detected. In this way the ancillary GBS single-photon source can be integrated with the actual GBS device under investigation. The simulator then effectively treats an n-mode GBS-device with m single-photon input states $|1\rangle$ as an $(n+m)$-mode linear interferometer where only one mode is left unmeasured, and the optimization is restricted to the tunable parameters of the main GBS device leaving the ancillary mode parameters fixed. An example with an N-mode GBS and a single-photon source is given in Fig. 10.

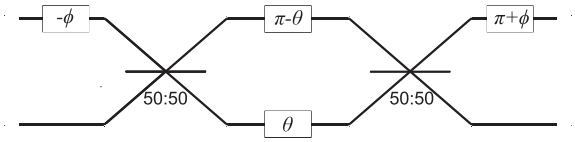

FIG. 11. Interferometer made of two symmetric 50 : 50 beam splitters and four phase shifters that realizes the evolution described in (A5).

The single-photon source (SPS) shown in the violet box of Fig. 10 is created itself with another GBS device. A Gaussian state can be prepared by squeezing single-mode vacuum states and letting them interfere in a linear interferometer. The single-mode squeeze operator $\boldsymbol{S}(r)$ with $r \in \mathbb{R}$ is expressed in terms of creation operator $\hat{a}^\dagger$ and annihilation operator $\hat{a}$ as

$$\boldsymbol{S}(r) = \exp\left[\frac{r}{2}(\hat{a}^2 - \hat{a}^{\dagger 2})\right]. \tag{A1}$$

The squeezed vacuum state $|r\rangle$ is then given by

$$|r\rangle = \boldsymbol{S}(r) = \sum_{n=0}^{\infty} \alpha_n(r)|2n\rangle, \tag{A2}$$

where

$$\alpha_n(r) = \frac{\sqrt{(2n)!}}{2^n n!}\frac{\tanh^n r}{\sqrt{\cosh r}}. \tag{A3}$$

As it has been shown above any linear N-mode linear interferometer can be decomposed into $N(N-1)/2$ beam splitters $\boldsymbol{\theta}$, $\boldsymbol{\varphi}$ and phase-shift gate $\boldsymbol{R}(\phi)$. The beam splitter operation in terms of creation and annihilation operator on the modes i and j is

$$\boldsymbol{B}_{ij}(\theta,\varphi) = \exp[\theta(e^{i\varphi}\hat{a}_i\hat{a}_j^\dagger - e^{-i\varphi}\hat{a}_i^\dagger\hat{a}_j)]. \tag{A4}$$

The unitary operator describing the evolution of the operators $\hat{a}_i$, $\hat{a}_j$ under the action of the beam splitter in (A4) is

$$\boldsymbol{U}(\theta,\varphi) = \begin{pmatrix} \cos\theta & e^{i\phi}\sin\theta \\ -e^{-i\phi}\sin\theta & \cos\theta \end{pmatrix}, \tag{A5}$$

where $\varphi = \pi - \phi$. This evolution can be realized with an interferometer made of two 50 : 50 beam splitters and four phase shifters arranged as displayed in Fig. 11.

Given a two-mode pure input Fock state $|n\rangle|m\rangle$, the output state produced by the beam splitter $\boldsymbol{B}(\theta,\phi)$ is [105]

$$\begin{aligned}\boldsymbol{B}(\theta,\phi)|n\rangle|m\rangle = &\sum_{q,q'}\binom{n}{q}\binom{m}{q'}\sqrt{\frac{(q+q')!(n+m-q-q')!}{n!m!}} \\ &\times \cos(\theta)^{m+q-q'}\sin(\theta)^{n-q+q'}e^{i(n-q-q')\phi}(-1)^{q'}|q+q', n+m-q-q'\rangle.\end{aligned} \tag{A6}$$

We can now see how the two mode Gaussian state $|\psi\rangle$ produced by interfering two single-mode squeezed vacuum states in the interferometer displayed in Fig. 11 can be expanded in the Fock basis. The 1 (2) label marks the first (second) mode:

$$\begin{aligned}|\psi\rangle &= \boldsymbol{B}(\theta,\phi)\boldsymbol{S}_2(r_2)\boldsymbol{S}_1(r_1)|0\rangle_1|0\rangle_2 = \sum_{n=0}^{\infty}\alpha_n(r_1)\boldsymbol{B}(\theta,\phi)\boldsymbol{S}_2(r_2)|2n\rangle_1|0\rangle_2 \\ &= \sum_{n,m=0}^{\infty}\alpha_n(r_1)\alpha_m(r_2)\boldsymbol{B}(\theta,\phi)|2n\rangle|2m\rangle \\ &= \sum_{n,m=0}^{\infty}\alpha_n(r_1)\alpha_m(r_2)\sum_{q,q'}\binom{n}{q}\binom{m}{q'}\sqrt{\frac{(q+q')!(2n+2m-q-q')!}{n!m!}} \\ &\quad\times\cos(\theta)^{2m+q-q'}\sin(\theta)^{2n-q+q'}e^{i(2n-q-q')\phi}(-1)^{q'}|q+q', 2n+2m-q-q'\rangle.\end{aligned} \tag{A7}$$

We know that a single-photon state can be generated by measuring an odd number of photons in the output mode. In particular, a single-photon Fock state whose stellar rank is equal to one can be produced even when only one photon is measured in the ancillary mode. In this case the unnormalized heralded state is

$$\begin{aligned}\langle 1|_2|\psi\rangle &= \langle 1|_2\boldsymbol{B}(\theta,\phi)\boldsymbol{S}_2(r_2)\boldsymbol{S}_1(r_1)|0\rangle_1|0\rangle_2 \\ &= 2\sum_{n,m=0}^{\infty}\frac{\tanh^n(r_1)\tanh^m(r_2)}{\sqrt{\cosh(r_1)\cosh(r_2)}}\frac{\sqrt{(2n+2m-1)!}}{2^{n+m}n!m!}[\cos(\theta)]^{2n+1}[e^{-i\phi}\sin(\theta)]^{2m-1}[n\tan^2(\theta)-m]|2(n+m)-1\rangle \\ &= \frac{2e^{i\phi}\cot\theta}{\sqrt{\cosh(r_1)\cosh(r_2)}}\sum_{N=1}^{\infty}\frac{\sqrt{(2N-1)!}}{2^N}\tanh^N(r_2)(e^{-i\phi}\sin\theta)^{2N}\sum_{n=0}^{N}\left(\frac{\tanh r_1}{\tanh r_2}\right)^n\frac{\left(e^{i\phi}\cot\theta\right)^{2n}}{n!(N-n!)}\left(\frac{n}{\cos^2(\theta)}-N\right)|2N-1\rangle.\end{aligned} \tag{A8}$$

The single-mode unnormalized state $\langle 1|_2|\psi\rangle$ can thus be written as

$$\langle 1|_2|\psi\rangle = \mathcal{N}\sum_{N=1}^{\infty} c_N|2N-1\rangle, \tag{A9}$$

where

$$\mathcal{N} = \frac{2e^{i\phi}\cot\theta}{\sqrt{\cosh(r_1)\cosh(r_2)}}$$

and c_N is the coefficient relative to the Fock state $|2N-1\rangle$. To determine which values of r_1, r_2, θ, and ϕ lead to a single-photon Fock state generation, we have to ensure that $c_1 \neq 0$ and $c_N = 0\ \forall\, N \geqslant 2$.

In general, we have that

$$c_N \propto \sum_{n=0}^{N}\left(\frac{\tanh r_1}{\tanh r_2}\right)^n \frac{(e^{i\phi}\cot\theta)^{2n}}{n!(N-n!)}\left(\frac{n}{\cos^2(\theta)} - N\right). \tag{A10}$$

By introducing the function $f(r_1, r_2) \equiv (\tanh r_1/\tanh r_2)$ we find that

$$c_1 \propto -1 + f(r_1, r_2)e^{2i\phi}, \tag{A11}$$

while

$$c_2 \propto -1 + f(r_1, r_2)e^{2i\phi}[1-\cot^2(\theta)] + f^2(r_1, r_2)e^{4i\phi}\cot^4(\theta). \tag{A12}$$

We proceed by setting $c_2 = 0$. We can prove by contradiction that $\phi \in \{\pi/2, 3\pi/2\}$ is a necessary condition.

Proof. Let us assume that there exists $\phi \notin \{\pi/2, 3\pi/2\}$ that satisfies $c_2 = 0$. If $c_2 = 0$, then both $\mathrm{Re}\{c_2\} = 0$, and $\mathrm{Im}\{c_2\} = 0$:

$$\mathrm{Im}\{c_2\} = 0 \Rightarrow \sin(2\phi)f(r_1, r_2)[1-\cot^2(\theta) + 2f(r_1, r_2)\cot^2(\theta)\cos(2\phi)] = 0, \tag{A13}$$

$$\Rightarrow 1 - \cot^2(\theta) + 2f(r_1, r_2)\cot^2(\theta)\cos(2\phi) = 0, \tag{A14}$$

$$\Rightarrow f(r_1, r_2) = \frac{\cot^2(\theta) - 1}{2\cot^2(\theta)\cos(2\phi)}; \tag{A15}$$

$$\mathrm{Re}\{c_2\} = 0 \Rightarrow \frac{\cot^2(\theta)-1}{2\cot^2(\theta)\cos(2\phi)}\cos(2\phi)[1-\cot^2(\theta)] + \frac{[\cot^2(\theta)-1]^2}{4\cot^4(\theta)\cos^2(2\phi)}\cot^2(\theta)[2\cos^2(2\phi)-1] = 1, \tag{A16}$$

$$\Rightarrow -\frac{[1-\cot^2(\theta)]^2}{2\cot^2(\theta)} + \frac{[1-\cot^2(\theta)]^2}{2\cot^2(\theta)} - \frac{[1-\cot^2(\theta)]^2}{4\cot^4(\theta)\cos^2(2\phi)} = 1, \tag{A17}$$

$$\Rightarrow 1 = -\frac{[1-\cot^2(\theta)]^2}{4\cot^4(\theta)\cos^2(2\phi)} \leqslant 0. \tag{A18}$$

This proves that there does not exist any $\phi \notin \{\pi/2, 3\pi/2\}$ that satisfies the condition $c_2 = 0$. While (A13) is verified only when $\sin(2\phi) = 0$, and $\phi \in \{\pi/2, 3\pi/2\}$. ■

From (A10) we can observe that the sign $e^{in\pi} = (-1)^n$ can be compensated by a change of sign of r_1 since $\tanh(r_1)$ is an odd function. As a consequence, we can set $\phi = \pi/2$ without loss of generality.

In this case we find that

$$c_2 = 0 \Rightarrow f(r_1, r_2)[1-\cot^2(\theta) + 2f(r_1, r_2)\cot^2(\theta)] = 0, \tag{A19}$$

$$\Rightarrow 1 + f(r_1, r_2) = f(r_1, r_2)\cot^2(\theta)[1 + f(r_1, r_2)]. \tag{A20}$$

Equation (A20) is verified when $f(r_1, r_2) = -1$. However, this condition also set c_1 in (A11) to zero. The alternative solution is

$$f(r_1, r_2) = \tan^2(\theta). \tag{A21}$$

This condition satisfies $c_N = 0$ for any $N \geqslant 2$.

Proof.

$$\begin{aligned} c_N &\propto \sum_{n=0}^{N}\frac{(-1)^n}{n!(N-n!)}\left(\frac{n}{\cos^2(\theta)} - N\right) = \sum_{n=0}^{N}\frac{(-1)^n}{n!(N-n!)}\frac{n}{\cos^2(\theta)} - N\sum_{n=0}^{N}\frac{(-1)^n}{n!(N-n!)} \\ &= \sum_{n=0}^{M+1}\frac{(-1)^n}{n!(M+1-n!)}\frac{n}{\cos^2(\theta)} - N\sum_{n=0}^{N}\frac{(1)^{N-n}(-1)^n}{n!(N-n!)} = \sum_{n=1}^{M+1}\frac{(-1)(-1)^{n-1}}{n(n-1)![M-(n-1)!]}\frac{n}{\cos^2(\theta)} - N(1-1)^N \\ &= -\frac{1}{\cos^2(\theta)}\sum_{m=0}^{M}\frac{(-1)^m}{m!(M-m!)} = -\frac{1}{\cos^2(\theta)}\sum_{m=0}^{M}\frac{(1)^{M-m}(-1)^m}{m!(M-m!)} = -\frac{1}{\cos^2(\theta)}(1-1)^M = 0\ \forall\, M \geqslant 1. \end{aligned} \tag{A22}$$

■

The squeezing intensities r_1, and r_2 are related with the beam splitter angle θ via the relation in (A21). They can be optimized to maximize the probability $P(r_1, r_2)$ of generating the single-photon Fock state. From (A8) we have

$$P(r_1, r_2) = \left|\langle 1|_1\langle 1|_2 \boldsymbol{B}\left(\theta, \frac{\pi}{2}\right)\boldsymbol{S}_2(r_2)\boldsymbol{S}_1(r_1)|0\rangle_1|0\rangle_2\right|^2 = \left|\frac{i\sin(2\theta)}{2\sqrt{\cosh(r_1)\cosh(r_2)}}(\tanh(r_1)+\tanh(r_2))\right|^2 \tag{A23}$$

$$= \left|\frac{2\tan(\theta)}{1+\tan^2(\theta)}\frac{\tanh(r_1)+\tanh(r_2)}{2\sqrt{\cosh(r_1)\cosh(r_2)}}\right|^2 = \left|\frac{\sqrt{\frac{\tanh r_1}{\tanh r_2}}}{1+\frac{\tanh r_1}{\tanh r_2}}\frac{\tanh(r_1)+\tanh(r_2)}{\sqrt{\cosh(r_1)\cosh(r_2)}}\right|^2 \tag{A24}$$

$$= \left|\frac{\sqrt{\sinh(r_1)\sinh(r_2)}}{\cosh(r_1)\cosh(r_2)}\right|^2 = \left|\frac{\sinh(r_1)\sinh(r_2)}{\cosh^2(r_1)\cosh^2(r_2)}\right|. \tag{A25}$$

So $P(r_1, r_2)$ is a multiplicatively separable function with respect to the variables r_1, and r_2. Because of the symmetry of the function, a maximum is found for $r_1 = r_2 = r^*$, $\theta = \pi/4$, and $r^* = \operatorname{arctanh}(1/\sqrt{2}) \approx 0.8814$ that maximizes the function $\sinh(r)/\cosh^2(r)$. In this case the probability of generating a single-photon Fock state is $P(r^*, r^*) = 1/4$.

[1] D. T. Pegg, L. S. Phillips, and S. M. Barnett, Optical state truncation by projection synthesis, Phys. Rev. Lett. **81**, 1604 (1998).

[2] A. I. Lvovsky and J. Mlynek, Quantum-optical catalysis: Generating nonclassical states of light by means of linear optics, Phys. Rev. Lett. **88**, 250401 (2002).

[3] J. Wenger, R. Tualle-Brouri, and P. Grangier, Non-Gaussian statistics from individual pulses of squeezed light, Phys. Rev. Lett. **92**, 153601 (2004).

[4] A. Zavatta, S. Viciani, and M. Bellini, Quantum-to-classical transition with single-photon-added coherent states of light, Science **306**, 660 (2004).

[5] A. Ourjoumtsev, R. Tualle-Brouri, J. Laurat, and P. Grangier, Generating optical Schrödinger kittens for quantum information processing, Science **312**, 83 (2006).

[6] H. M. Vasconcelos, L. Sanz, and S. Glancy, All-optical generation of states for "encoding a qubit in an oscillator," Opt. Lett. **35**, 3261 (2010).

[7] T. J. Bartley, G. Donati, J. B. Spring, X.-M. Jin, M. Barbieri, A. Datta, B. J. Smith, and I. A. Walmsley, Multiphoton state engineering by heralded interference between single photons and coherent states, Phys. Rev. A **86**, 043820 (2012).

[8] J. Etesse, M. Bouillard, B. Kanseri, and R. Tualle-Brouri, Experimental generation of squeezed cat states with an operation allowing iterative growth, Phys. Rev. Lett. **114**, 193602 (2015).

[9] T. J. Bartley and I. A. Walmsley, Directly comparing entanglement-enhancing non-Gaussian operations, New J. Phys. **17**, 023038 (2015).

[10] L.-Y. Hu, J.-N. Wu, Z. Liao, and M. S. Zubairy, Multiphoton catalysis with coherent state input: Nonclassicality and decoherence, J. Phys. B: At., Mol. Opt. Phys. **49**, 175504 (2016).

[11] R. J. Birrittella, M. E. Baz, and C. C. Gerry, Photon catalysis and quantum state engineering, J. Opt. Soc. Am. B **35**, 1514 (2018).

[12] S. Takeda and A. Furusawa, Toward large-scale fault-tolerant universal photonic quantum computing, APL Photonics **4**, 060902 (2019).

[13] M. Eaton, R. Nehra, and O. Pfister, Non-Gaussian and Gottesman-Kitaev-Preskill state preparation by photon catalysis, New J. Phys. **21**, 113034 (2019).

[14] K. K. Sabapathy, H. Qi, J. Izaac, and C. Weedbrook, Production of photonic universal quantum gates enhanced by machine learning, Phys. Rev. A **100**, 012326 (2019).

[15] D. Su, C. R. Myers, and K. K. Sabapathy, Conversion of Gaussian states to non-Gaussian states using photon-number-resolving detectors, Phys. Rev. A **100**, 052301 (2019).

[16] N. Quesada, L. G. Helt, J. Izaac, J. M. Arrazola, R. Shahrokhshahi, C. R. Myers, and K. K. Sabapathy, Simulating realistic non-Gaussian state preparation, Phys. Rev. A **100**, 022341 (2019).

[17] D. Gottesman, A. Kitaev, and J. Preskill, Encoding a qubit in an oscillator, Phys. Rev. A **64**, 012310 (2001).

[18] D. J. Weigand and B. M. Terhal, Generating grid states from Schrödinger-cat states without postselection, Phys. Rev. A **97**, 022341 (2018).

[19] I. Tzitrin, T. Matsuura, R. N. Alexander, G. Dauphinais, J. E. Bourassa, K. K. Sabapathy, N. C. Menicucci, and I. Dhand, Fault-tolerant quantum computation with static linear optics, PRX Quantum **2**, 040353 (2021).

[20] V. Dodonov, I. Malkin, and V. Man'ko, Even and odd coherent states and excitations of a singular oscillator, Physica **72**, 597 (1974).

[21] P. T. Cochrane, G. J. Milburn, and W. J. Munro, Macroscopically distinct quantum-superposition states as a bosonic code for amplitude damping, Phys. Rev. A **59**, 2631 (1999).

[22] H. Jeong and M. S. Kim, Efficient quantum computation using coherent states, Phys. Rev. A **65**, 042305 (2002).

[23] T. C. Ralph, A. Gilchrist, G. J. Milburn, W. J. Munro, and S. Glancy, Quantum computation with optical coherent states, Phys. Rev. A **68**, 042319 (2003).

[24] Z. Leghtas, G. Kirchmair, B. Vlastakis, R. J. Schoelkopf, M. H. Devoret, and M. Mirrahimi, Hardware-efficient autonomous quantum memory protection, Phys. Rev. Lett. **111**, 120501 (2013).

[25] Q. Xu, G. Zheng, Y.-X. Wang, P. Zoller, A. A. Clerk, and L. Jiang, Autonomous quantum error correction and fault-tolerant quantum computation with squeezed cat qubits, npj Quantum Inf. **9**, 78 (2023).

[26] S. Konno, W. Asavanant, F. Hanamura, H. Nagayoshi, K. Fukui, A. Sakaguchi, R. Ide, F. China, M. Yabuno, S. Miki, H. Terai, K. Takase, M. Endo, P. Marek, R. Filip, P. van Loock, and A. Furusawa, Logical states for fault-tolerant quantum computation with propagating light, Science **383**, 289 (2024).

[27] W. H. Zurek, Sub-Planck structure in phase space and its relevance for quantum decoherence, Nature (London) **412**, 712 (2001).

[28] F. Toscano, D. A. R. Dalvit, L. Davidovich, and W. H. Zurek, Sub-Planck phase-space structures and Heisenberg-limited measurements, Phys. Rev. A **73**, 023803 (2006).

[29] D. A. R. Dalvit, R. L. de Matos Filho, and F. Toscano, Quantum metrology at the Heisenberg limit with ion trap motional compass states, New J. Phys. **8**, 276 (2006).

[30] E. Schrödinger, Die gegenwärtige situation in der quantenmechanik, Naturwissenschaften **23**, 807 (1935).

[31] L. Souza, M. Nemes, M. França Santos, and J. Peixoto de Faria, Quantifying the decay of quantum properties in single-mode states, Opt. Commun. **281**, 4696 (2008).

[32] A. Z. Goldberg, A. B. Klimov, M. Grassl, G. Leuchs, and L. L. Sánchez-Soto, Extremal quantum states, AVS Quantum Sci. **2**, 044701 (2020).

[33] N. Akhtar, B. C. Sanders, and C. Navarrete-Benlloch, Sub-Planck structures: Analogies between the Heisenberg-Weyl and SU(2) groups, Phys. Rev. A **103**, 053711 (2021).

[34] A. Z. Goldberg and K. Heshami, How squeezed states both maximize and minimize the same notion of quantumness, Phys. Rev. A **104**, 032425 (2021).

[35] J. Marshall and N. Anand, Simulation of quantum optics by coherent state decomposition, Opt. Quantum **1**, 78 (2023).

[36] M. Walschaers, Non-Gaussian quantum states and where to find them, PRX Quantum **2**, 030204 (2021).

[37] R. Simon, N. Mukunda, and B. Dutta, Quantum-noise matrix for multimode systems: U(n) invariance, squeezing, and normal forms, Phys. Rev. A **49**, 1567 (1994).

[38] C. Weedbrook, S. Pirandola, R. García-Patrón, N. J. Cerf, T. C. Ralph, J. H. Shapiro, and S. Lloyd, Gaussian quantum information, Rev. Mod. Phys. **84**, 621 (2012).

[39] G. Giedke and J. Ignacio Cirac, Characterization of Gaussian operations and distillation of Gaussian states, Phys. Rev. A **66**, 032316 (2002).

[40] S. Tserkis and T. C. Ralph, Quantifying entanglement in two-mode Gaussian states, Phys. Rev. A **96**, 062338 (2017).

[41] S. Lloyd and S. L. Braunstein, Quantum computation over continuous variables, Phys. Rev. Lett. **82**, 1784 (1999).

[42] S. D. Bartlett, B. C. Sanders, S. L. Braunstein, and K. Nemoto, Efficient classical simulation of continuous variable quantum information processes, Phys. Rev. Lett. **88**, 097904 (2002).

[43] Y.-S. Ra, A. Dufour, M. Walschaers, C. Jacquard, T. Michel, C. Fabre, and N. Treps, Non-Gaussian quantum states of a multimode light field, Nat. Phys. **16**, 144 (2020).

[44] R. M. Gomes, A. Salles, F. Toscano, P. H. Souto Ribeiro, and S. P. Walborn, Quantum entanglement beyond Gaussian criteria., Proc. Natl. Acad. Sci. USA **106**, 21517 (2009).

[45] U. Chabaud and M. Walschaers, Resources for bosonic quantum computational advantage, Phys. Rev. Lett. **130**, 090602 (2023).

[46] K. Takase, J. I. Yoshikawa, W. Asavanant, M. Endo, and A. Furusawa, Generation of optical Schrödinger cat states by generalized photon subtraction, Phys. Rev. A **103**, 013710 (2021).

[47] W. Asavanant, K. Nakashima, Y. Shiozawa, J. I. Yoshikawa, and A. Furusawa, Generation of highly pure Schrödinger cat states and real-time quadrature measurements via optical filtering, Opt. Express **25**, 32227 (2017).

[48] A. L. Grimsmo and S. Puri, Quantum error correction with the Gottesman-Kitaev-Preskill code, PRX Quantum **2**, 020101 (2021).

[49] Z. Bao, Z. Wang, Y. Wu, Y. Li, W. Cai, W. Wang, Y. Ma, T. Cai, X. Han, J. Wang, Y. Song, L. Sun, H. Zhang, and L. Duan, Experimental preparation of generalized cat states for itinerant microwave photons, Phys. Rev. A **105**, 063717 (2022).

[50] Z. Wang, Z. Bao, Y. Wu, Y. Li, W. Cai, W. Wang, Y. Ma, T. Cai, X. Han, J. Wang, Y. Song, L. Sun, H. Zhang, and L. Duan, A flying Schrödinger cat in multipartite entangled states, Sci. Adv. **8**, eabn1778 (2022).

[51] J. Hastrup and U. L. Andersen, Protocol for generating optical Gottesman-Kitaev-Preskill states with cavity QED, Phys. Rev. Lett. **128**, 170503 (2022).

[52] I. Tzitrin, J. E. Bourassa, N. C. Menicucci, and K. K. Sabapathy, Progress towards practical qubit computation using approximate Gottesman-Kitaev-Preskill codes, Phys. Rev. A **101**, 032315 (2020).

[53] M. V. Larsen, C. Chamberland, K. Noh, J. S. Neergaard-Nielsen, and U. L. Andersen, Fault-tolerant continuous-variable measurement-based quantum computation architecture, PRX Quantum **2**, 030325 (2021).

[54] S. Haroche and J.-M. Raimond, *Exploring the Quantum: Atoms, Cavities, and Photons* (Oxford University Press, Oxford, England, 2006).

[55] A. Gaidash, A. Kozubov, and G. Miroshnichenko, Countermeasures for advanced unambiguous state discrimination attack on quantum key distribution protocol based on weak coherent states, Phys. Scr. **94**, 125102 (2019).

[56] M. Tatsuta, Y. Matsuzaki, and A. Shimizu, Quantum metrology with generalized cat states, Phys. Rev. A **100**, 032318 (2019).

[57] J. Hastrup and U. L. Andersen, All-optical cat-code quantum error correction, Phys. Rev. Res. **4**, 043065 (2022).

[58] M. Mirrahimi, Cat-qubits for quantum computation, C. R. Phys. **17**, 778 (2016).

[59] A. M. Steane, Error correcting codes in quantum theory, Phys. Rev. Lett. **77**, 793 (1996).

[60] D. S. Schlegel, F. Minganti, and V. Savona, Quantum error correction using squeezed Schrödinger cat states, Phys. Rev. A **106**, 022431 (2022).

[61] X. L. He, Y. Lu, D. Q. Bao, H. Xue, W. B. Jiang, Z. Wang, A. F. Roudsari, P. Delsing, J. S. Tsai, and Z. R. Lin, Fast generation of Schrödinger cat states using a Kerr-tunable superconducting resonator, Nat. Commun. **14**, 6358 (2023).

[62] A. Serafini, Quantum mechanics: Instructions for use, in *Quantum Continuous Variables* (CRC Press, Boca Raton, 2017), pp. 15–30.

[63] Š. Bräuer and P. Marek, Generation of quantum states with nonlinear squeezing by Kerr nonlinearity, Opt. Express **29**, 22648 (2021).
[64] K. Marshall, R. Pooser, G. Siopsis, and C. Weedbrook, Repeat-until-success cubic phase gate for universal continuous-variable quantum computation, Phys. Rev. A **91**, 032321 (2015).
[65] E. R. Zinatullin, S. B. Korolev, and T. Y. Golubeva, Teleportation protocols with non-Gaussian operations: Conditional photon subtraction versus cubic phase gate, Phys. Rev. A **107**, 022422 (2023).
[66] M. G. Genoni, F. A. Beduini, A. Allevi, M. Bondani, S. Olivares, and M. G. A. Paris, Non-Gaussian states by conditional measurements, Phys. Scr. **2010**, 014007 (2010).
[67] A. O. C. Davis, M. Walschaers, V. Parigi, and N. Treps, Conditional preparation of non-Gaussian quantum optical states by mesoscopic measurement, New J. Phys. **23**, 063039 (2021).
[68] C. S. Hamilton, R. Kruse, L. Sansoni, S. Barkhofen, C. Silberhorn, and I. Jex, Gaussian boson sampling, Phys. Rev. Lett. **119**, 170501 (2017).
[69] L. Valiant, The complexity of computing the permanent, Theor. Comput. Sci. **8**, 189 (1979).
[70] W. R. Clements, P. C. Humphreys, B. J. Metcalf, W. S. Kolthammer, and I. A. Walmsley, Optimal design for universal multiport interferometers, Optica **3**, 1460 (2016).
[71] K. Takase, K. Fukui, A. Kawasaki, W. Asavanant, M. Endo, J. I. Yoshikawa, P. van Loock, and A. Furusawa, Gottesman-Kitaev-Preskill qubit synthesizer for propagating light, npj Quantum Inf. **9**, 98 (2023).
[72] M. Reck, A. Zeilinger, H. J. Bernstein, and P. Bertani, Experimental realization of any discrete unitary operator, Phys. Rev. Lett. **73**, 58 (1994).
[73] U. Chabaud, D. Markham, and F. Grosshans, Stellar representation of non-Gaussian quantum states, Phys. Rev. Lett. **124**, 063605 (2020).
[74] J. Fiurášek, R. García-Patrón, and N. J. Cerf, Conditional generation of arbitrary single-mode quantum states of light by repeated photon subtractions, Phys. Rev. A **72**, 033822 (2005).
[75] M. Dakna, L. Knöll, and D.-G. Welsch, Quantum state engineering using conditional measurement on a beam splitter, Eur. Phys. J. D **3**, 295 (1998).
[76] J. C. F. Matthews, A. Politi, D. Bonneau, and J. L. O'Brien, Heralding two-photon and four-photon path entanglement on a chip, Phys. Rev. Lett. **107**, 163602 (2011).
[77] K. R. Motes, J. P. Olson, E. J. Rabeaux, J. P. Dowling, S. J. Olson, and P. P. Rohde, Linear optical quantum metrology with single photons: Exploiting spontaneously generated entanglement to beat the shot-noise limit, Phys. Rev. Lett. **114**, 170802 (2015).
[78] M. S. Winnel, J. J. Guanzon, D. Singh, and T. C. Ralph, Deterministic preparation of optical squeezed cat and Gottesman-Kitaev-Preskill states, arXiv:2311.10510.
[79] M. F. Melalkia, J. Huynh, S. Tanzilli, V. D'Auria, and J. Etesse, A multiplexed synthesizer for non-Gaussian photonic quantum state generation, Quantum Sci. Technol. **8**, 025007 (2023).
[80] M. Dakna, J. Clausen, L. Knöll, and D.-G. Welsch, Generation of arbitrary quantum states of traveling fields, Phys. Rev. A **59**, 1658 (1999).
[81] S.-Y. Lee and H. Nha, Quantum state engineering by a coherent superposition of photon subtraction and addition, Phys. Rev. A **82**, 053812 (2010).
[82] Ş. K. Özdemir, A. Miranowicz, M. Koashi, and N. Imoto, Quantum-scissors device for optical state truncation: A proposal for practical realization, Phys. Rev. A **64**, 063818 (2001).
[83] M. Koniorczyk, Z. Kurucz, A. Gábris, and J. Janszky, General optical state truncation and its teleportation, Phys. Rev. A **62**, 013802 (2000).
[84] C. J. Villas-Boas, Y. Guimarães, M. H. Y. Moussa, and B. Baseia, Recurrence formula for generalized optical state truncation by projection synthesis, Phys. Rev. A **63**, 055801 (2001).
[85] A. Miranowicz, Optical-state truncation and teleportation of qudits by conditional eight-port interferometry, J. Opt. B: Quantum Semiclassical Opt. **7**, 142 (2005).
[86] E. P. Mattos and A. Vidiella-Barranco, Enhancing nonclassical properties of quantum states of light using linear optics, Opt. Lett. **48**, 3645 (2023).
[87] K. J. Resch, J. S. Lundeen, and A. M. Steinberg, Quantum state preparation and conditional coherence, Phys. Rev. Lett. **88**, 113601 (2002).
[88] E. Bimbard, N. Jain, A. MacRae, and A. I. Lvovsky, Quantum-optical state engineering up to the two-photon level, Nat. Photonics **4**, 243 (2010).
[89] B. Lounis and M. Orrit, Single-photon sources, Rep. Prog. Phys. **68**, 1129 (2005).
[90] R. Uppu, F. T. Pedersen, Y. Wang, C. T. Olesen, C. Papon, X. Zhou, L. Midolo, S. Scholz, A. D. Wieck, A. Ludwig, and P. Lodahl, Scalable integrated single-photon source, Sci. Adv. **6**, eabc8268 (2020).
[91] N. Maring, A. Fyrillas, M. Pont, E. Ivanov, P. Stepanov, N. Margaria, W. Hease, A. Pishchagin, T. H. Au, S. Boissier, E. Bertasi, A. Baert, M. Valdivia, M. Billard, O. Acar, A. Brieussel, R. Mezher, S. C. Wein, A. Salavrakos, P. Sinnott *et al.*, A general-purpose single-photon-based quantum computing platform, arXiv:2306.00874.
[92] H. Larocque, M. A. Buyukkaya, C. Errando-Herranz, S. Harper, J. Carolan, C.-M. Lee, C. J. K. Richardson, G. L. Leake, D. J. Coleman, M. L. Fanto, E. Waks, and D. Englund, Tunable quantum emitters on large-scale foundry silicon photonics, arXiv:2306.06460.
[93] S. Olivares, M. Popovic, and M. G. A. Paris, Phase estimation with squeezed single photons, Quantum Meas. Quantum Metrol. **3**, 38 (2016).
[94] A. M. Brańczyk and T. C. Ralph, Teleportation using squeezed single photons, Phys. Rev. A **78**, 052304 (2008).
[95] Y. Miwa, J. I. Yoshikawa, N. Iwata, M. Endo, P. Marek, R. Filip, P. van Loock, and A. Furusawa, Exploring a new regime for processing optical qubits: Squeezing and unsqueezing single photons, Phys. Rev. Lett. **113**, 013601 (2014).
[96] M. Engelkemeier, L. Lorz, S. De, B. Brecht, I. Dhand, M. B. Plenio, C. Silberhorn, and J. Sperling, Quantum photonics with active feedback loops, Phys. Rev. A **102**, 023712 (2020).
[97] M. Engelkemeier, J. Sperling, J. Tiedau, S. Barkhofen, I. Dhand, M. B. Plenio, B. Brecht, and C. Silberhorn, Climbing the Fock ladder: Advancing multiphoton state generation, arXiv:2105.03720.

[98] A. Zavatta, S. Viciani, and M. Bellini, Single-photon excitation of a coherent state: Catching the elementary step of stimulated light emission, Phys. Rev. A **72**, 023820 (2005).

[99] V. Parigi, A. Zavatta, M. Kim, and M. Bellini, Probing quantum commutation rules by addition and subtraction of single photons to/from a light field, Science **317**, 1890 (2007).

[100] S. Olivares and M. G. A. Paris, Squeezed Fock state by inconclusive photon subtraction, J. Opt. B: Quantum Semiclassical Opt. **7**, S616 (2005).

[101] Xanadu Quantum Technologies. MrMustard (2022), https://github.com/XanaduAI/MrMustard.

[102] J. Li, R. Pereira, and S. Plosker, Some geometric interpretations of quantum fidelity, Lin. Alg. Appl. **487**, 158 (2015).

[103] N. Killoran, J. Izaac, N. Quesada, V. Bergholm, M. Amy, and C. Weedbrook, Strawberry fields: A software platform for photonic quantum computing, Quantum **3**, 129 (2019).

[104] T. R. Bromley, J. M. Arrazola, S. Jahangiri, J. Izaac, N. Quesada, A. D. Gran, M. Schuld, J. Swinarton, Z. Zabaneh, and N. Killoran, Applications of near-term photonic quantum computers: Software and algorithms, Quantum Sci. Technol. **5**, 034010 (2020).

[105] G. S. Agarwal, *Quantum Optics* (Cambridge University Press, Cambridge, UK, 2012).

Chapter 3

Adaptive Non-Gaussian Quantum State Engineering

3.1 Introduction

Looking again at the production of non-Gaussian states obtainable with GBS sources, we observe that higher-energy states can only be obtained with GBS setups that include many modes. However, although increasing the number of modes in the source guarantees better fidelity, this increase also leads to a lower success probability, since the number of PNRDs that must return a specific value to declare the source successful grows with the size of the source (here we can consider sources of single-mode states). In fact, the source described in Sec. 1.12.1 is constructed in such a way that if even one of the measurements does not return the expected value, the production is declared failed. However, we also observe that, a priori, a source optimized for a given measurement combination is not so different from a source that produces the same state with a measurement combination that is a permutation of the original one. The labels for the measurements are, after all, chosen conventionally, and

for every source that produces a state obtained by postselecting on $[n_1, ..., n_N]$, it is possible to find sibling sources, each producing the same state with the same success probability as the first source, but with a different permutation of the original measurement combination—provided that the source parameters, such as the transmittance and phase angles of the passive interferometer and the input states, are adjusted accordingly. However, once the measurement on one mode has been performed, it is no longer possible to retroactively modify the source to still ensure a successful outcome. Instead, an alternative approach is to define another type of source composed of multiple layers of passive interferometers acting on a subset of the modes. The measurement of a subset of modes can then be used to modify the following layers in order to increase the number of possible result outcomes that lead to declaring the source successful. Such a general definition of adaptive sources gives rise to multiple possible architectures.First of all, the number of layers can be made as large as the number of modes. In our work, we considered only sources with two layers. Each layer consists of input squeezed vacuum states and a passive interferometer. All modes except one are measured, and the resulting state is used as the input for the second interferometer, whose parameters are chosen adaptively depending on the measurement results. Also, the squeezing intensities of the other states input to the second layer are determined based on the results of the previous measurements. Finally, the desired state is generated by postselecting on the modes that have not yet been measured. Alternatively, we also consider the case involving active instead of passive interferometers. An adaptive interferometer is one that implements the most general symplectic transformation in quadrature space. By the Bloch-Messiah decomposition, all active interferometers can be implemented through a sequence of a passive interferometer, followed by inline squeezing operations, and then another

passive interferometer. Simulation of these sources shows that indeed the success probability of the sources can benefit from the introduction of adaptivity. We also considered the effect of loss, and although fidelity is strongly affected by it, the adaptive source still manages to yield better results, especially when the source parameters are optimized for the presence of known a priori loss intensity. Due to computational constraints, we simulate circuits with up to only three modes, but we anticipate that, given the nature of the scheme, improving source probability by considering alternative measurement patterns, adaptive schemes would perform even better with more modes.

PHYSICAL REVIEW A **112**, 053705 (2025)

Adaptive non-Gaussian quantum state engineering

Valerio Crescimanna [1,2,*] Shang Yu [1,3] Khabat Heshami [2,4,5] and Raj B. Patel [1,3,†]

[1]*Blackett Laboratory, Department of Physics, Imperial College London, Prince Consort Rd, London, SW7 2AZ, United Kingdom*

[2]*Department of Physics, University of Ottawa, 25 Templeton Street, Ottawa, Ontario, Canada K1N 6N5*

[3]*Centre for Quantum Engineering, Science and Technology (QuEST), Imperial College London, Prince Consort Rd, London, SW7 2AZ, United Kingdom*

[4]*National Research Council of Canada, 100 Sussex Drive, Ottawa, Ontario, Canada K1N 5A2*

[5]*Institute for Quantum Science and Technology, Department of Physics and Astronomy, University of Calgary, Alberta T2N 1N4, Canada*

(Received 19 February 2025; accepted 22 September 2025; published 6 November 2025)

Non-Gaussian quantum states of bosons are a key resource in quantum information science with applications ranging from quantum metrology to fault-tolerant quantum computation. Generation of photonic non-Gaussian resource states, such as Schrödinger's cat and Gottesman-Kitaev-Preskill states, is challenging. In this work, we go beyond existing passive architectures and explore a broad set of adaptive schemes. Our numerical results demonstrate a consistent improvement in the probability of success and fidelity of generating these non-Gaussian quantum states with equivalent resources. We also explore the effect of loss as the primary limiting factor and observe that adaptive schemes lead to more desirable outcomes in terms of overall probability of success and loss tolerance. Our work offers a versatile framework for non-Gaussian resource state generation with the potential to guide future experimental implementations.

DOI: 10.1103/jhkz-84dz

I. INTRODUCTION

In quantum information science, the ability to engineer and manipulate quantum states is paramount for developing advanced quantum technologies. Non-Gaussian quantum state engineering, in particular, stands out as an essential task for many technologies, providing capabilities that extend beyond the limitations of Gaussian operations [1,2]. Gaussian states and operations, characterized by their ease of implementation and mathematical simplicity, form the backbone of many quantum information protocols [3–6]. However, the intrinsic properties of Gaussian states are insufficient for achieving universal quantum computation and certain types of quantum error correction [7–10].

Non-Gaussian quantum states, which deviate from the Gaussian distribution in their Wigner function representation, offer unique and powerful resources necessary for the realization of more sophisticated quantum information tasks. These states enable the implementation of quantum gates and operations that are essential for universal quantum computation, facilitating complex quantum algorithms that cannot be accomplished with Gaussian states alone [11,12]. In quantum communication, non-Gaussian quantum states are strong candidates for overcoming the limitations imposed by repeaters relying solely on Gaussian operations [13,14]. Furthermore, non-Gaussian operations are pivotal in enhancing the robustness and efficacy of quantum error correction schemes, thereby improving the fidelity and scalability of quantum information systems [15].

The engineering of non-Gaussian states is also crucial for quantum metrology and sensing [16–20], where enhanced precision measurements are sought. By leveraging the distinct properties of non-Gaussian states, quantum sensors can achieve sensitivities that surpass those of Gaussian squeezed states.

Continuous-variable (CV) encoding of optical quantum information has been studied for many years. To achieve an advantage over classical computing, it is well known that some element of non-Gaussianity is required [21,22]. This may be introduced either in the resource states used in the protocol, in circuit operations, or at the measurement stage.

For quantum computing, discretizing and embedding quantum information in the infinite-dimensional space of an oscillator offers a route to implementing bosonic error-correcting codes (BECCs) [23–26] for fault-tolerant quantum computing using far fewer physical resources compared with discrete-variable encoding alone.

Nevertheless, fault-tolerant quantum computation can be achieved by encoding information into specific non-Gaussian quantum states capable of detecting and correcting shifts in the quadrature space due to noise in the system [27]. Efficient engineering of non-Gaussian states is therefore highly desirable to scale up fault-tolerant quantum computation (FTQC). However, while sources of non-Gaussian states can be deterministically produced with high fidelity in

*Contact author: [redacted]
†Contact author: [redacted]

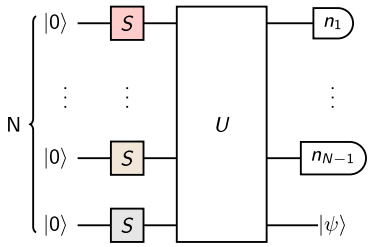

FIG. 1. GBS device with N squeezed displaced input vacuum states and $N-1$ photon-number-resolving detectors.

superconducting circuits, their generation presents greater challenges in photonic implementations where generation necessitates nonlinear gates or probabilistic preparation of the initial input states [28–34].

Here, we explore alternative conditional sources of optical non-Gaussian states. Specifically, we introduce an adaptive scheme comprising two or more layers of preparation, where the configuration of the subsequent circuit is set depending on the number of photons detected in the early stages. We compare their efficiency in terms of the quality of the generated state and the probability of success, for different input states and circuit configurations. Finally, we offer an outlook for potential experimental implementations.

II. APPROACHES TO NON-GAUSSIAN QUANTUM STATE ENGINEERING WITH GAUSSIAN BOSON SAMPLING DEVICES

A. Nonadaptive state engineering

In the continuous-variable domain, an n-mode quantum state ρ is Gaussian if its Wigner function $W(\rho)$ is Gaussian in shape, that is if it can be expressed as [29]

$$W(\boldsymbol{x}) = \frac{\exp\left[\frac{1}{2}(\boldsymbol{x}-\boldsymbol{\xi})^{\top}\boldsymbol{V}^{-1}(\boldsymbol{x}-\boldsymbol{\xi})\right]}{(2\pi)^{N}\sqrt{\det(\boldsymbol{V})}}, \tag{1}$$

where $\boldsymbol{V}$ is the covariance matrix and $\boldsymbol{\xi}$ is the displacement vector of the state. Any quantum state whose Wigner function cannot be expressed in terms of (1) is non-Gaussian. Similarly, quantum operators $\mathcal{O}$ are Gaussian if they transform one Gaussian state into another, and are non-Gaussian otherwise.

Considering photonic implementation, the operators that can be deterministically realized on the optical table—namely, single-mode squeezing, displacement, phase shifts, and two-mode beam splitting—are all Gaussian operations belonging to the Clifford group. Therefore, with these operations alone, it is impossible to transform the Gaussian vacuum state or any other Gaussian state into a single-mode non-Gaussian state.

A conditional scheme for non-Gaussian state generation with linear optics, in a Gaussian-boson-sampling–like (GBS-like) device, was originally proposed by Su *et al.* [35]. In this protocol, illustrated in Fig. 1, non-Gaussianity is introduced by projection measurements on non-Gaussian Fock states in the ancillary modes. Starting with an n-mode Gaussian state, measuring predefined combinations of photons in $n-1$ modes can herald the desired non-Gaussian state if the parameters of the source are set properly. However, in general, even the optimal squeezing intensities and angles of the passive interferometer do not guarantee measuring the expected pattern. Consequently, the probability of detecting the expected pattern, i.e., success probability, is also taken into account alongside the distance of the generated state from the target when optimizing parameters and measurement patterns.

Numerical optimizations of the parameters in GBS-like sources have been performed to realize Schrödinger cat states [35] and Gottesman–Kitaev–Preskill (GKP) states [36]. The results of these optimizations depend on the number of modes considered, the measurement patterns, and the optimization weight given to the quality of the output over the success probability. Overall, the results are promising but show significant room for improvement, especially in terms of probability, which is essential for enhancing computational efficiency.

Alternative schemes have indeed been proposed to improve the quality of the sources, for example, by incorporating additional non-Gaussian resources as input [37]. Moreover, one can envisage adapting the source so that a portion of the circuit can be reconfigured if some measurements do not yield the expected outcome.

B. Adaptive state engineering

The main limitation of a conditional source made with a GBS-like device lies in the probability of generating the state. Efficient state generation is crucial for most applications. Running the source several times would increase the operation time and, as a consequence, the probability of experiencing loss. On the other hand, multiplexing several sources requires a proportional use of costly resources. Moreover, large-scale computations rely heavily on non-Gaussian resources; therefore, even marginal improvements in the success rate of the source can yield substantial benefits for the overall computational process.

The success probability depends on the parameters of the sources, namely, the number of modes, the beam splitter ratios and phase shifting angles, and the squeezing intensities. Although the parameters can be tuned to increase the probability of success, this is done at the expense of the quality of the state that is generated in the heralded mode. Such an argument becomes particularly evident when considering the number of modes the source uses. Some states can be reached only with a minimum number of modes, but the combined probability of measuring a given number of photons in each mode decreases as a consequence [38].

Indeed, the system in II A does not yield the desired state unless all measurement outcomes are as expected. Still, the measurement pattern that enables the generation of the target state is, in general, not unique: a high-quality state can be generated using different circuits, each employing different combination of measurements, provided that each circuit is tuned according to its corresponding array of detections. For instance, adding a swap gate between two modes in the unitary passive interferometer forms a new interferometer that adapts to a permutation of the original measurement pattern.

However, once a measurement pattern is committed to, the source can only achieve success with that specific permutation. This restriction stems from the fact that the measurement layer represents the final step, preventing any retroactive

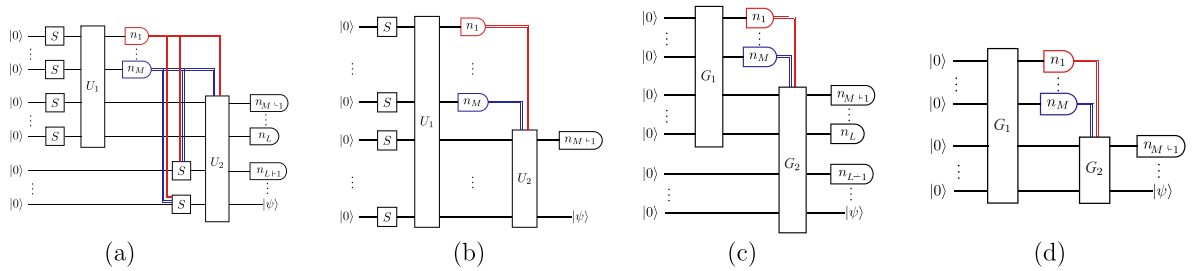

FIG. 2. (a) Adaptive non-Gaussian state generation with GBS-like devices. Here, S represents the squeezing operator, U represents the unitary linear interferometers, and n_i denotes the measurement outcome of the photon-number-resolving detector at the ith mode. Single lines represent quantum channels, while double lines represent classical channels. (b) Adaptive scheme where the interferometer U_2 is the sole element in the adaptive stage. (c) Adaptive scheme analogous to that shown in panel (a) with general Gaussian operations instead of passive unitary interferometers. (d) General adaptive scheme with Gaussian operations.

modifications to the interferometer or input states. This problem might be partially addressed by considering an alternative scheme, the adaptive GBS-like source. In this alternative source, depicted in Fig. 2, only some of the modes are manipulated in the first stage, and a subset of them gets measured. The measurement results obtained are then used to inform the second part of the circuit. The squeezing intensities of the remaining states, as well as the parameters of a second interferometer that acts on the unmeasured modes, are adjusted according to the outcomes of the first measurement.

A specific instance of this scheme is illustrated in Fig. 2, where all modes initially pass through a universal interferometer in the first layer, while the second interferometer is the only element that adapts based on the measurement outcomes from the first subset of modes.

The adaptive source can be generalized by allowing inline squeezing of states besides vacuum. In this case, we consider using generic Gaussian operations G, defined in terms of symplectic matrices, instead of the unitary interferometers as depicted in Fig. 2. According to the Bloch-Messiah decomposition [39], symplectic operations can be expressed as a series of two interferometers interspersed with a layer of inline squeezing single-mode operators. A schematic of the Bloch-Messiah decomposition is shown in Fig. 3.

In this scenario, the most general scheme consists of a series of symplectic operations acting on all available modes at each step, illustrated in Fig. 2.

A further generalization of the scheme can occur by considering a sequence of adaptable layers, with the information fed forward through each successive layer. In this regard, it is important to note that the number of modes and measured photons necessary to generate a state depends on the state itself and can be linked to its Stellar rank. Consequently, for states that are easier to generate, the initial layers of the adaptive scheme could be sufficient, and the additional layers may come into play only when the measurement pattern in the first layer is not desired, to increase the overall probability of success.

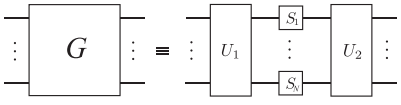

FIG. 3. Scheme of the Bloch-Messiah decomposition.

It is worth stressing that also in the adaptive case the optimization of the parameters used to find the ideal source is conventional. It can be biased toward either the success probability or the fidelity of the output state. Moreover, in the adaptive scheme, the optimization can be defined in such a way to favor the generation of the state already at the early stages or to maximize the overall probability by fixing the total number of steps. Finally, if we anticipate a high cost for the adaptivity of the circuit, the optimization could be built to favor the success for a given measurement.

The feed-forward scheme described so far can be enriched by introducing single Fock states into the input modes instead of vacuum states. Indeed, it has been shown in the nonadaptive scheme in Fig. 1 that introducing these non-Gaussian input states as an additional source of non-Gaussianity improves the efficiency of the GBS-like device in generating GKP and Schrödinger cat states. Here, we evaluate whether the Fock states actually enhances the efficiency of the adaptive source and compare its performance to a nonadaptive scheme with the same number of single Fock states as input. Schemes with different distributions of input Fock states are not considered here, but for them, we would anticipate that increasing the number of single-photon states would improve the overall efficiency of the source, similarly to what happens in nonadaptive sources [37]. In contrast, injecting an equivalent number of photons into a single mode would not be as effective, as suggested by the calculations on simulability via coherent-state decomposition [40]. Finally, we observe that adaptivity, consisting of the information from the measurement outcomes of some mode being fed forward to modify the rest of the circuit, has been shown to be beneficial for other quantum resource state sources that rely on homodyne detection and passive interferometers seeded with non-Gaussian states [41]. However, these architectures cannot be as easily generalized to produce arbitrary target states as GBS-like sources.

III. PHOTON LOSS IN ADAPTIVE STATE ENGINEERING

The discussion developed so far does not impose any specific constraints on the physical implementation on which

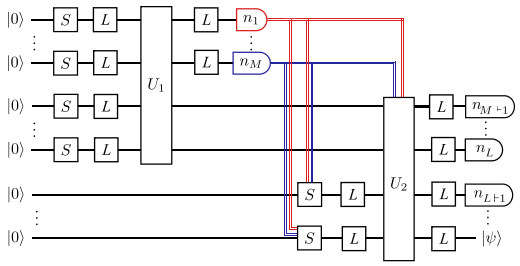

FIG. 4. Adaptive scheme with loss occurring before and after U_1 and U_2.

the source should be built, and experimentalists can choose their preferred one according to costs, availability, space, efficiency, and applications of the source itself. In any case, in the physical realization of the GBS-like device, certain physical limitations emerge that significantly impact the efficiency of the source. The primary issue encountered in photonic implementations in the real world is loss. For both the nonadaptive and adaptive sources introduced in Sec. II, loss affects the circuit mainly at the input and output.

A scheme including loss is illustrated in Fig. 4. Uniform losses are introduced in every mode twice: right after the squeezing operation acting on the vacuum state, before detection in the herald modes, and at the output of the unmeasured mode. The quality of the output state and, to a lesser extent the probability of detecting the expected measurement pattern, decrease depending on the intensity of the loss. The efficiency of the source's dependence on loss can thus serve as an additional figure of merit for comparing adaptive and nonadaptive schemes. Similarly, the performance of schemes using non-Gaussian input states can be evaluated.

If the loss is known *a priori*, the circuits can be optimized accordingly. Simulations on nonadaptive schemes have already been performed [36]. Similarly, we evaluate how loss affects the results of an adaptive scheme when the parameters are optimized for it, and assess whether the robustness of this scheme, which relies on feedforward information, is comparable to that of the nonadaptive approach.

IV. METHOD

To have a fair evaluation of the adaptive scheme introduced in Sec. II B, we compare its performance with that achievable using an analogous nonadaptive scheme as described in Sec. II A. In particular, we consider the amount of resources used in both schemes. We use the total number of modes in each source as the main criterion for a fair comparison. Whenever a squeezing bound is set in each mode, it is the same for both schemes. Similarly, the same number of single Fock states is used in each model, if any.

The sources are optimized using classical simulations of the circuit implemented with the Python library "Mr. Mustard" developed by Xanadu. Due to simulation constraints and for a clearer proof of principle, we consider small sources consisting of three and four modes, but we anticipate that the adaptive protocol would perform equally well or better as more modes can be modified based on the information fed forward.

The source parameters are optimized to maximize a reward function that is a linear combination of the probability of success P and fidelity with the target state $\mathcal{F}$. In particular, we set the reward function to $\mathcal{F}+P$, thus giving the same weight to both the figures of merit, as prioritizing one over the other may lead to sources that either have poor success rate or that generates low-quality states. To ensure a fair comparison between the protocols, the parameters of the adaptive source are optimized to match the fidelity achieved by the classical counterpart. The chosen target states are the Schrödinger cat states and the GKP grid states, both prominent examples of non-Gaussian quantum states with numerous applications such as communication, cryptography, and computation [36,42–46]. Specifically, we selected the amplitude and squeezing parameters of the cat states to be sufficiently challenging to produce using a two-mode circuit, representing the minimal nonadaptive approach, yet achievable with high fidelity using a three-mode source, which is the minimal configuration for a nontrivial adaptive scheme. Regarding GKP states, we approximated the ideal unphysical state $|\bar{0}_I\rangle$ with $|\bar{0}_\Delta\rangle$ such that

$$|\bar{0}_I\rangle \to |\bar{0}_\Delta\rangle \propto \sum_{n=-\infty}^{\infty} e^{\frac{1}{2}\Delta^2(2n\sqrt{\pi})^2}\hat{X}^2\,|\Delta\rangle_q\,, \tag{2}$$

where

$$\langle q\rangle\,\Delta = \left(\frac{1}{\pi\Delta^2}\right)^{\frac{1}{4}} e^{-\frac{q^2}{2\Delta^2}}. \tag{3}$$

Specifically, we target the truncated core state in

$$|0_{A4}\rangle = S(r)\underbrace{\sum_{n=0}^{4} c_n\,|n\rangle}_{\text{Core state}}, \tag{4}$$

where c_n are tuned to maximize $\langle 0_{A4}|0_{\Delta=10\text{dB}}|0_{A4}\rangle$ [36].

V. RESULTS

A. Adaptive state engineering with squeezed states and photon-number-resolving detector

1. Odd cat states

First, we compare two schemes made of three modes as shown in Fig. 5. We set the maximum threshold of the squeezing intensity of the input states to $r = 0.5$. The target state chosen for this comparison is a squeezed odd cat state with $\alpha = \sqrt{6}$, and $r = 0.5$, that, as desired, is a state that should present a sufficient challenge when produced with only two modes, yet it should still be attainable with satisfactory fidelity.

Initially, the optimization of the adaptive scheme is made such that it favors the generation of the state after the first measurement. Indeed, a two-mode circuit can be interpreted as a three mode circuit in which the third mode is not interfered. In this case, the fidelity between the generated and the target state is the same for both the adaptive and nonadaptive scheme when $n_{\text{tot}} = 3$ photons are measured: $\mathcal{F} \simeq 97.6\%$. The probability, on the other hand, is $P \simeq 0.43\%$ for the

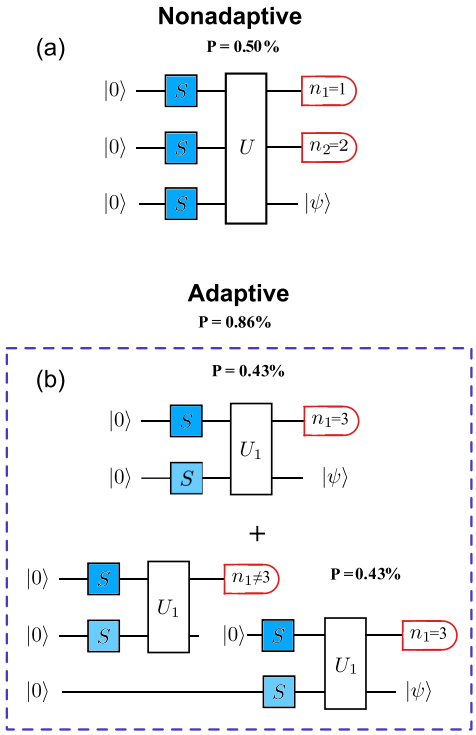

FIG. 5. Comparison between the (a) nonadaptive and (b) pseudo-adaptive schemes for generating the odd cat state. The squeezing is bounded by $r_{\max} = 0.5$. The darker shades in the squeezing boxes correspond to higher squeezing intensities, with the darkest blue representing $r = 0.5$. The pseudo-adaptive scheme is equivalent to running the nonadaptive scheme a second time. The target state is the odd cat state with $\alpha = \sqrt{6}$. The plus sign indicates that the probabilities corresponding to the two possible outcomes of the adaptive sources can be summed.

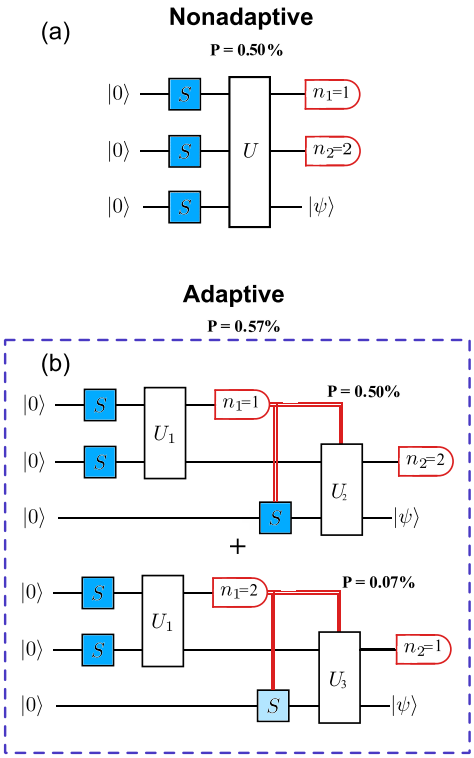

FIG. 6. Comparison between the (a) nonadaptive and (b) adaptive schemes for generating the odd cat state. The squeezing is bounded by $r_{\max} = 0.5$. The darker shades in the squeezing boxes correspond to higher squeezing intensities, with the darkest blue representing $r = 0.5$. The target state is the odd cat state with $\alpha = \sqrt{6}$. The plus sign indicates that the probabilities corresponding to the two possible outcomes of the adaptive sources can be summed.

two-mode circuit and $P \simeq 0.50\%$ for the three-mode circuit. Therefore, there is a relative gain in probability by adding a mode of approximately 16%. However, we observe that when the initial measurements n_1 of the adaptive circuit differ from the expected measurements, no combination of squeezing and interferometer U_2 can be found that produces a state close enough to the target. The scheme is effective only if we consider running it again, resulting in a doubling of the probability of producing the state, i.e., $P \simeq 0.86\% \geqslant 0.50\%$. This last result is indeed achievable with two beam splitters and two photon-number-resolving detectors (PNRDs), which are the same resources used in the nonadaptive scheme. Alternatively, one can view it as a scheme in which the state heralded by a measurement outcome different from the expected one is discarded, and a squeezed vacuum state is used instead to interfere with the state in the third mode at the second beam splitter. The schemes with their probabilities are shown in Fig. 5.

Then, we consider an alternative optimization of the adaptive scheme, which is shown with the nonadaptive counterpart in Fig. 6. In this second case, we neglect the circuit with only two modes and explore the squeezing and interferometers U_1 and U_2 that lead to the generation of states with good probability. We find that the states are generated with the same fidelity and a probability of 0.50% when one photon is measured in the first mode and two photons in the second mode. Interestingly, this probability is the same as that obtained with a general interferometer acting on three modes. However, using this second scheme allows for the adaptation of the second interferometer when the measurement on the first mode does not yield the expected outcome. Specifically, if we measure two photons in the first mode, and one in the second mode, a cat state can still be generated with the same fidelity and a probability of 0.07%. By summing the probabilities of the adaptive schemes, we conclude that it provides an advantage over the nonadaptive one.

We observe also that if the squeezing is not bounded then choosing squeezed cat states as alternative states does not help because the complexity depends only on the core of the stellar representation of the states, and not on the total squeezing that can be factorized out. The results for probability and fidelity obtained in this scenario are summarized in Table I. Similarly, the results achieved by unbinding the squeezing intensity and targeting the squeezed odd cat state of amplitude $\alpha = 2$ and $r = 0.5$ are given in Table II.

TABLE I. Results with and without 10% loss for the scheme shown in Fig. 6. The target is the odd cat state with amplitude $\alpha = \sqrt{6}$ squeezing $r = 0.5$. We limit the maximum squeezing intensity to $r_{\max} = 0.5$.

	MP	P	$P_{L=10\%}$	$\mathcal{F}$	$\mathcal{F}_{L=10\%}$
Nonadaptive	1,2	0.51%	0.44%	97.6%	66.1%
Adaptive	1,2	0.50%	0.42%	97.6%	41.7%
	2,1	0.07%	0.30%	97.6%	10.4%

2. GKP states

We consider now the core state $|0_4\rangle$ with $n_{\max} = 4$ but with a high $\Delta = 10$ dB, as described in Sec. IV. We consider three-mode circuits since the fidelity achievable with only two modes falls significantly short of 90%. The schemes with their probabilities are shown in Fig. 7.

In this scenario, by relaxing the constraint on maximum squeezing, we observe that we can achieve fidelities greater than 99% with a probability of approximately 2.2% using the nonadaptive scheme (by measuring two photons in each PNRD). With the adaptive scheme, the probability increases to over 3.7% [specifically, 1.8% for measurement pattern (3,1) and 1.9% for measurement pattern (2,2), while no parameters have been found to herald the state using other measurement patterns]. In this specific case, a state with fidelity larger than 90% is obtained with the same circuit optimized for the measurement pattern (3,1) even when we measure (1,3) which happens in 1.6% of the cases.

For even more energetic states or complex setups, we can consider schemes in which inline squeezing can be implemented in the heralded modes during intermediate steps of the scheme. Hence, the comparison involves active circuits in this context. When considering this approach, we find that the probability of generating $|0_4\rangle$ with the adaptive method is approximately 5.7%, as opposed to the previously reported 2.2% probability for the nonadaptive method. The results for Figs. 7(a) and 7(c) are reported in Table III.

3. Feed-forward concatenated with inline squeezing

As a final consideration, let us explore what happens when we extend this approach to more modes in a concatenated approach as shown in Fig. 8. First, if no photons are measured in the initial detectors, we can replicate the setup as it is. The results obtained for three-mode sources also hold for four-mode architectures, as smaller circuits can always be interpreted as special cases of larger circuits. We begin by considering the case in which no photons are measured in the initial detector. In this scenario, the conditional probability for the source to generate the state with these measurements is given by the product of the probability of measuring no photons in the first mode (31%) and the probability of producing the state with three modes (5.29%), which supplements the probability we calculated when measuring only three modes.

Similarly, looking at the other combinations when measuring up to four photons in three output modes we increase the probability of producing the state by an additional 2.77%. The overall probability for this setup is then $5.29\% + (31\% \times 5.29\%) + 2.77\% \simeq 9.7\%$.

TABLE II. Results with and without 10% loss for the scheme shown in Fig. 6. The target is the odd cat state with amplitude $\alpha = 2$ squeezing $r = 0.5$.

	MP	P	$P_{L=10\%}$	$\mathcal{F}$	$\mathcal{F}_{L=10\%}$
Nonadaptive	1,2	5.8%	5.54%	99.4%	69.0%
Adaptive	1,2	5.8%	5.50%	99.4%	69.1%
	2,1	0.54%	1.00%	99.4%	40.7%

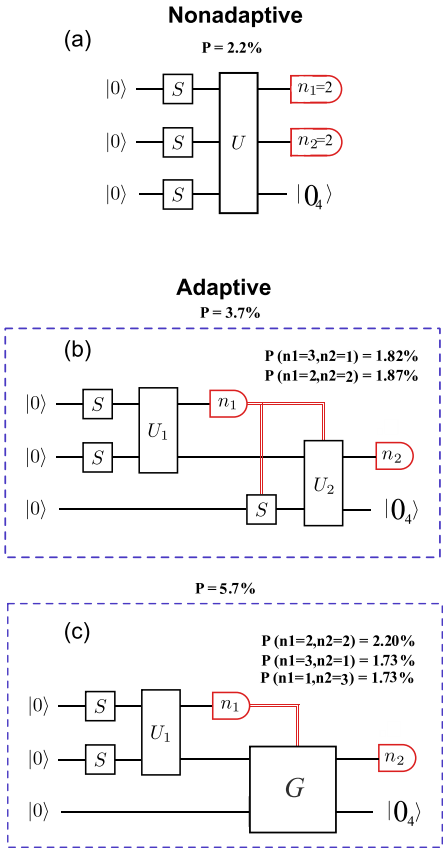

FIG. 7. Comparison between (a) nonadaptive and (b), (c) adaptive schemes for generating $|0_4\rangle$. Two adaptive schemes are shown in the figure: in panel (b) the scheme relies on squeezed vacuum states and passive interferometers only; in panel (c), the adaptive scheme contains a symplectic operation labeled by G, which here corresponds to a sequence of a beam splitter, two inline squeezers, and another beam splitter arranged as shown in Fig. 3.

B. Adaptive state engineering with squeezed and Fock states and photon-number-resolving detector

In this section, we evaluate whether the adaptive scheme proves advantageous even when a single-photon Fock state is used in one input mode of the circuit. The comparison between adaptive and nonadaptive schemes in this case is displayed in Fig. 9. To do so, we take the even cat state with

TABLE III. Results with and without a 5% and 10% loss for adaptive and nonadaptive schemes as shown on the schemes as shown in panels (a) and (c) of Fig. 7. The target state is the GKP state.

	MP	P	$P_{L=5\%}$	$P_{L=10\%}$	$\mathcal{F}$	$\mathcal{F}_{L=5\%}$	$\mathcal{F}_{L=10\%}$
Nonadaptive	2,2	2.2%	0.11%	0.055%	99.97%	85%	76%
Adaptive	2,2	2.2%	0.048%	0.031%	99.97%	86%	76%
	1,3	1.7%	0.120%	0.074%	>99.99%	82%	69%
	3,1	1.7%	0.019%	0.013%	>99.99%	83%	73%

$\alpha = \sqrt{8}$ as the target of the source. The fidelity achieved with only two modes and measuring three photons in the output is less than 93%.

Conversely, in a three-mode circuit with two two-mode interferometers U_1 and U_2 a fidelity of 95% can be reached with a probability of 2.4% for the measurement of one and two photons in the output ports and a probability of 1.3% for a circuit where the last squeezing and U_2 are optimized for the measurement of two and one photons.

The overall probability for this adaptive scheme turns out to be better than the probability achievable with a nonadaptive scheme with three modes, which is equal to 2.6%, once again proving the advantage of an adaptive scheme in certain scenarios while maintaining the same fidelity.

C. Loss and adaptivity

Here, we examine the impact of loss on the efficacy of the various protocols. Specifically, we evaluate how the adaptive schemes behave in the presence of loss compared with the schemes where no information is fed forward. In this context, the photon loss channel can be read a beam splitter with tunable transmission, where 100% transmission represents no loss and 0% corresponds to total loss. Unlike the setup used in Ref. [36], we introduce the loss channel only after the squeezing gates at each mode, and just before detection. Here, we consider all the loss channels to have the same transmissivity. In general, when considering different losses in the output, we observe that the loss introduced in the herald modes is mainly responsible for the drop in probability, while the loss in the undetected mode affects the fidelity of the generated state. If the loss is homogeneous among the modes, then the loss channels applied immediately after the squeezing operation in each mode can be replaced by loss channels with the same transmittivity applied after the passive interferometer. This allows us to shift all the loss introduced in our simulation to just before the measurement layer of the circuits. We also extend this approach to circuits relying on symplectic operations, for which the introduction of loss into all the input squeezed vacuum states cannot be done in the same way as in the case of passive interferometers alone, given that some vacuum states in the input modes interfere with other modes before being subjected to inline squeezing.

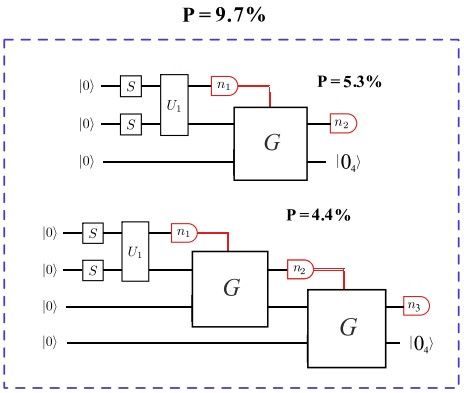

FIG. 8. Concatenated scheme to generate $|0_4\rangle$. The squares labeled by G represent symplectic operations in the input mode. Here, they correspond to a sequence of a beam splitter, two inline squeezers, and another beam splitter.

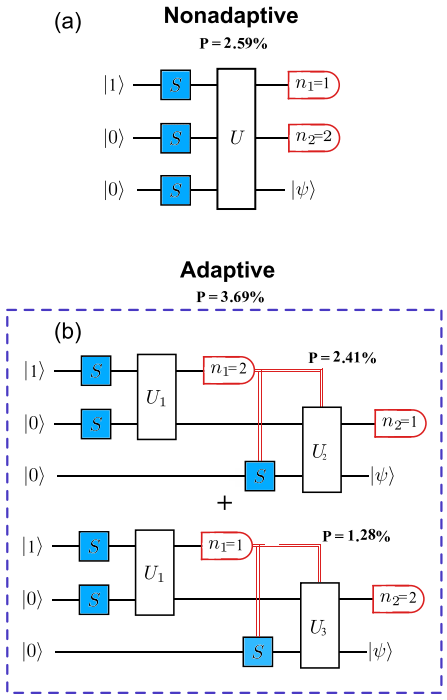

FIG. 9. Comparison between the (a) nonadaptive and (b) adaptive schemes for generating the odd cat state with one single-photon Fock state in input. The squeezing is bounded by $r_{\max} = 0.5$. The darker shades in the squeezing boxes correspond to higher squeezing intensities, with the darkest blue representing $r = 0.5$. The target state is the even cat state with $\alpha = \sqrt{8}$. The plus sign indicates that the probabilities corresponding to the two possible outcomes of the adaptive sources can be summed.

TABLE IV. Results with and without a 1% loss for adaptive and nonadaptive schemes as shown in panels (a) and (c) of Fig. 7. P' and $\mathcal{F}'$ refer to the probabilities and fidelities obtained with the circuits optimized for the presence of loss.

	MP	P	$P_{L=1\%}$	$P'_{L=1\%}$	$\mathcal{F}$	$\mathcal{F}_{L=1\%}$	$\mathcal{F}'_{L=1\%}$
Nonadaptive	2,2	2.2%	2.1%	1.9%	99.97%	91.87%	92.42%
Adaptive	2,2	2.2%	2.1%	1.8%	99.97%	91.86%	92.46%
	1,3	1.7%	1.7%	0.33%	>99.99%	88.51%	90.85%
	3,1	1.7%	1.7%	1.17%	>99.99%	89.41%	90.46%

To assess the robustness of the protocols, we initially consider an ideal scheme optimized for a specific target state, then we evaluate the probability of measuring the expected pattern and fidelity with the target under varying loss conditions.

First, we consider the effect of loss on the sources shown in Fig. 6 and in Fig. 7. In Table I, we report the results obtained with and without loss for the two schemes depicted in Fig. 6. The target is the odd cat state with amplitude $\alpha = \sqrt{6}$ and squeezing $r = 0.5$. We limit the maximum squeezing intensity to $r_{\max} = 0.5$.

Analogously, in Table II, we report the results obtained without any maximum threshold on the squeezing and targeting the odd cat state with amplitude $\alpha = 2$ squeezing $r = 0.5$.

Both the results in Table I and Table II show that there is no advantage in using the adaptive scheme, particularly because the fidelity achieved by the state heralded in a lossy circuit with a measurement pattern that is not used to optimize the first part of the circuit is significantly smaller than the other fidelities. A possible interpretation of this result may be connected to the fact that the optimization of the second part of the circuit is somehow deceived by a measurement that no longer corresponds to the expected heralded state.

Now, we want to evaluate how the two schemes compare when optimized with *a priori* knowledge of the loss in each mode. In this case, we consider a scheme with symplectic operations, as depicted in Fig. 7. In Table IV, we report the results obtained by optimizing the circuits with a loss channel defined at the end of each mode. The reported results correspond to circuits with loss levels of $L = 0\%$, $L = 5\%$, and $L = 10\%$. Our target is the GKP state $|0_4\rangle$ with a $\Delta = 10$ dB as introduced in Sec. V A 2.

As seen in Tables I–III we observe smaller fidelities for the states generated with measurement pattern different from (2,2) that is the measurement pattern used to optimize the first part of the circuit.

However, in the favorable case that even states with the smallest probability can be used in FTQC applications, the overall probability achievable with the adaptive scheme is greater than that of the nonadaptive scheme.

Finally, in Table IV, we compare the results in the presence of 1% when the circuit is optimized with and without the knowledge of the loss.

VI. PRACTICAL CONSIDERATIONS

The adaptive schemes we have outlined here necessitate photonic hardware with several key characteristics. Among these are high-gain squeezing, low-loss and phase-stable circuitry, optical delay lines, PNRDs and homodyne-detection.

In free-space implementations, high-gain squeezed light generation can be achieved with second-order nonlinearities in waveguide optical parametric amplifiers (OPAs) defined in periodically poled lithium niobate (ppLN) or potassium titanyl phosphate (ppKTP). Up to ≈20 dB of squeezing is attainable provided the losses between the squeezer and the circuit are mitigated. Recently, ≈8 dB of squeezing was measured from PPLN [47]. Further improvements in the fabrication of these devices, and improvements in collection efficiency, should push these values toward the threshold required for GKP error correction [48]. Electro-optic modulators (EOM) have found utility in time-bin encoded programmable interferometers [49], including those used for implementing GBS [50,51]. Optical fiber delay lines can store the quantum states of light in a subset of modes while the remaining modes are measured and their outcomes fed forward to additional stages of linear optical networks. In bulk optics, the length of the delay lines is predicated on the switching speeds of the tuneable elements found in the adapted unitary operations in later stages. For time-bin implementations, this switching speed is typically around 1 MHz, which requires optical fiber delays of ≈200 m.

Integrated photonics provides several attractive features, making it particularly well suited to adaptive non-Gaussian state generation. In thin-film lithium niobate (TFLN) integrated photonics, the OPA and circuit can be integrated together, thus minimizing the loss in-between. TFLN benefits from a strong electro-optic effect, enabling the integration of fast EOMs with up to 100 GHz bandwidth to facilitate fast reconfiguration of the adapted circuits. Such EOM performance should also facilitate multiplexing of multiple sources to improve further the probability of generating the state of choice. Long delay lines have recently been reported in time-bin entanglement experiments on TFLN [52]. Without integrated detectors on-chip, the out-coupling efficiency becomes a limiting factor in the end-to-end system efficiency. In TFLN, grating couplers with greater than 80% coupling efficiency have been demonstrated by incorporating metal mirrors [53] to reduce absorption in the substrate.

Finally, PNRDs are required to herald the desired non-Gaussian state. Superconducting transition-edge sensors (TESs), with operating temperatures of ≈100 mK, are currently the leading technology in this area. Detection efficiencies >95% can be achieved in the telecom C-band with photon-number resolution of up to 20 photons. TES typically suffer from long-reset times, limiting the rate at which states can be heralded to ≈100 kHz. However, ≈1 MHz rates have recently been reported [54] by improving the heat dissipation from the TES to the substrate, which together with advances in TES signal processing [55] could allow state generation rates approaching 5 MHz. For highly efficient detectors capable

of distinguishing small photon numbers, the fidelity of the generated states is not significantly affected by imperfections. This is because the expected number of detected photons is generally low, and at least two erroneous detections, one overestimating and one underestimating the result, must occur within the same iteration to herald a state different from the target.

VII. CONCLUSION

We introduced an alternative scheme for non-Gaussian quantum state generation based on the GBS-like source introduced in Ref. [35]. In our approach, rather than employing an input layer with squeezed vacuum states, a universal linear network layer, and a measurement layer, we considered a scheme consisting of several layers. Each layer has its own input states, unitary operations, and PNRDs, forming a concatenation of GBS-like non-Gaussian sources, where the output state of one layer is part of the input state for the next. The information on the number of photons detected is fed forward through the circuit, allowing the interferometer's parameters to be adapted accordingly. We used the number of modes as the key resource to ensure a fair comparison between our proposed scheme and the original. We optimized all parameters to maximize both the fidelity of the output state and the probability of success. Our results demonstrate an improvement in the quality of non-Gaussian state generation with the adaptive scheme, in terms of either success probability or fidelity. Even when a vacuum state is replaced by a single-photon state at the input, we observe a relative increase in probability of over 40%, attributable to the adaptive approach. Finally, simulations conducted on lossy circuits reveal that, although losses negatively impact both adaptive and nonadaptive schemes, the adaptive scheme remains preferable. More specifically, as seen in Table IV, the adaptive scheme is more resilient to doubling the loss compared with the nonadaptive approach. Our work provides a more versatile framework to optimize the generation of non-Gaussian resource states for applications in photonic quantum sensing and computation.

ACKNOWLEDGMENTS

R.B.P. would like to thank Miller Eaton for the fruitful discussions which motivated this work. R.B.P. acknowledges support from the UK Research & Innovation Future Leaders Fellowship program (project number: MR/W011794/1), the Engineering and Physical Sciences Research Council (EPSRC) UK Quantum Technologies Program's hubs for Quantum Computing & Simulation (project number: EP/T001062/1) and Quantum Computing via Integrated and Interconnected Implementations (project number: EP/Z53318X/1). S.Y. is supported by the UK Research and Innovation Guarantee Postdoctoral Fellowship (project number: EP/Y029631/1). V.C., K.H., and R.B.P. acknowledge support from Mitacs Globalink Research Award (IT37329). K.H. acknowledges support from NSERC's Discovery Grant and Alliance programs.

DATA AVAILABILITY

The data that support the findings of this article are not publicly available. The data are available from the authors upon reasonable request.

[1] A. Lvovsky, P. Grangier, A. Ourjoumtsev, V. Parigi, M. Sasaki, and R. Tualle-Brouri, Production and applications of non-Gaussian quantum states of light, arXiv:2006.16985.

[2] U. Chabaud and M. Walschaers, Resources for bosonic quantum computational advantage, Phys. Rev. Lett. **130**, 090602 (2023).

[3] X.-B. Wang, T. Hiroshima, A. Tomita, and M. Hayashi, Quantum information with Gaussian states, Phys. Rep. **448**, 1 (2007).

[4] S. Aaronson and A. Arkhipov, The computational complexity of linear optics, *Proceedings of the 43rd Annual ACM Symposium on Theory of Computing* (ACM, 2011), p. 333.

[5] C. Weedbrook, S. Pirandola, R. García-Patrón, N. J. Cerf, T. C. Ralph, J. H. Shapiro, and S. Lloyd, Gaussian quantum information, Rev. Mod. Phys. **84**, 621 (2012).

[6] R. C. Wagner and V. M. Kendon, The continuous-variable Deutsch–Jozsa algorithm using realistic quantum systems, J. Phys. A: Math. Theor. **45**, 244015 (2012).

[7] J. Niset, J. Fiurášek, and N. J. Cerf, No-go theorem for Gaussian quantum error correction, Phys. Rev. Lett. **102**, 120501 (2009).

[8] L. Magnin, F. Magniez, A. Leverrier, and N. J. Cerf, Strong no-go theorem for Gaussian quantum bit commitment, Phys. Rev. A **81**, 010302(R) (2010).

[9] L. Lami, B. Regula, X. Wang, R. Nichols, A. Winter, and G. Adesso, Gaussian quantum resource theories, Phys. Rev. A **98**, 022335 (2018).

[10] J. Dias and T. C. Ralph, Quantum error correction of continuous-variable states with realistic resources, Phys. Rev. A **97**, 032335 (2018).

[11] S. Ghose and B. C. Sanders, Non-Gaussian ancilla states for continuous variable quantum computation via Gaussian maps, J. Mod. Opt. **54**, 855 (2007).

[12] K. Miyata, H. Ogawa, P. Marek, R. Filip, H. Yonezawa, J.-i. Yoshikawa, and A. Furusawa, Implementation of a quantum cubic gate by an adaptive non-Gaussian measurement, Phys. Rev. A **93**, 022301 (2016).

[13] R. Namiki, O. Gittsovich, S. Guha, and N. Lütkenhaus, Gaussian-only regenerative stations cannot act as quantum repeaters, Phys. Rev. A **90**, 062316 (2014).

[14] F. Rozpędek, K. Noh, Q. Xu, S. Guha, and L. Jiang, Quantum repeaters based on concatenated bosonic and discrete-variable quantum codes, npj Quantum Inf. **7**, 102 (2021).

[15] B. M. Terhal, J. Conrad, and C. Vuillot, Towards scalable bosonic quantum error correction, Quantum Sci. Technol. **5**, 043001 (2020).

[16] W. H. Zurek, Sub-Planck structure in phase space and its relevance for quantum decoherence, Nature (London) **412**, 712 (2001).

[17] A. Gilchrist, K. Nemoto, W. J. Munro, T. C. Ralph, S. Glancy, S. L. Braunstein, and G. J. Milburn, Schrödinger cats and their

power for quantum information processing, J. Opt. B: Quantum Semiclassical Opt. **6**, S828 (2004).
[18] K. Duivenvoorden, B. M. Terhal, and D. Weigand, Single-mode displacement sensor, Phys. Rev. A **95**, 012305 (2017).
[19] Q. Zhuang, J. Preskill, and L. Jiang, Distributed quantum sensing enhanced by continuous-variable error correction, New J. Phys. **22**, 022001 (2020).
[20] C. H. Valahu, M. P. Stafford, Z. Huang, V. G. Matsos, M. J. Millican, T. Chalermpusitarak, N. C. Menicucci, J. Combes, B. Q. Baragiola, and T. R. Tan, Quantum-enhanced multi-parameter sensing in a single mode, Sci. Adv. **11**, eadw9757 (2025).
[21] S. D. Bartlett and B. C. Sanders, Universal continuous-variable quantum computation: Requirement of optical non-linearity for photon counting, Phys. Rev. A **65**, 042304 (2002).
[22] S. D. Bartlett and B. C. Sanders, Efficient classical simulation of optical quantum information circuits, Phys. Rev. Lett. **89**, 207903 (2002).
[23] A. L. Grimsmo, J. Combes, and B. Q. Baragiola, Quantum computing with rotation-symmetric bosonic codes, Phys. Rev. X **10**, 011058 (2020).
[24] W. Cai, Y. Ma, W. Wang, C.-L. Zou, and L. Sun, Bosonic quantum error correction codes in superconducting quantum circuits, Fundam. Res. **1**, 50 (2021).
[25] A. Joshi, K. Noh, and Y. Y. Gao, Quantum information processing with bosonic qubits in circuit QED, Quantum Sci. Technol. **6**, 033001 (2021).
[26] A. J. Brady, A. Eickbusch, S. Singh, J. Wu, and Q. Zhuang, Advances in bosonic quantum error correction with Gottesman–Kitaev–Preskill codes: Theory, engineering and applications, Prog. Quantum Electron. **93**, 100496 (2024).
[27] D. Gottesman, A. Kitaev, and J. Preskill, Encoding a qubit in an oscillator, Phys. Rev. A **64**, 012310 (2001).
[28] M. Yanagisawa, Non-Gaussian state generation from linear elements via feedback, Phys. Rev. Lett. **103**, 203601 (2009).
[29] M. Walschaers, Non-Gaussian quantum states and where to find them, PRX Quantum **2**, 030204 (2021).
[30] M. Endo, R. He, T. Sonoyama, K. Takahashi, T. Kashiwazaki, T. Umeki, S. Takasu, K. Hattori, D. Fukuda, K. Fukui, K. Takase, W. Asavanant, P. Marek, R. Filip, and A. Furusawa, Non-Gaussian quantum state generation by multi-photon subtraction at the telecommunication wavelength, Opt. Express **31**, 12865 (2023).
[31] T. Sonoyama, K. Takahashi, B. Charoensombutamon, S. Takasu, K. Hattori, D. Fukuda, K. Fukui, K. Takase, W. Asavanant, J.-i. Yoshikawa, M. Endo, and A. Furusawa, Non-Gaussian-state generation with time-gated photon detection, Phys. Rev. Res. **5**, 033156 (2023).
[32] Y. Cai, T. Zhao, S. Zhu, Y. Xu, C. Liu, and L. Hu, Preparation of non-Gaussian states based on three-photon quantum scissors, Results Phys. **55**, 107171 (2023).
[33] R. Nagai and T. Tomono, Optimization of non-Gaussian state generation using tensor networks and automatic differentiation, in *2022 IEEE International Conference on Quantum Computing and Engineering (QCE)* (IEEE, Broomfield, CO, 2022), p. 818.
[34] M. S. Winnel, J. J. Guanzon, D. Singh, and T. C. Ralph, Deterministic preparation of optical squeezed cat and Gottesman-Kitaev-Preskill states, Phys. Rev. Lett. **132**, 230602 (2024).
[35] D. Su, C. R. Myers, and K. K. Sabapathy, Conversion of Gaussian states to non-Gaussian states using photon-number-resolving detectors, Phys. Rev. A **100**, 052301 (2019).
[36] I. Tzitrin, J. E. Bourassa, N. C. Menicucci, and K. K. Sabapathy, Progress towards practical qubit computation using approximate Gottesman-Kitaev-Preskill codes, Phys. Rev. A **101**, 032315 (2020).
[37] V. Crescimanna, A. Z. Goldberg, and K. Heshami, Seeding Gaussian boson samplers with single photons for enhanced state generation, Phys. Rev. A **109**, 023717 (2024).
[38] K. K. Sabapathy, H. Qi, J. Izaac, and C. Weedbrook, Production of photonic universal quantum gates enhanced by machine learning, Phys. Rev. A **100**, 012326 (2019).
[39] S. L. Braunstein, Squeezing as an irreducible resource, Phys. Rev. A **71**, 055801 (2005).
[40] J. Marshall and N. Anand, Simulation of quantum optics by coherent state decomposition, Opt. Quantum **1**, 78 (2023).
[41] K. Takase, F. Hanamura, H. Nagayoshi, J. E. Bourassa, R. N. Alexander, A. Kawasaki, W. Asavanant, M. Endo, and A. Furusawa, Generation of flying logical qubits using generalized photon subtraction with adaptive Gaussian operations, Phys. Rev. A **110**, 012436 (2024).
[42] H. Jeong and M. S. Kim, Efficient quantum computation using coherent states, Phys. Rev. A **65**, 042305 (2002).
[43] T. C. Ralph, A. Gilchrist, G. J. Milburn, W. J. Munro, and S. Glancy, Quantum computation with optical coherent states, Phys. Rev. A **68**, 042319 (2003).
[44] Z. Leghtas, G. Kirchmair, B. Vlastakis, R. J. Schoelkopf, M. H. Devoret, and M. Mirrahimi, Hardware-efficient autonomous quantum memory protection, Phys. Rev. Lett. **111**, 120501 (2013).
[45] Q. Xu, G. Zheng, Y.-X. Wang, P. Zoller, A. A. Clerk, and L. Jiang, Autonomous quantum error correction and fault-tolerant quantum computation with squeezed cat qubits, npj Quantum Inf. **9**, 78 (2023).
[46] K. Fukui, R. N. Alexander, and P. van Loock, All-optical long-distance quantum communication with Gottesman-Kitaev-Preskill qubits, Phys. Rev. Res. **3**, 033118 (2021).
[47] T. Kashiwazaki, T. Yamashima, K. Enbutsu, T. Kazama, A. Inoue, K. Fukui, M. Endo, T. Umeki, and A. Furusawa, Over-8-dB squeezed light generation by a broadband waveguide optical parametric amplifier toward fault-tolerant ultrafast quantum computers, Appl. Phys. Lett. **122**, 234003 (2023).
[48] I. Tzitrin, T. Matsuura, R. N. Alexander, G. Dauphinais, J. E. Bourassa, K. K. Sabapathy, N. C. Menicucci, and I. Dhand, Fault-tolerant quantum computation with static linear optics, PRX Quantum **2**, 040353 (2021).
[49] S. Yu, W. Liu, S.-J. Tao, Z.-P. Li, Y.-T. Wang, Z.-P. Zhong, R. B. Patel, Y. Meng, Y.-Z. Yang, Z.-A. Wang *et al.*, A von-Neumann-like photonic processor and its application in studying quantum signature of chaos, Light: Sci. Appl. **13**, 74 (2024).
[50] S. Yu, Z.-P. Zhong, Y. Fang, R. B. Patel, Q.-P. Li *et al.*, A universal programmable Gaussian boson sampler for drug discovery, Nat. Comput. Sci. **3**, 839 (2023).
[51] L. S. Madsen, F. Laudenbach, M. Falamarzi. Askarani, F. Rortais, T. Vincent *et al.*, Quantum computational advantage with a programmable photonic processor, Nature (London) **606**, 75 (2022).

[52] G. Finco, F. Miserocchi, A. Maeder, J. Kellner, A. Sabatti, R. J. Chapman, and R. Grange, Time-bin entangled Bell state generation and tomography on thin-film lithium niobate, npj Quantum Inf. **10**, 135 (2024).

[53] B. Chen, Z. Ruan, X. Fan, Z. Wang, J. Liu, C. Li, K. Chen, and L. Liu, Low-loss fiber grating coupler on thin film lithium niobate platform, APL Photonics **7**, 076103 (2022).

[54] R. Hummatov, A. E. Lita, T. Farrahi, N. Otrooshi, S. Fayer, M. J. Collins, M. Durkin, D. Bennett, J. Ullom, R. P. Mirin, and S. Woo Nam, Fast transition-edge sensors suitable for photonic quantum computing, J. Appl. Phys. **133**, 234502 (2023).

[55] Z. Li, M. J. H. Kendall, G. J. Machado, R. Zhu, E. Mer, H. Zhan, A. Zhang, S. Yu, I. A. Walmsley, and R. B. Patel, Boosting photon-number-resolved detection rates of transition-edge sensors by machine learning, Optica Quantum **3**, 246 (2025).

Chapter 4

Exact simulation of realistic GKP cluster states

4.1 Introduction

Gottesman-Kitaev-Preskill states are the most promising bosonic quantum states for achieving fault-tolerant quantum computation with quantum optics. Their grid structure in phase space, in fact, enables state error detection and correction against random displacements in phase space. GKP states can then be used to perform measurement-based quantum computation. However, ideal GKP states are not physically realizable. In fact, GKP states have infinite energy (i.e., infinite mean photon number) and are not normalizable, with a Wigner function that extends periodically over the entire complex space. Therefore, the states that are actually implemented correspond to approximations of the ideal states. A defining characteristic of GKP states is the presence of stabilizers, which are operators for which the state is an eigenstate with eigenvalue one. Since Pauli operations on GKP qubits are described by displacements in the phase space of these states, any physical state with finite support

will only be an eigenstate of the identity displacement. However, the stabilizer operator will have an eigenvalue closer to one the more the physical state approaches the ideal one. For this reason, the absolute value of the stabilizer expectation is frequently used as a figure of merit for the quality of the physical state. Up to now, whenever one wanted to analytically evaluate the quality of an algorithm involving non-ideal GKP states generated through a specific protocol, it was common to use GKP-like states that mimic the behavior of the ideal states. Specifically, states were introduced that, by definition, yield the same stabilizer expectation values as the physically realizable state. The states defined for this purpose are called Gaussian Random Noise displaced states. GRN states correspond to a mixture of ideal GKP states displaced according to a two-dimensional Gaussian distribution. By definition, GRN states have the same stabilizer expectation value as the states they are meant to imitate. Even the two-mode stabilizer expectation values on the GKP states entangled via a 50:50 beam splitter is correctly determined by the GRN moded. However, these GRN states have limitations. First of all, they are ideal states that, by definition, cannot actually be implemented. Secondly, their ability to yield identical expectation values is limited to the states themselves and their entangled versions, but this breaks down as soon as any manipulation is applied, for example, when considering states obtained via postselection from homodyne detection of two entangled modes. This case is particularly interesting since cluster state computation can be performed in this way. One method used to generate GKP states involves entangling Schrödinger cat states via a beam splitter, performing homodyne measurement on one of the modes, and proceeding iteratively with additional beam splitters until a GKP state is obtained. The quality of this state, in terms of stabilizer expectation value, depends on the squeezing applied to the input squeezed cat states and the number of cycles, which

is limited by the maximum amplitude of the squeezed cat states. In the article, the performance of Gaussian Random Noise states in describing the behavior of non-ideal GKP states was evaluated by determining stabilizer expectation values. The results were compared with simulations, and it was concluded that the discrepancy between the expected values using GRN states and the actual values returned by the quantum states obtained through cat breeding increases the further the considered state is from the ideal GKP state (i.e., with unit expectation value). Considering that for any quantum state it is always possible to define a phase space representation as a possibly complex linear combination of Gaussian states, the expectation values of the states obtained via the breeding protocol on squeezed Schrödinger cat states were exactly determined analytically, for any amplitude and squeezing. Similarly, an exact formula is given for the expected stabilizer value of multimode entangled GKP states, and for the states heralded by homodyne measurement on arbitrary values of some modes within these cluster states. These expressions can therefore be used instead of GRN state expansions to obtain more accurate simulations of quantum algorithms using GKP cluster states.

PHYSICAL REVIEW A **112**, 052425 (2025)

Exact simulation of realistic Gottesman-Kitaev-Preskill cluster states

Milica Banić,[1,*] Valerio Crescimanna,[1,2] J. Eli Bourassa,[3] Carlos González-Arciniegas,[3] Rafael N. Alexander,[3] and Khabat Heshami[1,2,4]

[1]*National Research Council of Canada, 100 Sussex Drive, Ottawa, Ontario, Canada K1N 6N5*

[2]*Department of Physics, University of Ottawa, 25 Templeton Street, Ottawa, Ontario, Canada K1N 6N5*

[3]*Xanadu, 777 Bay Street, Toronto, Ontario, Canada M5G 2C8*

[4]*Institute for Quantum Science and Technology, Department of Physics and Astronomy, University of Calgary, Calgary, Alberta, Canada T2N 1N4*

(Received 14 April 2025; accepted 8 October 2025; published 13 November 2025)

We describe a method for simulating and characterizing realistic Gottesman-Kitaev-Preskill (GKP) cluster states, rooted in the representation of resource states in terms of sums of Gaussian distributions in phase space. We apply our method to study the generation of single-mode GKP states via cat state breeding, and the formation of multimode GKP cluster states via linear optical circuits and homodyne measurements. We characterize resource states by referring to expectation values of their stabilizers and witness operators constructed from them. Our method reproduces the results of standard Fock-basis simulations, while being more efficient and being applicable in a broader parameter space. We also comment on the validity of the heuristic Gaussian random noise model, through comparisons with our exact simulations: We find discrepancies in the stabilizer expectation values when homodyne measurement is involved in cluster state preparation, yet we find close agreement between the two approaches on average.

DOI: 10.1103/h6dj-cxsy

I. INTRODUCTION

Photonic implementations of quantum information processing (QIP) are motivated by the potential for room-temperature operation, scalability of hardware, low decoherence, and ability to physically transmit quantum information over long distances via optical fibers. A number of tasks in photonic QIP, including measurement-based quantum computation and all-optical quantum repeaters, require bosonic cluster states as resources [1–3]. One approach to constructing photonic cluster states is to encode information in the quadratures of the electromagnetic field. Particularly interesting is the case where the modes are Gottesman-Kitaev-Preskill (GKP) states [4–7], which are characterized by a periodic grid of peaks in phase space, with the logical information encoded in the positions of the peaks. This approach is further motivated by the relative ease with which GKP cluster states can be stitched together and processed, where Clifford gates, including entangling operations, can be implemented deterministically using Gaussian operations [8] and Pauli projections are implemented as homodyne measurements. Given the significance of these states and their applications, developing the ability to simulate and characterize such systems is essential and will have far-reaching implications for efforts towards implementing photonic QIP.

It is essential when studying such architectures to account for nonidealities in the resource states. These nonidealities are inevitable because ideal GKP states are not physical; in reality, one can only generate approximate GKP states having a finite extent in phase space, with the peaks having finite widths. Because this limits the distinguishability of the different logical states and the state's capacity for error correction [9–11], it is important to account for these features when devising and assessing the performance of continuous-variable (CV) quantum information protocols. However, accurately describing realistic GKP states can be challenging and numerically expensive; even dealing with energetic (high-quality) single-mode GKP states can be problematic, and the scaling becomes prohibitive when one treats cluster states of even a few modes. For this reason, the community typically relies on heuristic models such as the Gaussian random noise (GRN) model [12,13], in which a noisy channel is applied to ideal GKP states, resulting in a uniform broadening of the peaks to some finite width. Although this provides a more realistic picture, the GRN model does not capture all the features of approximate GKP states that can be generated in practice [14–19].

An accurate description of experimentally accessible GKP states is key to properly assessing and optimizing the performance of CV photonic architectures [20]. Progress in this direction will enable more realistic performance estimates for CV quantum protocols. It may also enable improvements in performance by allowing for more sophisticated encoding and decoding schemes and optimizing the architecture, with the aim of mitigating logical errors due to the nonidealness of realistic GKP states. More detailed simulations will also be useful in developing methods of characterizing realistic GKP states and assessing their usefulness. Motivated by these questions, we have developed an approach for exact simulations of

*Contact author: [redacted]

2469-9926/2025/112(5)/052425(25)

realistic GKP cluster state generation. We apply an approach in which CV states and operations are represented by sums of Gaussian distributions in phase space [21,22]. We extend earlier work, in which this method was used to characterize realistic single-mode GKP states to simulate GKP cluster state generation by entangling these single-mode inputs states through linear unitary circuits and homodyne measurement [23–25].

In Sec. II we review the details of this formalism, with a particular emphasis on the phase-space methods required to make these calculations tractable [21]. In Sec. III we turn our focus to the computation of stabilizer expectation values (EVs), as a useful figure of merit for realistic GKP cluster states. In Sec. IV we implement our expression for the stabilizer EV numerically. We address single-mode GKP states up to a linear three-photon cluster state. We compare our results to those obtained with Fock-basis simulations and with the GRN model. In Sec. V we summarize and discuss prospects for future work.

II. BACKGROUND

A. Phase-space formalism

The method presented in this paper makes use of the phase-space formalism for quantum optics [26]. We represent operators in terms of their Wigner functions; the Wigner function for an N-mode operator $\hat{\mathcal{O}}$ is given by

$$W_{\mathcal{O}}(\boldsymbol{r}) = \frac{1}{(2\pi)^{2N}} \int d^{2N}\boldsymbol{r}' e^{-i\boldsymbol{r}^T \boldsymbol{\Omega} \boldsymbol{r}'} \chi_{\mathcal{O}}(\boldsymbol{r}'), \tag{1}$$

$$\chi_{\mathcal{O}}(\boldsymbol{r}') = \mathrm{Tr}[\hat{D}(\boldsymbol{r}')\hat{\mathcal{O}}], \tag{2}$$

where

$$\boldsymbol{r} = (x_1, p_1, \ldots, x_N, p_N)^T \tag{3}$$

denotes a vector of $2N$ quadrature variables corresponding to the N modes, and likewise for $\boldsymbol{r}'$. By $\boldsymbol{\Omega}$ we denote the $2N \times 2N$ symplectic matrix

$$\boldsymbol{\Omega} = \bigoplus_{i=1}^{N} \begin{pmatrix} 0 & 1 \\ -1 & 0 \end{pmatrix}, \tag{4}$$

and

$$\hat{D}(\boldsymbol{r}') = e^{-i(\boldsymbol{r}')^T \boldsymbol{\Omega} \hat{\boldsymbol{r}}} \tag{5}$$

is the usual displacement operator, with $\hat{\boldsymbol{r}}$ the vector of $2N$ quadrature operators $(\hat{x}_1, \hat{p}_1, \ldots, \hat{x}_N, \hat{p}_N)^T$.

The Wigner function as defined in Eq. (1) is normalized such that

$$\int d^{2N}\boldsymbol{r}\, W_{\mathcal{O}}(\boldsymbol{r}) = \mathrm{Tr}(\hat{\mathcal{O}}), \tag{6}$$

resulting in the expected normalization condition when $\hat{\mathcal{O}}$ refers to the density operator of a normalized state. The expectation value of an operator $\hat{\mathcal{O}}$ with respect to the state $\hat{\rho}$ can written as

$$\langle \hat{\mathcal{O}} \rangle = \mathrm{Tr}(\hat{\rho}\hat{\mathcal{O}}) \tag{7}$$

$$= (2\pi)^N \int d\boldsymbol{r}\, W_{\rho}(\boldsymbol{r}) W_{\mathcal{O}}(\boldsymbol{r}), \tag{8}$$

where $W_{\rho}(\boldsymbol{r})$ and $W_{\mathcal{O}}(\boldsymbol{r})$ are the Wigner representations of the operators $\hat{\rho}$ and $\hat{\mathcal{O}}$, respectively.

B. Sum of Gaussians formalism

We adopt the approach described in Ref. [21], in which one writes the (in general, non-Gaussian) Wigner function of a state $\hat{\rho}$ as a sum of Gaussian functions

$$W_{\rho}(\boldsymbol{r}) = \sum_m c_m G_m(\boldsymbol{r}), \tag{9}$$

where the c_m are complex coefficients and

$$G_m(\boldsymbol{r}) = \frac{\exp\left[-\frac{1}{2}(\boldsymbol{r}-\boldsymbol{\mu}_m)^T \boldsymbol{\gamma}_m^{-1} (\boldsymbol{r}-\boldsymbol{\mu}_m)\right]}{\sqrt{\det(2\pi\boldsymbol{\gamma}_m)}} \tag{10}$$

denotes a normalized Gaussian with the mean vector $\boldsymbol{\mu}_m$ and covariance matrix $\boldsymbol{\gamma}_m$.

In principle, this expansion can be applied to any Wigner function, as long as arbitrarily many terms are allowed. Moreover, certain states of practical interest can be represented compactly in this way, despite their non-Gaussianity. For example, the Wigner function for a cat state can be written exactly in the form of Eq. (9) with four terms [21]. An especially attractive feature of the Gaussian expansion is that, unlike a naive Fock representation, the number of terms needed to describe a state does not necessarily increase for higher-energy states: For example, the expansion for a (squeezed) cat state is represented by four terms, regardless of its amplitude (and squeezing). For a GKP state, the number of peaks does tend to increase with energy and quality; thus, the number of terms needed to represent it increases as well.

The Wigner function for a tensor product of two states can be written as

$$W_{\rho\otimes\sigma}(\boldsymbol{r}) = W_{\rho}(\boldsymbol{r}_1) W_{\sigma}(\boldsymbol{r}_2), \tag{11}$$

where $\boldsymbol{r}_1$ and $\boldsymbol{r}_2$ denote the sets of phase-space variables associated the individual $\hat{\rho}$ and $\hat{\sigma}$, respectively. If both $W_{\rho}(\boldsymbol{r}_1)$ and $W_{\sigma}(\boldsymbol{r}_2)$ are expanded as in Eq. (9), one has

$$W_{\rho\otimes\sigma}(\boldsymbol{r}) = \sum_{m,n} c_m c_n G_m(\boldsymbol{r}_1) G_n(\boldsymbol{r}_2) \tag{12}$$

$$= \sum_{m,n} c_m c_n G_{mn}(\boldsymbol{r}), \tag{13}$$

where the mean and covariance matrix of $G_{mn}(\boldsymbol{r})$ are the direct products of the means and covariance matrices of $G_m(\boldsymbol{r}_1)$ and $G_n(\boldsymbol{r}_2)$:

$$\boldsymbol{\gamma}_{mn} = \boldsymbol{\gamma}_m \oplus \boldsymbol{\gamma}_n, \tag{14}$$

$$\boldsymbol{\mu}_{mn} = \boldsymbol{\mu}_m \oplus \boldsymbol{\mu}_n. \tag{15}$$

For GKP states, the specific forms of c_m, $\boldsymbol{\gamma}_m$, and $\boldsymbol{\mu}_m$ depend on the details of the protocol used to generate the state; these expansions are known for GKP states generated through cat state breeding and for the Fock damped description of finite-energy GKP states [21]. In this paper we focus on GKP states generated by breeding cat states [14,27,28], as indicated in Fig. 1; in this case, it can be shown (see Appendix B, and Refs. [14,29]) that the state generated after $\mathcal{M}$ rounds of

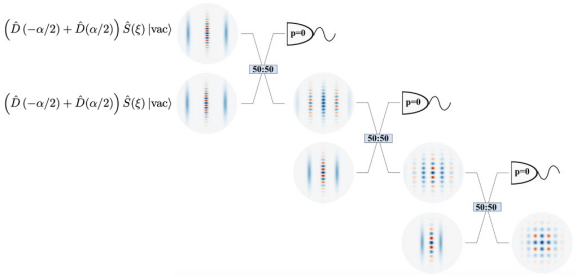

FIG. 1. Sketch of $\mathcal{M}=3$ rounds of a cat breeding protocol. The scheme involves interfering squeezed cat states at a balanced beam splitter, with one of the outputs subjected to homodyne detection (here we have taken the outcome $p=0$). The unmeasured mode becomes a closer approximation to a GKP state with each round of breeding. Details can be found in Refs. [14,27].

breeding is represented as

$$W_\rho(\boldsymbol{r}) = |\mathcal{N}|^2 \sum_{k,k'=0}^{\mathcal{M}+1} \binom{\mathcal{M}+1}{k}\binom{\mathcal{M}+1}{k'} \mathcal{A}_{k,k'} G_{k,k'}(\boldsymbol{r}), \tag{16}$$

with $G_{k,k'}(\boldsymbol{r})$ defined as in Eq. (10) and

$$\mathcal{A}_{k,k'} = \exp\left[-\tfrac{1}{2}e^{2\xi}(\beta_k-\beta_{k'})^2\right], \tag{17}$$

$$\boldsymbol{\gamma}_{k,k'} = \frac{1}{2}\begin{bmatrix} e^{-2\xi} & 0 \\ 0 & e^{2\xi}\end{bmatrix} \equiv \boldsymbol{\gamma}, \tag{18}$$

$$\boldsymbol{\mu}_{k,k'} = \sqrt{\frac{1}{2}}\begin{bmatrix} \beta_k+\beta_{k'} \\ ie^{2\xi}(\beta_{k'}-\beta_k)\end{bmatrix}, \tag{19}$$

$$\beta_k = \frac{[2k-(\mathcal{M}+1)]\alpha}{2\sqrt{2^{\mathcal{M}}}}, \tag{20}$$

where α and ξ are the amplitude and squeezing of the initial cat states, respectively, and $\mathcal{N}$ is a normalization constant. Similar expansions for other approximate GKP states can be derived [21], and in situations where the exact sum-of-Gaussians expansion is more difficult to derive, one can construct approximate expansions.

C. Description of entangling operations

Single-mode GKP states can be entangled by applying Gaussian unitaries and homodyne measurement [4,23–25]. For example, a GKP Bell state can be generated by applying the passive circuit shown in Fig. 2 to two single-mode GKP sensor states, which are defined as $|\varnothing\rangle = \hat{S}(\sqrt{2})|+\rangle$, where $\hat{S}(\sqrt{2})$ denotes a squeezing operation and

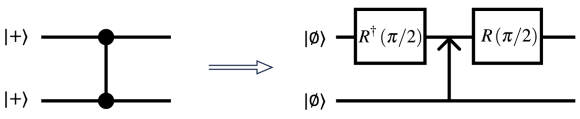

FIG. 2. Implementation of a GKP cz operation through static linear components. Here $\hat{R}(\theta)$ denotes a θ phase shift and the arrow represents a beam splitter, following the notation used in [30].

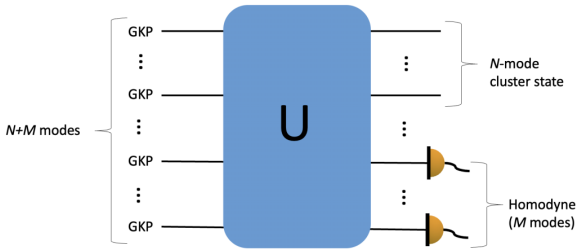

FIG. 3. Sketch of the cluster state generation circuits we consider in this paper: $M+N$ single-mode GKP states are sent through a linear unitary circuit (box labeled U) and M of the output modes are then subjected to homodyne measurement to yield an N-mode cluster state.

$|+\rangle = \frac{1}{\sqrt{2}}(|0\rangle_{\mathrm{GKP}} + |1\rangle_{\mathrm{GKP}})$ denotes the superposition state in a GKP encoding scheme [30].

More general cluster states can be formed by combining linear unitary circuits with homodyne measurement [25]; the general form of these so-called stitching circuits is sketched in Fig. 3, and a specific example is shown in Fig. 10.

If a state $\hat{\rho}$ evolves under a Gaussian unitary $\hat{U}$, the Wigner function for the evolved state $\hat{\bar{\rho}} = \hat{U}\hat{\rho}\hat{U}^\dagger$ is

$$W_{\bar{\rho}}(\boldsymbol{r}) = W_\rho(\boldsymbol{A}^{-1}\boldsymbol{r}), \tag{21}$$

where $W_\rho(\boldsymbol{r})$ is the Wigner function of the initial density operator (see Appendix A 1). The symplectic matrix $\boldsymbol{A}$ is defined by the action of the unitary; because $\hat{U}$ is Gaussian, one can write the simple input-output relation [26]

$$\hat{\boldsymbol{r}}' = \boldsymbol{A}\hat{\boldsymbol{r}}, \tag{22}$$

where $\hat{\boldsymbol{r}}$ is the vector of position and momentum operators corresponding to the input modes and

$$\hat{\boldsymbol{r}}' = (\hat{U}^\dagger\hat{x}_1\hat{U}, \hat{U}^\dagger\hat{p}_1\hat{U}, \ldots, \hat{U}^\dagger\hat{x}_N\hat{U}, \hat{U}^\dagger\hat{p}_N\hat{U})^T. \tag{23}$$

If the initial $\hat{\rho}$ is represented by a Wigner function of the sum-of-Gaussian form in Eq. (9), the evolved Wigner function is

$$W_{\bar{\rho}}(\boldsymbol{r}) = \sum_m c_m G_m(\boldsymbol{A}^{-1}\boldsymbol{r}) \tag{24}$$

$$= \sum_m c_m \overline{G}_m(\boldsymbol{r}), \tag{25}$$

where $\overline{G}_m(\boldsymbol{r})$ is a normalized Gaussian with the mean and covariance matrix

$$\overline{\boldsymbol{\mu}} = \boldsymbol{A}\boldsymbol{\mu}, \tag{26}$$

$$\overline{\boldsymbol{\gamma}} = \boldsymbol{A}\boldsymbol{\gamma}\boldsymbol{A}^T. \tag{27}$$

D. Measurement

We describe the homodyne detection and postselection as follows. Assume that an arbitrary quadrature operator

$$\hat{\eta}_\theta = \hat{p}\cos(\theta) - \hat{x}\sin(\theta) \tag{28}$$

is being measured, with $\tilde{\eta}$ denoting the measurement outcome. We write the state $\hat{\rho}'$ after the measurement as

$$\hat{\rho}' = \frac{\hat{K}_{\tilde{\eta}}^{\dagger}\hat{\tilde{\rho}}\hat{K}_{\tilde{\eta}}}{\mathrm{Tr}(\hat{K}_{\tilde{\eta}}^{\dagger}\hat{\tilde{\rho}}\hat{K}_{\tilde{\eta}})}, \tag{29}$$

where $\hat{\tilde{\rho}}$ is the state prior to measurement and [31]

$$\hat{K}_{\tilde{\eta}} = \int d\eta\, \Theta_{\tilde{\eta}}(\eta)|\eta\rangle\langle\eta|. \tag{30}$$

The function $\Theta_{\tilde{\eta}}(\eta)$ defines a window of homodyne outcomes centered at $\tilde{\eta}$. Here we will take the limit $|\Theta_{\tilde{\eta}}(\eta)|^2 \to \delta(\eta - \tilde{\eta})$ corresponding to an ideal postselection; nonideal postselection can be considered by adjusting the shape of $|\Theta_{\tilde{\eta}}(\eta)|^2$, for example, to be a Gaussian function. The Wigner representation of $\hat{F}_{\tilde{\eta}} = \hat{K}_{\tilde{\eta}}^{\dagger}\hat{K}_{\tilde{\eta}}$ is (see Appendix A 2)

$$W_{F_{\tilde{\eta}}}(\boldsymbol{r}) = \frac{1}{2\pi}|\Theta_{\tilde{\eta}}(\eta_\theta)|^2, \tag{31}$$

where $\eta_\theta = p\cos(\theta) - x\sin(\theta)$ is a phase-space variable corresponding to $\hat{\eta}_\theta$. Similarly, homodyne detection in M modes can be represented as

$$W_{F_{\tilde{\boldsymbol{\eta}}}}(\boldsymbol{r}) = \frac{1}{(2\pi)^M}\prod_{m=1}^{M}|\Theta_{\tilde{\eta}_m}(\eta_{\theta m})|^2, \tag{32}$$

where $\tilde{\boldsymbol{\eta}}$ denotes a vector of homodyne outcomes.

The formalism we have summarized enables a compact representation of multimode non-Gaussian states, like GKP cluster states, given compact Gaussian representations for the single-mode input states. With this, one can obtain the density operator of the multimode state, from which one can compute particular figures of merit.

E. Loss

Photon loss is considered to be the dominant source of noise in photonic approaches to quantum information. Its inclusion is essential in a realistic description of photonic devices. A conventional approach to modeling loss is to introduce a fictitious beam splitter that couples the physical mode to a loss mode, with the beam-splitter angle θ_i chosen to produce the correct transmittance of the physical mode [32–35]. Here we take the input to the loss mode to be vacuum, but the generalization to thermal states is easily made [21].

Applying loss to $\hat{\tilde{\rho}}$ [as defined in Eqs. (24)–(27)] amounts to making the substitutions

$$\overline{\boldsymbol{\mu}} \to \boldsymbol{T}\overline{\boldsymbol{\mu}}, \tag{33}$$

$$\overline{\boldsymbol{\gamma}} \to \boldsymbol{T}\overline{\boldsymbol{\gamma}}\boldsymbol{T}^T + \tfrac{1}{2}\boldsymbol{R}\boldsymbol{R}^T, \tag{34}$$

with

$$\boldsymbol{T} = \bigoplus_{i=1}^{N}\cos\theta_i\mathbb{1}, \tag{35}$$

$$\boldsymbol{R} = \bigoplus_{i=1}^{N}\sin\theta_i\mathbb{1}, \tag{36}$$

$$\theta_i = \cos^{-1}(\tau_i). \tag{37}$$

By θ_i we denote the effective beam-splitter angle for each lossy mode and τ_i is the transmittance of the channel. This result is quoted in Ref. [21], and its derivation is reviewed in Appendix A 4. The inclusion of loss does not significantly alter the numerical cost of simulations, because it does not increase the number of terms required for the Gaussian expansion of the Wigner function; one just needs to update the means and covariance matrices according to Eqs. (33) and (34).

III. STABILIZER EXPECTATION VALUES

A relevant set of parameters in quantum information processing applications is the expectation values of the cluster state's stabilizers. The stabilizer EVs can be used directly as a metric for the quality of a state, or they can be used to infer other relevant metrics such as effective squeezing or entanglement witnesses [36,37]. The operator $\hat{\mathcal{S}}$ is a stabilizer for a state $|\psi\rangle$ if it satisfies

$$\hat{\mathcal{S}}|\psi\rangle = |\psi\rangle. \tag{38}$$

An ideal N-mode cluster state is stabilized (and uniquely characterized) by products of single-mode Pauli operators [37]

$$\hat{\mathcal{S}}_k = \hat{X}^{(k)}\prod_{\text{neighbors } l \text{ of } k}\hat{Z}^{(l)}, \tag{39}$$

where k labels each of the N vertices of the cluster state such that the cluster state is specified by N distinct stabilizers with the form given in Eq. (39).

In a square lattice GKP encoding scheme, the generators of the Pauli group are $\sqrt{\pi}$ displacements in position and momentum. The logical Pauli $\hat{X}$ and $\hat{Z}$ operations correspond to position and momentum displacements, respectively, by odd integer multiples of $\sqrt{\pi}$ [4,30]. An ideal GKP qubit is stabilized by discrete displacements in phase space (by $2\sqrt{\pi}$ in position and momentum, corresponding to $\hat{X}^2$ and $\hat{Z}^2$), so the EV of these operators is unity, that is,

$$\mathrm{Tr}[\hat{\rho}_{\text{ideal}}\hat{D}(\bar{\boldsymbol{r}})] = 1 \tag{40}$$

for $\bar{\boldsymbol{r}} = (2n\sqrt{\pi}, 2m\sqrt{\pi})^T$, with $n, m \in \mathbb{Z}$.

For finite-energy approximations to GKP states, the EVs of the same operators are necessarily less than unity, due to the state's finite extent in phase space and due to the nonzero width of its peaks in phase space. Generally, the higher the state's quality, the closer to unity its stabilizer EVs. Hence stabilizer EVs can be used to gain insight into the quality of approximate GKP states and its dependence on various parameters involved in the state generation protocol. Although the elements of the Pauli group can be defined in terms of displacements by any integer multiple of $\sqrt{\pi}$, we will refer to stabilizer sets composed of displacements of minimal length, namely, displacements by $\sqrt{\pi}$. Implementations of stabilizers using larger displacements will result in a lower EV, again due to the realistic states' finite extent in phase space.

Using Eqs. (29) and (8), the stabilizer EV for a cluster state generated as described above can be written as

$$\langle\hat{\mathcal{S}}\rangle = \mathrm{Tr}(\hat{\rho}'\hat{\mathcal{S}}) = \frac{\mathrm{Tr}(\hat{\bar{\rho}}\hat{\mathcal{S}}\hat{K}_{\bar{\eta}}^{\dagger}\hat{K}_{\bar{\eta}})}{\mathrm{Tr}(\hat{\bar{\rho}}\hat{K}_{\bar{\eta}}^{\dagger}\hat{K}_{\bar{\eta}})} \tag{41}$$

$$= (2\pi)^{(N-M)}\frac{\int d\boldsymbol{r}\, W_{\bar{\rho}}(\boldsymbol{r})W_{F_{\bar{\eta}}}(\boldsymbol{r})W_{\mathcal{S}}(\boldsymbol{r})}{\int d\boldsymbol{r}\, W_{\bar{\rho}}(\boldsymbol{r})W_{F_{\bar{\eta}}}(\boldsymbol{r})}, \tag{42}$$

where $\hat{\rho}'$ is an N-mode density operator, $\hat{K}_{\bar{\eta}}^{\dagger}$ (or $\hat{F}_{\bar{\eta}} = \hat{K}_{\bar{\eta}}^{\dagger}\hat{K}_{\bar{\eta}}$) is an M-mode operator describing the homodyne measurement, and $\hat{\mathcal{S}}$ is a stabilizer defined over the unmeasured $N-M$ modes. The factor of $2\pi^{(N-M)}$ appears due to the implicit identity operator in the denominator of Eq. (41) (see Appendix C). In a GKP encoding scheme, $W_{\mathcal{S}}(\boldsymbol{r})$ is the Wigner representation of a displacement operator, which has the form

$$W_{D_{\bar{r}}}(\boldsymbol{r}) = \frac{1}{(2\pi)^N}e^{-i\boldsymbol{r}^T\boldsymbol{\Omega}\bar{\boldsymbol{r}}}, \tag{43}$$

with the displacement $\bar{\boldsymbol{r}}$ set to the relevant value for the stabilizer in question; for example, for a single-mode Pauli $\hat{X}$ operator, which is implemented by a position displacement by $m\sqrt{\pi}$ ($m \in \mathbb{Z}$), one would set $\bar{\boldsymbol{r}} = (m\sqrt{\pi}, 0)^T$.

Using a Gaussian expansion for $W_{\bar{\rho}}(\boldsymbol{r})$ in Eq. (42) results in Gaussian integrals that, due to the simple form of the stabilizer's Wigner representation, can easily be evaluated analytically. We neglect losses here for simplicity; the expressions including loss (and details of the derivation) are given in Appendix C. We obtain

$$\langle\mathcal{S}\rangle = \frac{\sum_{\boldsymbol{m}} c_{\boldsymbol{m}} g_{\boldsymbol{m}}(\tilde{\boldsymbol{\eta}};\boldsymbol{J})\exp(i\boldsymbol{J}^T\boldsymbol{P}_C\boldsymbol{A}\boldsymbol{\mu}_{\boldsymbol{m}})\exp(-\frac{1}{2}\boldsymbol{J}^T\boldsymbol{P}_C\boldsymbol{A}\boldsymbol{\gamma}_{\boldsymbol{m}}\boldsymbol{A}^T\boldsymbol{P}_C^T\boldsymbol{J})}{\sum_{\boldsymbol{m}} c_{\boldsymbol{m}} g_{\boldsymbol{m}}(\tilde{\boldsymbol{\eta}};\boldsymbol{0})}. \tag{44}$$

By $\boldsymbol{m}$ we denote a vector of indices $\boldsymbol{m} = (m_1, m_2, \ldots, m_N)^T$, where the index m_i refers to the Gaussian expansion [recall Eq. (9)] for one of the N inputs to the stitching circuit; in this work, all the inputs are identical single-mode states, but this can easily be generalized. The Wigner function of the N-mode input (separable) state is specified by

$$\boldsymbol{\gamma}_{\boldsymbol{m}} = \bigoplus_{i=1}^{N}\boldsymbol{\gamma}_{m_i}, \tag{45}$$

$$\boldsymbol{\mu}_{\boldsymbol{m}} = \bigoplus_{i=1}^{N}\boldsymbol{\mu}_{m_i}, \tag{46}$$

$$c_{\boldsymbol{m}} = \prod_{i=1}^{N} c_{m_i}, \tag{47}$$

where the $\boldsymbol{\gamma}_{m_i}$, $\boldsymbol{\mu}_{m_i}$, and c_{m_i} refer to the Gaussian expansion parameters for the ith input mode [recall the discussion around Eq. (11)]. The matrix $\boldsymbol{A}$ is defined by the Gaussian unitary [recall Eq. (22)], and the vector $\boldsymbol{J} = -\boldsymbol{\Omega}\bar{\boldsymbol{r}}$ defines the stabilizer operator [recall Eq. (43)]. We also introduce projection matrices $\boldsymbol{P}_H$ and $\boldsymbol{P}_C$: These project an object defined for the entire N-mode phase space into the subspace associated with the M measured quadratures and the $N-M$ unmeasured modes, respectively. Finally, $g_{\boldsymbol{m}}(\tilde{\boldsymbol{\eta}};\boldsymbol{J})$ is a Gaussian function in the postselected homodyne outcomes $\tilde{\boldsymbol{\eta}}$, with the mean and covariance matrix

$$\boldsymbol{\mu}'_{\boldsymbol{m}} = \boldsymbol{P}_H\boldsymbol{A}\boldsymbol{\mu}_{\boldsymbol{m}} + i\boldsymbol{P}_H\boldsymbol{A}\boldsymbol{\gamma}_{\boldsymbol{m}}\boldsymbol{A}^T\boldsymbol{P}_C^T\boldsymbol{J}, \tag{48}$$

$$\boldsymbol{\gamma}'_{\boldsymbol{m}} = \boldsymbol{P}_H\boldsymbol{A}\boldsymbol{\gamma}_{\boldsymbol{m}}\boldsymbol{A}^T\boldsymbol{P}_H^T. \tag{49}$$

Stabilizer EVs for realistic GKP cluster states can be numerically computed with Eq. (44): Gaussian expansions for the single-mode input GKP states are obtained and used to construct $\boldsymbol{\gamma}_{\boldsymbol{m}}$, $\boldsymbol{\mu}_{\boldsymbol{m}}$, and $c_{\boldsymbol{m}}$ according to Eqs. (45)–(47); the symplectic matrix $\boldsymbol{A}$ is derived for the Gaussian unitary circuit; the projectors $\boldsymbol{P}_H$ and $\boldsymbol{P}_C$ are defined according to the labeling of the modes to identify those modes that are measured and unmeasured, respectively (see Appendix C); the vector $\tilde{\boldsymbol{\eta}}$ specifies the homodyne measurement outcomes; and the vector $\boldsymbol{J}$ is defined according to the stabilizer of interest. Equation (44) can be used to explore the effect of various state preparation settings on the quality of the generated cluster states; for example, changes in the unitary circuit or homodyne outcomes are reflected by modifying $\boldsymbol{A}$ and $\tilde{\boldsymbol{\eta}}$, respectively, whereas changes in the protocol used to generate the single-mode GKP inputs are reflected in $\boldsymbol{\gamma}_{\boldsymbol{m}}$, $\boldsymbol{\mu}_{\boldsymbol{m}}$, and $c_{\boldsymbol{m}}$.

Gaussian random noise model

Exact simulations are not tractable for cluster states of an arbitrary size. A standard, scalable approach for modeling nonideal GKP states is to apply a Gaussian random noise channel to ideal GKP states, resulting in a mixed state $\hat{\tilde{\rho}}$ [6,25,30,38]. The effect of the GRN channel can be expressed as [39]

$$\hat{\tilde{\rho}} = \int_{\mathbb{C}} \mathrm{d}^2\alpha\, G_{\boldsymbol{\Delta}}(\alpha)\hat{D}(\alpha)|\psi\rangle\langle\psi|\hat{D}^{\dagger}(\alpha), \tag{50}$$

where

$$G_{\boldsymbol{\Delta}}(\alpha) = \frac{\exp\left(-\frac{\mathrm{Re}(\alpha)^2}{\Delta_x^2/2}\right)\exp\left(-\frac{\mathrm{Im}(\alpha)^2}{\Delta_p^2/2}\right)}{\pi\Delta_x\Delta_p/2} \tag{51}$$

and

$$\hat{D}(\alpha) = \exp(\alpha a^{\dagger} - \alpha^* a) \tag{52}$$

$$= \exp[\sqrt{2}i\,\mathrm{Im}(\alpha)\hat{x} - \sqrt{2}i\,\mathrm{Re}(\alpha)\hat{p}]. \tag{53}$$

The GRN state is characterized by a Wigner function with Gaussian (rather than δ-function) peaks. The p and x quadrature variance of the peaks is set by the effective squeezing parameters Δ_p and Δ_x, which are in turn often related to the performance of the GKP qubit [6,13,40,41]. The stabilizer EVs for a GRN state are related to the effective squeezing

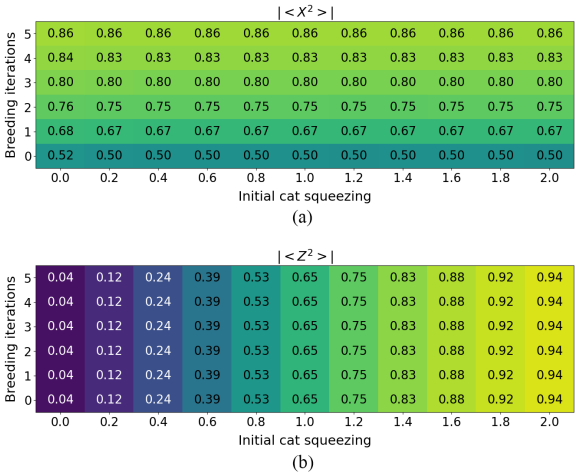

FIG. 4. Single-qubit stabilizer EVs for a single-mode GKP state, as a function of the parameters of the cat breeding protocol used to generate it. The stabilizer EVs increase as the squeezing of the input cat states and/or the number of iterations of cat state breeding are increased, reflecting the increasing quality of the GKP state.

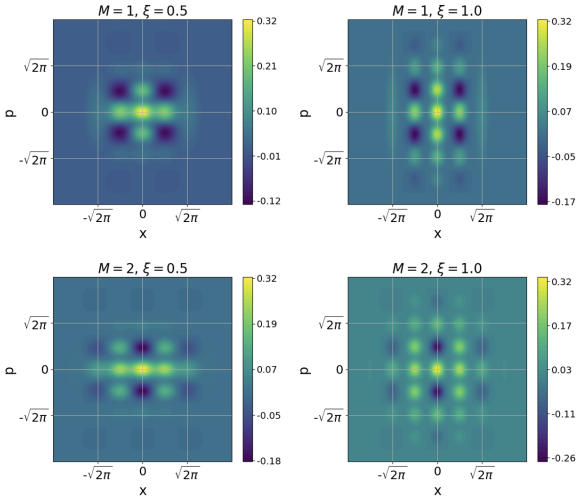

FIG. 5. Wigner functions of approximate GKP states generated by the breeding protocol described in Sec. II B, for various $\mathcal{M}$ and ξ (number of breeding iterations and cat squeezing, respectively).

parameters as follows [42]:

$$|\mathrm{Tr}(\hat{\mathcal{S}}_x\hat{\tilde{\rho}})| = \exp\big(-\pi\Delta_x^2/2\big), \tag{54}$$

$$|\mathrm{Tr}(\hat{\mathcal{S}}_p\hat{\tilde{\rho}})| = \exp\big(-\pi\Delta_p^2/2\big). \tag{55}$$

Here $\hat{\mathcal{S}}_x = \exp(is\hat{x})$ and $\hat{\mathcal{S}}_p = \exp(-is'\hat{p})$ denote the GKP stabilizers; the displacements s and s' depend on the lattice spacing of the GKP state.

The GRN model can be used for scalable simulations of cluster state formation by taking GRN states as the single-mode input states, with the effective squeezing parameters chosen to reproduce the stabilizer EVs of the approximate GKP states one could actually generate. The performance of a cluster state generated by stitching the input GRN states can be estimated following the methods described in Ref. [25], for example. However, this does not necessarily result in an accurate description of the inputs nor of the cluster state—approximate GKP states generated through realistic protocols cannot be fully characterized by effective squeezing parameters—and it is unclear how accurate GRN results are in different scenarios.

IV. NUMERICAL RESULTS

In this section we compute stabilizer expectation values for single-mode and multimode GKP states. We first consider single-mode approximate GKP states generated by breeding cat states (recall Fig. 1). In Fig. 4 we plot the stabilizer EVs for the bred GKP state as a function of the squeezing of the cat states and the number of rounds in the breeding protocol. The increasing stabilizer EVs reflect the increasing quality of the state as the key parameters of the breeding protocol are improved.

In particular, we see that $\langle\hat{X}^2\rangle$ depends mainly on the number of breeding iterations, while $\langle\hat{Z}^2\rangle$ is mainly determined by the initial cat squeezing. This is because each iteration of breeding increases the number of peaks in the x quadrature of the output state (see Fig. 5), which increases the periodicity of the state along the x quadrature, leaving the p quadrature unaffected [14,27,29]. On the other hand, the squeezing of the initial cat state sets the state's periodicity in the p quadrature and the sharpness of its peaks in the x quadrature; these features are reflected in $\langle\hat{Z}^2\rangle$, which by its definition relates to the periodicity of the state in the p quadrature and the sharpness of its peaks in the x quadrature.

Next we address GKP Bell pairs: These can be generated by the circuit sketched in Fig. 2, starting with approximate single-mode sensor states that can be generated, for example, through cat state breeding. Because the stitching circuit is unitary and because the stabilizers are displacement operators, the Bell state stabilizers can be obtained directly from the stabilizers of the input sensor states. It is easily shown that

$$\mathrm{Tr}[\hat{\tilde{\rho}}\hat{D}(\boldsymbol{r})] = \mathrm{Tr}[\hat{\rho}\hat{D}(\boldsymbol{r}')], \tag{56}$$

with

$$\boldsymbol{r}' = \boldsymbol{A}^{-1}\boldsymbol{r}, \tag{57}$$

where $\boldsymbol{r}'$ and $\boldsymbol{r}$ refer to quadrature variables [unlike in Eq. (22)], $\hat{\tilde{\rho}} = \hat{U}\hat{\rho}\hat{U}^\dagger$ is the state after the Gaussian unitary, and $\boldsymbol{A}$ is the symplectic matrix defined in Eq. (22). Because the input ρ is separable, the expectation value on the right-hand side of Eq. (56) can be written as a product of single-mode expectation values: In this way, the stabilizer EVs of the output state can be inferred from EVs of displacements on the input states. This is true regardless of the input state. The stabilizer EVs obtained using the GRN model are therefore guaranteed to match the results of exact simulations, provided the effective squeezing for the input GRN states is chosen to reproduce the stabilizer EVs of the realistic input states used in the full simulation (recall Sec. III).

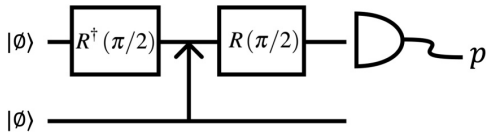

FIG. 6. Sketch of the scenario we consider in Figs. 7 and 9. We envision creating a GKP Bell state through the unitary circuit in Fig. 2, postselecting on a homodyne measurement outcome p in one of the modes, and characterizing the unmeasured mode.

The situation becomes more interesting when homodyne measurements are introduced: Because the evolution is no longer unitary, direct simulation is required to determine the stabilizers of the output state following measurement. We consider the scenario sketched in Fig. 6, in which one generates a GKP Bell state and measures the p quadrature of one mode, leaving one unmeasured mode that we characterize in terms of stabilizer EVs; if the GKP states were ideal, the unmeasured mode would be stabilized by $\hat{X}^2$ and $\hat{Z}^2$. In Fig. 7 we plot the stabilizer EVs for the unmeasured mode, focusing on the homodyne outcome $p = 0$ for odd breeding iterations and $p = \sqrt{\pi}/2$ for even breeding iterations; the different homodyne outcome for even $\mathcal{M}$ is chosen to compensate for the fact that the cat breeding protocol produces displaced sensor states for even $\mathcal{M}$ (recall Fig. 5 and see Appendix A 3). These results (and those summarized in Fig. 4) were verified by comparisons to Fock-basis simulations. The two approaches agree closely, provided a sufficiently high Fock-basis cutoff is used. In Fig. 8 we directly compare the results of Fock-basis simulations [43] and our exact sum-of-Gaussian description. The discrepancies between the two grow more significant as the breeding parameters are increased to produce energetic states, with the Fock-basis results tending to underestimate the stabilizer EVs. Increasing the photon-number cutoff for the Fock-basis simulations results in a closer approximation

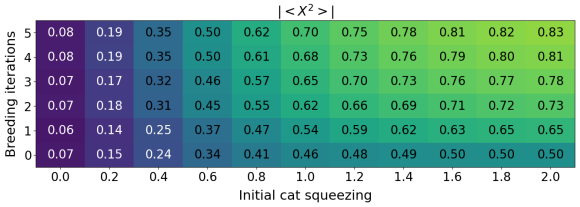

(a)

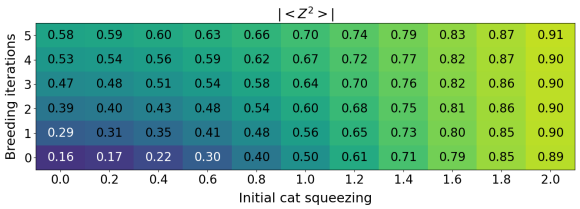

(b)

FIG. 7. EVs of single-qubit stabilizers evaluated for the unmeasured mode in the scheme sketched in Fig. 6. The results shown take the homodyne measurement outcome to be $p = 0$ for odd breeding iterations and $p = \sqrt{\pi}/2$ for even breeding iterations.

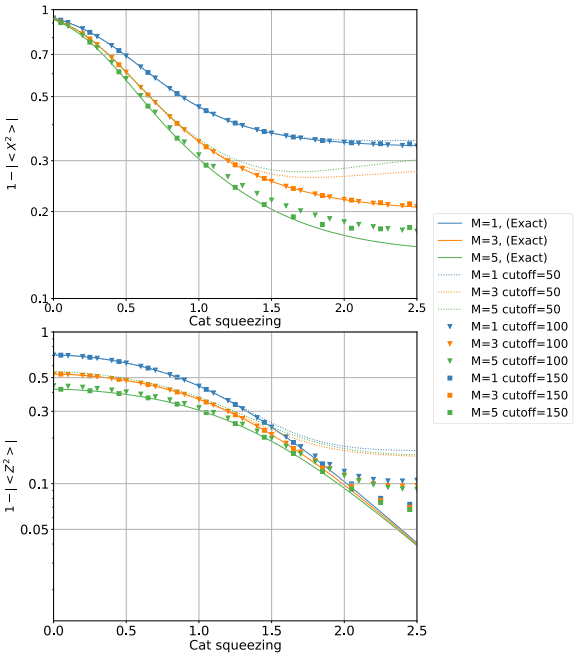

(a)

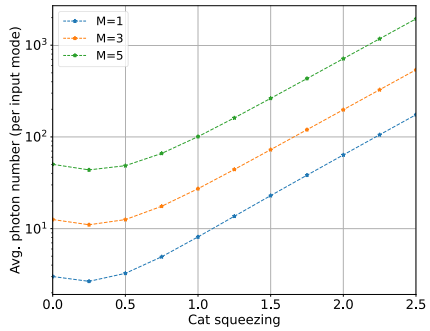

(b)

FIG. 8. (a) Stabilizer EVs computed through simulations in the Fock basis (dotted lines), compared to the exact Gaussian expansion (solid lines). Single-qubit stabilizer EVs are evaluated for the unmeasured mode in Fig. 6. (b) Average photon number for each input cat state for the GKP state preparation protocols considered in (a). The Fock-basis simulations deviate from the exact result when the average photon number for the input states exceeds the photon-number cutoff used in the simulation.

to the exact results, but even the cutoffs shown in Fig. 8, which are still not sufficient for certain breeding parameters, result in a costly computation that cannot be scaled to describe few-mode cluster states.

In Fig. 9 we fix a set of breeding parameters and we plot the simulated stabilizer EVs for the unmeasured mode of the Bell state as a function of the p measurement outcome. We compare this to the stabilizer EVs predicted by a GRN treatment, with the effective squeezing for the single-mode GKP states chosen to reproduce the stabilizer EVs of the bred states (see

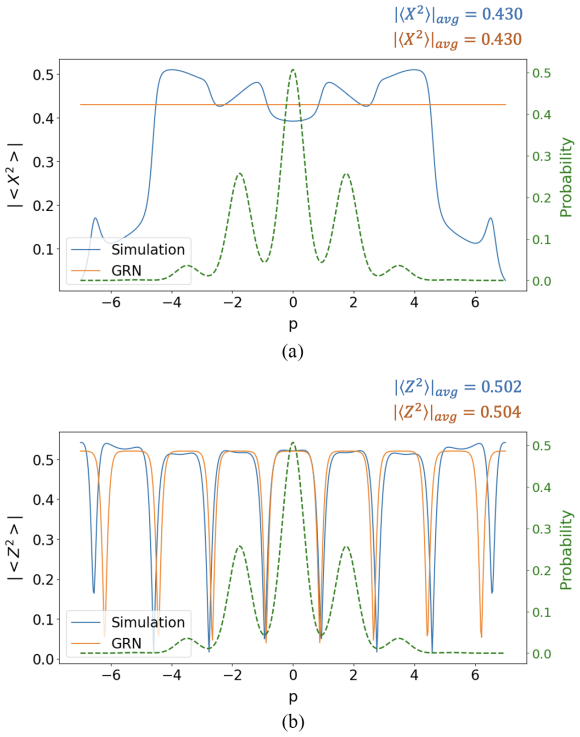

FIG. 9. Single-qubit stabilizer EVs evaluated for the unmeasured mode of a GKP Bell pair (see Fig. 6). We take the single-mode GKP states to be generated by $\mathcal{M} = 3$ rounds of breeding, with an initial cat squeezing of $\xi = 0.5$. We vary the measured p and plot the stabilizer EV for the unmeasured mode as calculated through direct simulation (blue line) and using the GRN model (orange line). The green dashed line represents the probability of measuring the various homodyne outcomes. The average EVs are indicated in the top right corner.

Sec. III and Appendix D). The predictions of the GRN model differ from the simulation results for most p measurement outcomes. There is also a clear qualitative difference, with the simulated results lacking the GRN results' periodicity over the p measurement outcomes. This reflects the fact that the peaks in the bred state are not all identical, unlike in the GRN state. In Fig. 9 we also indicate the average stabilizer EVs, weighted by the probabilities of the p measurement outcomes. We find good agreement between the average EVs: The values for $|\langle\hat{X}^2\rangle|$ obtained using the two models deviate at the seventh significant digit, and for $|\langle\hat{Z}^2\rangle|$ the two approaches deviate at the third significant digit.

We can apply our implementation of Eq. (44) to address the generation of more complex cluster states, requiring the use of unitary linear components and homodyne measurement. We first address the generation of a linear three-mode cluster state, through the circuit sketched in Fig. 10. The stabilizer EVs for the linear cluster state are plotted in Fig. 11(a). The stabilizer EVs [see Fig. 11(a)] indicate the increasing quality of the state as the number of breeding iterations is increased. Interestingly, the squeezing of the cat states has relatively little

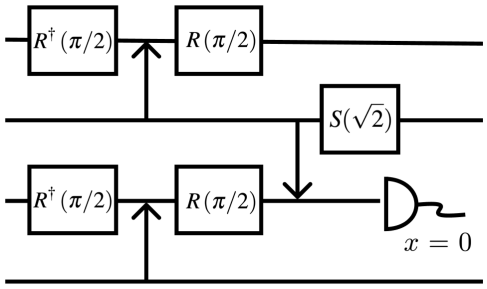

FIG. 10. Circuit used to create a three-mode linear cluster state, beginning with four single-mode approximate GKP states. Inline squeezing in the second mode is included for clarity, but in practice it can be eliminated, as long as the squeezing in this mode is accounted for in the postprocessing of measurement results (see Ref. [25]).

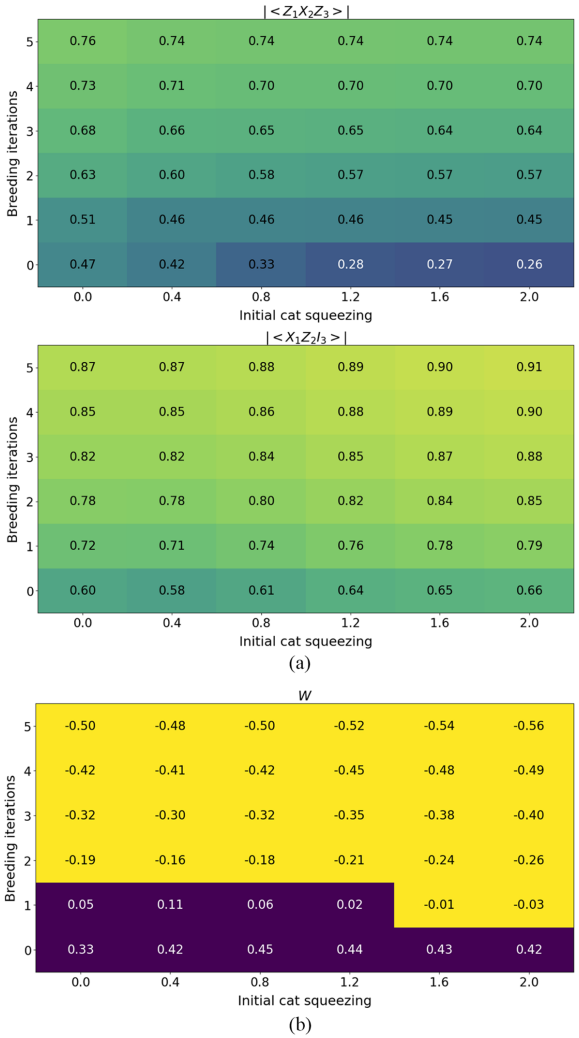

FIG. 11. (a) Stabilizer EVs for the three-mode linear cluster state (omitting $|\langle\hat{I}_1\hat{Z}_2\hat{X}_3\rangle| = |\langle\hat{X}_1\hat{Z}_2\hat{I}_3\rangle|$) and (b) expectation value of an entanglement witness derived from these stabilizers [37].

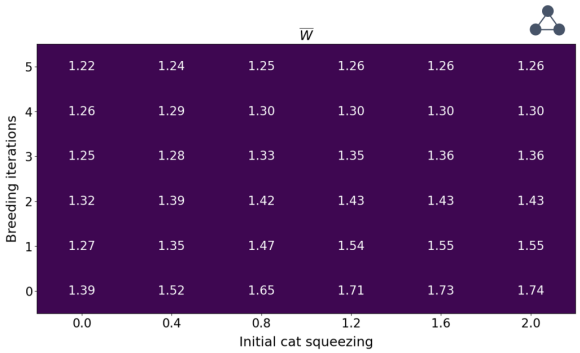

FIG. 12. EVs of the witness $\hat{\overline{W}}$ (designed to witness the tripartite graph state sketched in the top right), evaluated the linear GKP cluster state generated through the circuit in Fig. 10. The positive EVs indicate that, as expected, the distinct type of tripartite entanglement witnessed by $\hat{\overline{W}}$ is exhibited by the linear cluster state, even for parameters with which linear tripartite entanglement is witnessed in Fig. 11(b).

(and sometimes negative) impact on the stabilizer EVs. In Fig. 11(b) we plot the EVs of a witness operator constructed from the cluster state's stabilizers, as suggested by Tóth and Gühne [37]: We use

$$\hat{\mathcal{W}} = 2(\mathbb{1}) - \hat{I}_1\hat{Z}_2\hat{X}_3 - \hat{X}_1\hat{Z}_2\hat{I}_3 - \hat{Z}_1\hat{X}_2\hat{Z}_3. \tag{58}$$

A negative EV of the witness operator certifies genuine multipartite entanglement; interestingly, this threshold is crossed even with few rounds of breeding and low cat state squeezing. To confirm the significance of this witness EV's negativity, we compute the EV for the witness for a different tripartite cluster state

$$\hat{\overline{\mathcal{W}}} = 2(\mathbb{1}) - \hat{Z}_1\hat{Z}_2\hat{X}_3 - \hat{X}_1\hat{Z}_2\hat{Z}_3 - \hat{Z}_1\hat{X}_2\hat{Z}_3, \tag{59}$$

which is constructed to "witness" the cluster state sketched in Fig. 12. If the negative EVs of the witness in Fig. 11(b) carry any significance, the EVs of a different witness should remain positive to indicate that the linear GKP cluster state does not exhibit the "wrong" type of tripartite entanglement. This is confirmed by the results plotted in Fig. 12. An interesting direction for follow-up work will be to explore whether these witness operators are a relevant figure of merit for these types of resources and what can be inferred about the usefulness of the approximate GKP cluster state based on the witness EV.

V. CONCLUSION

We have addressed the problem of studying realistic GKP cluster states, demonstrating an approach for simulating these states by using Gaussian expansions in phase space [21] and referring to stabilizer EVs as figures of merit. We applied our approach to the generation of single-mode GKP states through "breeding" of Schrodinger cat states and to the generation of GKP cluster states by entangling these single-mode inputs through linear unitary components and homodyne measurement. We demonstrated that our method is suitable for studying a broader parameter space (and higher number of modes) compared to a typical Fock-basis representation. We explored the effect of state preparation parameters on the quality of the final cluster state and we compared our exact computations to predictions made using the GRN model.

Our comparisons to the GRN model open up a few questions for future work. We found deviations between the two models when homodyne measurement was introduced. These discrepancies may indicate an opportunity to improve the decoding of information encoded in GKP cluster states, for example, by adjusting the binning of the homodyne measurement outcome, using the more detailed picture of the states given by exact simulation. At the same time, the discrepancies between the GRN model and exact calculations are much smaller when one averages over measurement outcomes. More work is needed to understand what these small discrepancies mean on an operational level and how they scale with the complexity of the cluster state.

It will also be interesting to assess in more detail the usefulness of stabilizers, as well as witness operators constructed from them, in characterizing GKP cluster states, for example, by comparing stabilizer EVs to logical error rates for realistic states using exact simulations. Due to its efficiency, this method is also a possible tool for numerically optimizing state generation protocols, perhaps with reference to figures of merit based on stabilizers, rather than fidelity to a particular state [44]. Finally, we envision a number of generalizations to the formalism described here so that it can be applied to a more general class of state preparation protocols [15,17] and to other physical platforms [45–48]. For example, this will include describing photon-number-resolving measurement [17,20,49] and addressing different input states like imperfect cat states [50,51] or other relevant approximations to GKP states.

ACKNOWLEDGMENTS

The NRC headquarters is located on the traditional unceded territory of the Algonquin Anishinaabe and Mohawk people. The authors thank Noah Lupu-Gladstein, Anaelle Hertz, and Aaron Goldberg for helpful discussions. M.B. and K.H. acknowledge support from the Quantum Research and Development Initiative, led by the National Research Council Canada, under the National Quantum Strategy. K.H. acknowledges funding from the NSERC Discovery Grant and Alliance programs.

DATA AVAILABILITY

The data that support the findings of this article are not publicly available. The data are available from the authors upon reasonable request.

APPENDIX A: REVIEW OF SOME USEFUL RESULTS IN THE PHASE-SPACE FORMALISM

1. Wigner function of an operator under (Gaussian) unitary evolution

We first review the derivation of Eq. (21), which relates the Wigner functions of a state before ($\hat{\rho}$) and after ($\hat{\tilde{\rho}} = \hat{U}\hat{\rho}\hat{U}^\dagger$) evolution by a Gaussian unitary. The characteristic function of

$\hat{\tilde{\rho}}$ is

$$\chi_{\tilde{\rho}}(\boldsymbol{r}') = \mathrm{Tr}[\hat{D}(\boldsymbol{r}')\hat{\tilde{\rho}}] \tag{A1}$$
$$= \mathrm{Tr}[\hat{D}(\boldsymbol{r}')\hat{U}\,\hat{\rho}\hat{U}^\dagger] \tag{A2}$$
$$= \mathrm{Tr}[\hat{U}^\dagger\hat{D}(\boldsymbol{r}')\hat{U}\,\hat{\rho}]. \tag{A3}$$

We have

$$\hat{D}(\boldsymbol{r}') = e^{-i(\boldsymbol{r}')^T\boldsymbol{\Omega}\hat{\boldsymbol{r}}} \tag{A4}$$

and

$$\hat{U}^\dagger\hat{D}(\boldsymbol{r}')\hat{U} = \exp[-i(\boldsymbol{r}')^T\boldsymbol{\Omega}\hat{\boldsymbol{r}}'], \tag{A5}$$

with $\hat{\boldsymbol{r}}'$ as defined in Eq. (23). Using Eq. (22) (which holds for any Gaussian unitary), we have

$$\hat{U}^\dagger\hat{D}(\boldsymbol{r}')\hat{U} = \exp[-i(\boldsymbol{r}')^T\boldsymbol{\Omega}\boldsymbol{A}\hat{\boldsymbol{r}}] \tag{A6}$$
$$= \exp[-i(\boldsymbol{r}')^T\boldsymbol{\Omega}\boldsymbol{A}\boldsymbol{\Omega}^{-1}\boldsymbol{\Omega}\hat{\boldsymbol{r}}] \tag{A7}$$
$$= \exp[-i(\boldsymbol{r}'')^T\boldsymbol{\Omega}\hat{\boldsymbol{r}}] = \hat{D}(\boldsymbol{r}''), \tag{A8}$$

where

$$(\boldsymbol{r}'')^T = (\boldsymbol{r}')^T\boldsymbol{\Omega}\boldsymbol{A}\boldsymbol{\Omega}^{-1}, \tag{A9}$$

$$\boldsymbol{r}'' = \boldsymbol{\Omega}^{-1}\boldsymbol{A}^T\boldsymbol{\Omega}\boldsymbol{r}'. \tag{A10}$$

This gives

$$\chi_{\tilde{\rho}}(\boldsymbol{r}') = \mathrm{Tr}[\hat{D}(\boldsymbol{r}')\hat{\tilde{\rho}}] \tag{A11}$$
$$= \mathrm{Tr}[\hat{D}(\boldsymbol{r}'')\hat{\rho}] \tag{A12}$$
$$= \chi_\rho(\boldsymbol{r}''). \tag{A13}$$

The Wigner function of $\hat{\tilde{\rho}}$ is

$$W_{\tilde{\rho}}(\boldsymbol{r}) = \frac{1}{(2\pi)^{2N}}\int d\boldsymbol{r}'\, e^{-i(\boldsymbol{r})^T\boldsymbol{\Omega}\boldsymbol{r}'}\chi_{\tilde{\rho}}(\boldsymbol{r}') \tag{A14}$$
$$= \frac{1}{(2\pi)^{2N}}\int d\boldsymbol{r}''\, e^{-i(\boldsymbol{r})^T\boldsymbol{\Omega}(\boldsymbol{\Omega}^{-1}\boldsymbol{A}^T\boldsymbol{\Omega})^{-1}\boldsymbol{r}''}\chi_\rho(\boldsymbol{r}''). \tag{A15}$$

In (A15) we have changed variables using Eq. (A10) and recognizing that the Jacobian is unity. We insert a factor of $\mathbf{1} = \boldsymbol{\Omega}^{-1}\boldsymbol{\Omega}$ in the argument of the exponential and we define

$$\boldsymbol{R}^T = \boldsymbol{r}^T\boldsymbol{\Omega}(\boldsymbol{\Omega}^{-1}\boldsymbol{A}^T\boldsymbol{\Omega})^{-1}\boldsymbol{\Omega}^{-1} \tag{A16}$$
$$= \boldsymbol{r}^T\boldsymbol{\Omega}\boldsymbol{\Omega}^{-1}(\boldsymbol{A}^T)^{-1}\boldsymbol{\Omega}\boldsymbol{\Omega}^{-1} \tag{A17}$$
$$= \boldsymbol{r}^T(\boldsymbol{A}^{-1})^T. \tag{A18}$$

Then we have

$$W_{\tilde{\rho}}(\boldsymbol{r}) = \frac{1}{(2\pi)^{2N}}\int d\boldsymbol{r}''\, e^{-i\boldsymbol{R}^T\boldsymbol{\Omega}\boldsymbol{r}''}\chi_\rho(\boldsymbol{r}'') \tag{A19}$$
$$= W_\rho(\boldsymbol{R}). \tag{A20}$$

2. Wigner representation of our homodyne measurement operator

We define

$$\hat{K}_{\bar{\eta}} = \int d\eta\, \Theta_{\bar{\eta}}(\eta)|\eta\rangle\langle\eta|, \tag{A21}$$

$$\hat{F}_{\bar{\eta}} = \hat{K}_{\bar{\eta}}^\dagger\hat{K}_{\bar{\eta}} \tag{A22}$$

$$= \int d\eta \int d\eta'\,\Theta^*_{\bar{\eta}}(\eta)\Theta_{\bar{\eta}}(\eta')|\eta\rangle\langle\eta|\eta'\rangle\langle\eta'| \tag{A23}$$
$$= \int d\eta|\Theta_{\bar{\eta}}(\eta)|^2|\eta\rangle\langle\eta|. \tag{A24}$$

Due to the linearity of the Wigner transform, we have

$$W_{F_{\bar{\eta}}}(\boldsymbol{r}) = \int d\eta|\Theta_{\bar{\eta}}(\eta)|^2 W_{|\eta\rangle\langle\eta|}(\boldsymbol{r}), \tag{A25}$$

where $W_{|\eta\rangle\langle\eta|}(\boldsymbol{r})$ is the Wigner function of the generalized quadrature eigenstate associated with

$$\hat{\eta}_\theta = \hat{p}\cos(\theta) - \hat{x}\sin(\theta), \tag{A26}$$

which can be written in terms of the usual momentum eigenstate as

$$|\eta\rangle = \hat{R}(\theta)|P\rangle, \tag{A27}$$

$$\hat{R}(\theta) = \exp(-i\theta a^\dagger a). \tag{A28}$$

With Eqs. (A28) and (21) we have

$$W_{|\eta\rangle\langle\eta|}(\boldsymbol{r}) = W_{|P\rangle\langle P|}(\boldsymbol{A}^{-1}\boldsymbol{r}), \tag{A29}$$

where

$$\boldsymbol{A} = \begin{bmatrix}\cos(\theta) & -\sin(\theta)\\ \sin(\theta) & \cos(\theta)\end{bmatrix}. \tag{A30}$$

It is easy to show that

$$W_{|P\rangle\langle P|}(\boldsymbol{r}) = \frac{1}{2\pi}\delta(p - P), \tag{A31}$$

where p is a quadrature variable and P is the corresponding eigenvalue. Inverting Eq. (A30), we get

$$W_{|\eta\rangle\langle\eta|}(\boldsymbol{r}) = \frac{1}{2\pi}\delta(-x\sin(\theta) + p\cos(\theta) - \eta), \tag{A32}$$

where we have used the fact that the eigenvalues η and P are equal. One can also work in terms of rotated phase-space coordinates $\{\eta_\theta, \eta_\theta^\perp\}$ to write

$$W_{|\eta\rangle\langle\eta|}(\boldsymbol{r}) = \frac{1}{2\pi}\delta(\eta_\theta - \eta). \tag{A33}$$

Using this notation, we have

$$W_{F_{\bar{\eta}}}(\boldsymbol{r}) = \frac{1}{2\pi}\int d\eta|\Theta_{\bar{\eta}}(\eta)|^2\delta(\eta_\theta - \eta), \tag{A34}$$

as written in Sec. II D.

3. Accounting for displacements in input states

The breeding protocol described in Sec. II A produces the sensor state defined in Sec. II C for even breeding iterations and a displaced sensor state for odd breeding rounds. The relative displacement needs to be taken into account when comparing the results of a stitching protocol for a particular homodyne outcome.

Consider a state ρ characterized by quadrature operators $\hat{\boldsymbol{r}}$. Evolution through a Gaussian unitary can be understood as taking

$$\hat{\boldsymbol{r}} \to \boldsymbol{A}\hat{\boldsymbol{r}}, \tag{A35}$$

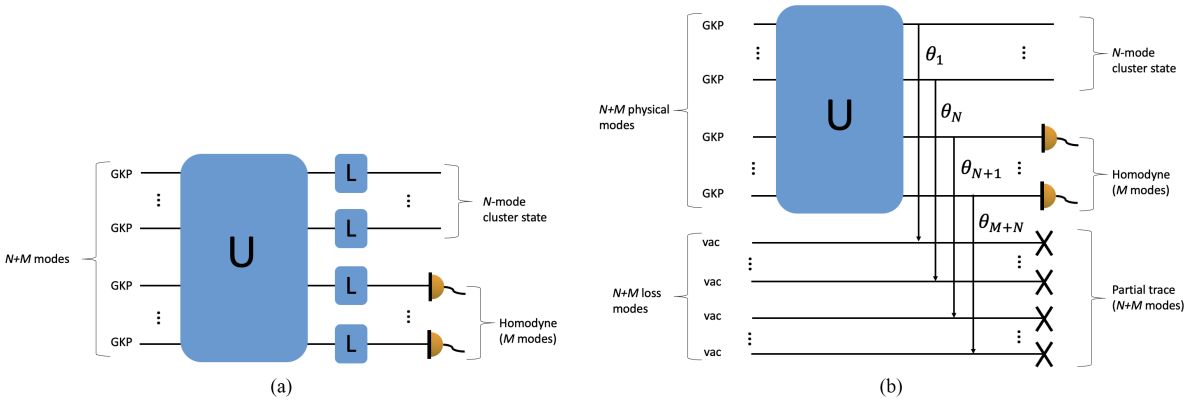

FIG. 13. Sketch of (a) the treatment of loss in physical modes as (b) a beam splitter coupling physical modes to loss modes.

with $\boldsymbol{A}$ a symplectic matrix defined in Eq. (22). Now we consider the displaced state evolving through the same unitary circuit. The displacement takes the form

$$\hat{\boldsymbol{r}} \to \hat{\boldsymbol{r}} + \bar{\boldsymbol{r}} \tag{A36}$$

and the unitary circuit

$$\hat{\boldsymbol{r}} + \bar{\boldsymbol{r}} \to \boldsymbol{A}\hat{\boldsymbol{r}} + \boldsymbol{A}\bar{\boldsymbol{r}}. \tag{A37}$$

The output in this case is displaced by $\boldsymbol{A}\bar{\boldsymbol{r}}$ relative to the scenario with undisplaced initial states, which can be accounted for by adjusting homodyne measurement outcomes accordingly. For example, the GKP state generated by odd $\mathcal{M}$ iterations of breeding is an approximate sensor state; even $\mathcal{M}$ produces an approximation of a sensor state displaced by $\bar{\boldsymbol{r}} = (\sqrt{\pi/2}, 0)^T$ (see Fig. 5). The dumbbell stitching circuit sketched in Fig. 2 is characterized by

$$\boldsymbol{A} = \frac{1}{\sqrt{2}} \begin{bmatrix} 1 & 0 & 0 & -1 \\ 0 & 1 & 1 & 0 \\ 0 & -1 & 1 & 0 \\ 1 & 0 & 0 & 1 \end{bmatrix}. \tag{A38}$$

We have

$$\boldsymbol{A}\bar{\boldsymbol{r}} = \frac{1}{\sqrt{2}} \begin{bmatrix} 1 & 0 & 0 & -1 \\ 0 & 1 & 1 & 0 \\ 0 & -1 & 1 & 0 \\ 1 & 0 & 0 & 1 \end{bmatrix} \begin{bmatrix} \sqrt{\pi/2} \\ 0 \\ \sqrt{\pi/2} \\ 0 \end{bmatrix} = \frac{\sqrt{\pi}}{2} \begin{bmatrix} 1 \\ 1 \\ 1 \\ 1 \end{bmatrix}, \tag{A39}$$

hence our choice of $p = 0$ and $p = \sqrt{\pi}/2$ as the homodyne measurement outcomes in Fig. 7 (for odd and even $\mathcal{M}$, respectively).

4. Modeling loss

We consider a scenario in which all the modes have the same transmissivity such that the loss in each mode can be aggregated and treated at one single point in the circuit, as shown in Fig. 13(a) [35]; more general scenarios could be treated by applying loss at multiple points in the circuit. We model each instance of loss as a coupling of the physical channel to a fictitious loss channel, through a beam splitter for which the angle θ_i is chosen to produce the correct transmission through the physical channel [see Fig. 13(b)].

Here we show that applying loss to the state $\hat{\bar{\rho}}$ characterized by

$$W_{\bar{\rho}}(\boldsymbol{r}) = \sum_m c_m \overline{G}_m(\boldsymbol{r}) \tag{A40}$$

can be described by making the substitution

$$\bar{\boldsymbol{\mu}} \to \boldsymbol{T}\bar{\boldsymbol{\mu}}\boldsymbol{T}^T, \tag{A41}$$

$$\bar{\boldsymbol{\gamma}} \to \boldsymbol{T}\bar{\boldsymbol{\gamma}}\boldsymbol{T}^T + \tfrac{1}{2}\boldsymbol{R}\boldsymbol{R}^T, \tag{A42}$$

with

$$\boldsymbol{T} = \bigoplus_{i=1}^{N} \cos\theta_i \mathbb{1}, \tag{A43}$$

$$\boldsymbol{R} = \bigoplus_{i=1}^{N} \sin\theta_i \mathbb{1}. \tag{A44}$$

Details

Using the notation of Sec. II C, the state following evolution via $\hat{U}$ is represented by

$$W_{\bar{\rho}} = \sum_m c_m \overline{G}_m(\boldsymbol{r}), \tag{A45}$$

with $\overline{G}_m(\boldsymbol{r})$ a $2(N+M)$-variable Gaussian with

$$\bar{\boldsymbol{\mu}} = \boldsymbol{A}\boldsymbol{\mu}, \tag{A46}$$

$$\bar{\boldsymbol{\gamma}} = \boldsymbol{A}\boldsymbol{\gamma}\boldsymbol{A}^T. \tag{A47}$$

We define $\hat{\tau}$ to be the composite density operator describing the physical modes and the loss modes. Then we have [cf. Eqs. (11)–(15) and (21)–(27)]

$$W_\tau(\boldsymbol{r}) = W_{\bar{\rho}}(\boldsymbol{r}_1) W_{\text{vac}}(\boldsymbol{r}_2) \tag{A48}$$

$$= \sum_m c_m G'_m(\boldsymbol{r}), \tag{A49}$$

where W_{vac} is the (Gaussian) Wigner function for vacuum in the $N+M$ loss modes, with

$$\boldsymbol{\mu}_{\text{vac}} = \bigoplus_{i=1}^{N} \mathbf{0}_{2\times 1}, \tag{A50}$$

$$\boldsymbol{\gamma}_{\text{vac}} = \bigoplus_{i=1}^{N} \tfrac{1}{2}\mathbb{1} \tag{A51}$$

its mean and covariance matrices. Then $G'_m(\boldsymbol{r})$ is a $4(M+N)$ -variable Gaussian with

$$\boldsymbol{\mu}' = \overline{\boldsymbol{\mu}} \oplus \boldsymbol{\mu}_{\text{vac}}, \tag{A52}$$

$$\boldsymbol{\gamma}' = \overline{\boldsymbol{\gamma}} \oplus \boldsymbol{\gamma}_{\text{vac}}. \tag{A53}$$

We point out that the number of terms in the Gaussian expansion does not grow with the inclusion of the loss modes, because the inputs to these are Gaussian states, namely, vacuum or thermal states.

Applying the beam splitters that are used to implement loss on the physical channels yields

$$W_{\bar{\tau}}(\boldsymbol{r}) = \sum_m c_m \overline{G}'_m(\boldsymbol{r}), \tag{A54}$$

$$\overline{\boldsymbol{\mu}}' = \boldsymbol{B}(\overline{\boldsymbol{\mu}} \oplus \boldsymbol{\mu}_{\text{vac}}), \tag{A55}$$

$$\overline{\boldsymbol{\gamma}}' = \boldsymbol{B}(\overline{\boldsymbol{\gamma}} \oplus \boldsymbol{\gamma}_{\text{vac}})\boldsymbol{B}^T. \tag{A56}$$

Here $\boldsymbol{B}$ denotes the $4(N+M)\times 4(N+M)$ symplectic matrix corresponding to the beam splitters in Fig. 13(b). A single beam splitter coupling modes i and j has the symplectic matrix [21]

$$\boldsymbol{B}_{ij} = \begin{bmatrix} \cos\theta\mathbb{1} & -\sin\theta\mathbb{1} \\ \sin\theta\mathbb{1} & \cos\theta\mathbb{1} \end{bmatrix}, \tag{A57}$$

with our usual ordering for the quadrature variables $\boldsymbol{r} = (x_i, p_i, x_j, p_j)^T$. Then the symplectic matrix for our scenario with $N+M$ beam splitters, in which each beam splitter couples a physical mode i to a loss mode $i+N+M$, is

$$\boldsymbol{B} = \begin{bmatrix} \boldsymbol{T} & -\boldsymbol{R} \\ \boldsymbol{R} & \boldsymbol{T} \end{bmatrix}, \tag{A58}$$

with $\boldsymbol{T}$ and $\boldsymbol{R}$ defined in Eqs. (A43) and (A44).

Tracing over the loss modes in $\hat{\bar{\tau}}$ yields the state $\hat{\bar{\rho}}$ of the lossy physical modes; we have

$$W_{\bar{\rho}}(\boldsymbol{r}_1) = \int d\boldsymbol{r}_2 W_{\bar{\tau}}(\boldsymbol{r}), \tag{A59}$$

where $\boldsymbol{r}_{1\,(2)}$ denotes the set of $2(N+M)$ quadrature variables associated with the physical (loss) modes. Integrating over $\boldsymbol{r}_2$ just amounts to a Gaussian marginalization [52]

$$\int d\boldsymbol{r}_2 \overline{G}'_m(\boldsymbol{r}) = \tilde{G}_m(\boldsymbol{r}), \tag{A60}$$

$$\tilde{\boldsymbol{\mu}} = \boldsymbol{P}\overline{\boldsymbol{\mu}}', \tag{A61}$$

$$\tilde{\boldsymbol{\gamma}} = \boldsymbol{P}\overline{\boldsymbol{\gamma}}'\boldsymbol{P}^T, \tag{A62}$$

where

$$\boldsymbol{P} = \begin{bmatrix} \mathbb{1}_{2(N+M)\times 2(N+M)} & \mathbf{0}_{2(N+M)\times 2(N+M)} \end{bmatrix} \tag{A63}$$

is a projection matrix that selects the components of $\overline{\boldsymbol{\mu}}'$ and $\overline{\boldsymbol{\gamma}}'$ associated with $\boldsymbol{r}_1$.

Using Eq. (A58), where the blocks $\boldsymbol{T}$ and $\boldsymbol{R}$ are $2(N+M)\times 2(N+M)$ matrices, we have

$$\boldsymbol{P}\boldsymbol{B} = [\boldsymbol{T} \quad -\boldsymbol{R}]. \tag{A64}$$

Then using Eqs. (A55), (A56), and (A64) in Eqs. (A61) and (A62), we have

$$\tilde{\boldsymbol{\mu}} = \boldsymbol{T}\overline{\boldsymbol{\mu}} - \boldsymbol{R}\boldsymbol{\mu}_{\text{vac}}, \tag{A65}$$

$$\tilde{\boldsymbol{\gamma}} = \boldsymbol{T}\overline{\boldsymbol{\gamma}}\boldsymbol{T}^T + \boldsymbol{R}\boldsymbol{\gamma}_{\text{vac}}\boldsymbol{R}^T. \tag{A66}$$

Using the definitions of $\boldsymbol{\mu}_{\text{vac}}$ and $\boldsymbol{\gamma}_{\text{vac}}$, we have

$$\tilde{\boldsymbol{\mu}} = \boldsymbol{T}\overline{\boldsymbol{\mu}}, \tag{A67}$$

$$\tilde{\boldsymbol{\gamma}} = \boldsymbol{T}\overline{\boldsymbol{\gamma}}\boldsymbol{T}^T + \tfrac{1}{2}\boldsymbol{R}\boldsymbol{R}^T. \tag{A68}$$

This now specifies the Wigner function of $\hat{\tilde{\rho}}$ including the effects of loss, and one can describe the effects of homodyne measurement and compute its stabilizers as described in Secs. II D and III. Coupling to thermal loss modes can be dealt with in the same way, by substituting

$$\boldsymbol{\mu}_{\text{therm}} = \bigoplus_{i=1}^{N} \mathbf{0}_{2\times 1}, \tag{A69}$$

$$\boldsymbol{\gamma}_{\text{therm}} = \bigoplus_{i=1}^{N} \left(\frac{1}{2} + \overline{n}_i\right)\mathbb{1}, \tag{A70}$$

where $\boldsymbol{\mu}_{\text{vac}}$ and $\boldsymbol{\gamma}_{\text{vac}}$ appear above.

APPENDIX B: GAUSSIAN EXPANSION OF GKP STATES PREPARED BY CAT STATE BREEDING

In this work we focus on GKP states generated by breeding squeezed cat states; here we lay out the derivation of the Gaussian expansion of the bred state. Our analysis is similar to those presented in Refs. [27,29], but we take a displaced initial state compared to theirs (to obtain bred states centered at the origin). We include a derivation here for clarity. We begin with ideal squeezed cat states of the form

$$[\hat{D}(-\alpha/2) + \hat{D}(\alpha/2)]\hat{S}(\xi)|\text{vac}\rangle, \tag{B1}$$

where

$$\hat{D}(\alpha) = \exp(\alpha\hat{a}^\dagger - \alpha^*\hat{a}) \tag{B2}$$

$$= \exp[\sqrt{2}i\,\mathrm{Im}(\alpha)\hat{q} - \sqrt{2}i\,\mathrm{Re}(\alpha)\hat{p}], \tag{B3}$$

and we take $\mathrm{Im}(\alpha) = 0$ for simplicity.

The input state to the breeding protocol is

$$|\psi\rangle = [\hat{D}_1(-\alpha/2) + \hat{D}_1(\alpha/2)][\hat{D}_2(-\alpha/2) + \hat{D}_2(\alpha/2)]\hat{S}_1(\xi)\hat{S}_2(\xi)|\mathrm{vac}\rangle, \tag{B4}$$

and the state following the first 50:50 beam splitter is

$$\hat{\mathcal{B}}|\psi\rangle = \hat{\mathcal{B}}[\hat{D}_1(-\alpha/2) + \hat{D}_1(\alpha/2)][\hat{D}_2(-\alpha/2) + \hat{D}_2(\alpha/2)]\hat{\mathcal{B}}^\dagger\hat{\mathcal{B}}\hat{S}_1(\xi)\hat{S}_2(\xi)\hat{\mathcal{B}}^\dagger|\mathrm{vac}\rangle, \tag{B5}$$

where

$$\hat{\mathcal{B}} = \exp\Big(-i\frac{\pi}{4}(\hat{q}_1\hat{p}_2 - \hat{p}_2\hat{q}_1)\Big) \tag{B6}$$

$$= \exp\Big(\frac{\pi}{4}(\hat{a}_1\hat{a}_2^\dagger - \hat{a}_2\hat{a}_1^\dagger)\Big) \tag{B7}$$

and we have used the fact that $\hat{\mathcal{B}}|\mathrm{vac}\rangle = |\mathrm{vac}\rangle$. Recalling that

$$\hat{S}_1(\xi)\hat{S}_2(\xi) = \exp\big[\tfrac{1}{2}\big(\xi^*\hat{a}_1^2 - \xi\hat{a}_1^{\dagger 2}\big)\big]\exp\big[\tfrac{1}{2}\big(\xi^*\hat{a}_2^2 - \xi\hat{a}_2^{\dagger 2}\big)\big] \tag{B8}$$

$$= \exp\big\{\tfrac{1}{2}\big[\xi^*\big(\hat{a}_1^2 + \hat{a}_2^2\big) - \xi\big(\hat{a}_1^{\dagger 2} + \hat{a}_2^{\dagger 2}\big)\big]\big\} \tag{B9}$$

and

$$\hat{\mathcal{B}}\hat{a}_1\hat{\mathcal{B}}^\dagger = \frac{\hat{a}_1 + \hat{a}_2}{\sqrt{2}}, \tag{B10}$$

$$\hat{\mathcal{B}}\hat{a}_2\hat{\mathcal{B}}^\dagger = \frac{\hat{a}_2 - \hat{a}_1}{\sqrt{2}}, \tag{B11}$$

we see that

$$\hat{\mathcal{B}}\hat{S}_1(\xi)\hat{S}_2(\xi)\hat{\mathcal{B}}^\dagger = \hat{S}_1(\xi)\hat{S}_2(\xi). \tag{B12}$$

Similarly, we have

$$\hat{\mathcal{B}}\hat{D}_1\Big(\pm\frac{\alpha}{2}\Big)\hat{\mathcal{B}}^\dagger = \hat{D}_1\Big(\pm\frac{\alpha}{2\sqrt{2}}\Big)\hat{D}_2\Big(\pm\frac{\alpha}{2\sqrt{2}}\Big), \tag{B13}$$

$$\hat{\mathcal{B}}\hat{D}_2\Big(\pm\frac{\alpha}{2}\Big)\hat{\mathcal{B}}^\dagger = \hat{D}_1\Big(\mp\frac{\alpha}{2\sqrt{2}}\Big)\hat{D}_2\Big(\pm\frac{\alpha}{2\sqrt{2}}\Big). \tag{B14}$$

After the beam splitter, the protocol involves measuring the p quadrature in mode 2 (see Fig. 4 and recall Sec. II D). Recalling that

$$f(\hat{p})|\tilde{p}\rangle = f(\tilde{p})|\tilde{p}\rangle \tag{B15}$$

and taking the homodyne outcome to be $\tilde{p} = 0$, we have (see Ref. [27] for a similar analysis)

$$|\psi\rangle_1 = \mathcal{N}\left[\hat{D}_1\left(\frac{\alpha}{2\sqrt{2}}\right) + \hat{D}_1\left(-\frac{\alpha}{2\sqrt{2}}\right)\right]^2\hat{S}(\xi)|\mathrm{vac}\rangle, \tag{B16}$$

where $|\psi\rangle_1$ represents the postselected state after one iteration of breeding and $\mathcal{N}$ denotes a normalization factor. The second round of breeding involves adding a second squeezed cat state input

$$|\psi''\rangle = \left[\hat{D}_2\left(\frac{\alpha}{2\sqrt{2}}\right) + \hat{D}_2\left(-\frac{\alpha}{2\sqrt{2}}\right)\right]\hat{S}_2(\xi)|\mathrm{vac}\rangle. \tag{B17}$$

Interfering this with $|\psi\rangle_1$ at a 50:50 beam splitter and again doing homodyne postselection on one output mode, this second iteration of breeding yields

$$|\psi\rangle_2 = \mathcal{N}\left[\hat{D}_1\left(\frac{\alpha}{2\sqrt{2^2}}\right) + \hat{D}_1\left(-\frac{\alpha}{2\sqrt{2^2}}\right)\right]^3\hat{S}(\xi)|\mathrm{vac}\rangle. \tag{B18}$$

After $\mathcal{M}$ iterations of breeding, one obtains

$$|\psi\rangle_{\mathcal{M}} = \mathcal{N}\left[\hat{D}_1\left(\frac{\alpha}{2\sqrt{2}^{\mathcal{M}}}\right) + \hat{D}_1\left(-\frac{\alpha}{2\sqrt{2}^{\mathcal{M}}}\right)\right]^{\mathcal{M}+1} \hat{S}(\xi)|\text{vac}\rangle \tag{B19}$$

$$= \mathcal{N}\sum_{k=0}^{\mathcal{M}+1}\binom{\mathcal{M}+1}{k}\hat{D}_1\left(\frac{\alpha}{2\sqrt{2}^{\mathcal{M}}}\right)^{k}\hat{D}_1\left(-\frac{\alpha}{2\sqrt{2}^{\mathcal{M}}}\right)^{\mathcal{M}+1-k}\hat{S}_1(\xi)|\text{vac}\rangle \tag{B20}$$

$$= \mathcal{N}\sum_{k=0}^{\mathcal{M}+1}\binom{\mathcal{M}+1}{k}\hat{D}_1\left(\frac{k\alpha}{2\sqrt{2}^{\mathcal{M}}}\right)\hat{D}_1\left(-\frac{\alpha(\mathcal{M}+1-k)}{2\sqrt{2}^{\mathcal{M}}}\right)\hat{S}_1(\xi)|\text{vac}\rangle \tag{B21}$$

$$= \mathcal{N}\sum_{k=0}^{\mathcal{M}+1}\binom{\mathcal{M}+1}{k}\hat{D}_1\left(\frac{\alpha(2k-(\mathcal{M}+1))}{2\sqrt{2}^{\mathcal{M}}}\right)\hat{S}_1(\xi)|\text{vac}\rangle. \tag{B22}$$

We write

$$\hat{\rho}_{\mathcal{M}} = |\psi\rangle\langle\psi|_{\mathcal{M}} = |\mathcal{N}|^2\sum_{k=0}^{\mathcal{M}+1}\sum_{k'=0}^{\mathcal{M}+1}\binom{\mathcal{M}+1}{k}\binom{\mathcal{M}+1}{k'}\hat{\mathcal{O}}_{k,k'}, \tag{B23}$$

$$\hat{\mathcal{O}}_{k,k'} = \hat{D}(\beta_k)\hat{S}(\xi)|\text{vac}\rangle\langle\text{vac}|\hat{S}^{\dagger}(\xi)\hat{D}^{\dagger}(\beta_{k'}), \tag{B24}$$

with

$$\beta_k = \frac{\alpha[2k-(\mathcal{M}+1)]}{2\sqrt{2}^{\mathcal{M}}}, \tag{B25}$$

and the Wigner function for Eq. (B23) is

$$W_{\rho}(\boldsymbol{r}) = |\mathcal{N}|^2\sum_{k=0}^{\mathcal{M}+1}\sum_{k'=0}^{\mathcal{M}+1}\binom{\mathcal{M}+1}{k}\binom{\mathcal{M}+1}{k'}W_{k,k'}(\boldsymbol{r}), \tag{B26}$$

where $W_{k,k'}$ is the Wigner representation of $\mathcal{O}_{k,k'}$. It can be shown that [27,29]

$$W_{k,k'}(\boldsymbol{r}) = \mathcal{A}_{k,k'}G_{k,k'}(\boldsymbol{r}), \tag{B27}$$

with $G_{k,k'}(\boldsymbol{r})$ defined as in Eq. (10) and

$$\mathcal{A}_{k,k'} = \exp\left[-\tfrac{1}{2}e^{2\xi}(\beta_k-\beta_{k'})^2\right], \tag{B28}$$

$$\boldsymbol{\gamma}_{k,k'} = \frac{1}{2}\begin{bmatrix} e^{-2\xi} & 0 \\ 0 & e^{2\xi}\end{bmatrix} \equiv \boldsymbol{\gamma}, \tag{B29}$$

$$\boldsymbol{\mu}_{k,k'} = \sqrt{\frac{1}{2}}\begin{bmatrix}\beta_k+\beta_{k'} \\ ie^{2\xi}(\beta_{k'}-\beta_k)\end{bmatrix}. \tag{B30}$$

APPENDIX C: DETAILS OF THE DERIVATION OF THE STABILIZER EXPECTATION VALUE

1. Integrals

We first address the numerator in Eq. (42). We have

$$\mathcal{I} = \int d\boldsymbol{r}\, W_{\rho}(\boldsymbol{r})W_{F_i}(\boldsymbol{r})W_{\mathcal{O}}(\boldsymbol{r}) \tag{C1}$$

$$= \sum_{\boldsymbol{m}} c_{\boldsymbol{m}}\int d\boldsymbol{r}\, G_{\boldsymbol{m}}(\boldsymbol{r})W_{F_i}(\boldsymbol{r})W_{\mathcal{O}}(\boldsymbol{r}). \tag{C2}$$

Recognize that $\boldsymbol{r}$ refers to the quadrature variables for all the N modes. We denote by $\boldsymbol{r}_C$ the $2(N-M)$ quadrature variables for the unmeasured modes. The quadrature variables that are measured are denoted by $\boldsymbol{r}_H$ (there are M of these), and the conjugate variables to these are $\boldsymbol{r}_H^{\perp}$ (again M of these). We now write

$$\mathcal{I} = \sum_{\boldsymbol{m}} c_{\boldsymbol{m}}\int d\boldsymbol{r}_C d\boldsymbol{r}_H d\boldsymbol{r}_H^{\perp} G_{\boldsymbol{m}}(\boldsymbol{r}_C,\boldsymbol{r}_H,\boldsymbol{r}_H^{\perp})W_F(\boldsymbol{r}_H)W_{\mathcal{O}}(\boldsymbol{r}_C). \tag{C3}$$

We do the integral over $\boldsymbol{r}_H^{\perp}$ by using the fact that [52]

$$\int d\boldsymbol{r}_2 G(\boldsymbol{r}_1, \boldsymbol{r}_2) = \tilde{G}(\boldsymbol{r}_1), \tag{C4}$$

where $\tilde{G}(r_1)$ is a normalized Gaussian defined by the mean vector and covariance matrix

$$\tilde{\boldsymbol{\mu}} = \boldsymbol{P}\boldsymbol{\mu}, \tag{C5}$$

$$\tilde{\boldsymbol{\gamma}} = \boldsymbol{P}\boldsymbol{\gamma}\boldsymbol{P}^T. \tag{C6}$$

By $\boldsymbol{P}$ we denote a rectangular matrix that selects the components of $\boldsymbol{\gamma}$ and $\boldsymbol{\mu}$ that are associated with a subset of quadrature variables that we associate with $\boldsymbol{r}_1$; effectively, $\tilde{\boldsymbol{\mu}}$ and $\tilde{\boldsymbol{\gamma}}$ are obtained by dropping all the elements of $\boldsymbol{\mu}$ and $\boldsymbol{\gamma}$ associated with $\boldsymbol{r}_2$. We have

$$\mathcal{I} = \sum_{\boldsymbol{m}} c_{\boldsymbol{m}} \int d\boldsymbol{r}_C d\boldsymbol{r}_H \tilde{G}_{\boldsymbol{m}}(\boldsymbol{r}_C, \boldsymbol{r}_H) W_F(\boldsymbol{r}_H) W_{\mathcal{O}}(\boldsymbol{r}_C), \tag{C7}$$

with $\tilde{\boldsymbol{\mu}}_m$ and $\tilde{\boldsymbol{\gamma}}_m$ defined as above. Next we use the δ functions in $W_F(\boldsymbol{r}_H)$ to get

$$\mathcal{I} = \frac{1}{(2\pi)^M} \sum_{\boldsymbol{m}} c_{\boldsymbol{m}} \int d\boldsymbol{r}_C \tilde{G}_{\boldsymbol{m}}(\boldsymbol{r}_C, \tilde{\boldsymbol{R}}_H) W_{\mathcal{O}}(\boldsymbol{r}_C), \tag{C8}$$

where $\tilde{\boldsymbol{R}}_H$ denotes the set of postselected homodyne outcomes.

We now use the Schur decomposition to write

$$\int d\boldsymbol{r}_C G(\boldsymbol{r}_C, \tilde{\boldsymbol{R}}_H) W_{\mathcal{O}}(\boldsymbol{r}_C) = \frac{1}{\sqrt{\det(2\pi\boldsymbol{\gamma})}} \exp\left[-\frac{1}{2}(\tilde{\boldsymbol{R}}_H - \boldsymbol{\mu}_H)^T \boldsymbol{\gamma}_{HH}^{-1} (\tilde{\boldsymbol{R}}_H - \boldsymbol{\mu}_H)\right] \tag{C9}$$

$$\begin{aligned}
&\int d\boldsymbol{r}_C \exp\left[-\frac{1}{2}\left(\boldsymbol{r}_C - \boldsymbol{\mu}_C - \boldsymbol{\gamma}_{CH}\boldsymbol{\gamma}_{HH}^{-1}(\tilde{\boldsymbol{R}}_H - \boldsymbol{\mu}_H)\right)\right]^T \boldsymbol{C}^{-1}\left[\boldsymbol{r}_C - \boldsymbol{\mu}_C - \boldsymbol{\gamma}_{CH}\boldsymbol{\gamma}_{HH}^{-1}(\tilde{\boldsymbol{R}}_H - \boldsymbol{\mu}_H)\right] W_{\mathcal{O}}(\boldsymbol{r}_C) \\
&= \frac{1}{\sqrt{\det(2\pi\boldsymbol{\gamma})}} \exp\left[-\frac{1}{2}(\tilde{\boldsymbol{R}}_H - \boldsymbol{\mu}_H)^T \boldsymbol{\gamma}_{HH}^{-1}(\tilde{\boldsymbol{R}}_H - \boldsymbol{\mu}_H)\right] \int d\boldsymbol{r}_C \exp\left[-\frac{1}{2}(\boldsymbol{r}_C - \boldsymbol{\xi})^T \boldsymbol{C}^{-1}(\boldsymbol{r}_C - \boldsymbol{\xi})\right] W_{\mathcal{O}}(\boldsymbol{r}_C),
\end{aligned} \tag{C10}$$

where

$$\boldsymbol{C} = \boldsymbol{\gamma}_{CC} - \boldsymbol{\gamma}_{CH}\boldsymbol{\gamma}_{HH}^{-1}\boldsymbol{\gamma}_{HC}, \tag{C11}$$

where $\boldsymbol{C}$ is the Schur complement of the lower right block of $\boldsymbol{\gamma}$ [52] and we have introduced

$$\boldsymbol{\xi} = \boldsymbol{\mu}_C + \boldsymbol{\gamma}_{CH}\boldsymbol{\gamma}_{HH}^{-1}(\tilde{\boldsymbol{R}}_H - \boldsymbol{\mu}_H). \tag{C12}$$

When $\hat{\mathcal{O}}$ is a displacement operator we have

$$W_{\mathcal{O}}(\boldsymbol{r}_C) = \frac{1}{(2\pi)^{(N-M)}} \exp(i\boldsymbol{J}^T \boldsymbol{r}_C). \tag{C13}$$

Now

$$\begin{aligned}
\int d\boldsymbol{r}_C G(\boldsymbol{r}_C, \tilde{\boldsymbol{R}}_H) W_{\mathcal{O}}(\boldsymbol{r}_C) = &\frac{1}{(2\pi)^{(N-M)}} \frac{1}{\sqrt{\det(2\pi\boldsymbol{\gamma})}} \exp\left[-\frac{1}{2}(\tilde{\boldsymbol{R}}_H - \boldsymbol{\mu}_H)^T \boldsymbol{\gamma}_{HH}^{-1}(\tilde{\boldsymbol{R}}_H - \boldsymbol{\mu}_H)\right] \\
&\times \int d\boldsymbol{r}_C \exp\left[-\frac{1}{2}(\boldsymbol{r}_C - \boldsymbol{\xi})^T \boldsymbol{C}^{-1}(\boldsymbol{r}_C - \boldsymbol{\xi})\right] \exp(i\boldsymbol{J}^T \boldsymbol{r}_C).
\end{aligned} \tag{C14}$$

We define $\boldsymbol{r}' = \boldsymbol{r}_C - \boldsymbol{\xi}$, so

$$\begin{aligned}
\int d\boldsymbol{r}_C G(\boldsymbol{r}_C, \tilde{\boldsymbol{R}}_H) W_{\mathcal{O}}(\boldsymbol{r}_C) = &\frac{1}{(2\pi)^{(N-M)}} \frac{1}{\sqrt{\det(2\pi\boldsymbol{\gamma})}} \exp\left[-\frac{1}{2}(\tilde{\boldsymbol{R}}_H - \boldsymbol{\mu}_H)^T \boldsymbol{\gamma}_{HH}^{-1}(\tilde{\boldsymbol{R}}_H - \boldsymbol{\mu}_H)\right] \\
&\times \exp(i\boldsymbol{J}^T \boldsymbol{\xi}) \int d\boldsymbol{r}' \exp\left[-\frac{1}{2}\boldsymbol{r}'^T \boldsymbol{C}^{-1} \boldsymbol{r}'\right] \exp(i\boldsymbol{J}^T \boldsymbol{r}').
\end{aligned} \tag{C15}$$

Using

$$\int d\boldsymbol{r} \exp\left(-\frac{1}{2}\boldsymbol{r}^T \boldsymbol{\gamma}^{-1} \boldsymbol{r}\right) \exp(i\boldsymbol{J}^T \boldsymbol{r}) = \sqrt{\det(2\pi\boldsymbol{\gamma})} \exp\left(-\frac{1}{2}\boldsymbol{J}^T \boldsymbol{\gamma} \boldsymbol{J}\right) \tag{C16}$$

and

$$\frac{\det(2\pi \boldsymbol{C})}{\det(2\pi \boldsymbol{\gamma})} = \frac{1}{\det(2\pi \boldsymbol{\gamma}_{HH})}, \tag{C17}$$

we have

$$\int d\boldsymbol{r}_C \tilde{G}(\boldsymbol{r}_C, \tilde{\boldsymbol{R}}_H) W_{\mathcal{O}}(\boldsymbol{r}_C) = \frac{1}{(2\pi)^{(N-M)}} \frac{1}{\sqrt{\det(2\pi \tilde{\boldsymbol{\gamma}}_{HH})}} \exp\left[-\frac{1}{2}(\tilde{\boldsymbol{R}}_H - \tilde{\boldsymbol{\mu}}_H)^T \tilde{\boldsymbol{\gamma}}_{HH}^{-1} (\tilde{\boldsymbol{R}}_H - \tilde{\boldsymbol{\mu}}_H)\right]$$
$$\times \exp(i\boldsymbol{J}^T \boldsymbol{\xi}) \exp\left(-\frac{1}{2}\boldsymbol{J}^T \boldsymbol{C} \boldsymbol{J}\right), \tag{C18}$$

where we have restored the tildes from Eq. (C8).

We now introduce the $\boldsymbol{P}_H$ and $\boldsymbol{P}_C$ such that

$$\tilde{\boldsymbol{\mu}}_H = \boldsymbol{P}_H \tilde{\boldsymbol{\mu}} = \boldsymbol{P}_H \boldsymbol{P} \boldsymbol{\mu}, \tag{C19}$$

$$\tilde{\boldsymbol{\gamma}}_{HH} = \boldsymbol{P}_H \tilde{\boldsymbol{\gamma}} \boldsymbol{P}_H^T, \tag{C20}$$

$$\tilde{\boldsymbol{\gamma}}_{CH} = \boldsymbol{P}_C \tilde{\boldsymbol{\gamma}} \boldsymbol{P}_H^T, \tag{C21}$$

and likewise for $\tilde{\boldsymbol{\mu}}_C$ and $\tilde{\boldsymbol{\gamma}}_C$. Similar to $\boldsymbol{P}$ defined in Eq. (C6), $\boldsymbol{P}_H$ picks out the matrix components associated with modes that are measured; $\boldsymbol{P}_C$ picks out matrix components associated with unmeasured modes comprising the cluster state. We have

$$\mathcal{I} = \frac{1}{(2\pi)^N} \sum_{\boldsymbol{m}} c_{\boldsymbol{m}} \frac{1}{\sqrt{\det(2\pi \boldsymbol{P}_H \tilde{\boldsymbol{\gamma}}_{\boldsymbol{m}} \boldsymbol{P}_H^T)}} \exp\left[-\frac{1}{2}(\tilde{\boldsymbol{R}}_H - \boldsymbol{P}_H \tilde{\boldsymbol{\mu}}_{\boldsymbol{m}})^T \left(\boldsymbol{P}_H \tilde{\boldsymbol{\gamma}}_{\boldsymbol{m}} \boldsymbol{P}_H^T\right)^{-1} (\tilde{\boldsymbol{R}}_H - \boldsymbol{P}_H \tilde{\boldsymbol{\mu}}_{\boldsymbol{m}})\right]$$
$$\times \exp(i\boldsymbol{J}^T \boldsymbol{\xi}_{\boldsymbol{m}}) \exp\left(-\frac{1}{2}\boldsymbol{J}^T \boldsymbol{C}_{\boldsymbol{m}} \boldsymbol{J}\right). \tag{C22}$$

The denominator can be obtained by setting $\boldsymbol{J} = \boldsymbol{0}$ in Eq. (C22). This can be seen by recognizing that the identity operator is equivalent to the displacement operator at zero displacement.

2. Cosmesis

We now have

$$\langle \hat{\mathcal{S}} \rangle = \frac{\sum_{\boldsymbol{m}} c_{\boldsymbol{m}} g_{\boldsymbol{m}}(\tilde{\boldsymbol{R}}_H) \exp\left(i\boldsymbol{J}^T \boldsymbol{\xi}_{\boldsymbol{m}} - \frac{1}{2}\boldsymbol{J}^T \boldsymbol{C}_{\boldsymbol{m}} \boldsymbol{J}\right)}{\sum_{\boldsymbol{m}} c_{\boldsymbol{m}} g_{\boldsymbol{m}}(\tilde{\boldsymbol{R}}_H)}, \tag{C23}$$

where

$$g_{\boldsymbol{m}}(\tilde{\boldsymbol{R}}_H) = \frac{1}{\sqrt{\det(2\pi \boldsymbol{\gamma}_{HH\boldsymbol{m}})}} \exp\left[-\frac{1}{2}(\tilde{\boldsymbol{R}}_H - \boldsymbol{\mu}_{H\boldsymbol{m}})^T (\boldsymbol{\gamma}_{HH\boldsymbol{m}})^{-1} (\tilde{\boldsymbol{R}}_H - \boldsymbol{\mu}_{H\boldsymbol{m}})\right], \tag{C24}$$

$$\boldsymbol{\xi} = \boldsymbol{\mu}_C + \boldsymbol{\gamma}_{CH} \boldsymbol{\gamma}_{HH}^{-1} (\tilde{\boldsymbol{R}}_H - \boldsymbol{\mu}_H), \tag{C25}$$

$$\boldsymbol{C} = \boldsymbol{\gamma}_{CC} - \boldsymbol{\gamma}_{CH} \boldsymbol{\gamma}_{HH}^{-1} \boldsymbol{\gamma}_{HC}. \tag{C26}$$

We use Eqs. (C25) and (C26) to write

$$\exp\left(i\boldsymbol{J}^T \boldsymbol{\xi}_{\boldsymbol{m}} - \tfrac{1}{2}\boldsymbol{J}^T \boldsymbol{C}_{\boldsymbol{m}} \boldsymbol{J}\right) = \exp\left(i\boldsymbol{J}^T \boldsymbol{\mu}_C - \tfrac{1}{2}\boldsymbol{J}^T \boldsymbol{\gamma}_{CC} \boldsymbol{J}\right) \exp\left[i\boldsymbol{J}^T \boldsymbol{\gamma}_{CH} \boldsymbol{\gamma}_{HH}^{-1} (\tilde{\boldsymbol{X}} - \boldsymbol{\mu}_H) + \tfrac{1}{2}\boldsymbol{J}^T \boldsymbol{\gamma}_{CH} \boldsymbol{\gamma}_{HH}^{-1} \boldsymbol{\gamma}_{HC} \boldsymbol{J}\right]. \tag{C27}$$

Using [52]

$$-\tfrac{1}{2}\boldsymbol{x}^T \boldsymbol{M} \boldsymbol{x} + (\boldsymbol{x}^T \boldsymbol{b})^T = -\tfrac{1}{2}(\boldsymbol{x} - \boldsymbol{M}^{-1}\boldsymbol{b})^T \boldsymbol{M} (\boldsymbol{x} - \boldsymbol{M}^{-1}\boldsymbol{b}) + \tfrac{1}{2}\boldsymbol{b}^T \boldsymbol{M}^{-1} \boldsymbol{b}, \tag{C28}$$

with $\boldsymbol{x} = i\boldsymbol{\gamma}_{HC}\boldsymbol{J}$, $\boldsymbol{b} = \boldsymbol{\gamma}_{HH}^{-1}(\tilde{\boldsymbol{R}}_H - \boldsymbol{\mu}_H)$, and $\boldsymbol{M} = \boldsymbol{\gamma}_{HH}^{-1}$, we write

$$i\boldsymbol{J}^T \boldsymbol{\gamma}_{CH} \boldsymbol{\gamma}_{HH}^{-1} (\tilde{\boldsymbol{R}}_H - \boldsymbol{\mu}_H) + \tfrac{1}{2}\boldsymbol{J}^T \boldsymbol{\gamma}_{CH} \boldsymbol{\gamma}_{HH}^{-1} \boldsymbol{\gamma}_{HC} \boldsymbol{J}$$
$$= -\tfrac{1}{2}\left[i\boldsymbol{\gamma}_{HC}\boldsymbol{J} - \boldsymbol{\gamma}_{HH}\boldsymbol{\gamma}_{HH}^{-1}(\tilde{\boldsymbol{R}}_H - \boldsymbol{\mu}_H)\right]^T \boldsymbol{\gamma}_{HH}^{-1}\left[i\boldsymbol{\gamma}_{HC}\boldsymbol{J} - \boldsymbol{\gamma}_{HH}\boldsymbol{\gamma}_{HH}^{-1}(\tilde{\boldsymbol{R}}_H - \boldsymbol{\mu}_H)\right] + \tfrac{1}{2}(\tilde{\boldsymbol{R}}_H - \boldsymbol{\mu}_H)^T \left(\boldsymbol{\gamma}_{HH}^{-1}\right)^T \boldsymbol{\gamma}_{HH} \boldsymbol{\gamma}_{HH}^{-1} (\tilde{\boldsymbol{R}}_H - \boldsymbol{\mu}_H) \tag{C29}$$

$$= -\tfrac{1}{2}[i\boldsymbol{\gamma}_{HC}\boldsymbol{J} - (\tilde{\boldsymbol{R}}_H - \boldsymbol{\mu}_H)]^T \boldsymbol{\gamma}_{HH}^{-1}[i\boldsymbol{\gamma}_{HC}\boldsymbol{J} - (\tilde{\boldsymbol{R}}_H - \boldsymbol{\mu}_H)] + \tfrac{1}{2}(\tilde{\boldsymbol{R}}_H - \boldsymbol{\mu}_H)^T \left(\boldsymbol{\gamma}_{HH}^{-1}\right)(\tilde{\boldsymbol{R}}_H - \boldsymbol{\mu}_H), \tag{C30}$$

so

$$\exp\big(i\boldsymbol{J}^T\boldsymbol{\xi}_{\boldsymbol{m}} - \tfrac{1}{2}\boldsymbol{J}^T\boldsymbol{C}_{\boldsymbol{m}}\boldsymbol{J}\big) = \exp\big[-\tfrac{1}{2}(\tilde{\boldsymbol{R}}_H - \boldsymbol{\mu}_H - i\boldsymbol{\gamma}_{HC}\boldsymbol{J})^T\boldsymbol{\gamma}_{HH}^{-1}(\tilde{\boldsymbol{R}}_H - \boldsymbol{\mu}_H - i\boldsymbol{\gamma}_{HC}\boldsymbol{J})\big] \times \exp\big(i\boldsymbol{J}^T\boldsymbol{\mu}_C - \tfrac{1}{2}\boldsymbol{J}^T\boldsymbol{\gamma}_{CC}\boldsymbol{J}\big)\exp\big[\tfrac{1}{2}(\tilde{\boldsymbol{R}}_H - \boldsymbol{\mu}_H)^T\big(\boldsymbol{\gamma}_{HH}^{-1}\big)(\tilde{\boldsymbol{R}}_H - \boldsymbol{\mu}_H)\big]. \tag{C31}$$

Putting this into Eq. (C23), it is clear that the final term in Eq. (C32) cancels the exponential term in $g_{\boldsymbol{m}}(\tilde{\boldsymbol{R}}_H)$. Now adopting the notation in the main text ($\tilde{\boldsymbol{\eta}} \equiv \tilde{\boldsymbol{R}}_H$), the result is

$$\langle\hat{\mathcal{S}}\rangle = \frac{\sum_{\boldsymbol{m}} c_{\boldsymbol{m}} g_{\boldsymbol{m}}(\tilde{\boldsymbol{\eta}};\boldsymbol{J})\exp\big(i\boldsymbol{J}^T\boldsymbol{\mu}_C - \frac{1}{2}\boldsymbol{J}^T\boldsymbol{\gamma}_{CC}\boldsymbol{J}\big)}{\sum_{\boldsymbol{m}} c_{\boldsymbol{m}} g_{\boldsymbol{m}}(\tilde{\boldsymbol{\eta}},\boldsymbol{0})} \tag{C32}$$

$$= \frac{\sum_{\boldsymbol{m}} c_{\boldsymbol{m}} g_{\boldsymbol{m}}(\tilde{\boldsymbol{\eta}};\boldsymbol{J})\exp\big(i\boldsymbol{J}^T\boldsymbol{P}_C\boldsymbol{A}\boldsymbol{\mu}_{\boldsymbol{m}} - \frac{1}{2}\boldsymbol{J}^T\boldsymbol{P}_C\boldsymbol{A}\boldsymbol{\gamma}_{\boldsymbol{m}}\boldsymbol{A}^T\boldsymbol{P}_C^T\boldsymbol{J}\big)}{\sum_{\boldsymbol{m}} c_{\boldsymbol{m}} g_{\boldsymbol{m}}(\tilde{\boldsymbol{\eta}},\boldsymbol{0})}, \tag{C33}$$

where

$$g_{\boldsymbol{m}}(\tilde{\boldsymbol{\eta}};\boldsymbol{J}) = \frac{1}{\sqrt{\det(2\pi\boldsymbol{\gamma}_{HH})}}\exp\left[-\frac{1}{2}(\tilde{\boldsymbol{\eta}} - \boldsymbol{\mu}_H - i\boldsymbol{\gamma}_{HC}\boldsymbol{J})^T\boldsymbol{\gamma}_{HH}^{-1}(\tilde{\boldsymbol{\eta}} - \boldsymbol{\mu}_H - i\boldsymbol{\gamma}_{HC}\boldsymbol{J})\right] \tag{C34}$$

and

$$\boldsymbol{\mu}_I = \boldsymbol{P}_I\boldsymbol{A}\boldsymbol{\mu}_{\boldsymbol{m}}, \tag{C35}$$

$$\boldsymbol{\gamma}_{IJ} = \boldsymbol{P}_I\boldsymbol{A}\boldsymbol{\gamma}_{\boldsymbol{m}}\boldsymbol{A}^T\boldsymbol{P}_J^T, \quad I,J = \{H,C\}. \tag{C36}$$

Using the results of Appendix A 4, the corresponding expressions including loss are

$$\langle\hat{\mathcal{S}}\rangle = \frac{\sum_{\boldsymbol{m}} c_{\boldsymbol{m}} g_{\boldsymbol{m}}(\tilde{\boldsymbol{\eta}};\boldsymbol{J})\exp\big(i\boldsymbol{J}^T\boldsymbol{P}_C\boldsymbol{T}\boldsymbol{A}\boldsymbol{\mu}_{\boldsymbol{m}} - \frac{1}{2}\boldsymbol{J}^T\boldsymbol{P}_C\boldsymbol{T}\boldsymbol{A}\boldsymbol{\gamma}_{\boldsymbol{m}}\boldsymbol{A}^T\boldsymbol{T}^T\boldsymbol{P}_C^T\boldsymbol{J} - \frac{1}{4}\boldsymbol{J}^T\boldsymbol{P}_C\boldsymbol{R}\boldsymbol{R}^T\boldsymbol{P}_C^T\boldsymbol{J}\big)}{\sum_{\boldsymbol{m}} c_{\boldsymbol{m}} g_{\boldsymbol{m}}(\tilde{\boldsymbol{\eta}},\boldsymbol{0})}, \tag{C37}$$

where $g_{\boldsymbol{m}}(\tilde{\boldsymbol{\eta}};\boldsymbol{J})$ is defined as in Eq. (C35), now with

$$\boldsymbol{\mu}_I = \boldsymbol{P}_I\boldsymbol{T}\boldsymbol{A}\boldsymbol{\mu}_{\boldsymbol{m}}, \tag{C38}$$

$$\boldsymbol{\gamma}_{IJ} = \boldsymbol{P}_I\boldsymbol{T}\boldsymbol{A}\boldsymbol{\gamma}_{\boldsymbol{m}}\boldsymbol{A}^T\boldsymbol{T}^T\boldsymbol{P}_J^T + \tfrac{1}{2}\boldsymbol{P}_I\boldsymbol{R}\boldsymbol{R}^T\boldsymbol{P}_J^T, \quad I,J = \{H,C\}. \tag{C39}$$

APPENDIX D: STABILIZER EXPECTATION VALUES OF GAUSSIAN RANDOM NOISE STATES

A Gaussian random noise state $\hat{\tilde{\rho}}$ is a mixed state resulting from the Gaussian random displacement of a pure state $\hat{\rho} = |\psi\rangle\langle\psi|$,

$$\hat{\tilde{\rho}} = \int_{\mathbb{C}} \mathrm{d}^2\alpha\, G_{\boldsymbol{\Sigma}}(\alpha)\hat{D}(\alpha)|\psi\rangle\langle\psi|\hat{D}^\dagger(\alpha), \tag{D1}$$

where $G_{\boldsymbol{\Sigma}}(\alpha)$ is a standard complex normal distribution [53] such that

$$G_{\boldsymbol{\Sigma}(\alpha)} = \frac{\exp\left(-\frac{\mathrm{Re}(\alpha)^2}{\Sigma_0}\right)\exp\left(-\frac{\mathrm{Im}(\alpha)^2}{\Sigma_1}\right)}{\pi\sqrt{\Sigma_0\Sigma_1}}, \tag{D2}$$

with

$$\hat{D}(\alpha) = \exp(\alpha\hat{a}^\dagger - \alpha^*\hat{a}) \tag{D3}$$

$$= \exp[\sqrt{2}i\,\mathrm{Im}(\alpha)\hat{x} - \sqrt{2}i\,\mathrm{Re}(\alpha)\hat{p}]. \tag{D4}$$

An ideal GKP state on a rectangular lattice is stabilized by (recall Sec. III)

$$\hat{\mathcal{S}}_x(s) = \exp(is\hat{x}) = \hat{D}\left(\frac{is}{\sqrt{2}}\right), \tag{D5}$$

$$\hat{\mathcal{S}}_p(s') = \exp(-is'\hat{p}) = \hat{D}\left(\frac{s'}{\sqrt{2}}\right), \tag{D6}$$

where s and s' depend on the lattice spacing.

We envision modeling an approximate GKP sensor state $\hat{\rho}$ using a Gaussian random noise state $\hat{\tilde{\rho}}$ obtained by applying Eq. (D1) to an ideal GKP sensor state $|\varnothing\rangle$, which is stabilized by $\hat{\mathcal{S}}_x(\sqrt{2\pi}) = \widehat{D}(i\sqrt{\pi})$ and $\hat{\mathcal{S}}_p(\sqrt{2\pi}) = \hat{D}(\sqrt{\pi})$. The GRN state

should be chosen to satisfy

$$\langle\hat{\mathcal{S}}_x(\sqrt{2\pi})\rangle_{\tilde{\rho}} = \langle\hat{\mathcal{S}}_x(\sqrt{2\pi})\rangle_{\rho}, \quad \langle\hat{\mathcal{S}}_p(\sqrt{2\pi})\rangle_{\tilde{\rho}} = \langle\hat{\mathcal{S}}_p(\sqrt{2\pi})\rangle_{\rho}. \tag{D7}$$

The equalities in Eq. (D7) are satisfied by setting

$$\Sigma_i = \frac{1}{2\pi}\log\frac{1}{|\langle\hat{\Theta}_i\rangle_\rho|^2}, \tag{D8}$$

where $\hat{\Theta}_0 = \hat{\mathcal{S}}_x(\sqrt{2\pi})$ and $\hat{\Theta}_1 = \hat{\mathcal{S}}_p(\sqrt{2\pi})$.

Proof.

$$\langle\hat{\Theta}_j\rangle_{\hat{\tilde{\rho}}} = \mathrm{Tr}(\hat{\Theta}_j\hat{\tilde{\rho}}) = \mathrm{Tr}\left(\hat{\Theta}_j\int_{\mathbb{C}} \mathrm{d}^2\alpha\, G_{\mathbf{\Sigma}}(\alpha)\hat{D}(\alpha)|\varnothing\rangle\langle\varnothing|\hat{D}^\dagger(\alpha)\right) \tag{D9}$$

$$= \int_{\mathbb{C}} \mathrm{d}^2\alpha\, G_{\mathbf{\Sigma}}(\alpha)\mathrm{Tr}[\hat{\Theta}_j\hat{D}(\alpha)|\varnothing\rangle\langle\varnothing|\hat{D}^\dagger(\alpha)] \tag{D10}$$

$$= \int_{\mathbb{C}} \mathrm{d}^2\alpha\, G_{\mathbf{\Sigma}}(\alpha)\mathrm{Tr}[\langle\hat{D}^\dagger(\alpha)\hat{\Theta}_j\hat{D}(\alpha)\rangle\varnothing] \tag{D11}$$

$$= \int_{\mathbb{C}} \mathrm{d}^2\alpha\, G_{\mathbf{\Sigma}}(\alpha)\mathrm{Tr}[\langle\hat{D}^\dagger(\alpha)\hat{D}(e^{i\pi(1-j)}\sqrt{\pi})\hat{D}(\alpha)\rangle\varnothing] \tag{D12}$$

$$= \int_{\mathbb{C}} \mathrm{d}^2\alpha\, G_{\mathbf{\Sigma}}(\alpha)e^{2i(1-j)\sqrt{\pi}\mathrm{Re}(\alpha)}e^{-2ij\sqrt{\pi}\mathrm{Im}(\alpha)}\mathrm{Tr}[\langle\hat{\Theta}_j\rangle\varnothing] \tag{D13}$$

$$= \int_{\mathbb{C}} \mathrm{d}^2\alpha\, G_{\mathbf{\Sigma}}(\alpha)e^{2i(1-j)\sqrt{\pi}\mathrm{Re}(\alpha)}e^{-2ij\sqrt{\pi}\mathrm{Im}(\alpha)} \tag{D14}$$

$$= \int_{\mathbb{C}} \mathrm{d}^2\alpha\, \frac{1}{\pi\sqrt{\Sigma_0\Sigma_1}}\exp\left(-\frac{\mathrm{Re}(\alpha)^2}{\Sigma_0}\right)\exp\left(-\frac{\mathrm{Im}(\alpha)^2}{\Sigma_1}\right)e^{2i(1-j)\sqrt{\pi}\mathrm{Re}(\alpha)}e^{-2ij\sqrt{\pi}\mathrm{Im}(\alpha)} \tag{D15}$$

$$= \frac{1}{\pi\sqrt{\Sigma_0\Sigma_1}}\int_{-\infty}^{\infty}\mathrm{d}\,\mathrm{Re}(\alpha)\exp\left(-\frac{\mathrm{Re}(\alpha)^2}{\Sigma_0}\right)e^{2i(1-j)\sqrt{\pi}\mathrm{Re}(\alpha)}$$
$$\times\int_{-\infty}^{\infty}\mathrm{d}\,\mathrm{Im}(\alpha)\exp\left(-\frac{\mathrm{Im}(\alpha)^2}{\Sigma_1}\right)e^{-2ij\sqrt{\pi}\mathrm{Im}(\alpha)} \tag{D16}$$

$$= \frac{1}{\pi\sqrt{\Sigma_0\Sigma_1}}\int_{-\infty}^{\infty}\mathrm{d}\,\mathrm{Re}(\alpha)\exp\left[-\left(\frac{\mathrm{Re}(\alpha)}{\sqrt{\Sigma_0}} - i(1-j)\sqrt{\pi\Sigma_0}\right)^2\right]\exp[-(1-j)^2\pi\Sigma_0]$$
$$\times\int_{-\infty}^{\infty}\mathrm{d}\,\mathrm{Im}(\alpha)\exp\left[-\left(\frac{\mathrm{Im}(\alpha)}{\sqrt{\Sigma_1}} + ij\sqrt{\pi\Sigma_1}\right)^2\right]\exp(-j^2\pi\Sigma_1) \tag{D17}$$

$$= \exp[-(1-j)\pi\Sigma_0]\exp(-j\pi\Sigma_1) \tag{D18}$$

$$= \exp\left(-(1-j)\pi\frac{1}{2\pi}\ln\frac{1}{|\langle\hat{\Theta}_0\rangle_\rho|^2}\right)\exp\left(-j\pi\frac{1}{2\pi}\ln\frac{1}{|\langle\hat{\Theta}_1\rangle_\rho|^2}\right) \tag{D19}$$

$$= |\langle\hat{\Theta}_0\rangle_\rho|^{(1-j)}|\langle\hat{\Theta}_1\rangle_\rho|^j = |\langle\hat{\Theta}_j\rangle_\rho|. \tag{D20}$$

■

Gaussian random noise states can be employed in place of the approximate GKP states to calculate the stabilizer expectation values of the two-mode entangled state obtained via a controlled-Z (CZ) operation onto two GKP qubits. The operation is realized with the optical circuit shown in Fig. 2. Here we verify that the stabilizer $\hat{D}_1(\sqrt{\pi/2})\otimes\hat{D}_2(i\sqrt{\pi/2})$ has the same expectation value for the output two-mode GKP state both when the input states of the circuit are two approximate GKP states $\hat{\rho}_1$ and $\hat{\rho}_2$ and when they are the respective GRN states $\hat{\tilde{\rho}}_1$ and $\hat{\tilde{\rho}}_2$, provided the GRN state parameters are chosen according to Eq. (D7).

Proof. The expectation value of the stabilizer is

$$\langle\hat{D}_1(\sqrt{\pi/2})\otimes\hat{D}_2(i\sqrt{\pi/2})\rangle_{\hat{\tilde{\rho}}_{\mathrm{out}}} = \mathrm{Tr}\left\{\hat{D}_1(\sqrt{\pi/2})\otimes\hat{D}_2(i\sqrt{\pi/2})\left[\hat{R}_1\left(\frac{\pi}{2}\right)\hat{B}\hat{R}_1\left(-\frac{\pi}{2}\right)\hat{\tilde{\rho}}_1\otimes\hat{\tilde{\rho}}_2\hat{R}_1\left(-\frac{\pi}{2}\right)\hat{B}^\dagger\hat{R}_1\left(\frac{\pi}{2}\right)\right]\right\}, \tag{D21}$$

where $\hat{B}$ refers to the operator describing the action of the symmetric beam splitter and $\hat{R}_i(\theta)$ marks the rotation gate of angle θ acting on the ith mode. The action of the beam-splitter operation onto the annihilation operators on the first and second modes

$(\hat{a}_1, \hat{a}_2)^T$ is described by the unitary matrix

$$\hat{B} = \frac{1}{\sqrt{2}}\begin{pmatrix} 1 & -1 \\ 1 & 1 \end{pmatrix}. \tag{D22}$$

We can then define the matrix for the operator $\hat{B}'$ such that

$$\hat{B}' \equiv \hat{R}_1\left(\frac{\pi}{2}\right)\hat{B}\hat{R}_1\left(-\frac{\pi}{2}\right) = \frac{1}{\sqrt{2}}\begin{pmatrix} i & 0 \\ 0 & 1 \end{pmatrix}\begin{pmatrix} 1 & -1 \\ 1 & 1 \end{pmatrix}\begin{pmatrix} -i & 0 \\ 0 & 1 \end{pmatrix} = \frac{1}{\sqrt{2}}\begin{pmatrix} 1 & -i \\ -i & 1 \end{pmatrix}. \tag{D23}$$

As a consequence,

$$\langle \hat{D}_1(\sqrt{\pi/2}) \otimes \hat{D}_2(i\sqrt{\pi/2})\rangle_{\hat{\rho}_{\text{out}}} = \mathrm{Tr}[\hat{B}'^{\dagger}\hat{D}_1(\sqrt{\pi/2}) \otimes \hat{D}_2(i\sqrt{\pi/2})\hat{B}'\hat{\rho}_1 \otimes \hat{\rho}_2] \tag{D24}$$

$$= \mathrm{Tr}\left[\hat{D}_1\left(\frac{\sqrt{\pi}}{2} - \frac{\sqrt{\pi}}{2}\right) \otimes \hat{D}_2\left(i\frac{\sqrt{\pi}}{2} + i\frac{\sqrt{\pi}}{2}\right)\hat{\rho}_1 \otimes \hat{\rho}_2\right] \tag{D25}$$

$$= \mathrm{Tr}[\hat{D}_2(i\sqrt{\pi})\hat{\rho}_1 \otimes \hat{\rho}_2] \tag{D26}$$

$$= \mathrm{Tr}[\hat{\mathcal{S}}_{x,2}(\sqrt{2\pi})\hat{\rho}_2] \tag{D27}$$

$$= \mathrm{Tr}[\hat{\mathcal{S}}_{x,2}(\sqrt{2\pi})\rho_2] \tag{D28}$$

$$= \langle \hat{D}_1(\sqrt{\pi/2}) \otimes \hat{D}_2(i\sqrt{\pi/2})\rangle_{\rho_{\text{out}}}. \tag{D29}$$

■

We can now consider the stabilizer expectation values of the state heralded by the homodyne detection of the two-mode entangled state ρ_{out}. The scheme that prepares the heralded state is shown in Fig. 6. The heralded state has two stabilizers $\hat{\mathcal{S}}_p(2\sqrt{\pi}) = \hat{D}(i\sqrt{2\pi})$ and $\hat{\mathcal{S}}_x(2\sqrt{\pi}) = \hat{D}(\sqrt{2\pi})$.

By postselecting on the measure of p_2 in the second mode, the stabilizer expectation value of $\hat{\mathcal{S}}_x(2\sqrt{\pi})$ in the first mode is

$$\langle \hat{\mathcal{S}}_x(2\sqrt{\pi})\rangle = \frac{\mathrm{Tr}[(|p_2\rangle\langle p_2|\hat{B}'^{\dagger}\hat{\rho}_1 \otimes \hat{\rho}_2\hat{B}')\hat{\mathcal{S}}_{x,1}(2\sqrt{\pi})]}{\mathrm{Tr}[|p_2\rangle\langle p_2|\hat{B}'^{\dagger}\hat{\rho}_1 \otimes \hat{\rho}_2\hat{B}']}. \tag{D30}$$

The denominator in Eq. (D30) can be rewritten as

$$\mathcal{N}_{p_2} \equiv \mathrm{Tr}(|p_2\rangle\langle p_2|\hat{B}'^{\dagger}\hat{\rho}_1 \otimes \hat{\rho}_2\hat{B}') \tag{D31}$$

$$= \mathrm{Tr}(\hat{B}'|p_2\rangle\langle p_2|\hat{B}'^{\dagger}\hat{\rho}_1 \otimes \hat{\rho}_2) \tag{D32}$$

$$= \mathrm{Tr}\left(\hat{B}'\underbrace{\int_{-\infty}^{\infty} \mathrm{d}l\,|l\rangle_x\langle l|_x}_{\mathbb{1}_1} \otimes |p_2\rangle_p\langle p_2|_p\hat{B}'^{\dagger}\hat{\rho}_1 \otimes \hat{\rho}_2\right) \tag{D33}$$

$$= \int_{-\infty}^{\infty} \mathrm{d}l\,\mathrm{Tr}(\hat{B}'|l\rangle_x|p_2\rangle_p\langle l|_x\langle p_2|_p\hat{B}'^{\dagger}\hat{\rho}_1 \otimes \hat{\rho}_2) \tag{D34}$$

$$= \int_{-\infty}^{\infty} \mathrm{d}l\,\mathrm{Tr}\left(\left|\frac{l+p_2}{\sqrt{2}}\right\rangle_x\left|-\frac{l-p_2}{\sqrt{2}}\right\rangle_p\left\langle\frac{l+p_2}{\sqrt{2}}\right|_x\left\langle-\frac{l-p_2}{\sqrt{2}}\right|_p\hat{\rho}_1 \otimes \hat{\rho}_2\right) \tag{D35}$$

$$= \int_{-\infty}^{\infty} \mathrm{d}l\left\langle\frac{l+p_2}{\sqrt{2}}\right|_x\left\langle-\frac{l-p_2}{\sqrt{2}}\right|_p\hat{\rho}_1 \otimes \hat{\rho}_2\left|\frac{l+p_2}{\sqrt{2}}\right\rangle_x\left|-\frac{l-p_2}{\sqrt{2}}\right\rangle_p \tag{D36}$$

$$= \int_{-\infty}^{\infty} \mathrm{d}l\left\langle\frac{l+p_2}{\sqrt{2}}\right|_x\hat{\rho}_1\left|\frac{l+p_2}{\sqrt{2}}\right\rangle_x\left\langle-\frac{l-p_2}{\sqrt{2}}\right|_p\hat{\rho}_2\left|-\frac{l-p_2}{\sqrt{2}}\right\rangle_p. \tag{D37}$$

Analogously, the numerator in Eq. (D30) is equal to

$$\mathrm{Tr}[(|p_2\rangle\langle p_2|\hat{B}'^{\dagger}\hat{\rho}_1 \otimes \hat{\rho}_2\hat{B}')\hat{\mathcal{S}}_{x,1}(2\sqrt{\pi})] = \mathrm{Tr}[\hat{B}'\hat{\mathcal{S}}_{x,1}(2\sqrt{\pi})|p_2\rangle\langle p_2|\hat{B}'^{\dagger}\hat{\rho}_1 \otimes \hat{\rho}_2] \tag{D38}$$

$$= \mathrm{Tr}[\hat{B}'\hat{\mathcal{S}}_{x,1}(2\sqrt{\pi})\hat{B}'^{\dagger}\hat{B}'|p_2\rangle\langle p_2|\hat{B}'^{\dagger}\hat{\rho}_1 \otimes \hat{\rho}_2] \tag{D39}$$

$$= \mathrm{Tr}[\hat{\mathcal{S}}_{x,1}(\sqrt{2\pi})\hat{\mathcal{S}}_{p,2}(\sqrt{2\pi})\hat{B}'|p_2\rangle\langle p_2|\hat{B}'^{\dagger}\hat{\rho}_1 \otimes \hat{\rho}_2] \tag{D40}$$

$$= \int_{-\infty}^{\infty} \mathrm{d}l\left\langle\frac{l+p_2}{\sqrt{2}}\right|_x\left\langle-\frac{l-p_2}{\sqrt{2}}\right|_p\hat{\rho}_1 \otimes \hat{\rho}_2\hat{\mathcal{S}}_{x,1}(\sqrt{2\pi})\hat{\mathcal{S}}_{p,2}(\sqrt{2\pi})\left|\frac{l+p_2}{\sqrt{2}}\right\rangle_x\left|-\frac{l-p_2}{\sqrt{2}}\right\rangle_p \tag{D41}$$

$$= \int_{-\infty}^{\infty} \mathrm{d}l \left\langle \frac{l+p_2}{\sqrt{2}} \right|_x \hat{\tilde{\rho}}_1 \hat{\mathcal{S}}_{x,1}(\sqrt{2\pi}) \left| \frac{l+p_2}{\sqrt{2}} \right\rangle_x \left\langle -\frac{l-p_2}{\sqrt{2}} \right|_p \hat{\tilde{\rho}}_2 \hat{\mathcal{S}}_{p,2}(\sqrt{2\pi}) \left| -\frac{l-p_2}{\sqrt{2}} \right\rangle_p \tag{D42}$$

$$= \int_{-\infty}^{\infty} \mathrm{d}l \left\langle \frac{l+p_2}{\sqrt{2}} \right|_x \hat{\tilde{\rho}}_1 \left| \frac{l+p_2}{\sqrt{2}} \right\rangle_x e^{i\sqrt{2\pi}[(l+p_2)/\sqrt{2}]} \left\langle -\frac{l-p_2}{\sqrt{2}} \right|_p \hat{\tilde{\rho}}_2 \left| -\frac{l-p_2}{\sqrt{2}} \right\rangle_p e^{i\sqrt{2\pi}[(l-p_2)/\sqrt{2}]} \tag{D43}$$

$$= \int_{-\infty}^{\infty} \mathrm{d}l \, e^{i2\sqrt{\pi}l} \left\langle \frac{l+p_2}{\sqrt{2}} \right|_x \hat{\tilde{\rho}}_1 \left| \frac{l+p_2}{\sqrt{2}} \right\rangle_x \left\langle -\frac{l-p_2}{\sqrt{2}} \right|_p \hat{\tilde{\rho}}_2 \left| -\frac{l-p_2}{\sqrt{2}} \right\rangle_p . \tag{D44}$$

We observe that

$$\langle q|_x \hat{\tilde{\rho}} |q\rangle_x = \langle q|_x \int_{\mathbb{C}} \mathrm{d}^2\alpha \, G_\Sigma(\alpha) \hat{D}(\alpha) |\varnothing\rangle\langle\varnothing| \hat{D}^\dagger(\alpha) |q\rangle_x \tag{D45}$$

$$= \int_{\mathbb{C}} \mathrm{d}^2\alpha \, G_\Sigma(\alpha) \langle q|_x \hat{D}(\alpha) |\varnothing\rangle\langle\varnothing| \hat{D}^\dagger(\alpha) |q\rangle_x \tag{D46}$$

$$= \int_{\mathbb{C}} \mathrm{d}^2\alpha \, G_\Sigma(\alpha) |\langle\varnothing| \hat{D}^\dagger(\alpha) |q\rangle_x|^2 \tag{D47}$$

$$= \int_{\mathbb{C}} \mathrm{d}^2\alpha \, G_\Sigma(\alpha) |\langle\varnothing| q - \sqrt{2}\mathrm{Re}(\alpha)\rangle_x|^2 \tag{D48}$$

$$= \frac{1}{\pi\sqrt{\Sigma_0\Sigma_1}} \int_{-\infty}^{\infty} \mathrm{d}\,\mathrm{Re}(\alpha) e^{-\mathrm{Re}(\alpha)^2/\Sigma_0} |\langle\varnothing| q - \sqrt{2}\mathrm{Re}(\alpha)\rangle_x|^2 \int_{-\infty}^{\infty} \mathrm{d}\,\mathrm{Im}(\alpha) e^{-\mathrm{Im}(\alpha)^2/\Sigma_1} \tag{D49}$$

$$= \frac{1}{\sqrt{\pi\,\Sigma_0}} \int_{-\infty}^{\infty} \mathrm{d}\,\mathrm{Re}(\alpha) e^{-\mathrm{Re}(\alpha)^2/\Sigma_0} |\langle\varnothing| q - \sqrt{2}\mathrm{Re}(\alpha)\rangle_x|^2 \tag{D50}$$

$$= \frac{1}{\sqrt{\pi\,\Sigma_0}} \int_{-\infty}^{\infty} \mathrm{d}\,\mathrm{Re}(\alpha) e^{-\mathrm{Re}(\alpha)^2/\Sigma_0} \left| M \sum_{n=-\infty}^{\infty} \langle\sqrt{2\pi}n| q - \sqrt{2}\mathrm{Re}(\alpha)\rangle_x \right|^2 \tag{D51}$$

$$= \frac{M^2}{\sqrt{\pi\,\Sigma_0}} \int_{-\infty}^{\infty} \mathrm{d}\,\mathrm{Re}(\alpha) e^{-\mathrm{Re}(\alpha)^2/\Sigma_0} \sum_{n=-\infty}^{\infty} |\langle\sqrt{2\pi}n| q - \sqrt{2}\mathrm{Re}(\alpha)\rangle_x|^2 \tag{D52}$$

$$= \frac{M^2}{\sqrt{\pi\,\Sigma_0}} \int_{-\infty}^{\infty} \mathrm{d}\,\mathrm{Re}(\alpha) e^{-\mathrm{Re}(\alpha)^2/\Sigma_0} \sum_{n=-\infty}^{\infty} \delta^2(q - \sqrt{2}\mathrm{Re}(\alpha) - \sqrt{2\pi}n) \tag{D53}$$

$$= \frac{M^2}{\sqrt{\pi\,\Sigma_0}} \sum_{n=-\infty}^{\infty} \int_{-\infty}^{\infty} \mathrm{d}\,\mathrm{Re}(\alpha) e^{-\mathrm{Re}(\alpha)^2/\Sigma_0} \delta^2(q - \sqrt{2}\mathrm{Re}(\alpha) - \sqrt{2\pi}n) \tag{D54}$$

$$= \frac{M^2}{\sqrt{\pi\,\Sigma_0}} \sum_{n=-\infty}^{\infty} \delta(0) \exp\left(-\frac{\left(\frac{q}{\sqrt{2}} - \sqrt{\pi}n\right)^2}{\Sigma_0} \right) \tag{D55}$$

and

$$\langle q|_p \hat{\tilde{\rho}} |q\rangle_p = \langle q|_p \int_{\mathbb{C}} \mathrm{d}^2\alpha \, G_{\Sigma,2}(\alpha) \hat{D}(\alpha) |\varnothing\rangle\langle\varnothing| \hat{D}^\dagger(\alpha) |q\rangle_p \tag{D56}$$

$$= \int_{\mathbb{C}} \mathrm{d}^2\alpha \, G_{\Sigma,2}(\alpha) \langle q|_p \hat{D}(\alpha) |\varnothing\rangle\langle\varnothing| \hat{D}^\dagger(\alpha) |q\rangle_p \tag{D57}$$

$$= \int_{\mathbb{C}} \mathrm{d}^2\alpha \, G_{\Sigma,2}(\alpha) |\langle\varnothing| \hat{D}^\dagger(\alpha) |q\rangle_p|^2 \tag{D58}$$

$$= \int_{\mathbb{C}} \mathrm{d}^2\alpha \, G_{\Sigma,2}(\alpha) |\langle\varnothing| q - \sqrt{2}\mathrm{Im}(\alpha)\rangle_p|^2 \tag{D59}$$

$$= \frac{1}{\pi\sqrt{\Sigma_0\Sigma_1}} \int_{-\infty}^{\infty} \mathrm{d}\,\mathrm{Re}(\alpha) e^{-\mathrm{Re}(\alpha)^2/\Sigma_0} \int_{-\infty}^{\infty} \mathrm{d}\,\mathrm{Im}(\alpha) e^{-\mathrm{Im}(\alpha)^2/\Sigma_1} |\langle\varnothing| q - \sqrt{2}\mathrm{Im}(\alpha)\rangle_p|^2 \tag{D60}$$

$$= \frac{1}{\sqrt{\pi\,\Sigma_1}} \int_{-\infty}^{\infty} \mathrm{d}\,\mathrm{Im}(\alpha) e^{-\mathrm{Im}(\alpha)^2\Sigma_1} |\langle\varnothing| q - \sqrt{2}\mathrm{Im}(\alpha)\rangle_p|^2 \tag{D61}$$

$$= \frac{1}{\sqrt{\pi\,\Sigma_1}} \int_{-\infty}^{\infty} \mathrm{d}\,\mathrm{Im}(\alpha) e^{-\mathrm{Im}(\alpha)^2/\Sigma_1} \left| M \sum_{m=-\infty}^{\infty} \langle \sqrt{2\pi} n | q - \sqrt{2}\mathrm{Im}(\alpha) \rangle_p \right|^2 \tag{D62}$$

$$= \frac{M^2}{\sqrt{\pi\,\Sigma_1}} \int_{-\infty}^{\infty} \mathrm{d}\,\mathrm{Im}(\alpha) e^{-\mathrm{Im}(\alpha)^2/\Sigma_1} \sum_{m=-\infty}^{\infty} |\langle \sqrt{2\pi} m | q - \sqrt{2}\mathrm{Im}(\alpha) \rangle_p|^2 \tag{D63}$$

$$= \frac{M^2}{\sqrt{\pi\,\Sigma_1}} \int_{-\infty}^{\infty} \mathrm{d}\,\mathrm{Im}(\alpha) e^{-\mathrm{Im}(\alpha)^2/\Sigma_1} \sum_{m=-\infty}^{\infty} \delta^2(q - \sqrt{2}\mathrm{Im}(\alpha) - \sqrt{2\pi} m) \tag{D64}$$

$$= \frac{M^2}{\sqrt{\pi\,\Sigma_1}} \sum_{m=-\infty}^{\infty} \int_{-\infty}^{\infty} \mathrm{d}\,\mathrm{Im}(\alpha) e^{-\mathrm{Im}(\alpha)^2/\Sigma_1} \delta^2(q - \sqrt{2}\mathrm{Im}(\alpha) - \sqrt{2\pi} m) \tag{D65}$$

$$= \frac{M^2}{\sqrt{\pi\,\Sigma_1}} \sum_{m=-\infty}^{\infty} \delta(0) \exp\left(-\frac{\left(\frac{p}{\sqrt{2}} - \sqrt{\pi} m\right)^2}{\Sigma_1} \right). \tag{D66}$$

By inserting the results of Eqs. (D57) and (D69) into Eqs. (D37) and (D45) we can rewrite Eq. (D30) as

$$\Rightarrow \langle \hat{\mathcal{S}}_x \rangle = \frac{1}{N_{p_2}} \int_{-\infty}^{\infty} \mathrm{d}l\, e^{i2\sqrt{\pi} l} \left\langle \frac{l+p_2}{\sqrt{2}} \middle|_x \hat{\tilde{\rho}}_1 \middle| \frac{l+p_2}{\sqrt{2}} \right\rangle_x \left\langle -\frac{l-p_2}{\sqrt{2}} \middle|_p \hat{\tilde{\rho}}_2 \middle| -\frac{l-p_2}{\sqrt{2}} \right\rangle_p \tag{D67}$$

$$= \frac{1}{N_{p_2}} \int_{-\infty}^{\infty} \mathrm{d}l\, e^{i2\sqrt{\pi} l} \left\langle \frac{l+p_2}{\sqrt{2}} \middle|_x \hat{\tilde{\rho}}_1 \middle| \frac{l+p_2}{\sqrt{2}} \right\rangle_x \left\langle -\frac{l-p_2}{\sqrt{2}} \middle|_p \hat{\tilde{\rho}}_2 \middle| -\frac{l-p_2}{\sqrt{2}} \right\rangle_p \tag{D68}$$

$$= \frac{\int_{-\infty}^{\infty} \mathrm{d}l\, e^{i2\sqrt{\pi} l} \left\langle \frac{l+p_2}{\sqrt{2}} \middle|_x \hat{\tilde{\rho}}_1 \middle| \frac{l+p_2}{\sqrt{2}} \right\rangle_x \left\langle -\frac{l-p_2}{\sqrt{2}} \middle|_p \hat{\tilde{\rho}}_2 \middle| -\frac{l-p_2}{\sqrt{2}} \right\rangle_p}{\int_{-\infty}^{\infty} \mathrm{d}l \left\langle \frac{l+p_2}{\sqrt{2}} \middle|_x \hat{\tilde{\rho}}_1 \middle| \frac{l+p_2}{\sqrt{2}} \right\rangle_x \left\langle -\frac{l-p_2}{\sqrt{2}} \middle|_p \hat{\tilde{\rho}}_2 \middle| -\frac{l-p_2}{\sqrt{2}} \right\rangle_p} \tag{D69}$$

$$= \frac{\int_{-\infty}^{\infty} \mathrm{d}l\, e^{i2\sqrt{\pi} l} \frac{M^2}{\sqrt{\pi\,\Sigma_{0,1}}} \sum_{n=-\infty}^{\infty} \delta(0) \exp\left(-\frac{(\frac{l}{2} + \frac{p_2}{2} - \sqrt{\pi} n)^2}{\Sigma_{0,1}} \right) \frac{M^2}{\sqrt{\pi\,\Sigma_{1,2}}} \sum_{m=-\infty}^{\infty} \delta(0) \exp\left(-\frac{(\frac{l}{2} - \frac{p_2}{2} - \sqrt{\pi} m)^2}{\Sigma_{1,2}} \right)}{\int_{-\infty}^{\infty} \mathrm{d}l \frac{M^2}{\sqrt{\pi\,\Sigma_{0,1}}} \sum_{n=-\infty}^{\infty} \delta(0) \exp\left(-\frac{(\frac{l}{2} + \frac{p_2}{2} - \sqrt{\pi} n)^2}{\Sigma_{0,1}} \right) \frac{M^2}{\sqrt{\pi\,\Sigma_{1,2}}} \sum_{m=-\infty}^{\infty} \delta(0) \exp\left(-\frac{(\frac{l}{2} - \frac{p_2}{2} - \sqrt{\pi} m)^2}{\Sigma_{1,2}} \right)} \tag{D70}$$

$$= \frac{\sum_{n,m=-\infty}^{\infty} \int_{-\infty}^{\infty} \mathrm{d}l\, e^{i2\sqrt{\pi} l} \exp\left(-\frac{(\frac{l}{2} + \frac{p_2}{2} - \sqrt{\pi} n)^2}{\Sigma_{0,1}} \right) \exp\left(-\frac{(\frac{l}{2} - \frac{p_2}{2} - \sqrt{\pi} m)^2}{\Sigma_{1,2}} \right)}{\sum_{n,m=-\infty}^{\infty} \int_{-\infty}^{\infty} \mathrm{d}l \exp\left(-\frac{(\frac{l}{2} + \frac{p_2}{2} - \sqrt{\pi} n)^2}{\Sigma_{0,1}} \right) \exp\left(-\frac{(\frac{l}{2} - \frac{p_2}{2} - \sqrt{\pi} m)^2}{\Sigma_{1,2}} \right)} \tag{D71}$$

$$= \frac{\sum_{n,m=-\infty}^{\infty} 2\sqrt{\frac{\Sigma_{0,1}\Sigma_{1,2}}{\Sigma_{0,1}+\Sigma_{1,2}}\pi} \exp\left(-\frac{[\sqrt{\pi}(n-m)-p_2]^2}{\Sigma_{0,1}+\Sigma_{1,2}} \right) \exp\left(-4\pi \frac{\Sigma_{0,1}\Sigma_{1,2}}{\Sigma_{0,1}+\Sigma_{1,2}} \right) \exp\left(i4\pi \frac{\Sigma_{1,2} n + \Sigma_{0,1} m}{\Sigma_{1,2}+\Sigma_{0,1}} \right) \exp\left(-i2\sqrt{\pi} \frac{\Sigma_{1,2}-\Sigma_{0,1}}{\Sigma_{1,2}+\Sigma_{0,1}} p_2 \right)}{\sum_{n,m=-\infty}^{\infty} 2\sqrt{\frac{\Sigma_{0,1}\Sigma_{1,2}}{\Sigma_{0,1}+\Sigma_{1,2}}\pi} \exp\left(-\frac{[\sqrt{\pi}(n-m)-p_2]^2}{\Sigma_{0,1}+\Sigma_{1,2}} \right)} \tag{D72}$$

$$= \exp\left(-4\pi \frac{\Sigma_{0,1}\Sigma_{1,2}}{\Sigma_{0,1}+\Sigma_{1,2}} \right) \exp\left(-i2\sqrt{\pi} \frac{\Sigma_{1,2}-\Sigma_{0,1}}{\Sigma_{1,2}+\Sigma_{0,1}} p_2 \right) \times \frac{\sum_{n=-\infty}^{\infty} \sum_{m=-\infty}^{\infty} \exp\left(-\frac{[\sqrt{\pi}(n-m)-p_2]^2}{\Sigma_{0,1}+\Sigma_{1,2}} \right) \exp\left(i4\pi \frac{\Sigma_{1,2} n + \Sigma_{0,1} m}{\Sigma_{1,2}+\Sigma_{0,1}} \right)}{\sum_{n=-\infty}^{\infty} \sum_{m=-\infty}^{\infty} \exp\left(-\frac{[\sqrt{\pi}(n-m)-p_2]^2}{\Sigma_{0,1}+\Sigma_{1,2}} \right)} \tag{D73}$$

$$\overset{m'=m-n}{=} \exp\left(\frac{-4\pi\,\Sigma_{0,1}\Sigma_{1,2} - 2i\sqrt{\pi}\,p_2(\Sigma_{1,2}-\Sigma_{0,1})}{\Sigma_{0,1}+\Sigma_{1,2}} \right) \times \frac{\sum_{n=-\infty}^{\infty} \sum_{m'=-\infty}^{\infty} \exp\left(-\frac{[\sqrt{\pi} m' + p_2]^2}{\Sigma_{0,1}+\Sigma_{1,2}} \right) \exp\left(i4\pi \frac{\Sigma_{1,2}+\Sigma_{0,1}}{\Sigma_{1,2}+\Sigma_{0,1}} n + i4\pi \frac{\Sigma_{0,1} m'}{\Sigma_{1,2}+\Sigma_{0,1}} \right)}{\sum_{n=-\infty}^{\infty} \sum_{m'=-\infty}^{\infty} \exp\left(-\frac{[\sqrt{\pi} m' + p_2]^2}{\Sigma_{0,1}+\Sigma_{1,2}} \right)} \tag{D74}$$

$$= \exp\left(\frac{-4\pi\,\Sigma_{0,1}\Sigma_{1,2} - 2i\sqrt{\pi}\,p_2(\Sigma_{1,2}-\Sigma_{0,1})}{\Sigma_{0,1}+\Sigma_{1,2}} \right) \frac{\sum_{m'=-\infty}^{\infty} \exp\left(-\frac{[\sqrt{\pi} m' + p_2]^2}{\Sigma_{0,1}+\Sigma_{1,2}} \right) \exp\left(i4\pi \frac{\Sigma_{0,1} m'}{\Sigma_{1,2}+\Sigma_{0,1}} \right)}{\sum_{m'=-\infty}^{\infty} \exp\left(-\frac{[\sqrt{\pi} m' + p_2]^2}{\Sigma_{0,1}+\Sigma_{1,2}} \right)} \tag{D75}$$

$$= \exp\left(\frac{-4\pi\Sigma_{0,1}\Sigma_{1,2} - 2i\sqrt{\pi}p_2(\Sigma_{1,2}-\Sigma_{0,1})}{\Sigma_{0,1}+\Sigma_{1,2}}\right) \times \frac{\sqrt{\Sigma_{0,1}+\Sigma_{1,2}}\exp(-4\pi\frac{\Sigma_{0,1}^2}{\Sigma_{0,1}+\Sigma_{1,2}})\exp(-4i\sqrt{\pi}\frac{\Sigma_{0,1}}{\Sigma_{0,1}+\Sigma_{1,2}}p_2)\theta_3(-\sqrt{\pi}p_2+2i\pi\Sigma_{0,1}, e^{-(\Sigma_{0,1}+\Sigma_{1,2})\pi})}{\sqrt{\Sigma_{0,1}+\Sigma_{1,2}}\theta_3(-\sqrt{\pi}p_2, e^{-(\Sigma_{0,1}+\Sigma_{1,2})\pi})} \tag{D76}$$

$$= \exp(-4\pi\Sigma_{0,1} - 2i\sqrt{\pi}p_2)\frac{\theta_3(\sqrt{\pi}p_2 - 2i\pi\Sigma_{0,1}, e^{-(\Sigma_{0,1}+\Sigma_{1,2})\pi})}{\theta_3(\sqrt{\pi}p_2, e^{-(\Sigma_{0,1}+\Sigma_{1,2})\pi})}, \tag{D77}$$

where $\Sigma_{i,j}$ is the Σ_i of the state in the jth mode, while the Jacobi theta function $\theta_3(z,q) = \sum_{n=-\infty}^{\infty} q^{n^2}e^{2inz}$.

The expectation value of the second operator $\hat{\mathcal{S}}_p$ will be given instead by

$$\langle\hat{\mathcal{S}}_p\rangle = \frac{\mathrm{Tr}[(|p_2\rangle\langle p_2|\hat{B}'^{\dagger}\hat{\rho}_1\otimes\hat{\rho}_2\hat{B}')\hat{\mathcal{S}}_{p,1}(2\sqrt{\pi})]}{\mathrm{Tr}(|p_2\rangle\langle p_2|\hat{B}'^{\dagger}\hat{\rho}_1\otimes\hat{\rho}_2\hat{B}')}. \tag{D78}$$

The numerator of Eq. (D81) is

$$\mathrm{Tr}[(|p_2\rangle\langle p_2|\hat{B}'^{\dagger}\hat{\rho}_1\otimes\hat{\rho}_2\hat{B}')\hat{\mathcal{S}}_{p,1}(2\sqrt{\pi})] = \mathrm{Tr}[\hat{B}'\hat{\mathcal{S}}_{p,1}(2\sqrt{\pi})|p_2\rangle\langle p_2|\hat{B}'^{\dagger}\hat{\rho}_1\otimes\hat{\rho}_2] \tag{D79}$$

$$= \mathrm{Tr}[\hat{B}'\hat{\mathcal{S}}_{p,1}(2\sqrt{\pi})\hat{B}'^{\dagger}\hat{B}'|p_2\rangle\langle p_2|\hat{B}'^{\dagger}\hat{\rho}_1\otimes\hat{\rho}_2] \tag{D80}$$

$$= \mathrm{Tr}[\hat{\mathcal{S}}_{p,1}(\sqrt{2\pi})\hat{\mathcal{S}}_{x,2}(-\sqrt{2\pi})\hat{B}'|p_2\rangle\langle p_2|\hat{B}'^{\dagger}\hat{\rho}_1\otimes\hat{\rho}_2] \tag{D81}$$

$$= \int_{-\infty}^{\infty}\mathrm{d}l\left\langle\frac{l+p_2}{\sqrt{2}}\right|_x\left\langle-\frac{l-p_2}{\sqrt{2}}\right|_p\hat{\rho}_1\otimes\hat{\rho}_2\hat{\mathcal{S}}_{p,1}(\sqrt{2\pi})\hat{\mathcal{S}}_{x,2}(-\sqrt{2\pi})\left|\frac{l+p_2}{\sqrt{2}}\right\rangle_x\left|-\frac{l-p_2}{\sqrt{2}}\right\rangle_p \tag{D82}$$

$$= \int_{-\infty}^{\infty}\mathrm{d}l\left\langle\frac{l+p_2}{\sqrt{2}}\right|_x\hat{\rho}_1\hat{\mathcal{S}}_{p,1}(\sqrt{2\pi})\left|\frac{l+p_2}{\sqrt{2}}\right\rangle_x\left\langle-\frac{l-p_2}{\sqrt{2}}\right|_p\hat{\rho}_2\hat{\mathcal{S}}_{x,2}(-\sqrt{2\pi})\left|-\frac{l-p_2}{\sqrt{2}}\right\rangle_p. \tag{D83}$$

The left term in the integral of Eq. (D87) is

$$\langle q|_x\hat{\tilde{\rho}}\hat{\mathcal{S}}_p(\sqrt{2\pi})|q\rangle_x = \langle q|_x\int_{\mathbb{C}}\mathrm{d}^2\alpha\, G_{\Sigma}(\alpha)\hat{D}(\alpha)|\varnothing\rangle\langle\varnothing|\hat{D}^{\dagger}(\alpha)\hat{\mathcal{S}}_p(\sqrt{2\pi})|q\rangle_x \tag{D84}$$

$$= \int_{\mathbb{C}}\mathrm{d}^2\alpha\, G_{\Sigma}(\alpha)\langle q|_x\hat{D}(\alpha)|\varnothing\rangle\langle\varnothing|\hat{D}^{\dagger}(\alpha)\hat{\mathcal{S}}_p(\sqrt{2\pi})|q\rangle_x \tag{D85}$$

$$= \int_{\mathbb{C}}\mathrm{d}^2\alpha\, G_{\Sigma}(\alpha)\langle q|_x\hat{D}(\alpha)|\varnothing\rangle\langle\varnothing|\hat{\mathcal{S}}_p(\sqrt{2\pi})\hat{D}^{\dagger}(\alpha)|q\rangle_x e^{-2i\sqrt{\pi}\mathrm{Im}(\alpha)} \tag{D86}$$

$$= \int_{\mathbb{C}}\mathrm{d}^2\alpha\, G_{\Sigma}(\alpha)e^{-2i\sqrt{\pi}\mathrm{Im}(\alpha)}\langle q|_x\hat{D}(\alpha)|\varnothing\rangle\langle\varnothing|\hat{D}^{\dagger}(\alpha)|q\rangle_x \tag{D87}$$

$$= \int_{\mathbb{C}}\mathrm{d}^2\alpha\, G_{\Sigma}(\alpha)e^{-2i\sqrt{\pi}\mathrm{Im}(\alpha)}|\langle\varnothing|\hat{D}(-\alpha)|q\rangle_x|^2 \tag{D88}$$

$$= \int_{\mathbb{C}}\mathrm{d}^2\alpha\, G_{\Sigma}(\alpha)e^{-2i\sqrt{\pi}\mathrm{Im}(\alpha)}|\langle\varnothing|q-\sqrt{2}\mathrm{Re}(\alpha)\rangle_x|^2 \tag{D89}$$

$$= \int_{\mathbb{C}}\mathrm{d}^2\alpha\frac{1}{2\pi\sqrt{\Sigma_0\Sigma_1}}\exp\left(-\frac{\mathrm{Re}(\alpha)^2}{\Sigma_0}\right)\exp\left(-\frac{\mathrm{Im}(\alpha)^2}{\Sigma_1}\right)\exp[-2i\sqrt{\pi}\mathrm{Im}(\alpha)]|\langle\varnothing|q-\sqrt{2}\mathrm{Re}(\alpha)\rangle_x|^2 \tag{D90}$$

$$= \frac{1}{\pi\sqrt{\Sigma_0\Sigma_1}}\int_{-\infty}^{\infty}\mathrm{d}\,\mathrm{Re}(\alpha)\exp\left(-\frac{\mathrm{Re}(\alpha)^2}{\Sigma_0}\right)|\langle\varnothing|q-\sqrt{2}\mathrm{Re}(\alpha)\rangle_x|^2 \times\int_{-\infty}^{\infty}\mathrm{d}\,\mathrm{Im}(\alpha)\exp\left(-\frac{\mathrm{Im}(\alpha)^2}{\Sigma_1}\right)e^{-2i\sqrt{\pi}\mathrm{Im}(\alpha)} \tag{D91}$$

$$= \frac{1}{\pi\sqrt{\Sigma_0\Sigma_1}}\int_{-\infty}^{\infty}\mathrm{d}\,\mathrm{Re}(\alpha)\exp\left(-\frac{\mathrm{Re}(\alpha)^2}{\Sigma_0}\right)|\langle\varnothing|q-\sqrt{2}\mathrm{Re}(\alpha)\rangle_x|^2 \times\int_{-\infty}^{\infty}\mathrm{d}\,\mathrm{Im}(\alpha)\exp\left[-\left(\frac{\mathrm{Im}(\alpha)}{\sqrt{\Sigma_1}}+i\sqrt{\pi\Sigma_1}\right)^2\right]\exp(-\pi\Sigma_1) \tag{D92}$$

$$= \frac{\exp(-\pi\,\Sigma_1)}{\pi\sqrt{\Sigma_0\,\Sigma_1}} \int_{-\infty}^{\infty} \mathrm{d}\,\mathrm{Re}(\alpha)\exp\left(-\frac{\mathrm{Re}(\alpha)^2}{\Sigma_0}\right)|\langle\varnothing|q-\sqrt{2}\mathrm{Re}(\alpha)\rangle_x|^2$$
$$\times \int_{-\infty}^{\infty} \mathrm{d}\,\mathrm{Im}(\alpha)\exp\left(-\frac{\mathrm{Im}(\alpha)^2}{\Sigma_1}\right) \tag{D93}$$
$$= \frac{\exp(-\pi\,\Sigma_1)}{\pi\sqrt{\Sigma_0\,\Sigma_1}} \int_{-\infty}^{\infty} \mathrm{d}\,\mathrm{Re}(\alpha)\exp-\frac{\mathrm{Re}(\alpha)^2}{\Sigma_0}$$
$$\times \int_{-\infty}^{\infty} \mathrm{d}\,\mathrm{Im}(\alpha)\exp\left(-\frac{\mathrm{Im}(\alpha)^2}{\Sigma_1}\right)|\langle\varnothing|\hat{D}^\dagger(\alpha)|q\rangle_x|^2 \tag{D94}$$
$$= \exp(-\pi\,\Sigma_1)\int_{-\infty}^{\infty} \mathrm{d}^2\alpha\; G_\Sigma(\alpha)\langle q|_x\hat{D}(\alpha)|\varnothing\rangle\langle\varnothing|\hat{D}^\dagger(\alpha)|q\rangle_x \tag{D95}$$
$$= \exp(-\pi\,\Sigma_1)\langle q|_x\hat{\tilde{\rho}}|q\rangle_x. \tag{D96}$$

The right term in the integral of Eq. (D87) is

$$\langle q|_p\hat{\tilde{\rho}}\hat{\mathcal{S}}_x(-\sqrt{2\pi})|q\rangle_p = \langle q|_p\int_{\mathbb{C}} \mathrm{d}^2\alpha\; G_\Sigma(\alpha)\hat{D}(\alpha)|\varnothing\rangle\langle\varnothing|\hat{D}^\dagger(\alpha)\hat{\mathcal{S}}_x(-\sqrt{2\pi})|q\rangle_p \tag{D97}$$
$$= \int_{\mathbb{C}} \mathrm{d}^2\alpha\; G_\Sigma(\alpha)\langle q|_p\hat{D}(\alpha)|\varnothing\rangle\langle\varnothing|\hat{D}^\dagger(\alpha)\hat{\mathcal{S}}_x(-\sqrt{2\pi})|q\rangle_p \tag{D98}$$
$$= \int_{\mathbb{C}} \mathrm{d}^2\alpha\; G_\Sigma(\alpha)\langle q|_p\hat{D}(\alpha)|\varnothing\rangle\langle\varnothing|\hat{\mathcal{S}}_x(-\sqrt{2\pi})\hat{D}^\dagger(\alpha)|q\rangle_p e^{-2i\sqrt{\pi}\mathrm{Re}(\alpha)} \tag{D99}$$
$$= \int_{\mathbb{C}} \mathrm{d}^2\alpha\; G_\Sigma(\alpha)e^{-2i\sqrt{\pi}\mathrm{Re}(\alpha)}\langle q|_p\hat{D}(\alpha)|\varnothing\rangle\langle\varnothing|\hat{D}^\dagger(\alpha)|q\rangle_p \tag{D100}$$
$$= \int_{\mathbb{C}} \mathrm{d}^2\alpha\; G_\Sigma(\alpha)e^{-2i\sqrt{\pi}\mathrm{Re}(\alpha)}|\langle\varnothing|\hat{D}(-\alpha)|q\rangle_p|^2 \tag{D101}$$
$$= \int_{\mathbb{C}} \mathrm{d}^2\alpha\; G_\Sigma(\alpha)e^{-2i\sqrt{\pi}\mathrm{Re}(\alpha)}|\langle\varnothing|q-\sqrt{2}\mathrm{Im}(\alpha)\rangle_p|^2 \tag{D102}$$
$$= \int_{\mathbb{C}} \mathrm{d}^2\alpha\frac{1}{\pi\sqrt{\Sigma_0\,\Sigma_1}}\exp\left(-\frac{\mathrm{Re}(\alpha)^2}{\Sigma_0}\right)\exp\left(-\frac{\mathrm{Im}(\alpha)^2}{\Sigma_1}\right)\exp[-2i\sqrt{\pi}\mathrm{Re}(\alpha)]|\langle\varnothing|q-\sqrt{2}\mathrm{Im}\{\alpha\}\rangle_p|^2 \tag{D103}$$
$$= \frac{1}{\pi\sqrt{\Sigma_0\,\Sigma_1}}\int_{-\infty}^{\infty} \mathrm{d}\,\mathrm{Re}(\alpha)\exp\left(-\frac{\mathrm{Re}(\alpha)^2}{\Sigma_0}\right)e^{-2i\sqrt{\pi}\mathrm{Re}(\alpha)}$$
$$\times \int_{-\infty}^{\infty} \mathrm{d}\,\mathrm{Im}(\alpha)\exp\left(-\frac{\mathrm{Im}(\alpha)^2}{\Sigma_1}\right)|\langle\varnothing|q-\sqrt{2}\mathrm{Im}(\alpha)\rangle_p|^2 \tag{D104}$$
$$= \frac{1}{\pi\sqrt{\Sigma_0\,\Sigma_1}}\int_{-\infty}^{\infty} \mathrm{d}\,\mathrm{Re}(\alpha)\exp-\left(\frac{\mathrm{Re}(\alpha)}{\sqrt{\Sigma_0}}+i\sqrt{\pi\,\Sigma_0}\right)^2\exp(-\pi\,\Sigma_0)$$
$$\times \int_{-\infty}^{\infty} \mathrm{d}\,\mathrm{Im}(\alpha)\exp\left(-\frac{\mathrm{Im}(\alpha)^2}{\Sigma_1}\right)|\langle\varnothing|q-\sqrt{2}\mathrm{Im}(\alpha)\rangle_p|^2 \tag{D105}$$
$$= \frac{\exp(-\pi\,\Sigma_0)}{\pi\sqrt{\Sigma_0\,\Sigma_1}}\int_{-\infty}^{\infty} \mathrm{d}\,\mathrm{Re}(\alpha)\exp\left(-\frac{\mathrm{Re}(\alpha)^2}{\Sigma_0}\right)$$
$$\times \int_{-\infty}^{\infty} \mathrm{d}\,\mathrm{Im}(\alpha)\exp\left(-\frac{\mathrm{Im}(\alpha)^2}{\Sigma_1}\right)|\langle\varnothing|q-\sqrt{2}\mathrm{Im}(\alpha)\rangle_p|^2 \tag{D106}$$
$$= \frac{\exp(-\pi\,\Sigma_0)}{\pi\sqrt{\Sigma_0\,\Sigma_1}}\int_{-\infty}^{\infty} \mathrm{d}\,\mathrm{Re}(\alpha)\exp\left(-\frac{\mathrm{Re}(\alpha)^2}{\Sigma_0}\right)$$
$$\times \int_{-\infty}^{\infty} \mathrm{d}\,\mathrm{Im}(\alpha)\exp\left(-\frac{\mathrm{Im}(\alpha)^2}{\Sigma_1}\right)|\langle\varnothing|\hat{D}^\dagger(\alpha)|q\rangle_p|^2 \tag{D107}$$

$$= \exp(-\pi\,\Sigma_0)\int_{-\infty}^{\infty} \mathrm{d}^2\alpha\, G_\Sigma(\alpha)\langle q|_p\hat{D}(\alpha)|\varnothing\rangle\langle\varnothing|\hat{D}^\dagger(\alpha)|q\rangle_p \tag{D108}$$

$$= \exp(-\pi\,\Sigma_0)\langle q|_p\hat{\tilde{\rho}}|q\rangle_p. \tag{D109}$$

By inserting the results of Eqs. (D101) and (D115) into Eq. (D87), we find that the stabilizer of $\hat{\mathcal{S}}_p$ introduced in (D81) becomes

$$\langle\hat{\mathcal{S}}_p\rangle = \frac{\mathrm{Tr}[(|p_2\rangle\langle p_2|\hat{B}'^\dagger\hat{\tilde{\rho}}_1\otimes\hat{\tilde{\rho}}_2\hat{B}\hat{S}')\hat{\mathcal{S}}_{p,1}(2\sqrt{\pi})]}{\mathrm{Tr}(|p_2\rangle\langle p_2|\hat{B}'^\dagger\hat{\tilde{\rho}}_1\otimes\tilde{\rho}_2\hat{B}')} \tag{D110}$$

$$= \frac{1}{N_{p_2}}\int_{-\infty}^{\infty}\mathrm{d}l\left\langle\frac{l+p_2}{\sqrt{2}}\right|_x\hat{\tilde{\rho}}_1\hat{\mathcal{S}}_{p,1}(\sqrt{2\pi})\left|\frac{l+p_2}{\sqrt{2}}\right\rangle_x\left\langle-\frac{l-p_2}{\sqrt{2}}\right|_p\hat{\tilde{\rho}}_2\hat{\mathcal{S}}_{x,2}(-\sqrt{2\pi})\left|-\frac{l-p_2}{\sqrt{2}}\right\rangle_p \tag{D111}$$

$$= \frac{1}{N_{p_2}}\int_{-\infty}^{\infty}\mathrm{d}l\,\exp(-\pi\,\Sigma_{1,1})\left\langle\frac{l+p_2}{\sqrt{2}}\right|_x\hat{\tilde{\rho}}_1\left|\frac{l+p_2}{\sqrt{2}}\right\rangle_x\exp(-\pi\,\Sigma_{0,2})\left\langle-\frac{l-p_2}{\sqrt{2}}\right|_p\hat{\tilde{\rho}}_2\left|-\frac{l-p_2}{\sqrt{2}}\right\rangle_p \tag{D112}$$

$$= \exp(-\pi\,\Sigma_{1,1})\exp(-\pi\,\Sigma_{0,2})\frac{\int_{-\infty}^{\infty}\mathrm{d}l\langle\frac{l+p_2}{\sqrt{2}}|_x\hat{\tilde{\rho}}_1|\frac{l+p_2}{\sqrt{2}}\rangle_x\langle-\frac{l-p_2}{\sqrt{2}}|_p\hat{\tilde{\rho}}_2|-\frac{l-p_2}{\sqrt{2}}\rangle_p}{N_{p_2}} \tag{D113}$$

$$= \exp(-\pi\,\Sigma_{1,1})\exp(-\pi\,\Sigma_{0,2}) \tag{D114}$$

$$= \exp\left[-\pi\left(\frac{1}{2\pi}\log\frac{1}{|\langle\hat{\mathcal{S}}_{p,1}\rangle_{\rho_1}|^2}+\frac{1}{2\pi}\log\frac{1}{|\langle\hat{\mathcal{S}}_{x,2}^\dagger\rangle_{\rho_2}|^2}\right)\right] \tag{D115}$$

$$= |\langle\hat{\mathcal{S}}_{p,1}\rangle_{\rho_1}||\langle\hat{\mathcal{S}}_{x,2}^\dagger\rangle_{\rho_2}|. \tag{D116}$$

[1] D. E. Browne and T. Rudolph, Resource-efficient linear optical quantum computation, Phys. Rev. Lett. **95**, 010501 (2005).

[2] R. Raussendorf, D. E. Browne, and H. J. Briegel, Measurement-based quantum computation on cluster states, Phys. Rev. A **68**, 022312 (2003).

[3] K. Azuma, S. E. Economou, D. Elkouss, P. Hilaire, L. Jiang, H.-K. Lo, and I. Tzitrin, Quantum repeaters: From quantum networks to the quantum internet, Rev. Mod. Phys. **95**, 045006 (2023).

[4] D. Gottesman, A. Kitaev, and J. Preskill, Encoding a qubit in an oscillator, Phys. Rev. A **64**, 012310 (2001).

[5] A. L. Grimsmo and S. Puri, Quantum error correction with the Gottesman-Kitaev-Preskill code, PRX Quantum **2**, 020101 (2021).

[6] F. Rozpędek, K. Noh, Q. Xu, S. Guha, and L. Jiang, Quantum repeaters based on concatenated bosonic and discrete-variable quantum codes, npj Quantum Inf. **7**, 102 (2021).

[7] Z. Wang and L. Jiang, Passive environment-assisted quantum communication with GKP states, Phys. Rev. X **15**, 021003 (2025).

[8] J. E. Bourassa, R. N. Alexander, M. Vasmer, A. Patil, I. Tzitrin, T. Matsuura, D. Su, B. Q. Baragiola, S. Guha, G. Dauphinais, K. K. Sabapathy, N. C. Menicucci, and I. Dhand, Blueprint for a scalable photonic fault-tolerant quantum computer, Quantum **5**, 392 (2021).

[9] S. Glancy and E. Knill, Error analysis for encoding a qubit in an oscillator, Phys. Rev. A **73**, 012325 (2006).

[10] T. Matsuura, H. Yamasaki, and M. Koashi, Equivalence of approximate Gottesman-Kitaev-Preskill codes, Phys. Rev. A **102**, 032408 (2020).

[11] G. Zheng, W. He, G. Lee, K. Noh, and L. Jiang, Performance and achievable rates of the Gottesman-Kitaev-Preskill code for pure-loss and amplification channels, PRX Quantum **6**, 030314 (2025).

[12] N. C. Menicucci, Fault-tolerant measurement-based quantum computing with continuous-variable cluster states, Phys. Rev. Lett. **112**, 120504 (2014).

[13] K. Noh and C. Chamberland, Fault-tolerant bosonic quantum error correction with the surface–Gottesman-Kitaev-Preskill code, Phys. Rev. A **101**, 012316 (2020).

[14] H. M. Vasconcelos, L. Sanz, and S. Glancy, All-optical generation of states for "encoding a qubit in an oscillator", Opt. Lett. **35**, 3261 (2010).

[15] D. Su, C. R. Myers, and K. K. Sabapathy, Conversion of Gaussian states to non-Gaussian states using photon-number-resolving detectors, Phys. Rev. A **100**, 052301 (2019).

[16] R. Yanagimoto, R. Nehra, R. Hamerly, E. Ng, A. Marandi, and H. Mabuchi, Quantum nondemolition measurements with optical parametric amplifiers for ultrafast universal quantum information processing, PRX Quantum **4**, 010333 (2023).

[17] N. Quesada, L. G. Helt, J. Izaac, J. M. Arrazola, R. Shahrokhshahi, C. R. Myers, and K. K. Sabapathy, Simulating realistic non-Gaussian state preparation, Phys. Rev. A **100**, 022341 (2019).

[18] M. Eaton, R. Nehra, and O. Pfister, Non-Gaussian and Gottesman–Kitaev–Preskill state preparation by photon catalysis, New J. Phys. **21**, 113034 (2019).

[19] K. Takase, F. Hanamura, H. Nagayoshi, J. E. Bourassa, R. N. Alexander, A. Kawasaki, W. Asavanant, M. Endo, and A. Furusawa, Generation of flying logical qubits using generalized photon subtraction with adaptive Gaussian operations Phys. Rev. A **110**, 012436 (2024).

[20] I. Tzitrin, J. E. Bourassa, N. C. Menicucci, and K. K. Sabapathy, Progress towards practical qubit computation using

approximate Gottesman-Kitaev-Preskill codes, Phys. Rev. A **101**, 032315 (2020).
[21] J. E. Bourassa, N. Quesada, I. Tzitrin, A. Száva, T. Isacsson, J. Izaac, K. K. Sabapathy, G. Dauphinais, and I. Dhand, Fast simulation of bosonic qubits via Gaussian functions in phase space, PRX Quantum **2**, 040315 (2021).
[22] B. Dias and R. König, Classical simulation of non-Gaussian bosonic circuits, Phys. Rev. A **110**, 042402 (2024).
[23] N. C. Menicucci, P. van Loock, M. Gu, C. Weedbrook, T. C. Ralph, and M. A. Nielsen, Universal quantum computation with continuous-variable cluster states, Phys. Rev. Lett. **97**, 110501 (2006).
[24] G. Pantaleoni, B. Q. Baragiola, and N. C. Menicucci, Hidden qubit cluster states, Phys. Rev. A **104**, 012431 (2021).
[25] B. W. Walshe, B. Q. Baragiola, H. Ferretti, J. Gefaell, M. Vasmer, R. Weil, T. Matsuura, T. Jaeken, G. Pantaleoni, Z. Han, T. Hillmann, N. C. Menicucci, I. Tzitrin, and R. N. Alexander, Linear-optical quantum computation with arbitrary error-correcting codes, Phys. Rev. Lett. **134**, 100602 (2025).
[26] A. Serafini, *Quantum Continuous Variables: A Primer of Theoretical Methods* (CRC Press, Boca Raton, 2017).
[27] D. J. Weigand and B. M. Terhal, Generating grid states from Schrödinger-cat states without postselection, Phys. Rev. A **97**, 022341 (2018).
[28] A. J. Pizzimenti and D. Soh, Optical Gottesman-Kitaev-Preskill qubit generation via approximate squeezed coherent state superposition breeding, Phys. Rev. A **110**, 062619 (2024).
[29] A. Hertz, A. Z. Goldberg, and K. Heshami, Quadrature coherence scale of linear combinations of Gaussian functions in phase space, Phys. Rev. A **110**, 012408 (2024).
[30] I. Tzitrin, T. Matsuura, R. N. Alexander, G. Dauphinais, J. E. Bourassa, K. K. Sabapathy, N. C. Menicucci, and I. Dhand, Fault-tolerant quantum computation with static linear optics, PRX Quantum **2**, 040353 (2021).
[31] E. Oudot, G. Massé, X. Valcarce, and A. Acín, Realistic Bell tests with homodyne measurements, arXiv:2402.01530.
[32] C. Weedbrook, S. Pirandola, R. García-Patrón, N. J. Cerf, T. C. Ralph, J. H. Shapiro, and S. Lloyd, Gaussian quantum information, Rev. Mod. Phys. **84**, 621 (2012).
[33] V. V. Albert, K. Noh, K. Duivenvoorden, D. J. Young, R. T. Brierley, P. Reinhold, C. Vuillot, L. Li, C. Shen, S. M. Girvin, B. M. Terhal, and L. Jiang, Performance and structure of single-mode bosonic codes, Phys. Rev. A **97**, 032346 (2018).
[34] L. G. Helt and N. Quesada, Degenerate squeezing in waveguides: A unified theoretical approach, J. Phys.: Photonics **2**, 035001 (2020).
[35] M. Oszmaniec and D. J. Brod, Classical simulation of photonic linear optics with lost particles, New J. Phys. **20**, 092002 (2018).
[36] S. Sciara, C. Reimer, M. Kues, P. Roztocki, A. Cino, D. J. Moss, L. Caspani, W. J. Munro, and R. Morandotti, Universal N-partite d-level pure-state entanglement witness based on realistic measurement settings, Phys. Rev. Lett. **122**, 120501 (2019).
[37] G. Tóth and O. Gühne, Entanglement detection in the stabilizer formalism, Phys. Rev. A **72**, 022340 (2005).
[38] N. Raveendran, N. Rengaswamy, F. Rozpędek, A. Raina, L. Jiang, and B. Vasić, Finite rate QLDPC-GKP coding scheme that surpasses the CSS Hamming bound, Quantum **6**, 767 (2022).
[39] N. J. Cerf, G. Leuchs, and E. S. Polzik, *Quantum Information with Continuous Variables of Atoms and Light* (World Scientific, Singapore, 2007).
[40] K. Fukui, A. Tomita, and A. Okamoto, Analog quantum error correction with encoding a qubit into an oscillator, Phys. Rev. Lett. **119**, 180507 (2017).
[41] M. Lin and K. Noh, Exploring the quantum capacity of a Gaussian random-displacement channel using Gottesman-Kitaev-Preskill codes and maximum-likelihood decoding, Phys. Rev. A **111**, 052445 (2025).
[42] K. Duivenvoorden, B. M. Terhal, and D. Weigand, Single-mode displacement sensor, Phys. Rev. A **95**, 012305 (2017).
[43] Fock-basis simulations are carried out in python using Mr Mustard, https://mrmustard.Readthedocs.Io/en/stable/.
[44] V. Crescimanna, A. Z. Goldberg, and K. Heshami, Seeding Gaussian boson samplers with single photons for enhanced state generation, Phys. Rev. A **109**, 023717 (2024).
[45] B. C. Travaglione and G. J. Milburn, Preparing encoded states in an oscillator, Phys. Rev. A **66**, 052322 (2002).
[46] C. Flühmann, T. L. Nguyen, M. Marinelli, V. Negnevitsky, K. Mehta, and J. P. Home, Encoding a qubit in a trapped-ion mechanical oscillator, Nature (London) **566**, 513 (2019).
[47] P. Campagne-Ibarcq, A. Eickbusch, S. Touzard, E. Zalys-Geller, N. E. Frattini, V. V. Sivak, P. Reinhold, S. Puri, S. Shankar, R. J. Schoelkopf, L. Frunzio, M. Mirrahimi, and M. H. Devoret, Quantum error correction of a qubit encoded in grid states of an oscillator, Nature (London) **584**, 368 (2020).
[48] B. Royer, S. Singh, and S. M. Girvin, Stabilization of finite-energy Gottesman-Kitaev-Preskill states, Phys. Rev. Lett. **125**, 260509 (2020).
[49] U. Chabaud, D. Markham, and F. Grosshans, Stellar representation of non-Gaussian quantum states, Phys. Rev. Lett. **124**, 063605 (2020).
[50] A. I. Lvovsky and J. Mlynek, Quantum-optical catalysis: Generating nonclassical states of light by means of linear optics, Phys. Rev. Lett. **88**, 250401 (2002).
[51] A. Ourjoumtsev, R. Tualle-Brouri, J. Laurat, and P. Grangier, Generating optical Schrödinger kittens for quantum information processing, Science **312**, 83 (2006).
[52] K. B. Petersen and M. S. Pedersen, The Matrix Cookbook, version 20121115 (2012), http://matrixcookbook.com/.
[53] H. H. Andersen, M. Højbjerre, D. Sørensen, P. Eriksen, H. Andersen, M. Højbjerre, D. Sørensen, and P. Eriksen, *Linear and Graphical Models: for the Multivariate Complex Normal Distribution*, Lecture Notes in Statistics Vol. 101 (Springer, New York, 1995), pp. 15–37.

Chapter 5

Quantum Control of Rydberg Atoms for Quantum State and Circuit Preparation

5.1 Introduction

Rydberg atoms can also serve as a physical platform for the efficient realization of universal quantum computation. As mentioned in Section 1.13, "Rydberg atoms" can potentially refer to various implementations, including trapped ions or semiconductor platforms. However, if we focus specifically on neutral atoms, we observe that they can be trapped with relative ease and positioned in space—with respect to one another—with good precision. When encoding the qubit in the energy levels of Rydberg atoms, these systems exhibit long coherence times. Manipulation of the qubit state—corresponding to transitions between different electronic energy levels—can be achieved using laser driving at the resonance frequency, which enables high-fidelity single-qubit gates. Regarding two-qubit gates, the Rydberg blockade

phenomenon can be exploited to implement controlled operations: an atom located within the Rydberg radius of another can be either excited or not, depending on its Rydberg state, to allow or block operations on the neighboring atom. To implement controlled gates between atoms separated by more than the Rydberg radius, one can resort to multi-qubit entangling gates using intermediary atoms. Yet, this approach may be challenging, as each gate introduces noise, and the increased computation time makes the system more susceptible to decoherence. An alternative method for preparing arbitrary quantum states relies on the quantum approximate optimization algorithm, introduced in Section 1.3.4.1. The idea behind QAOA developed from the more well-known Quantum Annealing (QA), which allows a quantum system to evolve toward the ground state of a Hamiltonian H_Z, starting from an eigenstate of another Hamiltonian H_X, under the time evolution of a total Hamiltonian as described in Equation (1.28). In contrast, QAOA aims to approximate a target state after a finite evolution time t_p, and it can target arbitrary quantum states, not necessarily eigenstates of any Hamiltonian. Looking at the Hamiltonians in Equation (1.30), we observe that this approach is particularly well-suited to implementation with Rydberg atoms, as it requires only two-qubit gates. In our work, we considered a linear array of five Rydberg atoms and applied QAOA to obtain different quantum states, including a quantum error correction circuit, which is difficult to implement using a conventional gate-based approach. The results show that, for a sufficient number of iterations—each involving the application of the cost and mixing Hamiltonians—the desired states and circuits can be produced with high fidelity. These results were obtained by classically optimizing the application times α, β for each Hamiltonian, corresponding to the duration of the laser pulses at the specific resonance frequencies. Similarly, it was observed that even in the presence of laser amplitude noise, the

states still achieve good fidelity, albeit slightly lower than those achieved in noiseless circuits with the same number of iterations. Lastly, although in our work we did not consider the case where Rydberg blockade affects non-nearest-neighbor qubits, the method can be extended to account for this type of interaction as well.

Quantum Control of Rydberg Atoms for Mesoscopic Quantum State and Circuit Preparation

Valerio Crescimanna,[1,2,*,†] Jacob Taylor,[1,3,†] Aaron Z. Goldberg,[1,2] and Khabat Heshami[1,2,4]

[1] *National Research Council of Canada, 100 Sussex Drive, Ottawa, Ontario K1N 5A2, Canada*

[2] *Department of Physics, University of Ottawa, 25 Templeton Street, Ottawa, Ontario K1N 6N5 Canada*

[3] *Institute for Quantum Computing University of Waterloo, 200 University Avenue West, Waterloo, Ontario N2L 3G1, Canada*

[4] *Institute for Quantum Science and Technology, Department of Physics and Astronomy, University of Calgary, Alberta T2N 1N4, Canada*

(Received 6 February 2023; revised 22 June 2023; accepted 26 July 2023; published 11 September 2023)

Individually trapped Rydberg atoms show significant promise as a platform for scalable quantum simulation and for the development of programmable quantum computers. In particular, the Rydberg-blockade effect can be used to facilitate both fast qubit-qubit interactions and long coherence times via low-lying electronic states encoding the physical qubits. To bring existing Rydberg-atom-based platforms a step closer to fault-tolerant quantum computation, we demonstrate high-fidelity state and circuit preparation in a system of five atoms. We specifically show that quantum control can be used to reliably generate fully connected cluster states and to simulate the error-correction encoding circuit based on the "Perfect Quantum Error Correcting Code" by Laflamme *et al.* [Phys. Rev. Lett. **77**, 198 (1996)]. Our results make these ideas and their implementation directly accessible to experiments and demonstrate a promising level of noise tolerance with respect to experimental errors. With this approach, we motivate the application of quantum control in small subsystems in combination with the standard gate-based quantum circuits for direct and high-fidelity implementation of few-qubit modules.

DOI: 10.1103/PhysRevApplied.20.034019

I. INTRODUCTION

Quantum computing represents a paradigm shift in information processing. A scalable and fault-tolerant quantum computer will likely offer computational advantage in particular areas. Arguably, gate-based quantum computation and, to some extent, measurement-based quantum computation [1–3] are the current dominant paths forward for the leading implementations of quantum computing [4–10]. Unlocking the full potential of quantum computation will depend on our ability to resolve barriers to scalability and fault tolerance. Quantum control is effective in optimizing the performance of individual gates [11–13]. In this work, we extend the application of quantum control to high-fidelity generation of multiqubit quantum states and circuits where sequential application of multiple multiqubit gates is necessary.

Our approach to extending quantum control to multiple qubits is based on unitary constructions inspired by the quantum approximate optimization algorithm (QAOA) [14]. The QAOA, by Farhi *et al.*, proposes an approach to find approximate solutions to combinatorial optimization problems that are achieved by a Trotterized approximation of the quantum adiabatic dynamics [14]. This has been shown to be universal for quantum computation with Hamiltonians that are homogeneous sums of single-qubit Pauli X and two-local ZZ operators [15]. One necessity of quantum technologies is to prepare specific quantum states or enact specific unitary operations. This should always be possible but may require prohibitively complex multiqubit quantum gates. Here, instead, we apply quantum control to realize desired states and circuits through an algorithm that requires interactions among qubits that are at most two-local and are restricted to a linear geometry.

Rydberg atoms are a particularly attractive system for implementing these ideas. With the remarkable progress in development of arrays of individually trapped Rydberg atoms and their application in quantum simulation [16–21], it is desirable to enhance our abilities in quantum computation with Rydberg atoms. In fact, Rydberg atoms can today be aligned with optical tweezers to form an array of tens of atoms, making this one of the largest platforms for physically realizing quantum computers in terms of number of qubits [19]. The local gates controlling the single atoms can be realized through Rabi oscillations

*[redacted]

†These authors contributed equally to this work.

by properly setting the frequency, intensity, and exposure times to laser pulses [22]. The strong long-range interaction that leads to the so-called Rydberg blockade [23,24] is activated by, instead, exciting atoms to their high-lying Rydberg states. In such a way, all the operators required by our algorithm can be experimentally realized with optimization variables that are mapped accordingly to tunable physical parameters of the lasers [25–27].

Thus far, Rydberg atoms have been used for generating and detecting nontrivial quantum states of many atoms [28–30], based on engineering the energy spectrum of a Rydberg-atom quantum simulator. As some quantum states remain far from the energy eigenstates of any local Hamiltonian [31], it is important to consider methods such as ours for the generation of arbitrary quantum states or simulation of quantum circuits beyond a single operation.

We begin with an introduction to the QAOA, a comparison with quantum annealing (QA), and a description of the universal quantum control developed from the optimization algorithm. We discuss the mapping of the parameters used for the implementation with the Rydberg atoms in Sec. IV. In Sec. V, we introduce state-preparation and circuit-simulation examples to test our protocol. We then evaluate the performance of the algorithm for different implementation depths and noise levels in Sec. VI, providing an important perspective on resource trade-offs for quantum control in realistic conditions.

II. THE QAOA

The QAOA is a hybrid classical-quantum variational algorithm able to provide approximate solutions to optimization problems. The QAOA was originally introduced to address the MaxCut problem [14], an important combinatorial problem in graph theory. In turn, the MaxCut problem can be encoded into the Sherrington-Kirkpatrick model for spin glasses by tuning the interactions among a series of spins. Due to this equivalence, finding the ground state of a spin-glass Hamiltonian is equivalent to finding the solution of the MaxCut problem encoded within. In a similar way, whenever an analogous encoding into a physical system can be found for a combinatorial problem under investigation, the solution corresponds to the ground state of the Hamiltonian of the system. The QAOA then guarantees that we can find the ground state of such a Hamiltonian with a fidelity that increases with the number of steps chosen for the algorithm.

The QAOA can be interpreted as an evolved version of the well-known QA algorithm. With QA, the initial state is set to be the ground state of an initial Hamiltonian, which is the so-called mixing Hamiltonian. Then, the state is allowed to evolve under a time-dependent Hamiltonian that converges, after a sufficiently long time, to the cost Hamiltonian the ground state of which is sought. This scheme was originally proposed to solve the Ising problem [32], where the Ising model is a well-known specialization of the Sherrington-Kirkpatrick model, which has been conveniently used to encode the MaxCut problem and has a broad range of additional applications [33].

A system of N spins can have couplings with any number of the other spins arbitrarily far away and will have its energy affected by an external magnetic field **h**. If the direction of this field is chosen to be the z axes of the spins, the resulting generalized Sherrington-Kirkpatrick model has the Hamiltonian [34]

$$H_Z = \sum_{i_1}^{N} h_{i_1} Z_{i_1} + \sum_{i_1,i_2}^{N} J_{i_1 i_2} Z_{i_1} Z_{i_2} + \sum_{i_1,i_2,i_3}^{N} J_{i_1 i_2 i_3} Z_{i_1} Z_{i_2} Z_{i_3} + \cdots . \tag{1}$$

Here, $J_{i\ldots k}$ is the k-local interaction energy between the qubits at sites $i,\ldots,k$ and Z_i represents the Pauli operator σ_z acting on the ith qubit of the N-qubit state. The different parameters $J_{i\ldots k}$ correspond to different physical situations and also to different combinatorial problems.

In order to identify the ground state of the cost Hamiltonian given in Eq. (1), QA proposes to initialize an N-qubit state that is a linear superposition of all of the computational basis states. This is chosen to be an easy-to-prepare eigenstate of the mixing Hamiltonian, where the latter is so named because it combines all of the basis states. An example of such a state is $|+ + \cdots +\rangle$, which is an eigenstate of the Hamiltonian $H_X = \sum_i X_i$ with eigenvalue $+N$. Due to this initialization, any eigenstate of the cost Hamiltonian H_Z can be reached when the state evolves under a time-dependent Hamiltonian that starts from H_X and equals the cost Hamiltonian after a sufficiently long time τ. The Hamiltonian used to evolve the state in the QA is a time-dependent linear combination of the cost Hamiltonian H_Z and the mixing Hamiltonian H_X:

$$H(t) = \left(1 - \frac{t}{\tau}\right) H_X + \frac{t}{\tau} H_Z. \tag{2}$$

Since the cost and the mixing Hamiltonian do not commute with each other, realizing the evolution under each of the two terms independently requires using the Suzuki-Trotter decomposition into a formally infinite number of alternating steps of applying H_X and H_Z: $\exp(A+B) = \lim_{p\to\infty} \left(e^{A/p} e^{B/p}\right)^p$.

The probability of evolving to the actual ground state of the cost Hamiltonian H_Z improves for larger values of the coefficient τ that defines the temporal dependence of the Hamiltonian. However, letting the system evolve for excessively long times tends to expose it to decoherence. The QAOA partially intervenes to solve this kind of problem. In the QAOA, the Suzuki-Trotter formula is used to separate the noncommuting terms that form the time-dependent Hamiltonian of QA, the mixing Hamiltonian,

and the cost Hamiltonian but with the caveat that each is only applied a finite number of times. The QAOA thus ends up being an algorithm with p steps, where the unitary evolutions under the two Hamiltonians can be more easily realized, since they are time independent and can be encoded in quantum gates.

In fact, the Trotterization of QA with a finite number of steps p directly approximates the evolution that one would have with the time-dependent Hamiltonian required by QA. However, each of the time parameters of the QAOA can be classically optimized to provide a state the fidelity of which is larger than what QA might provide after annealing for the same amount of time. The optimal state is then found by alternatively applying the unitary evolutions that describe the evolution under H_X and H_Z:

$$\begin{aligned}\left|\psi_f\right\rangle = &\exp\left(-\mathrm{i}\alpha_p H_X\right)\exp\left(-\mathrm{i}\beta_p H_Z\right)\cdots \\ &\times \exp(-\mathrm{i}\beta_1 H_Z)\left|\psi_i\right\rangle, \end{aligned} \tag{3}$$

where the parameters α_i and β_i are the so-called Rabi angles at the ith step. To wit, the QAOA can be read as a Trotterization of an adiabatic schedule with a finite number of iterations in which the time parameters are tuned through a classical optimization.

Moreover, the QAOA is a universal algorithm [15]. In fact, if the mixing Hamiltonian H_X and the cost Hamiltonian H_Z are set to be

$$\begin{aligned} H_X &= \sum_i X_i, \\ H_Z &= \sum_i \beta^{(0)} Z_{2i} + \beta^{(1)} Z_{2i+1} + \gamma^{(0)} Z_{2i} Z_{2i+1} \\ &\quad + \gamma^{(1)} Z_{2i+1} Z_{2i} \\ &\equiv \beta^{(0)} H_Z^{(0)} + \beta^{(1)} H_Z^{(1)} + \gamma^{(0)} H_{ZZ}^{(0)} + \gamma^{(1)} H_{ZZ}^{(1)}, \end{aligned} \tag{4}$$

the algorithm is capable of reaching any desired state. In the above equations, the sum is made over all of the qubits of the N-qubit state and X_i is the σ_x Pauli operator applied to the ith qubit. In this case, Eq. (3) reads

$$\begin{aligned}\left|\psi_f\right\rangle = &\,\mathrm{e}^{-\mathrm{i}\alpha_n H_X}\mathrm{e}^{-\mathrm{i}\beta_n^{(0)} H_Z^{(0)}}\mathrm{e}^{-\mathrm{i}\beta_n^{(1)} H_Z^{(1)}}\mathrm{e}^{-\mathrm{i}\gamma_n^{(0)} H_{ZZ}^{(0)}}\mathrm{e}^{-\mathrm{i}\gamma_n^{(1)} H_{ZZ}^{(1)}} \\ &\times\cdots\mathrm{e}^{-\mathrm{i}\alpha_1 H_X}\mathrm{e}^{-\mathrm{i}\beta_1^{(0)} H_Z^{(0)}}\mathrm{e}^{-\mathrm{i}\beta_1^{(1)} H_Z^{(1)}}\mathrm{e}^{-\mathrm{i}\gamma_1^{(0)} H_{ZZ}^{(0)}} \\ &\times\mathrm{e}^{-\mathrm{i}\gamma_1^{(1)} H_{ZZ}^{(1)}}\left|\psi_i\right\rangle. \end{aligned} \tag{5}$$

All of the terms in the Hamiltonian have the advantage of being at most two-local, so they do not require physical systems with long range interactions. Since all the terms in the cost Hamiltonian commute, the Baker-Campbell-Hausdorff formula has been used to write the exponential of the sum as a product of exponentials, given that the individual exponentials can be more easily encoded in a gate-based circuit. Despite the just-described similarity between the QAOA and a Trotterization of QA, there exists a deep difference between the two protocols. With QA, the ground state of a given cost Hamiltonian is obtained by evolving the initial state under the time-dependent Hamiltonian $H(t)$ of Eq. (2). In fact, given a cost Hamiltonian H_Z and an initial state $|\psi_i\rangle$, the resulting state, $|\psi\rangle = \int_0^\tau e^{-iH(t)}|\psi_i\rangle\,\mathrm{d}t$, should minimize $\langle\psi|H_Z|\psi\rangle$ for sufficiently large values of τ. The optimization of the parameters α and $\boldsymbol{\beta}$ in Eq. (5) can be performed in a similar fashion to generate an evolution that minimizes $\left\langle\psi_f\right|H_Z\left|\psi_f\right\rangle$, where $\left|\psi_f\right\rangle$ is as defined in Eq. (5). However, the protocol is much more general than this and the parameters $(\alpha, \boldsymbol{\beta})$ can be used to find the ground state of any cost Hamiltonian H_C by minimizing $\left\langle\psi_f\right|H_C\left|\psi_f\right\rangle$, or even quantum states $|\psi_T\rangle$ that are far from the ground state of any local Hamiltonian if the cost function to minimize is set to be $-|\langle\psi_T|\psi_f\rangle|^2$. Analogously, with the QAOA, we can approximate with arbitrary precision an target operator O. With regard to these last two applications, the terms H_X and H_Z of Eq. (4) lose the role of mixing and cost Hamiltonian, respectively, which has been given to them in the context of QA, but the evolution of the states under these Hamiltonians remains functional for the QAOA. In summary, the QAOA can be used to realize any state with arbitrary precision by only employing Hamiltonians that are at most two-local. The use of longer sequences allows the creation of more complicated states, the entanglement of which can grow in a known fashion [35]. The algorithm then provides a recipe for the realization of any quantum state in the chosen physical implementation. This has an advantage over other generation protocols that rely on extra resources such as ancillary qubits, perfect local operations, and Bell-state measurements [36]; our algorithm has the benefit of being able to incorporate realistic experimental imperfections.

By using the QAOA protocol, we investigate the generation of a variety of states including absolutely maximally entangled states with five and six qubits and Greenberger-Horne-Zeilinger (GHZ) states, all of which can successfully be generated by the protocol. Some of those specific states can be created with specific protocols but ours can be applied to the preparation of arbitrary states and circuits. We focus our in-depth discussion on fully connected cluster states and on the error-correction encoding circuit, which are challenging to produce with alternative approaches. As an example, in a Rydberg platform, an error-encoding circuit might be more conveniently generated if long range interactions beyond nearest neighbors can be introduced; however, this would come at the cost of larger errors proportional to the number of sites involved in the interaction itself [37], which is why we seek alternative strategies that rely only on simpler interactions.

III. RYDBERG SCHEME

Rydberg states are particular excited states of an electron of an atom that is subjected to a Coulomb potential [38]. Those states are usually realized with atoms of alkali elements such as potassium, cesium, and, most often, rubidium. In the alkali elements, the electron farthest from the nucleus is shielded from the attractive potential of the latter by all the other electrons, which completely fill the lower energetic levels of the same atom. The less intense effective potential leads to easier control of the outermost electron and, as a result, Rydberg atoms behave in many respects like hydrogen atoms and can be described accordingly for several applications.

Rydberg atoms can be collected in arrays using dipole traps such as the optical tweezers depicted in Fig. 1(a). For each atom, we define three accessible energetic levels [Fig. 1(b)]. The ground state $|g\rangle \equiv |0\rangle$ and the excited state $|e\rangle \equiv |1\rangle$ are set to be the states defining the computational basis. Furthermore, the electron may accede to the Rydberg state, a third energetic level $|r\rangle$ with larger energy.

The Rydberg state allows the realization of an entangling gate between a pair of Rydberg atoms due to the long-range interaction that arises when one atom is on this last energetic level; this phenomenon is known as the Rydberg blockade. In the Rydberg blockade, one atom in the Rydberg state acts as the control by shifting the same energetic level of the target atom through van der Waals forces, due to a specific dipole interaction between the atoms that increases with the distance of the electron from the nucleus. The Hamiltonian that describes the interactions of the Rydberg atoms with themselves and a shining laser is

$$\frac{H}{\hbar} = \sum_i \frac{\Omega_i(t)}{2}\left(\sigma_i^{1\mapsto r} + \sigma_i^{r\mapsto 1}\right) - \sum_i \Delta(t) n_i + \sum_{i>j} V_{ij} n_i n_j , \tag{6}$$

where i ranges over all of the atoms, $\sigma_i^{m\mapsto n} = |n\rangle_i\langle m|$ sends the ith atom in state $|m\rangle$ to state $|n\rangle$, and $n_i = |r\rangle_i\langle r|$, while Ω is the Rabi frequency, Δ is the detuning, and V labels the so-called van der Waals interaction that scales with the sixth power of the distance between the atoms [16]. The influence of this interaction extends up to the so-called blockade radius, so it can be switched off for non-nearest-neighbor qubits with a suitable choice of the spacing between atoms [24].

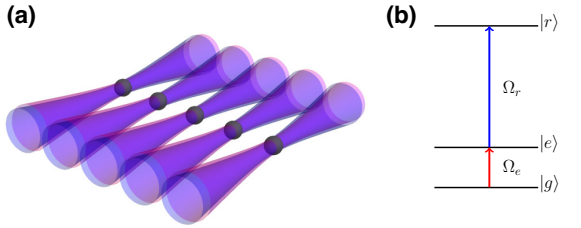

FIG. 1. (a) Dipole-trapped Rydberg atoms within a line separated by a distance of 5.74 μm, used for the purpose of generating nontrivial states, with an inlay of the Rydberg level structure. (b) The red arrow represents the global driving pulse, driving $|g\rangle \mapsto |e\rangle$, the blue arrow represents the atom-specific resonant driving pulse from $|e\rangle \mapsto |r\rangle$, and the dipole trapping consists of a third set of lasers perpendicular to the plane.

When the control atom is in the Rydberg state and the target atom is in the excited state, a 2π pulse on the target does not lead to any change of phase, whereas such a pulse would flip the phase if the control atom was in the ground state. This behavior allows us to implement the two-qubit logical gate required by the QAOA.

IV. RYDBERG EQUIVALENCE

In order to experimentally realize the single-qubit operators on the dipole-trapped Rydberg atoms, the Rabi cycle is used. In the rotating-wave approximation and when the frequency of the laser is resonant with the energy splitting between the two logical states, the Hamiltonian for a particular atom is given by

$$H_x = \Omega\sigma_x, \tag{7}$$

where Ω is one half of the Rabi frequency of the system and σ_x is the NOT or bit-flip quantum gate that acts on one qubit. As a consequence, the mapping between the time parameter α introduced in Eq. (5) and the pulse time of the laser is fixed by $\alpha = \Omega t$; the same pulse must act on all N qubits to enact H_X.

The second operator that is used to realize universal quantum control with the QAOA is the single-qubit operator σ_z. The unitary operator that describes the evolution under the Hamiltonian for a two-level atom driven by a coherent laser with detuning Δ and generalized Rabi frequency $\Omega' = \sqrt{\Omega^2 + \Delta^2}$ is

$$U(t) = \begin{pmatrix} e^{\frac{i\Delta t}{2}}\left(\cos\left(\frac{\Omega' t}{2}\right) - i\frac{\Delta}{\Omega'}\sin\left(\frac{\Omega' t}{2}\right)\right) & ie^{\frac{i\Delta t}{2}}\frac{\Omega}{\Omega'}\sin\left(\frac{\Omega' t}{2}\right) \\ ie^{-\frac{i\Delta t}{2}}\frac{\Omega}{\Omega'}\sin\left(\frac{\Omega' t}{2}\right) & e^{-\frac{i\Delta t}{2}}\left(\cos\left(\frac{\Omega' t}{2}\right) + i\frac{\Delta}{\Omega'}\sin\left(\frac{\Omega' t}{2}\right)\right). \end{pmatrix} \tag{8}$$

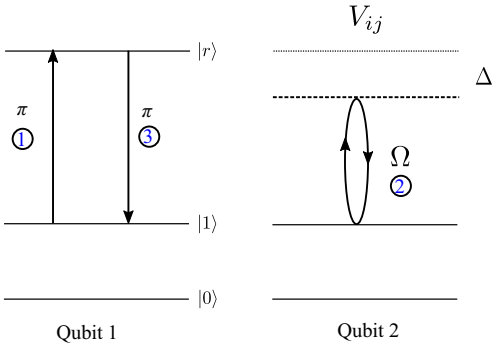

FIG. 2. The formulation of the H_{ZZ} unitary operator in the Rydberg system: it consists of two Rydberg atoms and three pulses. We have updated the labels $|g\rangle$ and $|e\rangle$ to be $|0\rangle$ and $|1\rangle$ to enforce their role as logical qubit states.

When the time is $t = 2\pi/\Omega'$ and the detuning Δ is fixed to $\Delta = -\frac{\beta\Omega}{\sqrt{\pi^2-\beta^2}}$, the evolution of Eq. (8) corresponds to evolution under the Hamiltonian Z for a particular qubit: $U_Z(t) = \exp(-i\beta Z)$. Acting with the same gate on the even (odd) qubits with a detuning fixed by $\beta^{(0)}$ ($\beta^{(1)}$) enacts $H_Z^{(0)}$ ($H_Z^{(1)}$).

Finally, we want to implement a two-qubit entangling operator. The scheme to realize a controlled-Z (CZ) gate consists of three steps as depicted in Fig. 2. First, a π pulse is applied to the control atom; this pulse drives the excited state to the Rydberg state, while it leaves the ground state unaltered. Then, the 2π pulse is applied to the target state as described above. This will lead to a change of phase of the qubit if the control atom is in the ground state, while nothing occurs when it is in the Rydberg state. Finally, a π pulse is again applied to the control atom to drive the Rydberg state to the excited state and thus to repopulate the computational levels. The Rydberg level is indeed only an ancillary level, as the Rydberg states would lie outside the Hilbert space spanned by the states of the computational basis. In such a way, the operator implemented is a CZ gate instead of the ZZ gate presented in Eq. (5). ZZ, however, differs from the CZ gate by just single-qubit operators and a global phase. The mapping of all the parameters used in the QAOA with Rydberg atoms is thus complete and can be used to create the desired state with Rydberg atoms.

V. CLUSTER STATE AND ERROR-CORRECTION ENCODING CIRCUIT

The algorithm described in this work is general and can even be applied to any physical architecture for which the control Hamiltonians H_X and H_Z are applicable but for an analysis of the results we focus on the success of the scheme for generating a five-qubit full cluster state and for realizing the perfect error-correction encoding circuit using the Rydberg-atom platform.

A. Cluster state

Cluster states were first introduced by Briegel and Raussendorf [39]. A general cluster state $|C\rangle$ is defined through the following eigenvalue equation:

$$K_a |C\rangle = (-1)^{k_a} |C\rangle , \tag{9}$$

where the correlation operators are $K_a = X_a \otimes_{b\in N(a)} Z_b$, $N(a)$ identifies the neighborhood of the qubit $a \in C$, and $k_a \in \{0, 1\}$.

A cluster state is a highly entangled state in terms of the Schmidt measure and, compared to other notorious quantum states such as GHZ and W states of the same size, it requires more projective measurements to be disentangled. This property, the so-called persistency of entanglement, is at the basis of one-way quantum computation with cluster states. In one-way quantum computation, a sequence of m projective measurements is realized on a given subset of m qubits of a $(n + m)$-qubit cluster state. The complementary subset of n qubits that have not been measured will then define the n-qubit target state. This scheme, also known as measurement-based quantum computing, is realizable when the initial states have an unbound entanglement width. In fact, this measure of bipartite entanglement is bound for most entangled states, including GHZ states, but it is unbound for cluster states. As such, the cluster state represents a precious resource for universal quantum computation, so as to deserve the great attention that it has attracted since being introduced. As an example, the implementation of this scheme for universal quantum computation has been proposed with Rydberg atoms.

In order to test our scheme, we consider generating a fully entangled cluster state with $k_a = 0$ and in which all the qubits are nearest neighbors of each other and are as depicted in Fig. 3.

B. Error-correction encoding circuit

The efficacy of our algorithm is also evaluated by using it to directly implement the five-qubit circuit used to robustly encode quantum information in the Perfect

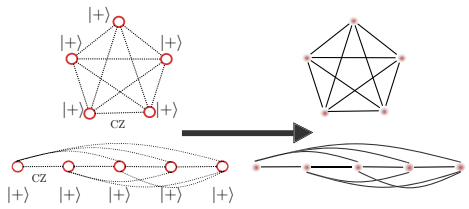

FIG. 3. A diagram of an ideal five-atom cluster state. Starting with all qubits (red circles) in the $|+\rangle$ state, the qubits are then entangled using a CZ gate to each adjacent (i.e., connected with a line) qubit within the diagram. Two separate geometries are depicted that realize the same cluster state.

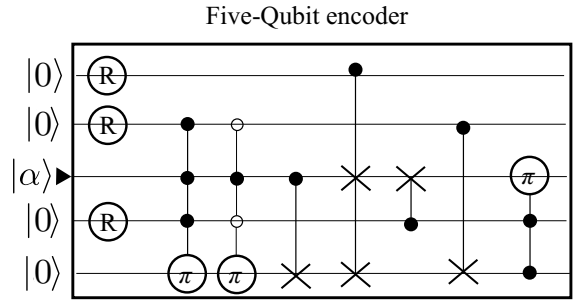

FIG. 4. The perfect quantum error-correction gate [40], where the ith row refers to the ith qubit. The circled "R" represents the application of a Hadamard gate, the circled π represents a π phase change, and the $\times$ symbol represents a NOT gate. These gates are conditional upon all of the circles connected to them being satisfied, where a hollow circle implies the control state needing to be $|0\rangle$ while a filled circle is conditional on $|1\rangle$. The state being encoded is $|\alpha\rangle$, while the rest are auxiliary qubits initialized in state $|0\rangle$.

Quantum Error Correcting Code [40]. In this scheme, the quantum circuit reduces the errors on a logical qubit by distributing the information over five physical qubits: the qubit in the state one wants to preserve and four auxiliary qubits. Once the information of the qubit has been encoded in the five-qubit state, it is possible to retrieve it through a decoder circuit symmetric to the encoder. In fact, the states of the four auxiliary qubits will provide a diagnosis of the error witnessed by the system. Specifically, the code can detect both a sign and a spin flip of any of the qubits. The initial state can finally be restored with a simple unitary transformation of the main qubit. A scheme of the error-correction encoding circuit is shown in Fig. 4.

VI. RESULTS

A. Circuit depth

The number of parameters used to prepare the target state or circuit is not fixed *a priori* and the experimentalist chooses the one that provides satisfactory results on each occasion. We have investigated how the quality of the algorithm depends on the depth of the circuit.

First, we examine the abstract formulation shown in Eq. (5). Optimizing the time parameters for this general formulation is in fact less time consuming than taking into account the Rydberg equivalences described in Sec. V. Moreover, we observe that the Rabi angles found for the general case are good starting values for a subsequent optimization that incorporates details of the physical implementation.

The algorithm is tested by optimizing over different depths p. Once we have fixed the number of parameters $\mathcal{N} = 5p$, we have optimized them to find the state $|\psi_f\rangle$ generated by the algorithm that maximizes the fidelity $\mathcal{F} = \left|\langle |\psi_f\, |C\rangle\right|^2$ with the target state $|C\rangle$. We have sampled 40 states in this way. We have proceeded in an analogous way for different values of $\mathcal{N}$, by sampling 40 states for each $\mathcal{N}$. In particular, we have considered a number of parameters ranging from 20 to 45 for the cluster state. The optimization algorithm used in this analysis is the annealing optimization algorithm. It does not guarantee to provide the optimal set of parameters but the fidelity of the state generated with the parameters provided by this optimization approximates the fidelity of the optimal state. In general, the optimization algorithm provides different results at each run, especially when the parameter space has many dimensions. Therefore, averaging over 40 sampled states for each number of parameters improves the reliability of the results. A monotonic increase for the mean of the fidelities is observed by increasing the depth of the circuit. In fact, the absolute value of the correlation coefficient between the logarithm of the deviation from fidelity and the number of sequences is larger than 97%. A plot of the results for the fidelities obtained for the cluster state and their dependence on the depth of the circuit is shown in Fig. 5. Similarly, in Fig. 6, we report the fidelities obtained for the error-correction encoding circuits generated by the QAOA with different depths. In the case of the error-correction encoding circuit, the fidelity between unitary operators V and U has been defined as $\mathcal{F} = |\mathrm{Tr}\left(V^\dagger U\right)|/\mathrm{Tr}\left(U^\dagger U\right)$.

Many time-consuming runs of the classical optimization algorithm are required to produce the plots reported in this work, with a significant number of parameter-dependent fidelities that are calculated at each depth. As a consequence, the plots show the results up to a given depth and do not necessarily show the best ones for the target circuit. However, higher depths are investigated with the even more time-consuming method that considers the

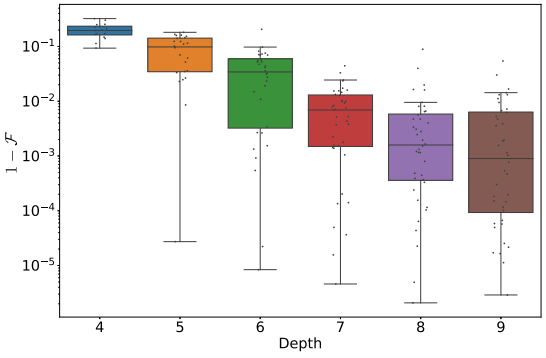

FIG. 5. One minus fidelities of the cluster states generated with the QAOA after a dual annealing optimization of the parameters, plotted against the depth of the quantum algorithm. The semilogarithmic scale emphasizes the success of this method and how it grows with the circuit depth.

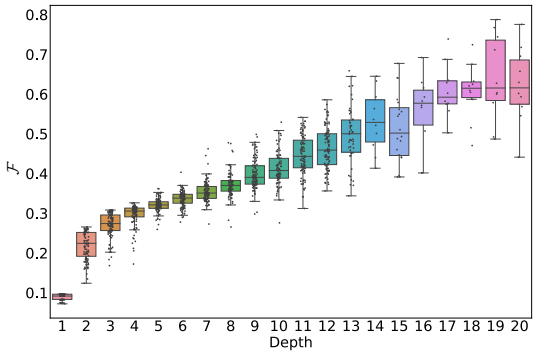

FIG. 6. The fidelities of the error-correction encoding circuit generated with the QAOA after a dual annealing optimization of the parameters versus the depth of the quantum algorithm.

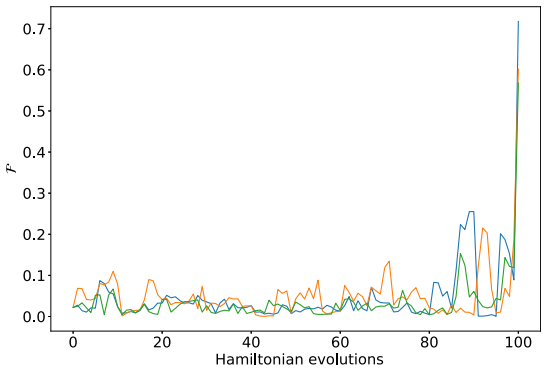

FIG. 7. A plot of the fidelities with the target error-correction encoding circuit and the operation realized after a given Hamiltonian evolution for three instances of the QAOA of depth $p = 20$. In general, the fidelity is far from its final value until the last step.

Rydberg-atom implementation as described in Sec. V. The quality of the prepared state witnesses an improvement with the depth of the algorithm in this case as well. The best results of the fidelities obtained for the error-correction encoding circuits increases linearly with a Pearson coefficient larger than 99%, from a depth $p = 18$, where $\mathcal{F} \simeq 90.0\%$, up to a depth $p = 25$, where $\mathcal{F} = 1$ is reached up to machine precision.

Each point in the scatter plots of Figs. 5 and 6 refers to a value of the fidelity that has been evaluated as a result of an optimization of the Rabi angles for the cluster state and the error-correction encoding circuit, respectively. Each optimization provides a different result because of the intrinsic randomness of the optimization algorithm that has been used. Therefore, the optimization result is not necessarily the best result possible at the given depth. In order to provide the reader with a measure of the behavior of the optimization algorithm and of the probability of getting a given result with it, we have chosen to report all of the evaluated fidelities with overlain scatter and box plots. As an alternative to this representation, we pondered about realizing the extreme-value analysis of the collected results. The extreme-value statistics would have provided the probability density of obtaining a given fidelity value after a fixed number of optimizations. In order to do so, we would need to identify the probability density that fits the observed distribution of data around the expected maximum. However, this identification has proved to be prohibitive in our case. The maximum reachable fidelity at each depth has not been identified here, with the results providing just a minimum for it. Moreover, even fixing a value for this maximum, the number of recorded fidelities is not large enough to determine the fitting parameters with satisfactory accuracy.

To gain more insight into the optimization procedure, the plot in Fig. 7 displays three examples of the evolution of the fidelity with the Perfect Quantum Error Correcting Code after each Hamiltonian evolution of the algorithm with a depth of 20. By the expression "Hamiltonian evolution," we refer to each of the terms introduced in Eq. (5). We observe that the fidelity does not increase steadily toward the final value but, instead, experiences an abrupt jump at the last step for each of the three examples. This suggests that the fidelity might not be the best measure to use to capture the path of the state toward the target. Analogously, the plots for instances with depths equal to 4, 8, 12, 16, and 20 are compared in Fig. 8. We observe that the states have unique fidelity trajectories for different depths, evolving along paths through Hilbert space that are nonmonotonic in any distance measure induced by the fidelity. Importantly, the optimal results for greater-depth circuits are not obtained by adding fine-tuning steps after the optimal results of the shorter-depth circuits; each trajectory is

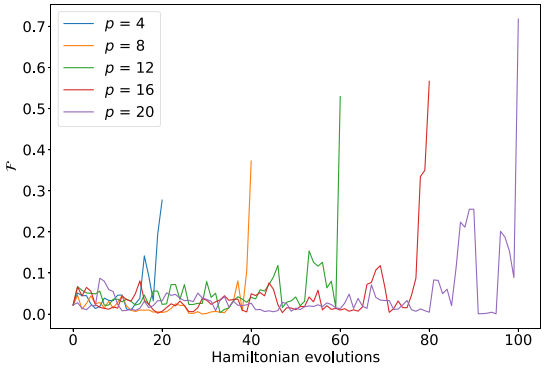

FIG. 8. A plot of the fidelities with the target error-correction encoding circuit and the operation realized after a given Hamiltonian evolution for five instances of the QAOA of depth $p = 4, 8, 12, 16$ and 20. In general, the fidelity is far from its final value until the last step.

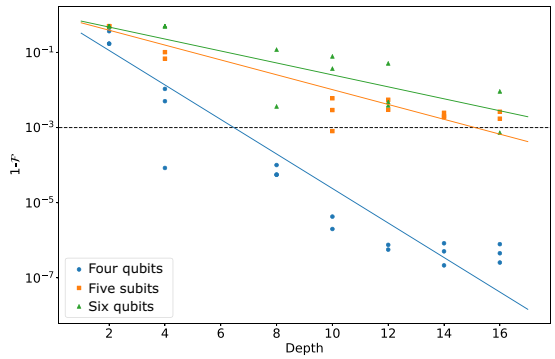

FIG. 9. The fidelities obtained by simulating control on four, five, and six Rydberg atoms to create four-, five-, and six-qubit fully connected cluster states using the QAOAs of different depths. The dots represent the classical optimization run at each depth for four-, five-, and six-qubit cluster state; the straight lines are the exponential fit of the observed data. Fixing one minus the fidelity of the initial n-qubit state to a_n, the parameters λ_n of the fitting function $a_n e^{-\lambda_n p}$ take the following values: $\lambda_4 \simeq 1.06, \lambda_5 \simeq 0.46$, and $\lambda_6 \simeq 0.37$. The line at $\mathcal{F} = 99.9\%$ highlights how systems with a smaller number of qubits reach this fidelity value at a lower depth.

unique. These counterintuitive paths demonstrate the usefulness of relying on our algorithm to find optimal control operations.

In order to evaluate how the fidelities at given depths scale with the number of qubits of the target state, we analyze the trend of the fidelities obtained by simulating control on four, five, and six Rydberg atoms, as described in Sec. IV, to realize four-, five-, and six-qubit cluster states, respectively. The results are plotted in Fig. 9. We observe that at a given depth, target states with fewer qubits can be realized with higher fidelity. We can conclude that for a given threshold fidelity, larger depths are required to realize larger qubit states. As an example, a fidelity of 99.9% is reached at depths of $p = 4$, 10, and 16 for the four-, five-, and six-qubit cluster states, respectively.

B. Robustness

In the analysis undertaken so far, no error has been introduced in the calculations but errors cannot be neglected in real-life experiments with Rydberg atoms. The lifetime of the Rydberg atoms and the Rydberg shift in the blockade are indeed the main features affecting the fidelity of the results. Therefore, a careful choice of the intensities of the pulses is crucial to increase the fidelity of the results [22]. On one hand, each intensity needs to be large enough to allow short time pulses while, on the other, we want to limit, as best as possible, the off-resonant transitions that arise from excessively strong pulses. As such, we investigate how the fidelity of the generated state and, therefore, the optimal depth of the circuit are affected by the presence of some noise in the system.

In our theoretical model, we incorporate all of the errors from different sources into deviations from the optimal parameters of the QAOA found for the noiseless system. To this end, we have exploited the periodicity over 2π of the arguments of the unitary operators in Eq. (5). Indeed, a different value randomly picked from a uniform distribution in the interval $[-\pi R, \pi R]$ is added to each parameter of every optimal sequence. The coefficient R is referred to as the magnitude of the error. When R is equal to zero, no change is made to the sequences of parameters and when R is equal to 1, the parameters turn out to be uniformly distributed in an interval of length 2π, thus losing any information about the target state. Finally, for each sequence, we calculate the fidelity of the state produced by the new set of parameters. This procedure is repeated many times for each state, in order to average over the statistical fluctuations of the simulated noise.

The differences between the results obtained with no noise and after introducing a noise level $R = 1\%$ are reported for the cluster state and the error-correction encoding circuit in Figs. 10 and 11, respectively, as a function of the depth of the circuit. For both applications, we observe a loss of fidelity that increases with the depth of the circuit. This behavior suggests the existence of a threshold depth for a given noise level that maximizes the quality of the generated state. The depths considered in this work, however, do not allow us to identify such a threshold value; one might be found by investigating the results obtained with deeper circuits. The values of fidelities with $R = 0$, 10^{-3}, and 10^{-2} reachable by the QAOA protocol for absolutely maximally entangled (AME) states with five (AME5) and six (AME6) qubits and for the GHZ state are shown in Table I.

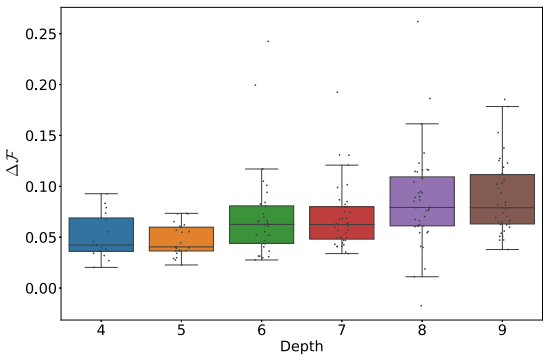

FIG. 10. Decreases in the fidelities of the cluster states generated with the QAOA after a dual annealing optimization of the parameter with noise level $R = 1\%$ relative to the same optimization without noise, plotted against the depth of the quantum algorithm.

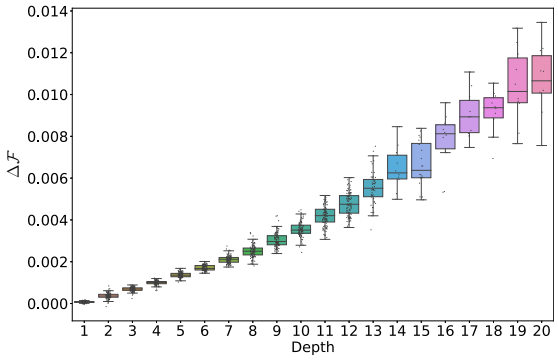

FIG. 11. The difference between the fidelities of the error-correction encoding circuit generated with the QAOA after a dual annealing optimization of the parameter without noise and with noise level $R = 1\%$ against the depth of the quantum algorithm.

C. Physical implementation

The physical implementation considered in the simulation is mostly based upon the experimental setup proposed in Ref. [16]. The isotopes of ^{87}Rb that are used as Rydberg atoms are arranged in a linear array of trough optical tweezers. The spacing is set to 5.24 μm, which results in a nearest-neighbor interaction strength of $V_{i,i+i} = 2\pi \times 24$ MHz. The equivalences between the logical and the Rydberg states and the energetic levels of the atoms are $|0\rangle = \left|5S_{1/2}, F = 2, m_F = -2\right\rangle$, $|1\rangle = \left|6SP_{13/2}, F = 3, m_F = -3\right\rangle$, and $|r\rangle = \left|70S_{1/2}, J = 1/2, m_J = -1/2\right\rangle$. The frequencies of the driving pulses from the ground to the excited state Ω_b and from the excited to the Rydberg state Ω_r are $\Omega_b = 2\pi \times 60$ MHz and $\Omega_r = 2\pi \times 36$ MHz.

With these numbers, one can use the algorithm to construct a set of pulse sequences required to create any state or enact any quantum circuit. As an example, the pulses required to prepare a five-qubit error-correction encoding circuit are reported in Fig. 12. The intensity of the laser illuminating the target qubit, in the sequences of pulses that realize the CZ operators, has been set to be smaller than the intensity used for all the other pulses, so as to minimize the possibility of off-resonant transitions when the Rydberg blockade is induced by the control qubit.

The state $|e\rangle$ is not long lived compared to the duration of the sequence or the ground ($|g\rangle$) and the Rydberg ($|r\rangle$) states. This necessitates using an ancillary pulse to coherently shuffle population between the intermediate state ($|e\rangle$) and an additional long-lived ground spin state of the Rb atom. This is routinely done in quantum memory experiments with atomic ensembles.

TABLE I. The fidelity of the generated states with and without noise.

State	Fidelity	$R = 1\%$	$R = 0.1\%$
GHZ	99.93%	97.7%	99.91%
AME5	99.9%	98.5%	99.86%
AME6	99.83%	98.3%	99.82%

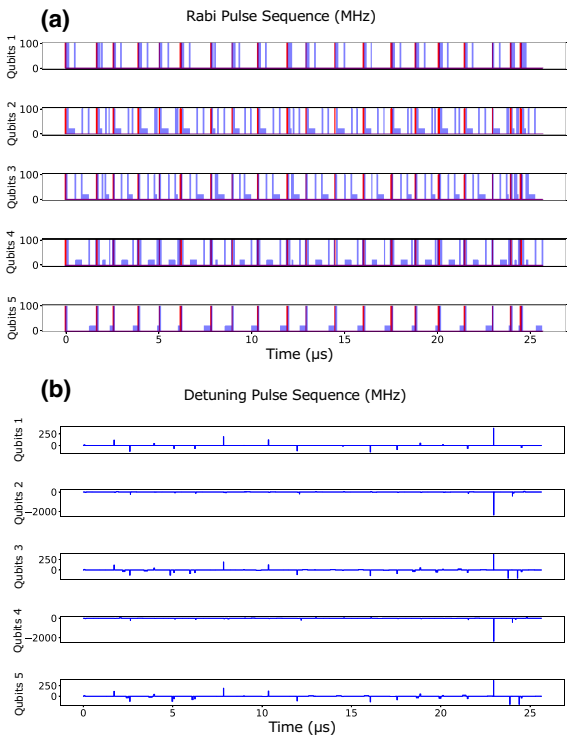

FIG. 12. (a) The Rabi-frequency pulse sequence for the generation of the error-correction encoding circuit. The pulse sequence consists of a series of square-shaped pulses acting upon the different qubits 1–5, where the red pulses refer to driving fields from $|0\rangle \mapsto |1\rangle$ and the blue pulses refer to driving fields from $|1\rangle \mapsto |r\rangle$. (b) The frequency detuning Δ of the blue pulses.

VII. DISCUSSION AND CONCLUSIONS

The quantum circuit model is the most common model of quantum computation. It makes use of multiqubit states on which the information is encoded, processed, and extracted and quantum circuits that realize these operations. Therefore, the quantum state and the circuit generation are crucial prerequisites for efficient quantum computation. As an example, entangled states are an especially precious resource for quantum computation without any classical counterpart. However, their preparation turns out to be, in general, a complex task that might require significant resources to be realized [41]. Our state-generation scheme with the QAOA aims to overcome these challenges by employing a classical optimization of the parameters and a widely used physical implementation.

The universality of the QAOA is the main cue for the realization of universal quantum control with this algorithm. The protocol proposed in this work guarantees that any n-qubit state can be achieved with the desired approximation just by using local and two-local interactions among qubits. The depth of the circuit and the interaction times are determined according to the target state and the fidelity that the experimenter wants to reach. The theoretical description of the scheme and the efficiency in its abstract formulation are independent of the possible implementation. Only once a physical setup is chosen for the implementation of the scheme must a proper, eventually nontrivial, mapping of the parameters in terms of the system Hamiltonian be taken into account. An array of Rydberg atoms, where the two-atom interaction is realized through the Rydberg-blockade phenomenon, is chosen for its popularity.

The results achieved for the quantum states taken into consideration show that quantum control with the QAOA can be a valid scheme for many applications. The efficacy of the scheme appears more clearly when one wants to initialize more complex states, e.g., with a higher entanglement, and where other protocols require a significant amount of resources. Indeed, it is less affected by the state that must be initialized; it operates on a widely employed implementation that requires just nearest-neighbor interactions and a limited number of pulses to produce highly entangled quantum states and even a five-qubit quantum circuit with a significant number of gates. The fidelity of the states and circuits might be further increased through a more reliable optimization of the parameters realizable with more computational power and advanced optimization protocols.

The simulation that supports the findings of this study is openly available on GitHub [42].

ACKNOWLEDGMENTS

We acknowledge that the National Research Council headquarters is located on the traditional unceded territory of the Algonquin Anishinaabe and Mohawk people. This work was supported by the Natural Sciences and Engineering Research Council of Canada (NSERC) through its Discovery Grant (DG) program and Postdoctoral Fellowships (PDF) program.

[1] M. A. Nielsen and I. Chuang, *Quantum Computation and Quantum Information* (Cambridge University Press, Cambridge, 2002).

[2] R. Raussendorf and H. J. Briegel, A one-way quantum computer, Phys. Rev. Lett. **86**, 5188 (2001).

[3] H. J. Briegel, D. E. Browne, W. Dür, R. Raussendorf, and M. Van den Nest, Measurement-based quantum computation, Nat. Phys. **5**, 19 (2009).

[4] R. Acharya, I. Aleiner, R. Allen, T. I. Andersen, M. Ansmann, F. Arute, K. Arya, A. Asfaw, J. Atalaya, and R. Babbush *et al.*, Suppressing quantum errors by scaling a surface code logical qubit, arXiv preprint arXiv:2207.06431 (2022).

[5] S. Krinner, N. Lacroix, A. Remm, A. Di Paolo, E. Genois, C. Leroux, C. Hellings, S. Lazar, F. Swiadek, J. Herrmann, G. J. Norris, C. K. Andersen, M. Müller, A. Blais, C. Eichler, and A. Wallraff, Realizing repeated quantum error correction in a distance-three surface code, Nature **605**, 669 (2022).

[6] J. Benhelm, G. Kirchmair, C. F. Roos, and R. Blatt, Towards fault-tolerant quantum computing with trapped ions, Nat. Phys. **4**, 463 (2008).

[7] L. Postler, S. Heußen, I. Pogorelov, M. Rispler, T. Feldker, M. Meth, C. D. Marciniak, R. Stricker, M. Ringbauer, R. Blatt, P. Schindler, M. Müller, and T. Monz, Demonstration of fault-tolerant universal quantum gate operations, Nature **605**, 675 (2022).

[8] I. Cong, H. Levine, A. Keesling, D. Bluvstein, S.-T. Wang, and M. D. Lukin, Hardware-Efficient, Fault-Tolerant Quantum Computation with Rydberg Atoms, Phys. Rev. X **12**, 021049 (2022).

[9] C. Ryan-Anderson, J. G. Bohnet, K. Lee, D. Gresh, A. Hankin, J. P. Gaebler, D. Francois, A. Chernoguzov, D. Lucchetti, N. C. Brown, T. M. Gatterman, S. K. Halit, K. Gilmore, J. A. Gerber, B. Neyenhuis, D. Hayes, and R. P. Stutz, Realization of Real-Time Fault-Tolerant Quantum Error Correction, Phys. Rev. X **11**, 041058 (2021).

[10] J. E. Bourassa, R. N. Alexander, M. Vasmer, A. Patil, I. Tzitrin, T. Matsuura, D. Su, B. Q. Baragiola, S. Guha, G. Dauphinais, K. K. Sabapathy, N. C. Menicucci, and I. Dhand, Blueprint for a scalable photonic fault-tolerant quantum computer, Quantum **5**, 392 (2021).

[11] L. M. K. Vandersypen and I. L. Chuang, Nmr techniques for quantum control and computation, Rev. Mod. Phys. **76**, 1037 (2005).

[12] E. Zahedinejad, J. Ghosh, and B. C. Sanders, High-Fidelity Single-Shot Toffoli Gate via Quantum Control, Phys. Rev. Lett. **114**, 200502 (2015).

[13] H. Ball, M. J. Biercuk, A. R. Carvalho, J. Chen, M. Hush, L. A. De Castro, L. Li, P. J. Liebermann, H. J. Slatyer, C. Edmunds, V. Frey, C. Hempel, and A. Milne, Software tools for quantum control: Improving quantum computer performance through noise and error suppression, Quantum Sci. Technol. **6**, 044011 (2021).

[14] E. Farhi, J. Goldstone, and S. Gutmann, A quantum approximate optimization algorithm, arXiv:1411.4028 [quant-ph] (2014).

[15] S. Lloyd, Quantum approximate optimization is computationally universal, arXiv:1812.11075 [quant-ph] (2018).

[16] H. Bernien, S. Schwartz, A. Keesling, H. Levine, A. Omran, H. Pichler, S. Choi, A. S. Zibrov, M. Endres, M. Greiner, V. Vuletić, and M. D. Lukin, Probing many-body dynamics on a 51-atom quantum simulator, Nature **551**, 579 (2017).

[17] A. Keesling, A. Omran, H. Levine, H. Bernien, H. Pichler, S. Choi, R. Samajdar, S. Schwartz, P. Silvi, S. Sachdev, P. Zoller, M. Endres, M. Greiner, V. Vuletić, and M. D. Lukin, Quantum Kibble-Zurek mechanism and critical dynamics

on a programmable Rydberg simulator, Nature **568**, 207 (2019).
[18] A. Browaeys and T. Lahaye, Many-body physics with individually controlled Rydberg atoms, Nat. Phys. **16**, 132 (2020).
[19] S. Ebadi, T. T. Wang, H. Levine, A. Keesling, G. Semeghini, A. Omran, D. Bluvstein, R. Samajdar, H. Pichler, W. W. Ho, S. Choi, S. Sachdev, M. Greiner, V. Vuletić, and M. D. Lukin, Quantum phases of matter on a 256-atom programmable quantum simulator, Nature **595**, 227 (2021).
[20] P. Scholl, M. Schuler, H. J. Williams, A. A. Eberharter, D. Barredo, K.-N. Schymik, V. Lienhard, L.-P. Henry, T. C. Lang, T. Lahaye, A. M. Läuchli, and A. Browaeys, Quantum simulation of 2D antiferromagnets with hundreds of Rydberg atoms, Nature **595**, 233 (2021).
[21] J. Taylor, S. Goswami, V. Walther, M. Spanner, C. Simon, and K. Heshami, Simulation of many-body dynamics using Rydberg excitons, Quantum Sci. Technol. **7**, 035016 (2022).
[22] X. L. Zhang, A. T. Gill, L. Isenhower, T. G. Walker, and M. Saffman, Fidelity of a Rydberg-blockade quantum gate from simulated quantum process tomography, Phys. Rev. A **85**, 042310 (2012).
[23] M. Saffman, T. G. Walker, and K. Mølmer, Quantum information with Rydberg atoms, Rev. Mod. Phys. **82**, 2313 (2010).
[24] N. Šibalić and C. S. Adams, *Rydberg Physics* (IOP Publishing, Bristol, 2018).
[25] D. Jaksch, J. I. Cirac, P. Zoller, S. L. Rolston, R. Côté, and M. D. Lukin, Fast Quantum Gates for Neutral Atoms, Phys. Rev. Lett. **85**, 2208 (2000).
[26] M. Saffman, T. G. Walker, and K. Mølmer, Quantum information with Rydberg atoms, Rev. Mod. Phys. **82**, 2313 (2010).
[27] S.-L. Su, E. Liang, S. Zhang, J.-J. Wen, L.-L. Sun, Z. Jin, and A.-D. Zhu, One-step implementation of the Rydberg-Rydberg-interaction gate, Phys. Rev. A **93**, 012306 (2016).
[28] A. Omran, H. Levine, A. Keesling, G. Semeghini, T. T. Wang, S. Ebadi, H. Bernien, A. S. Zibrov, H. Pichler, S. Choi, J. Cui, M. Rossignolo, P. Rembold, S. Montangero, T. Calarco, M. Endres, M. Greiner, V. Vuletić, and M. D. Lukin, Generation and manipulation of Schrödinger cat states in Rydberg atom arrays, Science **365**, 570 (2019).
[29] D. Bluvstein, H. Levine, G. Semeghini, T. T. Wang, S. Ebadi, M. Kalinowski, A. Keesling, N. Maskara, H. Pichler, M. Greiner, V. Vuletić, and M. D. Lukin, A quantum processor based on coherent transport of entangled atom arrays, Nature **604**, 451 (2022).
[30] I. S. Madjarov, J. P. Covey, A. L. Shaw, J. Choi, A. Kale, A. Cooper, H. Pichler, V. Schkolnik, J. R. Williams, and M. Endres, High-fidelity entanglement and detection of alkaline-earth Rydberg atoms, Nat. Phys. **16**, 857 (2020).
[31] H. L. Haselgrove, M. A. Nielsen, and T. J. Osborne, Quantum States far from the Energy Eigenstates of Any Local Hamiltonian, Phys. Rev. Lett. **91**, 210401 (2003).
[32] T. Kadowaki and H. Nishimori, Quantum annealing in the transverse Ising model, Phys. Rev. E **58**, 5355 (1998).
[33] R. Verresen, Everything is a quantum Ising model, arxiv:2301.11917 (2023).
[34] D. Panchenko, The Sherrington-Kirkpatrick model: An overview, J. Stat. Phys. **149**, 362 (2012).
[35] M. Dupont, N. Didier, M. J. Hodson, J. E. Moore, and M. J. Reagor, Entanglement perspective on the quantum approximate optimization algorithm, Phys. Rev. A **106**, 022423 (2022).
[36] L. Piroli, G. Styliaris, and J. I. Cirac, Quantum Circuits Assisted by Local Operations and Classical Communication: Transformations and Phases of Matter, Phys. Rev. Lett. **127**, 220503 (2021).
[37] L. Isenhower, M. Saffman, and K. Mølmer, Multibit C_kNOT quantum gates via Rydberg blockade, Quantum Inf. Process. **10**, 755 (2011).
[38] M. Schäfer and F. Merkt, in *Frontiers of Molecular Spectroscopy*, edited by J. Laane (Elsevier, Amsterdam, 2009), p. 35.
[39] H. J. Briegel and R. Raussendorf, Persistent Entanglement in Arrays of Interacting Particles, Phys. Rev. Lett. **86**, 910 (2001).
[40] R. Laflamme, C. Miquel, J. P. Paz, and W. H. Zurek, Perfect Quantum Error Correcting Code, Phys. Rev. Lett. **77**, 198 (1996).
[41] M. Li and Y. Shang, Entangled state generation via quantum walks with multiple coins, npj Quantum Inf. **7**, 70 (2021).
[42] https://github.com/jtaylormade/RydbergAtomQuantumControl

Chapter 6

Conclusion

This thesis dealt with the preparation of quantum states in photonic and Rydberg atom implementations. In chapters 2 and 3, two alternative sources of non-Gaussian states that are necessary to realize universal quantum computation are proposed. Specifically, GKP states and Schrödinger cat states have been chosen as targets of the simulations for their role in fault-tolerant quantum computation, among other applications. For both schemes, the simulations reveal that the alternative sources guarantee a significant advantage over the conditional source on which they are based. The results on the circuit with non-Gaussian inputs, as well as the source relying on adaptive tuning of the parameters, also suggest that the efficiency and the advantage over the original source can be further increased by using larger circuits. Chapter 4, instead, focuses on the exact simulations of GKP states realized with the cat breeding protocol. The breeding protocol is used, for example, by Xanadu together with a conditional generation realized with PNRD to generate the GKP states that form the cluster used in the computation. Yet, the description of the states is in general approximate, since it is given in terms of Gaussian Random Noise states. The manuscript instead shows the discrepancies revealed by numerical simulation and the

expectation values of stabilizer operators calculated by manipulations of GRN states, and provides the analytical description that allows one to find the stabilizers analytically. The manipulation of Rydberg atoms to prepare any state or qubit is finally proposed in the last chapter. The results show the versatility of the QAOA, which allows one to approximate any state with arbitrary precision. Moreover, the scheme is not constrained to fulfill a possibly challenging-to-realize sequence of gates, and it can be adapted to general experimental parameters and geometries of the Rydberg atoms.

6.1 Outlook

While this thesis addresses the research carried out up to this point, additional work is currently underway within the group. Specifically, further research is being conducted to use the GBS and GBS-like devices introduced in the thesis as conditional sources of non-Gaussian states to realize quantum reservoir computing in photonic implementation by encoding the information into the parameters of the input states or the passive interferometer.

Preliminary results suggest that the determination of the encoding of the information into the parameters of the GBS setup is crucial to establish an advantage over classical schemes. However, the early results reveal an advantage when comparing the time series predicted with a GBS reservoir and the series achievable using only linear regression.

Another project, in collaboration with Prof. Stephan de Bièvre from the University of Lille, involves the characterization of Cubic Gaussian states. In particular, numerical simulations are employed to determine the entanglement produced when two cubic Gaussian states are interfered in a beam splitter. The results are then

compared with other common CV states.

Finally, in September, a collaboration with Xanadu will start on quantum computation with non-Gaussian resource states. The aim is to introduce new metrics and figures of merit for the quality of the error-correcting states, which may lead to the identification of novel state sources that are more efficient and robust.

References

[1] D. J. Griffiths and D. F. Schroeter, *Introduction to quantum mechanics*. Cambridge university press, 2018.

[2] D. B. Skinner, *Principles of quantum mechanics: Part II*, 2021.

[3] P. A. M. Dirac, *A new notation for quantum mechanics*, *Mathematical Proceedings of the Cambridge Philosophical Society* **35** (1939), no. 3 416–418.

[4] D. Poulin and R. Blume-Kohout, *Compatibility of quantum states*, *Physical Review A* **67** (2003), no. 1 010101.

[5] J. J. Sakurai and J. Napolitano, *Modern Quantum Mechanics*. Cambridge University Press, 3 ed., 2020.

[6] R. Shankar, *Principles of quantum mechanics*. Springer Science & Business Media, 2012.

[7] G. Teschl, *Mathematical methods in quantum mechanics*, vol. 157. American Mathematical Soc., 2014.

[8] J. Pade, *Quantum mechanics for pedestrians 1: Fundamentals*. Springer, 2018.

[9] M. A. Nielsen and I. L. Chuang, *Quantum computation and quantum information*. Cambridge university press, 2010.

[10] B. Schumacher, *Quantum coding*, *Phys. Rev. A* **51** (Apr, 1995) 2738–2747.

[11] D. Gottesman, *The heisenberg representation of quantum computers*, 1998.

[12] A. Y. Kitaev, *Quantum computations: algorithms and error correction*, *Russian Mathematical Surveys* **52** (1997), no. 6 1191.

[13] T. Kadowaki and H. Nishimori, *Quantum annealing in the transverse ising model*, *Phys. Rev. E* **58** (Nov, 1998) 5355–5363.

[14] S. Hadfield, Z. Wang, B. O'Gorman, E. G. Rieffel, D. Venturelli, and R. Biswas, *From the quantum approximate optimization algorithm to a quantum alternating operator ansatz*, *Algorithms* **12** (2019), no. 2.

[15] P. Díez-Valle, F. J. Gómez-Ruiz, D. Porras, and J. J. García-Ripoll, *Universal resources for qaoa and quantum annealing*, 2025.

[16] E. Farhi, J. Goldstone, and S. Gutmann, *A quantum approximate optimization algorithm*, 2014.

[17] S. Lloyd, *Quantum approximate optimization is computationally universal*, 2018.

[18] H. M. Wiseman and G. J. Milburn, *Quantum Measurement and Control*. Cambridge University Press, 2009.

[19] N. Bohr, *I. on the constitution of atoms and molecules*, *The London, Edinburgh, and Dublin Philosophical Magazine and Journal of Science* **26** (1913), no. 151 1–25.

[20] L. Ortiz-Gutiérrez, B. Gabrielly, L. F. Muñoz, K. T. Pereira, J. G. Filgueiras, and A. S. Villar, *Continuous variables quantum computation over the vibrational modes of a single trapped ion*, *Optics Communications* **397** (2017) 166–174.

[21] S. L. Braunstein and P. van Loock, *Quantum information with continuous variables*, *Rev. Mod. Phys.* **77** (Jun, 2005) 513–577.

[22] C. Gerry and P. Knight, *Introductory Quantum Optics*. Cambridge University Press, 2004.

[23] L. Mandel and E. Wolf, *Optical Coherence and Quantum Optics*. Cambridge University Press, 1995.

[24] M. O. Scully and M. S. Zubairy, *Quantum Optics*. Cambridge University Press, 1997.

[25] R. A. Bertlmann, "Theoretical physics T2 quantum mechanics."

[26] U. Leonhardt, *Essential Quantum Optics: From Quantum Measurements to Black Holes*. Cambridge University Press, 2010.

[27] M. Reck, A. Zeilinger, H. J. Bernstein, and P. Bertani, *Experimental realization of any discrete unitary operator*, *Phys. Rev. Lett.* **73** (Jul, 1994) 58–61.

[28] P. Kok, W. J. Munro, K. Nemoto, T. C. Ralph, J. P. Dowling, and G. J. Milburn, *Linear optical quantum computing with photonic qubits*, *Rev. Mod. Phys.* **79** (Jan, 2007) 135–174.

[29] J. C. Garcia-Escartin, V. Gimeno, and J. J. Moyano-Fernández, *Multiple photon effective hamiltonians in linear quantum optical networks*, *Optics Communications* **430** (2019) 434–439.

[30] W. R. Clements, *Linear Quantum Optics: Components and Applications*. PhD thesis, University of Oxford, 2018.

[31] S. L. Braunstein, *Squeezing as an irreducible resource*, *Phys. Rev. A* **71** (May, 2005) 055801.

[32] M. Reck, A. Zeilinger, H. J. Bernstein, and P. Bertani, *Experimental realization of any discrete unitary operator*, *Physical review letters* **73** (1994), no. 1 58.

[33] J. B. Brask, *Gaussian states and operations–a quick reference*, *arXiv preprint arXiv:2102.05748* (2021).

[34] C. Weedbrook, S. Pirandola, R. García-Patrón, N. J. Cerf, T. C. Ralph, J. H. Shapiro, and S. Lloyd, *Gaussian quantum information*, *Rev. Mod. Phys.* **84** (May, 2012) 621–669.

[35] A. Z. Goldberg and D. F. V. James, *Nonclassical mixed states that generate zero entanglement with a beam splitter*, *Journal of Physics A: Mathematical and Theoretical* **51** (aug, 2018) 385303.

[36] E. Knill, R. Laflamme, and G. Milburn, *Efficient linear optics quantum computation*, 2000.

[37] R. Schnabel, *Squeezed states of light and their applications in laser interferometers*, *Physics Reports* **684** (2017) 1–51.

[38] A. Z. Goldberg and K. Heshami, *How squeezed states both maximize and minimize the same notion of quantumness*, *Phys. Rev. A* **104** (Sep, 2021) 032425.

[39] M. G. Paris, *Displacement operator by beam splitter*, *Physics Letters A* **217** (1996), no. 2 78–80.

[40] M. Houde and N. Quesada, *Perfect pulsed inline twin-beam squeezers*, *AVS Quantum Science* **6** (06, 2024) 021402, https://pubs.aip.org/avs/aqs/article-pdf/doi/10.1116/5.0203013/19979873/0214

[41] T. Yoshida, D. Okuno, T. Kashiwazaki, T. Umeki, S. Miki, F. China, M. Yabuno, H. Terai, and S. Takeda, *Sequential and programmable squeezing gates for optical non-gaussian input states*, *PRX Quantum* **6** (Jan, 2025) 010311.

[42] T. Tyc and B. C. Sanders, *Operational formulation of homodyne detection*, *Journal of Physics A: Mathematical and General* **37** (jul, 2004) 7341.

[43] M. Jönsson and G. Björk, *Evaluating the performance of photon-number-resolving detectors*, *Phys. Rev. A* **99** (Apr, 2019) 043822.

[44] N. M. Sullivan, B. Braverman, J. Upham, and R. W. Boyd, *Photon number resolving detection with a single-photon detector and adaptive storage loop*, *New Journal of Physics* **26** (may, 2024) 043026.

[45] J. Xuereb, "Notes on quantum optics." Lecture notes, 2021.

[46] M. M. Wilde, "Lecture 13-14." Lecture notes, PHYS 7895: Gaussian Quantum Information, Cornell University, 2023.

[47] A. Serafini, *Quantum continuous variables: a primer of theoretical methods*. CRC press, 2023.

[48] U. Chabaud, *Continuous Variable Quantum Advantages and Applications in Quantum Optics*. PhD thesis, Sorbonne Université, 2020.

[49] K. E. Cahill and R. J. Glauber, *Density operators and quasiprobability distributions*, *Phys. Rev.* **177** (Jan, 1969) 1882–1902.

[50] K. Husimi, *Some formal properties of the density matrix*, *Proceedings of the Physico-Mathematical Society of Japan. 3rd Series* **22** (1940), no. 4 264–314.

[51] G. Ferrari, *Optical non-classicality as a quantum resource in continuous-variable quantum information*, .

[52] C. Bloch and A. Messiah, *The canonical form of an antisymmetric tensor and its application to the theory of superconductivity*, *Nuclear Physics* **39** (1962) 95–106.

[53] M. Walschaers, *Non-gaussian quantum states and where to find them*, *PRX quantum* **2** (2021), no. 3 030204.

[54] S. Lloyd and S. L. Braunstein, *Quantum computation over continuous variables*, *Phys. Rev. Lett.* **82** (Feb, 1999) 1784–1787.

[55] C. N. Gagatsos and S. Guha, *Impossibility to produce arbitrary non-gaussian states using zero-mean gaussian states and partial photon number resolving detection*, *Phys. Rev. Res.* **3** (Dec, 2021) 043182.

[56] V. V. Dodonov, O. V. Man'ko, and V. I. Man'ko, *Multidimensional hermite polynomials and photon distribution for polymode mixed light*, *Phys. Rev. A* **50** (Jul, 1994) 813–817.

[57] D. Su, C. R. Myers, and K. K. Sabapathy, *Conversion of gaussian states to non-gaussian states using photon-number-resolving detectors*, *Phys. Rev. A* **100** (Nov, 2019) 052301.

[58] R. Hudson, *When is the wigner quasi-probability density non-negative?*, *Reports on Mathematical Physics* **6** (1974), no. 2 249–252.

[59] F. Soto and P. Claverie, *When is the wigner function of multidimensional systems nonnegative?*, *Journal of Mathematical Physics* **24** (01, 1983) 97–100, [https://pubs.aip.org/aip/jmp/article-pdf/24/1/97/19128812/97_1_online.pdf].

[60] D. Gottesman, A. Kitaev, and J. Preskill, *Encoding a qubit in an oscillator*, *Phys. Rev. A* **64** (Jun, 2001) 012310.

[61] B. Q. Baragiola, G. Pantaleoni, R. N. Alexander, A. Karanjai, and N. C. Menicucci, *All-gaussian universality and fault tolerance with the gottesman-kitaev-preskill code*, *Phys. Rev. Lett.* **123** (Nov, 2019) 200502.

[62] A. Giani, M. Z. Win, and A. Conti, *Quantum sensing and communication via non-gaussian states*, *IEEE Journal on Selected Areas in Information Theory* **6** (2025) 18–33.

[63] S. M. Barnett and P. M. Radmore, *Methods in Theoretical Quantum Optics*. Oxford University Press, 11, 2002.

[64] E. Schrödinger, *Die gegenwärtige situation in der quantenmechanik*, *Naturwissenschaften* **23** (1935), no. 50 844–849.

[65] J. Paavola, M. J. W. Hall, M. G. A. Paris, and S. Maniscalco, *Finite-time quantum-to-classical transition for a schrödinger-cat state*, *Phys. Rev. A* **84** (Jul, 2011) 012121.

[66] K. K. Mishra, D. Yadav, G. Shukla, and D. K. Mishra, *Non-classicalities exhibited by the superposition of schrödinger's cat state with the vacuum of the optical field*, *Physica Scripta* **96** (2021), no. 4 045102.

[67] L. Maccone, *Schrödinger cats and quantum complementarity*, *Foundations of Physics* **54** (2024), no. 1 17.

[68] A. P. Lund, T. C. Ralph, and H. L. Haselgrove, *Fault-tolerant linear optical quantum computing with small-amplitude coherent states*, *Phys. Rev. Lett.* **100** (Jan, 2008) 030503.

[69] T. C. Ralph, A. Gilchrist, G. J. Milburn, W. J. Munro, and S. Glancy, *Quantum computation with optical coherent states*, *Phys. Rev. A* **68** (Oct, 2003) 042319.

[70] M. Mirrahimi, *Cat-qubits for quantum computation*, *Comptes Rendus. Physique* **17** (2016), no. 7 778–787.

[71] J. Joo, W. J. Munro, and T. P. Spiller, *Quantum metrology with entangled coherent states*, *Phys. Rev. Lett.* **107** (Aug, 2011) 083601.

[72] A. Facon, E.-K. Dietsche, D. Grosso, S. Haroche, J.-M. Raimond, M. Brune, and S. Gleyzes, *A sensitive electrometer based on a rydberg atom in a schrödinger-cat state*, *Nature* **535** (2016), no. 7611 262–265.

[73] B. Hacker, S. Welte, S. Daiss, A. Shaukat, S. Ritter, L. Li, and G. Rempe, *Deterministic creation of entangled atom–light schrödinger-cat states*, *Nature Photonics* **13** (2019), no. 2 110–115.

[74] F. Schmidt, D. Miller, and P. van Loock, *Error-corrected quantum repeaters with gkp qudits*, 2023.

[75] I. Tzitrin, J. E. Bourassa, N. C. Menicucci, and K. K. Sabapathy, *Progress towards practical qubit computation using approximate gottesman-kitaev-preskill codes*, *Phys. Rev. A* **101** (Mar, 2020) 032315.

[76] S. D. Bartlett, B. C. Sanders, S. L. Braunstein, and K. Nemoto, *Efficient classical simulation of continuous variable quantum information processes*, *Phys. Rev. Lett.* **88** (Feb, 2002) 097904.

[77] M. Gu, C. Weedbrook, N. C. Menicucci, T. C. Ralph, and P. van Loock, *Quantum computing with continuous-variable clusters*, *Phys. Rev. A* **79** (Jun, 2009) 062318.

[78] P. Marek, R. Filip, and A. Furusawa, *Deterministic implementation of weak quantum cubic nonlinearity*, *Phys. Rev. A* **84** (Nov, 2011) 053802.

[79] K. Marshall, R. Pooser, G. Siopsis, and C. Weedbrook, *Repeat-until-success cubic phase gate for universal continuous-variable quantum computation*, *Phys. Rev. A* **91** (Mar, 2015) 032321.

[80] M. Takeoka and M. Sasaki, *Conditional generation of an arbitrary superposition of coherent states*, *Phys. Rev. A* **75** (Jun, 2007) 064302.

[81] M. Eaton, R. Nehra, and O. Pfister, *Non-gaussian and gottesman–kitaev–preskill state preparation by photon catalysis*, *New Journal of Physics* **21** (nov, 2019) 113034.

[82] A. J. Pizzimenti, J. M. Lukens, H.-H. Lu, N. A. Peters, S. Guha, and C. N. Gagatsos, *Non-gaussian photonic state engineering with the quantum frequency processor*, *Phys. Rev. A* **104** (Dec, 2021) 062437.

[83] K. Takase, K. Fukui, A. Kawasaki, W. Asavanant, M. Endo, J.-i. Yoshikawa, P. van Loock, and A. Furusawa, *Gottesman-kitaev-preskill qubit synthesizer for propagating light*, *npj Quantum Information* **9** (2023), no. 1 98.

[84] W. Asavanant and A. Furusawa, *Optical Quantum Computers: A Route to Practical Continuous Variable Quantum Information Processing*. AIP Publishing LLC, 2022.

[85] J. F. F. Bulmer, B. A. Bell, R. S. Chadwick, A. E. Jones, D. Moise, A. Rigazzi, J. Thorbecke, U.-U. Haus, T. V. Vaerenbergh, R. B. Patel, I. A. Walmsley, and A. Laing, *The boundary for quantum advantage in gaussian boson sampling*, *Science Advances* **8** (2022), no. 4 eabl9236, [https://www.science.org/doi/pdf/10.1126/sciadv.abl9236].

[86] B. T. Gard, K. R. Motes, J. P. Olson, P. P. Rohde, and J. P. Dowling, *An Introduction to Boson-Sampling*, ch. Chapter 8, pp. 167–192. World Scientific, 2015. https://www.worldscientific.com/doi/pdf/10.1142/9789814678704_0008.

[87] A. P. Lund, M. J. Bremner, and T. C. Ralph, *Quantum sampling problems, bosonsampling and quantum supremacy*, *npj Quantum Information* **3** (2017), no. 1 15.

[88] D. Grier, D. J. Brod, J. M. Arrazola, M. B. de Andrade Alonso, and N. Quesada, *The complexity of bipartite gaussian boson sampling*, *Quantum* **6** (2022) 863.

[89] A. Barvinok, *Combinatorics and complexity of partition functions*, vol. 30. Springer, 2016.

[90] M. Schuld, K. Brádler, R. Israel, D. Su, and B. Gupt, *Measuring the similarity of graphs with a gaussian boson sampler*, *Phys. Rev. A* **101** (Mar, 2020) 032314.

[91] N. R. Solomons, *Applications of Gaussian boson sampling in graph theory*. PhD thesis, University of Bristol, 2024.

[92] N. Quesada and J. M. Arrazola, *Exact simulation of gaussian boson sampling in polynomial space and exponential time*, *Phys. Rev. Res.* **2** (Apr, 2020) 023005.

[93] S. Jahangiri, J. M. Arrazola, N. Quesada, and N. Killoran, *Point processes with gaussian boson sampling*, *Phys. Rev. E* **101** (Feb, 2020) 022134.

[94] N. Quesada, R. S. Chadwick, B. A. Bell, J. M. Arrazola, T. Vincent, H. Qi, and R. García−Patrón, *Quadratic speed-up for simulating gaussian boson sampling*, *PRX Quantum* **3** (Jan, 2022) 010306.

[95] Z. Kolarovszki, Á. Kaposi, T. Kozsik, and Z. Zimborás, *Simulating sparse and shallow gaussian boson sampling*, in *International Conference on Computational Science*, pp. 209–223, Springer, 2023.

[96] T.-Y. Yang and X.-B. Wang, *Speeding up the classical simulation of gaussian boson sampling with limited connectivity*, *Scientific Reports* **14** (2024), no. 1 7680.

[97] M. Tillmann, B. Dakić, R. Heilmann, S. Nolte, A. Szameit, and P. Walther, *Experimental boson sampling*, *Nature photonics* **7** (2013), no. 7 540–544.

[98] J. B. Spring, B. J. Metcalf, P. C. Humphreys, W. S. Kolthammer, X.-M. Jin, M. Barbieri, A. Datta, N. Thomas-Peter, N. K. Langford, D. Kundys, J. C. Gates, B. J. Smith, P. G. R. Smith, and I. A. Walmsley, *Boson sampling on a photonic chip*, *Science* **339** (2013), no. 6121 798–801, [https://www.science.org/doi/pdf/10.1126/science.1231692].

[99] M. A. Broome, A. Fedrizzi, S. Rahimi-Keshari, J. Dove, S. Aaronson, T. C. Ralph, and A. G. White, *Photonic boson sampling in a tunable circuit*, *Science* **339** (2013), no. 6121 794–798, [https://www.science.org/doi/pdf/10.1126/science.1231440].

[100] M. Bentivegna, N. Spagnolo, C. Vitelli, F. Flamini, N. Viggianiello, L. Latmiral, P. Mataloni, D. J. Brod, E. F. Galvão, A. Crespi, R. Ramponi, R. Osellame, and F. Sciarrino, *Experimental scattershot boson sampling*, *Science Advances* **1** (2015), no. 3 e1400255, [https://www.science.org/doi/pdf/10.1126/sciadv.1400255].

[101] H.-S. Zhong, H. Wang, Y.-H. Deng, M.-C. Chen, L.-C. Peng, Y.-H. Luo, J. Qin, D. Wu, X. Ding, Y. Hu, et al., *Quantum computational advantage using photons*, *Science* **370** (2020), no. 6523 1460–1463.

[102] U. Chabaud, D. Markham, and F. Grosshans, *Stellar representation of non-gaussian quantum states*, *Phys. Rev. Lett.* **124** (Feb, 2020) 063605.

[103] H. M. Vasconcelos, L. Sanz, and S. Glancy, *All-optical generation of states for "encoding a qubit in an oscillator"*, *Opt. Lett.* **35** (Oct, 2010) 3261–3263.

[104] Y. Zheng, A. Ferraro, A. F. Kockum, and G. Ferrini, *Gaussian conversion protocol for heralded generation of generalized gottesman-kitaev-preskill states*, *Phys. Rev. A* **108** (Jul, 2023) 012603.

[105] S. Konno, W. Asavanant, F. Hanamura, H. Nagayoshi, K. Fukui, A. Sakaguchi, R. Ide, F. China, M. Yabuno, S. Miki, et al., *Logical states for fault-tolerant quantum computation with propagating light*, *Science* **383** (2024), no. 6680 289–293.

[106] M. S. Winnel, J. J. Guanzon, D. Singh, and T. C. Ralph, *Deterministic preparation of optical squeezed cat and gottesman-kitaev-preskill states*, *Phys. Rev. Lett.* **132** (Jun, 2024) 230602.

[107] A. J. Pizzimenti and D. Soh, *Optical gottesman-kitaev-preskill qubit generation via approximate squeezed coherent state superposition breeding*, 2025.

[108] D. J. Weigand and B. M. Terhal, *Generating grid states from schrödinger-cat states without postselection*, *Phys. Rev. A* **97** (Feb, 2018) 022341.

[109] N. Šibalic and C. S. Adams, *Rydberg physics*, *Rydberg physics* (2018) 2399–2891.

[110] J. Yuan, W. Yang, M. Jing, H. Zhang, Y. Jiao, W. Li, L. Zhang, L. Xiao, and S. Jia, *Quantum sensing of microwave electric fields based on rydberg atoms*, *Reports on Progress in Physics* **86** (2023), no. 10 106001.

[111] T. F. Gallagher, *Rydberg atoms*, *Reports on Progress in Physics* **51** (feb, 1988) 143.

[112] C. S. Adams, J. D. Pritchard, and J. P. Shaffer, *Rydberg atom quantum technologies*, *Journal of Physics B: Atomic, Molecular and Optical Physics* **53** (dec, 2019) 012002.

[113] J. Marshall and N. Anand, *Simulation of quantum optics by coherent state decomposition*, *Optica Quantum* **1** (Dec, 2023) 78–93.